Fluid Flow Processes Within Gas-solids Fluidized Beds

Xiaoxu Li

Submitted in accordance with the requirements for the degree of
Doctor of Philosophy

The University of Leeds
School of Civil Engineering, Faculty of Engineering

November 2016

The candidate confirms that the work submitted is his own, except where work which has formed part of jointly-authored publications has been included. The contribution of the candidate and the other authors to this work has been explicitly indicated below. The candidate confirms that appropriate credit has been given within the thesis where reference has been made to the work of others.

Part of the work of jointly-authored publications are presented in Chapter 3, Chapter 4 and Chapter 6 of this thesis.

The first paper was presented in the Proceedings of the Word Congress on Engineering, London, 29 June - 1 July, 2016. The title is ‘‘Application of a Twin-plane Electrical Capacitance Tomography Sensor for Characterising Bubble Behaviour in a Gas-solids Fluidized Bed ’’. Authors are Xiaoxu Li, Artur J. Jaworski, and Xiaoan Mao. This paper describes experiments carried out in a bench-scale fluidized bed using air and silica sand and studied the location effect on the estimation of bubble characteristics. This work was done by the candidate under supervision of Professor Jaworski and Dr Mao.

The second paper was presented in the 8th World Congress on Industrial Process Tomography, Iguassu Falls, Brazil. 26 - 29 September 2016. The title is ‘‘Investigation of bubble behaviour in a gas-solid fluidized bed by means of a twin-plane ECT sensor ’’. Authors are Xiaoxu Li, Artur J. Jaworski and Xiaoan Mao. This paper demonstrated the effects of different individual cut-off values in estimating bubble diameter and the results were compared and evaluated with empirical correlations. This work was done by the candidate under supervision of Professor Jaworski and Dr Mao.

Acknowledgements

First and foremost, I would like to express my sincere gratitude to my primary supervisor Professor Artur J. Jaworski for providing me with the great opportunity to study for this degree and for his invaluable guidance, ideas and continued encouragement and support throughout my PhD study period.

I would like to thank my co-supervisor Dr Xiaoan Mao for his patience, support and valuable in-depth research discussions he generously provided that were very important in directing me on the right path.

I would also like to thank the technicians at the University of Leeds for helping in the construction of the experimental rigs, especially Mr Michael Marsden and Mrs Susanne Patel for particle size analysis, Mr David Instrell, Mr Robert Harris and Mr Gurdev Bhogal for the experimental set-ups and Mrs Punitha Sellamuthu for the help with PCB etching.

I am thankful for the helpful suggestions from Mr Malcolm Byars from Process Tomography Ltd and Mr Yunjie Yang from the University of Edinburgh in designing, simulating and constructing the ECT sensor. I would also like to thank Professor Mi Wang and Mr Qiang Wang for allowing me to use their equipment. I am thankful too for the proofreading assistance provided by Mrs Judith Sherrington.

I would like to acknowledge the maintenance funding from The China Scholarship Council (CSC) and tuition fees funding from the School of Civil Engineering, University of Leeds in support of my PhD programme.

Last but by no means least, I am indebted to my parents and my two younger brothers for their steadfast understanding, encouragement, love and support.

Abstract

Fluidized beds have been widely utilized in many industrial applications, such as chemical reactions, power generation, pharmaceuticals and food processing. Nevertheless, further applications are still hindered due to inadequate comprehension of the complex internal hydrodynamic characteristics. Conventional measurement techniques are not able to avoid the introduction of interference within the internal flow structure and so distorted and inaccurate result are obtained. Electrical capacitance tomography (ECT) has been developed as a non-intrusive measurement technique and applied into the application of gas-solids fluidized beds. However, understanding of the bubble behaviour in gas-solids fluidized beds is still limited.

A customized ECT twin-plane sensor has been designed and constructed to further study the fluid flow structure and processes within a bench-scale gas-solids fluidized bed. A detailed calibration process has been conducted with plastic balls of different diameter to derive the reference cut-off values in estimating bubble diameter in the bubbling regime. The bubble diameter has been estimated by means of the individual cut-off values, linear fitted curves and second-order fitted curves with the derived reference cut-off values. A statistic average approach was proposed and evaluated in estimating the averaged axial bubble rising velocity compared with other approaches, including a three-dimensional utilization of the cross-correlation technique on a pixel-by-pixel basis.

Non-intrusive pressure fluctuation measurements have been carried out in order to compare with the ECT measurements in terms of the capability in investigating the bubble and bed behaviour within the gas-solids fluidized bed. The performance of estimating the minimum fluidization velocity and minimum slugging velocity from both methods have been compared and evaluated. Qualitative analysis of the signal amplitude and quantitative analysis of the dominant frequency results, solids concentration results and bubble rising velocity results derived from both methods have been conducted.

Table of Contents

List of Tables

List of Figures

Chapter 1
Introduction

1.1 Background to the Project

Fluidized beds have been broadly utilized in industrial applications. The earliest application can be traced back to as early as 1926 when they were first put into service commercially in the Winkler process for the purpose of gasification of coal [1]. However, the utilization of fluidized beds was not as popular after this time due to a variety of reasons until the start of the Second World War. After that, a group of companies including Standard Oil New Jersey, Shell and Universal Oil Products constructed the first fluid bed catalytic cracker (FCC), which was primarily designed for exploiting gasoline manufacturing [2]. This fluidized process has since been a cornerstone of all the following developments in the field of fluidized beds.

Fluidization is a process by which fine solid particles are able to behave like a liquid by means of contacting with a gas or liquid [3]. Fluidized beds typically consist of a container (pressure vessel) where a layer of granular material is fluidized by the upward flow of gas or liquid. Due to the popular usage and enormous applications of gas-solids fluidized beds, gas-solids fluidized beds will be the prior research object and liquid-solid fluidized beds are outside the scope of this thesis. The principle components of a gas-solids fluidized bed are a container, a powder, a source of gas, and a gas distributor, as indicated in the numbers 1 to 4, respectively, shown [1] in Figure 1.1. The need to use other items appearing in Figure 1.1 undoubtedly depends on the specific applications. For example, components of number 5, 6 and 7 may be required for some applications in respect of heat transfer.

Assuming a layer of granular solid particles are put in a cylindrical container with a perforated plate underneath, the whole arrangement can be treated as a fixed bed when the upward flowing gas is at a low flow rate as the fluid only percolates through the interval space between fine particles [2, 3]. When the flow rate of the gas is increased, the drag force exerted by the gas on solid particles is increased accordingly until one point is reached when the drag force is equal to the gravitational force of the particles. At this point, solid particles move apart from each other, the bed height starts to expand and the solid particles are subsequently said to be fluidized. The gas velocity is referred to as the minimum fluidization velocity [4].

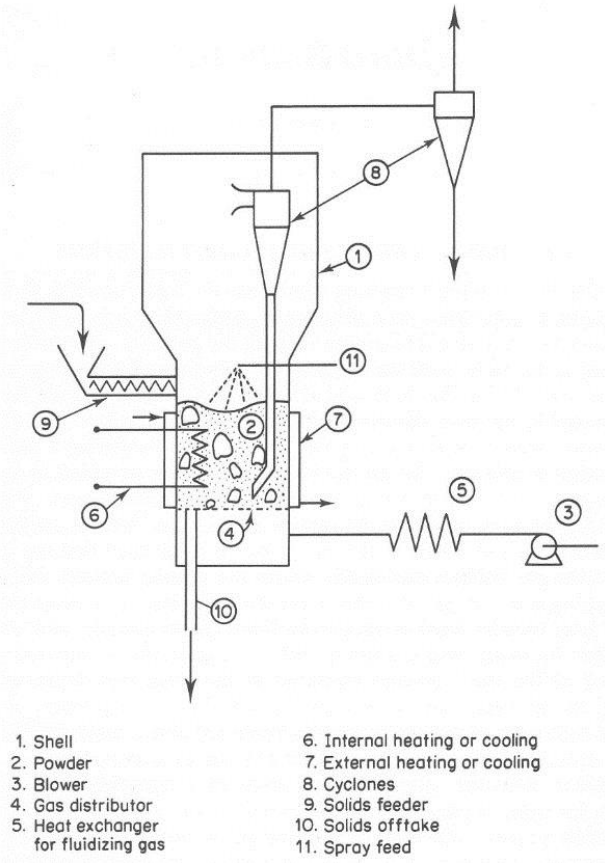

Figure 1.1: A conceptualized fluidized bed which could be used for a wide variety of applications[1]

Once the solid materials have been fluidized, they are able to behave more advantageously than other contacting methods. One outstanding advantage of fluidization is the liquid-like property of the fluidized beds when the gas velocity is beyond the minimum fluidization value. For example, a large and light object can be pushed into the bed and the surface, namely, freeboard, of the bed can stabilize like a liquid surface once the force on the object is released. The surface can be maintained in a horizontal state even if the bed is tilted. Moreover, when the gas velocity is high enough, the solids can be entrained out of the bed like liquid without involving any further external force [3]. This exceptional advantage enables fluidized bed usage in solid particles pneumatic transport in an economic manner [5, 6].

Apart from the above merits of fluidized beds, rapid and extensive solids mixing can be achieved between gas and solids, which could give high rates of heat transfer (from the bed surface to the particles, from the particles to the neighbouring particles and from the particles to the gas) and high rates of mass transfer among particles and gas. The high heat transfer rates and rapid

mixings are responsible for isothermal conditions throughout the bed [1], which makes the maintenance and operation of fluidized beds easy and reliable in an industrial environment.

By virtue of the aforementioned advantages of fluidized beds in modern industrial applications, fluidized beds usually have the following three types of utilization, e.g., chemical reactions, energy conversions and physical contacting [3, 7, 8]. In chemical reactions, the Fluidized Catalytic Cracking (FCC) process is one of the most successful applications and it is also widely used in petroleum refining technology. In energy conversion applications, gasification and coal combustion have exclusively utilized the concept of fluidized beds. The former refers to a series of processes that aim to obtain combustible gas by converting solid or liquid fuels [9] and the latter involves the operation of generating a gas stream, which propels the gas turbine to generate electricity in fluidized bed boilers. In physical contacting, the processes of coating and drying are typical applications of fluidized beds in the pharmaceutical and food manufacturing industry, such as coating of medical tablets and drying of food.

However, without exception of any technique, there are some disadvantages to fluidized beds. Due to vigorous mixing of solid particles, solid fines are generated during this process through attrition among solid particles [4]. Moreover, erosion could occur on bed internals, heat transfer coils and valves because of some chemical properties of fluidization medium [3, 10]. Also, the intensity of solids mixing may be reduced because of the phenomenon of gas passing through bubbles [11]. Additionally, reliable scale-up from bench scale to full-scale plant sometimes can be difficult to fulfil which is caused by the limited understanding of the internal physics of fluidization [2].

Therefore, this inevitably gives challenges in the research within the fluidization field. On one hand, with a comprehensive understanding of the complex nature of fluidized beds, deliberate efforts can be put into place to prevent these drawbacks from happening to ensure the advantageous features prevail [3]. On the other hand, especially in an industrial environment, good performance and safe operations are dependent on the proper design, scale-up and operation of bench-scale fluidized beds, which largely relies on the understanding of the fundamentals of the hydrodynamics of the fluidization process [12].

Fluidized beds have been a subject of research since the 1960s [1-3, 13]. Precise measurements of the internal fluid flow processes and perception of flow patterns inside fluidized beds has been instrumental in our understanding

of the inherit complex and hydrodynamic characteristics [14-17]. A large number of conventional measurement techniques have been developed extensively to study the hydrodynamic characteristics within gas-solids fluidized beds. These include pressure probes inserted inside of the beds, capacitance probes and fibre optic probes [18-24]. There is a growing body of literature that recognises the importance and achievements of these approaches [13, 25]. However, these approaches have been considered unavoidably to interfere with the internal flow structure and the results obtained through these methods are inevitably distorted or inaccurate to some extent [26-28].

1.2 Motivation of the Study

Electrical capacitance tomography (ECT) has been developed rapidly in the last few decades and applied into the applications of the gas-solids fluidized beds since it was regarded as a simple, fast, low-cost and no radiation technique [29-31]. The primary advantage of it is the non-intrusive nature, which allows accurate and reliable investigation to be accomplished without disturbing the fluid flow processes inside of the bed [14, 32, 33].

ECT is able to produce images (normally 32 x 32 pixels) reconstructed from permittivity distribution of two materials with different permittivity by measuring the capacitance of different measuring electrodes pairs situated around a bed pipe [34-36].By virtue of the advantages of the ECT measurement technique, different flow regimes within a gas-solids fluidized bed have been characterized by means of the ECT technique [37-39]. Due to the importance of bubbles played in determining the quality of fluidization, bubble behaviour in bubbling regime have been investigated by numerous of previous researchers [40-42]. Specifically, bubble diameter, bubble rising velocity and bubble frequency have been studied via ECT measurements[16, 17, 26, 40, 43-45].

However, there is no systematic study performed yet on the cut-off value (a grey level in a pixel distinguishing bubble phase and solid phase in ECT images) in the process of determining bubble diameter in bubbling regime. In addition, the bubble rising velocity profile in bubbling regime derived from ECT measurement has not been investigated in a three-dimensional form though the bubbles within the gas-solids fluidized bed are full of three-dimensional.

Another non-intrusive measurement technique in studying gas-solids fluidized beds is the pressure fluctuation measurement where pressure probes are

placed flush with the bed wall surface [46, 47]. It is believed the pressure fluctuation measurement is not only capable of capturing the local flow structure near the measurement locations but able to perceive the flow information propagating in the beds [8, 48]. Different flow regimes have been investigated by many scholars by means of two general analysis methods, namely, the time domain and the frequency domain analysis [46]. Some essential characteristics of bubble behaviour within bubbling regime has been linked with the measured pressure fluctuation signal in regardless of that some conflicting conclusions are still existing [8, 49, 50].

ECT and pressure fluctuation measurements have showed and demonstrated their potential in characterizing the bubble behaviour in bubbling regime [14, 51, 52]. Nevertheless, very few study have been carried out to evaluate and compare the performance of both methods in revealing the internal feature of the gas-solids fluidized beds.

1.3 Aims and Objectives of the Study

The proposed study will look at the flow structures present in a bench-scale gas-solids fluidized bed and their spatial and temporal development by means of the two aforementioned, non-intrusive, measurement techniques, ECT and pressure fluctuation measurements. Generally speaking, there are two main aims of the present study. The first one is to seek the most appropriate cut-off value in estimating bubble diameter using ECT measurement. The second one is to comprehensively evaluate the performance of the two non-intrusive measurement techniques in characterising bubble behaviour in gas-solids fluidized beds. In order to fulfil the two general aims, the subsequent specific objectives are outlined as follows:

a) Numerical simulation to establish the feasibility of designing the proposed twin-plane ECT sensor which is to be fitted with a current data acquisition system provided by Process Tomography Ltd. Based on the conclusion from the numerical simulation, construct the customized ECT sensor.

b) Conduct a systematic calibration process in deriving cut-off values using different sizes of plastic balls. Based on the derived cut-off values, the process of estimating bubble diameter at various gas superficial velocities is to be carried out.

c) Estimate bubble rising velocity in a three-dimensional form based on a pixel-to-pixel approach with ECT measurements. A a statistic average approach will be proposed and used to extract the bubble rising velocity.

d) Derive the minimum fluidization velocity and minimum slugging regime by means of ECT and pressure fluctuation measurement to evaluate the performance of both methods.

e) To further assess the capability of the two non-intrusive methods, conduct a comparative study in terms of the amplitude of the measured signal, dominant frequency, solids concentration and bubble rising velocity.

1.4 Overall Structure of the Thesis

Following this chapter of Introduction,

Chapter 2 will present a state of the art review of fluidization study including classification of the fluidized bed particles, different flow regimes within fluidized beds, measurement techniques which comprises conventional measurements and non-invasive measurement techniques with special emphasis on ECT and pressure fluctuation measurements in characterizing bubble behaviour in gas-solids fluidized beds.

Chapter 3 gives a brief latest review on numerical simulation of electrostatic fields within the ECT sensor area. Then, a numerical simulation in designing a customized twin-plane ECT sensor is carried out. Due to the plastic ball wall being not ideally thin and being different, a numerical simulation is performed to investigate the plastic ball wall effect on the simulated capacitance values between measuring electrode pairs. After that, some key issues in constructing the sensor including the number and length of measuring electrodes, driven guard electrodes and resistors are addressed in detail.

Chapter 4 deals mainly with the experimental set-ups of ECT and pressure fluctuation measurements. In addition, the experimental setup for the plastic ball calibration process is introduced as well.

Chapter 5 gives the results concerning the determination of the minimum fluidization velocity and the minimum slugging velocity derived from ECT and pressure fluctuation measurements. Moreover, the performance of different estimation approaches are compared and evaluated.

Chapter 6 encompasses the derived cut-off values results from the plastic ball calibration process and the results for the bubble diameters which are

estimated using the derived cut-off values with two different image reconstruction algorithms. Bubble rising velocities are then estimated via different approaches including cross-correlation techniques, detailed mathematical calculation, three dimensional form on a pixel-by-pixel basis and a statistic average methods.

Chapter 7 involves a comparative study of ECT and pressure fluctuation measurements. Four parameters are compared, which include the signal amplitude analysis, dominant frequency analysis, solids concentration analysis and bubble rising velocity analysis.

Chapter 8 lays out the conclusions of this thesis and suggests future work which could be carried out in terms of ECT and pressure fluctuation measurements.

Chapter 2
Literature Review

2.1 Phenomenon of fluidization and its applications

Fluidization is observed when a pack of fine solid particles start to behave as a liquid by contacting with a vertical upward fluid flow, which has an intermediate moving speed or velocity [3, 13]. A fluidized bed is a device designed to accommodate the fine solid particles and fluid flow. Different granular materials can showcase different fluidization properties, which will be illustrated later in section 2.2. The general process of forming fluidization can be found in Figure 2.1.

At low velocities of fluid flow, the bed of solid particles remains in a fixed state where the bed is said to be a fixed bed because the interstitial pores between fine particles can exert adequate resistance towards the up-flowing fluid [53], which consequently generates a pressure drop (as can be seen in set-up A, Figure 2.1).

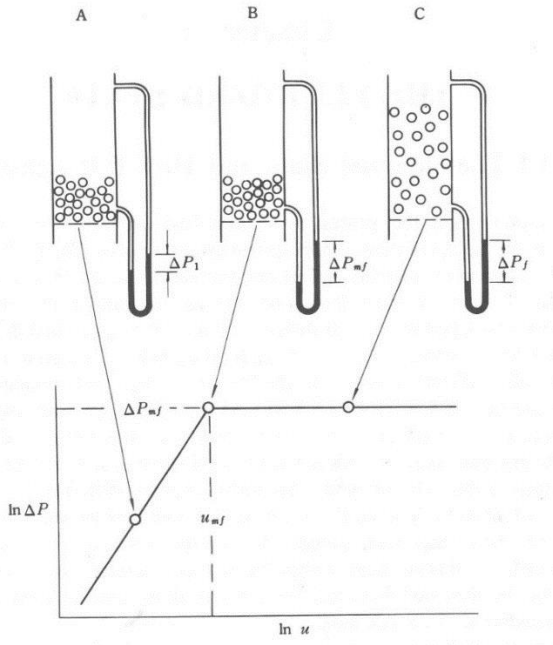

Figure 2.1: Fluidization of solid particles by steady fluid flow [53].

The pressure drop increases with the increase of fluid flow velocity until a particular flow velocity where its value is equivalent to the weight of the solid particles. Meanwhile, the particles are starting to lose contact with the neighbourhood and buoy up (set-up B, Figure 2.1). Further increase in fluid velocity cannot create more pressure drop as the suspended particles cannot provide any more resistance because of their finite mass (set-up C, Figure

2.1). Therefore, the pressure drop stays at the same level as depicted in the curve at the lower part of Figure 2.1 and the particles are pushed further apart by the increased upward fluid flow.

The point when the particles start to move apart from each other is referred to as the incipient or minimum fluidization point. The corresponding velocity is called the minimum fluidization velocity and the bed is regarded as the incipiently fluidized bed or a bed at minimum fluidization [3]. The corresponding pressure drop is equal to the weight of the solids in the bed [53].

$$\Delta P = \left(\rho_s - \rho_f\right)\left(1 - \varepsilon_{mf}\right) g L_0 \qquad (2.1)$$

where ρ_s Density of the solid particles; ρ_f Density of the fluid; ε_{mf} Voidage, or fraction void, in the granular solids bed at minimum fluidization; L_0 Height of the fixed solids bed before fluidization commences.

The fluidization fluid medium can be liquid or gas. A liquid-solids system always exhibits a smooth and steady expansion of the bed when the velocity of the liquid is above the minimum fluidization velocity. However, vigorous movements and heterogeneity of properties, such as bubbling and channelling, take place in gas-solids systems. Such behaviour of the gas-solids fluidized beds sometimes makes them a popular choice in industrial applications. Thus the present research will focus on gas-solids instead of liquid-solid systems.

One of the practical advantages of fluidization is the liquid-like property of the fluidized beds when the gas velocity is beyond the minimum fluidization value. For example, a large and light object can be pushed into the bed and the surface, namely, a freeboard, of the bed can stabilize like a liquid surface once the force on the object is released. The surface can be maintained in a horizontal state even when the bed is tilted. Moreover, when the gas velocity is high enough, the solids can be entrained out of the bed like liquid without involving any further external force. This exceptional advantage puts it into use for solid particles pneumatic transport in an economic manner.

Besides the above liquid-like behaviour property of the gas-solids fluidized beds, there are several other unique advantages, such as rapid mixing between gas and solids which can almost reach isothermal conditions within the fluidized beds; heat and mass transfer rates are relatively high compared with other conventional contacting or mixing methods; large-scale operations can be readily made.

By virtue of these advantages, the gas-solids fluidized beds are widely applied in the following applications [3], i.e. pneumatic fine particles transport, fluidized mixer for powdery materials, coating of plastic materials on metal surfaces, drying and sizing, fluid catalytic cracking, carbonization and gasification and power generation combustion, etc.

2.2 Two-phase theory of fluidization

In order to propose and clarify some basic definitions which may appear in the following sections of this thesis, it is essential to introduce the two-phase theory of fluidization. The two-phase theory was initially proposed by Toomey and Johnstone [54]. Under the theory, when the gas velocity is increased above the minimum fluidization velocity, the bed is basically composed of two phases, namely, the dense phase (also known as the emulsion phase, or particulate phase) where gas percolates through individual solid particles and the lean phase or bubble phase which is formed by the remaining gas flow, obtained from the total gas flow, in excess of that required for minimum fluidization [2, 4].

Therefore, suppose Q_T is the total volumetric flowrate into the bed, Q_{mf} is the minimum fluidization flowrate which is the product of the minimum fluidization gas velocity by multiplying the bed cross-sectional area and Q_b is the bubble flowrate, the two-phase theory can be expressed mathematically as follows:

$$Q_T = Q_b + Q_{mf} \tag{2.2}$$

The gas velocities referred to in fluidized beds are normally termed superficial velocities defined as the volumetric flow through the bed divided by the bed area, A [7]. Hence the above equation can be re-written as:

$$\frac{Q_b}{A} = U - U_{mf} \tag{2.3}$$

For some fluidization systems, the theory works well for having a relatively good approximation of the two phases. However, in recent years, with the emergence of a large quantity of experimental observations by which the bubble flow in fluidized beds can be measured, a correction factor may be needed to adjust the two-phase theory due to the conclusions drawn that the bubble phases are commonly overestimated.

$$\frac{Q_b}{A} = U - kU_{mf} \qquad \text{with } k > 1.0 \tag{2.4}$$

There are probably two reasons, as suggested by Grace and Clift [55], attributed to that deviation, i.e. one for the increased interstitial gas velocity in

the dense phase above that required for minimum fluidization and another for the possible existence through flow inside the bubbles. Hence Equation 2.4 is then modified by Grace and Clift [55].

$$\frac{Q_b}{A} = U - U_{mf}(1 + n\bar{\varepsilon}_B)$$

$$= U - [U_{mf}(1 - \bar{\varepsilon}_B) + (n + 1)U_{mf}\bar{\varepsilon}_B] \quad (2.5)$$

where $\bar{\varepsilon}_B$ is the average volume fraction of visible bubble phase in the bed. The gas flow through the emulsion phase is:

$$\text{Flow through emulsion phase} = U_{mf}(1 - \bar{\varepsilon}_B)A \quad (2.6)$$

and the through flow relative to the bubbles is:

$$\text{Through flow relative to the bubbles} = (n + 1)U_{mf}\bar{\varepsilon}_B A \quad (2.7)$$

Ideally when n = 0, the above Equation 2.5 turns into the classic two-phase theory. However, in reality, the number of n is not constant and universal. Experimental evidence shows that it varies from one system to another and even differs within the same system under different operating conditions. Moreover, the measurement of the invisible flow components such as flow through the emulsion phase and through flow relative to bubbles, is still difficult. Thus, the division of gas flow between the two phases and what factors may govern it are still open to debate [2].

2.3 Classification of granular materials

Although fluidized beds have such extensive industrial applications, it is well acknowledged that the quality or behaviour of fluidization is truly dependent on the physical properties of the fluidising granular materials, i.e. solid particle size and its distribution, density, shape, etc. [4, 13]. Conclusions which are drawn from one type of specific solid particle are not recommended to be applied to another type. In order to avoid some tedious repetition work recognizing the similar or different properties among different solid materials in real industrial applications, the first systematic study of grouping granular materials was reported by Geldart in 1973 [56].

A detailed diagram for distinguishing different granular materials into different groups based on the particle size and density difference (solid particles and gas) is shown in Figure. 2.2. All the experimental work was conducted at ambient temperatures and pressures. As can be seen in Figure 2.2, there are four groups in total, viz. Group A, B, C and D, whose properties are stated as follows.

Group A particles - the size of this type of material are within a relatively small range between 30 and 150 microns. The density difference is less than 1500 kg/m^3. The fluidized bed using this type of particles undergoes a so called particulate flow regime, which exhibits significant bed expansion after minimum fluidization velocity and before the commencement of velocity bubbling, which is recognized as the minimum bubbling velocity.

Group B particles - comparing with Group A, this group of particles allows bubbles to appear just after the onset of minimum fluidization velocity. The particle size normally ranged from 150 to 500 microns with a density difference span between 1500 and 4000 kg/m^3. This type of material which contains most of the medium particles and silica sand, which can be readily obtained, is a typical example. Therefore, silica sand is the fluidization solid material applied in the following experimental work conducted in this thesis.

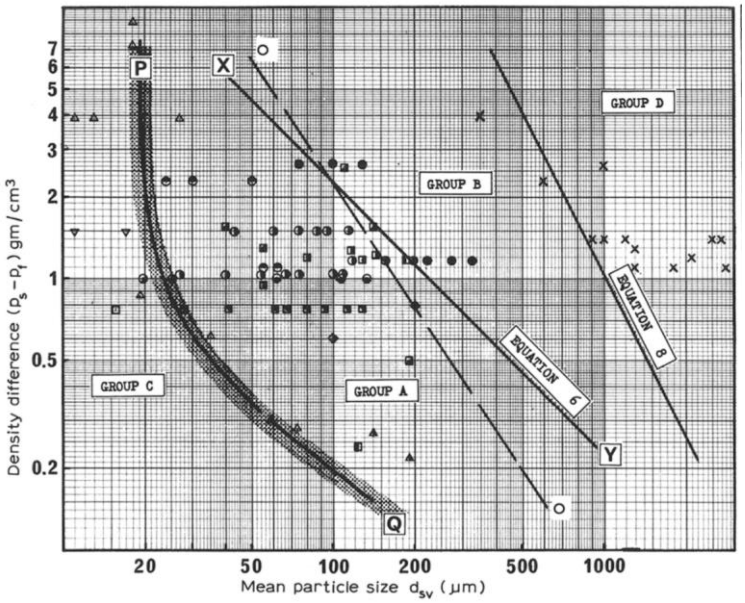

Figure 2.2: Diagram for classifying powder into groups having broadly similar fluidization characteristics [1].

Group C particles - this group of particles have the smallest size (usually less than 30 microns) and they are mostly cohesive and very difficult to fluidize. Due to severe non-spherical shape, channellings can be easily observed. However, by using some mechanical approaches, such as mechanical stirrers or vibrators, the occurrence of fluidization can be possible.

Group D particles - some very large or dense particles belong to this group of materials and can be fluidized. It is worth noting that normally the large bubbles formed rise more slowly than the interstitial gas flow so that gas exchange and by-passing can be observed which is different from Group A or

B particles. A spouted fluidized bed can be formed if the fluidizing gas which is introduced through a single orifice or nozzle at the bottom.

In practice, operators are recommended to firstly have a consideration of this particles grouping criterion before carrying out any designing either in on a laboratory scale or an industrial pilot-scale fluidized bed application.

2.4 Flow regimes in a fluidized bed

It is well known that a fluidized bed behaves differently with different superficial velocities, gas and solid properties. A systematic diagram of different distinguishable flow regimes with varied upward gas flow velocity proposed by Grace [57] is shown in Figure 2.3. It is worth mentioning that although fluidized beds behave differently with different types of particles, the diagram is just concerned with Group B particles which are also the particle type used in this thesis. The six distinct flow regimes appear in Figure 2.3 below.

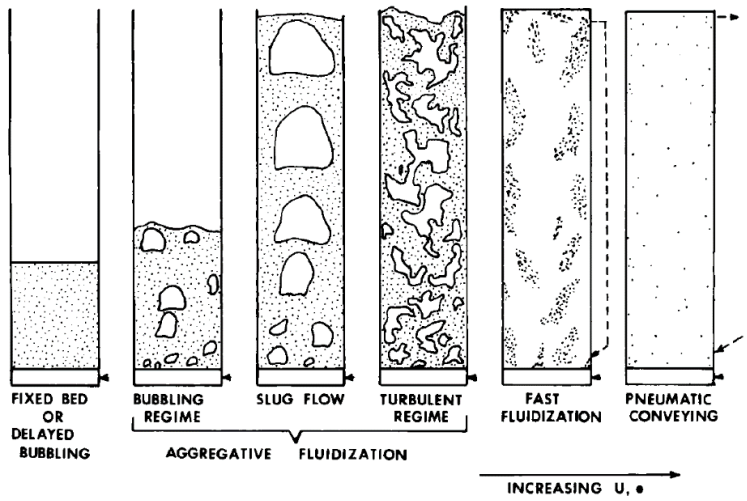

Figure 2.3: Principal flow regimes for upward flow of gas through solid particulate materials [57].

2.4.1 Fixed bed and minimum fluidization

The fixed bed is sometimes called the packed bed which plays an important role in chemical processes. [4] It is formed by a layer of granular materials which are put in the bed with a gas distributor underneath, as shown in Figure 2.3. A gas flow is introduced vertically at the bottom of the bed. The primary operating cost and the most essential issue of the fixed bed is the pressure drop which is required for the gas flow to go through the bed at a specific superficial velocity. There has been a great deal of research which has been committed to flow through a fixed bed[13]. From the perspective of fluid mechanics, the most popular and widely accepted empirical correlation

governing the flow velocity and pressure drop within the packed bed is call the Ergun equation [58].

$$f_p = \frac{150}{Re_p} + 1.75 \qquad (2.8)$$

where the friction factor f_p for the fixed bed, and the Reynolds number Re_p , are defined as follows.

$$f_p = \frac{\Delta p}{L}\frac{D_p}{\rho {V_s}^2}\left(\frac{\varepsilon^3}{1-\varepsilon}\right) \qquad (2.9)$$

$$Re_p = \frac{D_p V_s \rho}{(1-\varepsilon)\mu} \qquad (2.10)$$

where Δp: Pressure drop; L: Length of the bed; D_p: Equivalent spherical diameter of the particle; ρ: Density of the fluid; μ: Dynamic viscosity of the fluid; V_s: Superficial velocity; ε: Void fraction of the bed (ε is the ratio of the void volume to the total volume of the bed).

Now, if the superficial velocity is increased further, a point will be reached when the drag force entered by the upward flowing gas on the particles is equal to the weight of the particles, as illustrated in section 2.1. This point is referred to as the onset point of the minimum fluidization and the corresponding superficial velocity is known as the minimum fluidization velocity, U_{mf}. At this stage, Equation 2.1 was applied for regulating the pressure drop and net weight of the particles. Meanwhile, the voidage within neighbouring particles was increased and the bed started to expand slightly. The U_{mf} can be calculated by combining the Equation 2.1 and 2.8-2.10. However, the parameter of void fraction of the bed cannot be obtained straightforwardly although other parameters only relate to the basic properties of gas and solid particles.

As the U_{mf} is the demarcation point between the fixed bed and the onset of fluidization, it is necessary to find an easier way of estimating the U_{mf} to save time in repeating work which may occur in industrial applications. Numerous studies have attempted to generalize a method to estimate the minimum fluidization velocity. The one proposed by Wen and Yu [59] is recognized as one of most extensively accepted empirical correlations.

$$(N_{Re})_{mf} = \sqrt{(33.7)^2 + 0.0408 N_{Ga}} - 33.7 \qquad (2.11)$$

where N_{Re} Particle Reynolds number = $(d_p \rho_f U/\mu)$; $(N_{Re})_{mf}$ Particle Reynolds number at the onset of fluidization; N_{Ga} Galileo number, or Archimedes number = ${d_p}^3 \rho_f(\rho_s - \rho_f) g/\mu^2$; d_p Particle diameter; g Acceleration due to gravity; ρ_s Particle density; ρ_f Fluid density; μ Fluid viscosity; U Superficial fluid velocity.

Apart from the empirical correlations as mentioned above, some other newly derived experimental methods have been introduced recently to estimate the minimum fluidization velocity, such as via a pressure fluctuation signal. These will be illustrated in Chapter 5.

2.4.2 Bubbling regime

Once the minimum fluidization point is reached, as outlined in section 2.4.1, further increase of the superficial gas velocity will cause the bed to expand more significantly, accompanied by the increased voidage between solid particles. The amount of increased gas results in the bed being characterized in two phases, as illustrated by the two-phase theory in section 2.2. One phase is called the dense phase (also known as the emulsion phase or particulate phase) and another one is termed the bubble phase or lean phase, which is attributed to the name origin of the bubbling regime which can be seen in Figure 2.3. This type of fluidization has also been called 'aggregative' fluidization.

It is acknowledged that the bubbles coalesce with neighbouring ones while they rise upwards through the bed and burst on the bed surface which is also called the freeboard. It is also interesting to note that the behaviour of the bubbles which appeared in the bubbling regime in the gas solid fluidized beds has a similar manner as the bubbles in a gas liquid column. The corresponding liquid-like properties of bubbles will not be shown here again as they have already been mentioned in section 2.1. The specific behaviour and characteristics of bubbles in a bubbling regime, such as bubble shape, bubble growth and coalescence, bubble size, bubble rising velocity, will be illustrated in detail in the following section 2.5.

2.4.3 Slugging regime

Suppose a fluidized bed has been in the contacting mode of a bubbling regime, as stated in section 2.4.2. If the superficial velocity is increased further, the bubbles in the bed move more vigorously and their size becomes bigger and bigger due to bubble coalescence phenomenon. When the superficial velocity is at a specific superficial velocity, U_{ms}, and the bubble size is comparable with the diameter of the bed, then the bed is said to be in a slugging regime, as shown in Figure 2.3. The corresponding superficial velocity is referred to as the minimum slugging velocity. The value of it can be derived by the following empirical correlation proposed by Stewart and Davidson [60]:

$$U_{ms} = U_{mf} + 0.07 \times \sqrt{gD} \qquad (2.12)$$

where g is the gravitational constant and D is the bed diameter.

The property of slugs at this stage is largely dependent on the bed diameter rather than the bubble diameter. This can be evidenced by the following empirical correlation for deriving slug rising velocity [13]:

$$U_{s\infty} = 0.35 \times \sqrt{gD} \qquad (2.13)$$

It needs to be clarified that the slugging regime does not happen in all the fluidized beds systems. Generally large ratio (larger than about 2) of bed height to bed diameter is preferable for the existence of a slugging regime. However, three typical conditions normally need to be met, i.e. the maximum stable bubble size is greater than 0.6 D (where D is the diameter of the bed); the gas velocity is sufficiently high; the bed is sufficiently deep [1]. Therefore the slugging regime is inclined to occur in laboratory scale and a pilot scale fluidized bed rather than in industrial scale beds whose diameter are normally too large compared with the maximum bubble size.

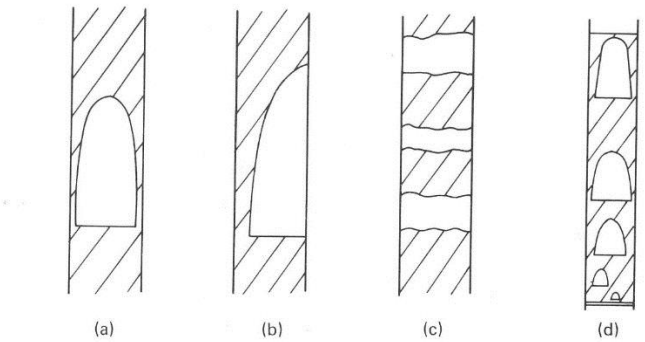

Figure 2.4: Slug flow in fluidized beds (schematic). (a) conventional single slug (b) single wall slug; (c) continuous plugs, or square-nosed slugs; (d) continuous slug flow[13].

There are typically two kinds of slug flow patterns, as shown in Figure 2.4. The first type of slug shape is presented in Figure 2.4(a). This axisymmetric round nosed gas slug is analogous with, and adopted from, slug of gas rising in liquid columns. The solids particles can only pass through downwards and sideways. Its continuous motion mode is shown in Figure 2.4(d). These types of slugs are normally formed in the fluidized beds with solid particles of Group A and B which can be easily fluidized as explained in section 2.3.The second kind of slug pattern is the so called plugs or square-nosed slugs, which is demonstrated in Figure 2.4 (c). The gas slugs occupy the bed cross section completely. The dense phase and slugs are separated by the virtually horizontal interphases. The solids can only pass through the slugs by ‘raining down’ through the slugs as solids streamers [4]. These kind of slugs normally

occur in beds with cohesive particles or particles of angular shape. The slug shape exhibited in Figure 2.4(b) is often termed as the wall slug, which is conventionally classified as a variation of the first type of slugs [4].

2.4.4 Turbulent regime

Assuming the bed is in slugging regime, if the superficial velocity is steadily increased further the slugs become bigger and bigger and the bed is in a more vigorous motion. When the superficial velocity reaches one point, U_c, where large bubbles or slugs start to break up, it is said the bed is in the turbulent flow regime. Unlike the unambiguous two phases in bubbling or slugging regimes, two phases in the turbulent regime cannot be observed as either continuous or discontinuous [13]. Discrete bubbles or slugs are not visible anymore. Subsequently, the structure of the turbulent flow regime is more homogeneous, which can be seen in Figure 2.3. The top freeboard cannot be recognized easily. Clusters, which are identified as a group of particles travelling together because of hydrodynamic forces, are appearing in the bed. Although it is still open to debate on the determination of the onset superficial velocity of the turbulent flow regime, the point when the standard deviation of the pressure fluctuation across the bed reaches a steady level is considered as the transition velocity from bubbling to the turbulent flow regime. There are also some empirical correlations available to estimate this velocity. Within the turbulent bed, solid mixing is more aggressive, the interaction of the two phases is stronger and the contact between gas and solids is exceedingly efficient. Therefore the heat transfer rate is apt to become high level and isothermal conditions can be readily achieved. Thus, these merits provide wide industrial applications relating to mixing operations. However, since high velocity flow regimes (apart from the turbulent flow regime, it also includes the fast fluidization and the pneumatic conveying, which will be introduced shortly) are not in the main scope of this thesis, for a full review of this information please refer to Davidson and Harrison's text book [13].

2.4.5 Fast fluidization

If the superficial velocity is increased beyond a velocity known as transport velocity, U_{tr}, which is capable of transporting all the solid particles out of the bed, the bed is then termed the fast flow fluidized bed. Its schematic drawing can be found in Figure 2.3. The top freeboard is no longer distinguishable compared with previous low velocity regimes. Solid particles are transported out of the bed and the bed would be virtually empty very rapidly if there were no solids feeding or recycling. From the perspective of application the widely

used, so-called circulating fluidization beds (CFB) are constructed mostly based on this fast fluidization.

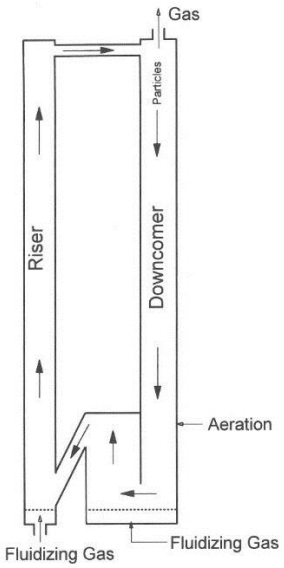

Figure 2.5: Typical configuration for circulating fluidized bed system [61].

At this stage, the resulting solids concentration or density in the bed not only depends on the superficial gas velocity but the solids feed rate. If the solid feed rate is low, dilute phase flow will occur. On the contrary, if the solid feed rate is kept at a relatively high rate by using standpipes or external cyclones, then it is possible to reserve a relative large solid concentration in the bed [13]. Due to the lack of bubbles in the fast fluidization, gas-solids mixing intensity is enhanced much more significantly. Owing to that, the CFB has come to prominence over the last several decades and has been applied in the chemical process industry, mineral processing and coal combustion in power stations [61].

2.4.6 Pneumatic conveying

Continuing increase of superficial velocity beyond that required for fast fluidization means that a new flow regime featured as pneumatic conveying will take place, which is shown in Figure 2.3. This is normally a once-through operation [4]. All the particles are transported out of the bed in dilute phase whose concentration changes along the bed height.

Pneumatic conveying systems are principally quite simple. The only drive force it needs is the feeding of gas flow [5] . With some conveying pipes and auxiliary equipment to process the conveyed goods, bulk materials can be transported flexibly. Additionally, pneumatic conveying systems are versatile and can meet the requirements of any local Health and Safety legislation with

ease. Such advantages of pneumatic conveying make it popular in an enormous number of industrial applications such as agricultural, chemical, pharmaceutical and petroleum transporting and food processing. As this kind of fluidized bed flow regime is not the subject of this thesis, more detailed information on pneumatic conveying is available from the book by David Mills [5].

2.5 Characteristics of bubbles in bubbling regime

In many chemical process and energy conversion operations, bubbling regime still features more dominantly than other contacting modes to provide good gas-solids contact. The probable reason behind this largely depends on the fact that the rising bubbles are the main source of motion of the two phases which promotes further the solids mixing in beds [1].

The performance of a fluidized bed reactor is essentially influenced by the internal fluid flow hydrodynamic characteristics such as bubble frequency, bubble size and bubble rising velocity, etc. Consequently, substantial understanding of the bubble features plays a vital role in maintaining good performance in the proper design of fluidized beds, scale up and industrial applications [12].

Moreover, the bubbles formed in the bubbling regime becomes one of the most intriguing properties of fluidized beds. The fundamental origin or reasons for forming bubbles in beds are still not clear-cut though a great deal of theoretical and experimental work has been carried out [2] . This reflects on the research objectives in the introduction section of this thesis. In this chapter, some previous essential research on bubble shape, bubble size and bubble rising velocity will be reviewed.

2.5.1 Bubble shape

To study the bubble's characteristics, its shape is usually the normal starting point. In the very beginning, a two-dimensional fluidized bed is formed by two parallel transparent glass plates with a narrow width of approximately 1 cm to observe the shape of the bubble [2] . A schematic diagram of this apparatus is shown in Figure 2.6. It is clear that this bubble has a round frontal cap and the bottom is a little indented. Also it is believed that, to some extent, it is akin to the shape of a bubble formed by injecting air into a liquid column. The bubble is inevitably elongated by two closely separated walls due to the two dimensional nature of the bed.

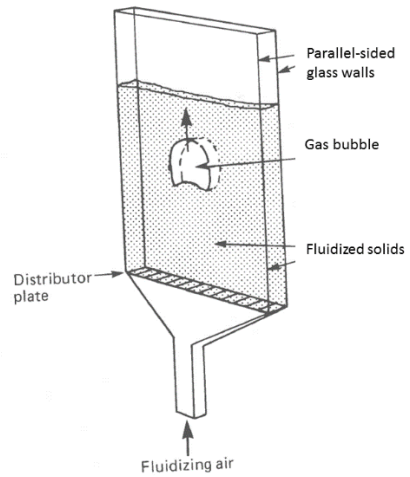

Figure 2.6: A gas bubble rising in a two-dimensional fluidized bed [2].

To overcome this obstacle, a novel X-ray techniques was applied by Rowe *et al.* [62] to study the feature of the bubbles in a fluidized bed in a three dimensional fashion. An X-ray photograph of the typical three dimensional bubble is presented in Figure 2.7. This type of bubble normally appears in beds with Group A and B particles.

As it is shown, the bubble is observed to have an approximate spherical frontal cap which is similar to the bubble in the two dimensional bed. The rear part of it is indented. The indented base is normally termed as the wake of the bubble, which is illustrated in Figure 2.8. Small bubbles tend to grow and coalesce with vicinal ones while they are travelling upwards in the bed. The detailed information of bubble growth and coalescence will be given in the following section 2.5.2. The rising velocity is proportional to the size of them. In the process of rising, a cluster of particles accompany the bubbles by filling the indented bottom area. The bubbles burst when they reach the top of the freeboard, the cluster of particles are abandoned on to the freeboard. It is convincingly concluded that this feature of bubbles contributes significantly to the fundamental mechanism of solids mixing.

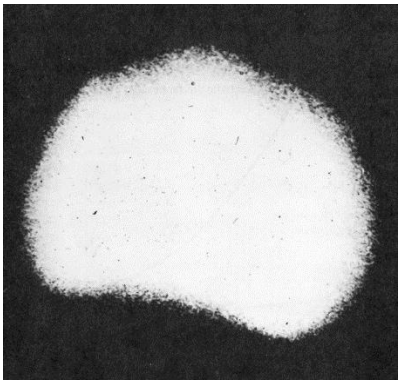

Figure 2.7: X-ray photography of a three dimensional bubble in a bed of catalyst-grade alumina of mean particle size of 150 microns [63].

Although bubbles appeared in the gas solid fluidized beds they can always be analogous with bubbles in gas liquid columns, some distinctions between them can always be found. Among these, the definition of the boundary that is for distinguishing the emulsion phase and bubble phase may be the most apparent one. Unlike the bubbles in liquid columns, the gas bubbles in gas solid fluidized beds have no unambiguous boundary, which is permeable for gas travelling though the bubbles. Therefore, the exchange between the gas inside the bubbles and the gas in emulsion phase prevails. On one hand, suppose in a fluid-bed catalytic reactor, the two phase conversion factor becomes much higher due to this gas exchange. On the other hand, if the rate of the exchange is not well controlled, serious gas by-passing may happen, which is not expected.

An idealized spherical-cap bubble shape is proposed by Rowe *et al.* [62] who investigated the bubble shape extensively using X-ray techniques. As shown in Figure 2.8**,** the top half has a spherical shape and its radius of the curvature is entitled as r. Since the r is not always straightforwardly attainable, it is practical to express the diameter of the bubble in a volume equivalent manner, which means the bubble diameter is equal to the diameter of a perfect sphere whose volume is equal to the volume of the bubble. It is mathematically demonstrated as follows:

$$d_{eq} = (\frac{6V_b}{\pi})^{1/3} \qquad (2.14)$$

where V_b is the bubble volume, which can be seen schematically in Figure 2.8. The shape of the bubble is characterized by the wake angle, known as θ_w. The wake angle is formed by the vertical centreline and the lower rim straight line. The value of the wake angle θ_w is dependent on the bubble Reynolds number as indicated by Grace [64].Some other important parameters of interest are also shown in Figure 2.8. The frontal diameter of the bubble is denoted as d_b. The volume of the wake base is marked as V_w. The ratio of wake volume to the whole sphere volume is expressed as $3V_w/4\pi r^3$, which is also practically called wake fraction symbolized as f_w.

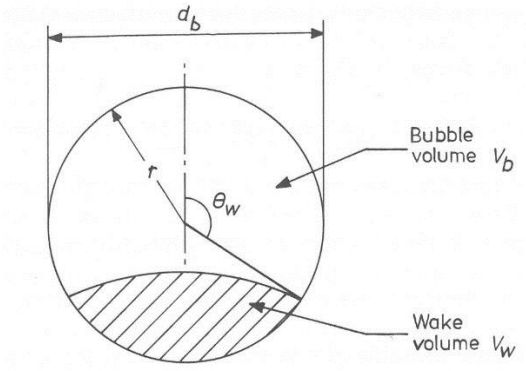

Figure 2.8: Idealized spherical-cap bubble shape [1]

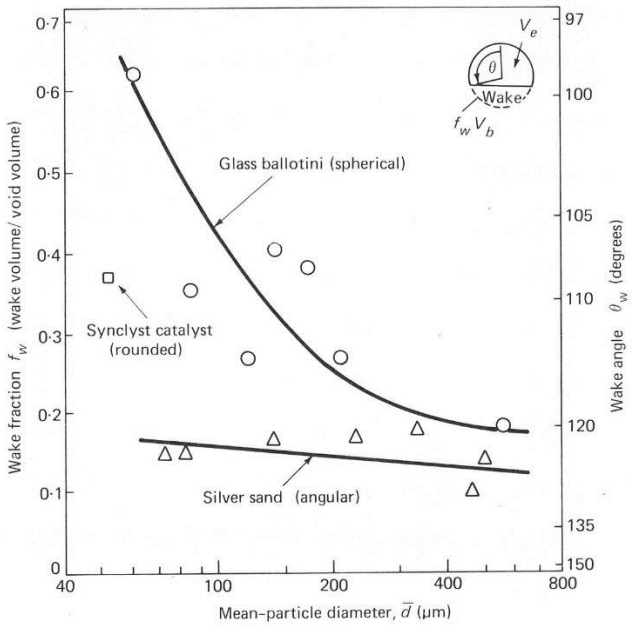

Figure 2.9: Wake angle θ_w and wake fraction f_w for bubbles in a three-dimensional fluidized bed as observed using X-ray photography by Rowe and Partridge (1965) [63]

The value of the wake angle θ_w differs from one fluidized bed system to another. Correspondingly the wake fraction f_w varies as the wake angle does. Figure 2.9 summarizes the experimental results for wake fraction and wake angle values of three types of solid particles with different shapes. The results were obtained from X-ray measurements conducted by Rowe and Partridge [63]. The results from Figure 2.9 demonstrate that the wake angle becomes larger with increasing particle mean diameter. That means the bubbles are more likely to be rounded in shape (at least for spherical particles). Moreover, another conclusion which can be drawn is that the wake angles obtained from angular particles are universally lower than the wake angles for rounded particles. Therefore, the bubbles formed from angular particles have the tendency to be more spherical. Nevertheless, the results from Figure 2.9 can

only serve as a reference and practical results have to be collected and analysed based on individual experimental rigs.

2.5.2 Growth and coalescence of bubbles

Once the bed is fluidized when the superficial gas velocity is higher than the minimum fluidization value, bubbles are expected to emerge continuously in the bubbling regime. It is normally observed that in the vicinity of the distributor area there are a large number of small bubbles, whereas near the area of the top freeboard of the bed a small quantity of large bubbles is discovered. The bubble growth and coalescence process largely contributed to this phenomenon [2].

Although the mechanisms of the bubble growth and coalescence between two dimensional and three dimensional fluidized beds has been confirmed as not being inherently identical, some common processes are still useful in perceiving the nature of them. These were initiated by Sit and Grace [11] who studied the transfer of ozone gas between the bubble phase and emulsion phase. The general process is composed of the following four sub-stages. The first stage is from the time-spot when both lower bubbles and upper bubbles have been formed properly to the moment when the frontal area of the lower bubble touches the wake boundary (as illustrated in Figure 2.8) of the upper bubbler. During the second stage, the lower bubble moves forward further until its frontal nose touches the lower surface of the leader bubble. The third stage is referred to as the essential coalescence stage when these two bubbles merge but have not been in stable shape. The final step is called the post period of coalescence when the coalesced bubble adjusts to get its final shape.

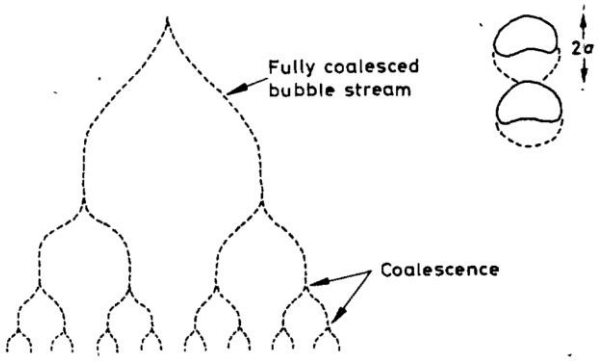

Figure 2.10: Bubble paths during coalescence. The process should be visualized in three dimensions [65]

A great deal of experimental work has been carried out despite the fact that the physical principle behind the bubble growth and coalescence phenomenon is still unclear. Many empirical correlations were proposed by

previous researchers to seek out any potential connections between different sets of parameters in respect of solid and gas properties and the varying bubble size, which will be shown in the next section, 2.5.3. Among these investigators, Darton [65] initially proposed a mechanistic bubble growth and coalescence model which is displayed in Figure 2.10.

In this coalescence model, lateral movements are put into consideration of forming bubbles coalescence apart from the vertical merging processes which were mentioned by Sit and Grace [11]. The separated distance between two bubbles before they merge is approximately twice the radius of the spherical region which surrounds the bubble and the wake of it, as shown in Figure 2.10. Based on his bubble coalescence model, an empirical correlation integrating previous literature's experimental data was also proposed by Darton, which attracted much popular usage due to good agreement with various experimental results and will be introduced in the following section of 2.5.3.

2.5.3 Correlations for bubble size

Bubble size is one of the most essential parameters for characterizing the feature of the bubbles in fluidized beds. Thorough understanding of bubble size enables the operators to make the most of the fluidization process and prevent any potential unexpected consequences occurring in fluidized beds used in industrial applications, which are sometimes very costly. Therefore, a great deal of research has been conducted to characterize bubble size. Consequently, many empirical or semi-empirical correlations abound in the literature. These correlations are normally obtained by virtue of a considerable amount of experimental data along with some underlying theoretical evaluations. Then, relative parameters and constants are derived to constitute the correlations.

Some widely accepted empirical correlations for estimating bubble size will be reviewed in this section and the work done by Karimipour and Pugsely [66] will be considered extensively. In their study, twenty five correlations for bubble size estimation have been examined by calculating the squared difference between the empirical correlations and the corresponding experimental data available in the literature. In this section, generally, the correlations for estimating a single bubble generated just above the gas distributor (also referred as the initial bubble) will be presented. After that, the correlations for estimating bubbles in beds considering the aforementioned bubble growth and coalescences phenomenon will be shown.

As in most cases, the value of the initial bubble size is one of the parameters used in some empirical correlations to estimate the bubble sizes in the fluidized beds. Besides, the initial bubble is the basis of the grown bubble in the upper part of the bed. Hence it is necessary to firstly introduce the correlations for the initial bubble size. Miwa [67] proposed a correlation with both porous and perforated distributors. As the distributor used in the following study of this thesis is a perforated air distributor, only correlation of the initial bubble diameter generated above the perforated type of distributor will be shown here for the sake of simplicity.

$$\mathrm{d_0} = 0.347\{\mathrm{A_t}(\mathrm{U_0} - \mathrm{U_{mf}})/\mathrm{n}\}^{2/5} \qquad (2.15)$$

where n is the number of holes in the cross section of the gas distributor; $\mathrm{A_t}$ is the cross-sectional area of the fluidized bed; $\mathrm{U_0}$ is superficial gas velocity; $\mathrm{U_{mf}}$ is the minimum fluidization velocity.

Once bubbles have been formed just above the gas distributor, they will grow and coalesce as indicated by the previous bubble behaviour of bubble growth and coalescence in section 2.5.2. Accordingly, the size of them will vary in this process. A great deal of research has been conducted by previous researchers to investigate the approach to estimate the bubble diameter. Therefore, some empirical or semi-empirical correlations are given in Table 2.1.

As mentioned earlier, Darton [65] proposed his empirical correlation to estimate a bubble's diameter based on his bubble growth and coalescence model which has been demonstrated in section 2.5.2. Their model has become one of the most popular bubble size correlations in the literature. Details of the correlation are presented in Table 2.1. By looking at the correlation, it can be seen that the bubble size is largely dependent on the height above the distributor h. Also, A_0 denotes the 'catchment area' for the bubble stream at the distributor plate, which characterizes different distributors and is generally the area of plate per hole for a perforated distributor.

Rowe and his co-workers have utilized X-ray facilities to observe bubble behaviour in fluidized beds [63, 68-71]. They used different types and sizes of solid particles and concluded that the bubble shape was virtually hemispherical in most cases. Meanwhile the wake angle (see Figure 2.8 for illustration) of bubbles tended to decrease and level off with increased particle size for spherical particles. The issue of the transition from two dimensional experimental results to three dimensional results has been addressed and it is found that the bubble size largely dominates the bubble behaviour. Based

on the above findings and experimental results, Rowe suggested an empirical correlation for characterising bubble size expressed as a function of excess velocity, which is shown in Table 2.1. In the correlation, the parameter of h_0 stands for a measure of the initial bubble size.

Mori and Wen (1975) [72] proposed a correlation for predicting bubble size in gaseous fluidized beds in order to account for the effect of the bed diameter on the bubble diameter, which has not been accounted for by preceding investigators. The correlation is listed in Table 2.1. The most distinct feature of this correlation with others is that it relates the maximum bubble size, which is the maximum bubble size a bubble can reach due to coalescence, initial bubble size, height above the gas distributor and the bed diameter.

Werther (1978) [73] has extensively examined the bubble characteristics by means of capacitance probes which will be illustrated in more detail in the later section 2.6.2. Werther [74-76] found a non-uniform bubble size distribution in the radial direction across the bed. It has been found that bubble size increases at a specific height above the distributor with reduced bed diameter. This could stem from the rapid development of the bubble in smaller beds. Based on the bubble characteristics Werther discovered, he proposed a correlation, which is presented in Table 2.1, to estimate bubble size initially for a porous distributor but eventually it has been extended to a perforated gas distributor. In this correlation, bubble coalescence is assumed as the principle bubble size development. Another generalized correlation which appeared in Table 2.1 was brought by Cai [77]. In his experiment, he considered the influence of pressure applied in the pressurized fluidized bed combustors (PFBC) on bubble size observation. The correlation is claimed as being applicable to atmospheric operating conditions although it was derived from pressurized general form.

It is worth noting that all of the five empirical correlations for bubble size estimation has been evaluated by Karimipour and Pugsley [66]. They are in the top five best correlations for estimating bubble size under three different criteria, viz, a) the bed is fluidized with Group B particles, b) the bed is operated with low operating velocity (less than 10 U_{mf}) and c) the bed is fitted with a perforated gas distributor. Hence, these five empirical correlations will be used later for comparative purposes with bubble sizes estimated from ECT experimental measurements.

Table 2.1 Correlations of bubble diameter in fluidized beds

No.	Authors	Correlations	Particles Group	Measurement Type	Distributor Type
1	Darton 1977 [65]	$D_B = 0.54 \times (U - U_{mf})^{0.4} \times (h + 4{A_0}^{0.5})^{0.8}/g^{0.2}$	Group A,B and D	Capacitance probe, X-ray and Photography	Porous and Perforated
2	Mori and Wen 1975[72]	$\frac{D_{BM} - D_B}{D_{BM} - D_{BO}} = \exp(-0.3h/D_t)$ $D_{BO} = 0.347 \times \{A_t(U - U_{mf})/n_d\}^{2/5}$ $D_{BM} = 1.87 D_{BO}$	Group A,B and D	Different	Porous and Perforated
3	Rowe 1976[78]	$D_B = \left(U - U_{mf}\right)^{1/2}(h + h_0)^{3/4}\mathrm{g}^{1/4}$	Group A,B and D	X-ray Photography	Porous and Perforated
4	Werther 1978 [73]	$d_v = d_0[1 + 0.272 \times \left(U - U_{mf}\right)]^{1/3}(1 + 0.0684\mathrm{h})^{1.21}$ $d_0 = 0.853$ for Group B particles	Group A,B and D	Capacitance Probe	Porous and Perforated
5	Cai 1994 [77]	$D_{bh} = 0.38 \times H^{0.8}\left(U - U_{mf}\right)^{0.42}$ $\times \exp[-0.25 \times \left(U - U_{mf}\right)^2 - 0.1\left(U - U_{mf}\right)]$	Group A,B and D	Different	Porous and Perforated

2.5.4 Correlations for bubble rising velocity

Less empirical correlations are available in the literature compared with the bubble size estimation correlations. This may be due to the fact that there are difficulties encountered in experimental design and set-up to obtain bubble rising velocity data. The main experimental approaches are optical probes [79, 80] and capacitance probes, which are separated for a certain distance [76]. Bubble rising velocities are calculated by the distance being divided by the time period when the bubble is passing from one probe to another. As Karimipour and Pugsley [66] evaluated on bubble rising velocity, it was a surprise to discover that the simple correlation derived by Davidson and Harrison [13] gave quite good performance. The correlation is displayed in Table 2.2. It can be found that there is one parameter, namely, single bubble rising velocity, which needs to be determined before achieving the bubble rising velocity U_{br}.

In the literature, most of the correlations for deriving single bubble rising velocity are obtained based on the original equation of Davis and Tylor [81] who proposed an equation for estimating bubble rising velocity in liquids. However, the one derived by Davidson and Harrison [13] is regarded as the most popular one used for estimating single bubble rising velocity in fluidized beds, which is expressed as follows. It can be seen that the bubble rising velocity is mostly influenced by the bubble diameter.

$$U_{br} = 0.71 \times \sqrt{g d_b} \qquad (2.16)$$

Apart from the above Equation 2.16, another correlation initiated by Werther [76] has also gained much popularity in estimating bubble rising velocity. He used two needle capacitance probes to measure the averaged bubble rising velocity and found there were some deviations from the two-phase theory proposed by Toomey and Johnstone [54]. After conducting a series of experiments with different bed heights and bed diameters, he found that the predication from the two-phase theory would be much more accurate with data obtained from smaller laboratory scale beds. Based on his experimental data and theoretical analysis, a correlation is proposed, which is shown in Table.2.2. From the correlation it can be seen that instead of using the single bubble rising velocity value, he put forward one constant, φ, which varied for different particle types. The corresponding value of this constant for Group B particles is presented following the main correlation. The value is influenced by the bed diameter D. According to the evaluation from Karimipour and Pugsley [66], Werther's correlation performed as the best one for all types of particles giving a least squares difference between the original experimental

data and the predicted data from the correlation. Therefore, the two correlations shown in Table 2.2 will be applied in further comparison with ECT and pressure fluctuation experimental data measurements to identify the capability of the corresponding measuring techniques.

2.6 Conventional instrumentation and measurement techniques for fluidization

Fluidized beds have been utilized in chemical process engineering and energy sectors such as coal combustion at power generating stations, although they have been most favoured in the process of fluidized catalytic cracking (FCC) [10]. However, despite some fundamental theoretical or experimental discoveries which have been achieved over the last few decades, the complex intrinsic flow structure and hydrodynamic characteristics of the gas solid fluidized beds are still a hindrance to further usage of the fluidization technology.

This consequently imposes great challenge for the development of the experimental measurement techniques. Because the quality of experiments often derives from ingenious measuring instruments and precise and reliable measurements are the priority condition for good understanding of the nature of the fluidized beds. From the point view of industrial applications, such robust measurements can be used for monitoring of fluidization reactor performance, reaction process optimization and problem troubleshooting during the reaction process [18]. On the other hand, essential measurements are still vital for many phenomenological models which need empirical input [19]. Therefore, the output quality of the models truly rely upon the quality of the experimental measurements.

Fluidized beds have been studied by many researchers using different approaches which have undergone several stages of development along the evolution of fluidization technology [10, 18, 20, 45]. Some of them have been proved to be reliable and easy to handle both in laboratory scale and industrial routine measurements, such as pressure measurements (measured by water monometer or pressure sensors, etc.) and temperature measurements (measured, for example, by heat transfer probes). However, temperature measurements will not be included in this section as there are no heating elements involved in the following experiments of this thesis.

Table 2.2 Correlations of bubble rising velocity in fluidized beds

No.	Authors	Correlations	Particles Group	Measurement Type	Distributor Type
1	Davidson and Harrison 1963 [82]	$U_b = U_{br} + (U - U_{mf})$	Group A,B and D	Different	Porous and Perforated
2	Werther 1978 [73]	$U_b = \varphi\sqrt{g d_b}$ For Geldart B particles: $\varphi = \begin{cases} 0.64 & D \ll 10 \\ 0.254 \times D^{0.4} & 10 < D < 100 \\ 1.6 & D \gg 100 \end{cases}$	Group A,B and D	Capacitance Probe	Porous and Perforated

In the following section, a few conventional measurement techniques will be introduced in detail. They are pressure measurements, optical probe measurements and capacitance probe measurements.

2.6.1 Pressure measurements

Pressure is one of most vital parameters in describing the characteristics of a gas solid fluidized bed as the stable pressure drop across the bed features in the onset of the minimum fluidization phenomenon, as indicated in Figure 2.1. Once the bed is in a fluidized state, the solid particles are suspended in the bed by virtue of the upward flowing gas. This state can be approximately governed by the following equation, which can be regarded as a modification of Equation 2.1.

$$\Delta P \approx \left(\rho_s - \rho_f\right) C_v \, g \, \Delta h \qquad (2.17)$$

where C_v is the average solid volume concentration in the volume element $A_t \Delta h$ of the bed. A_t is the cross-sectional area of the fluidized bed. The pressure drop at different heights above the gas distributor across the bed has a linear relationship with the averaged bed pressure drop and bed height, which is shown in Figure 2.11. This phenomenon is attributed to the fact that in a bubbling fluidized bed, the average solid concentration is virtually independent of the bed height [18].

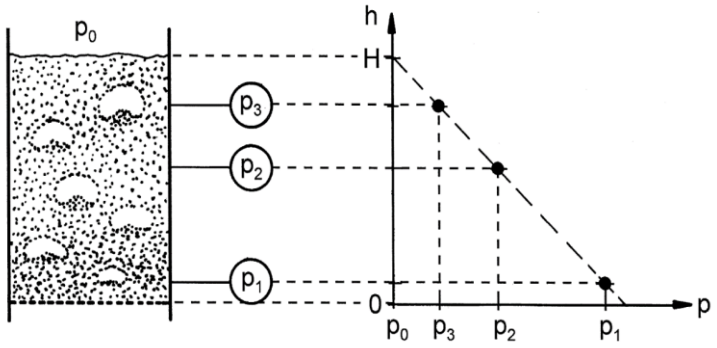

Figure 2.11: Determination of the expanded bed height in a bubbling fluidized bed [18]

According to Figure 2.11, the bed height corresponding to a specific pressure measuring location can be derived by extrapolating the measured pressure profile with the data obtained by a number of pressure measurements along the bed height. It is a standard measuring routine both in bench-scale platform and industrial applications. However, attention needs to be paid to the pressure pores which are sometimes easily blocked by agglomerated fine particles.

In addition to the averaged pressure drop in fluidized beds, pressure fluctuation measured by rapid response pressure transducers has been proved very useful in studying the internal flow structure within fluidized beds. There are normally two types of pressure fluctuation measurements in respect of the assembly on how pressure probes are connected with the fluidized bed.

One can be treated as an invasive action if the pressure probes or transducers are immersed totally or partially in the body of the bed (either in the centre or at an edge location). The other type is non-invasive pressure fluctuation measurements by which one end of a pressure probe is assembled flush with the fluidized bed inner wall surface and no parts of the probe intrude into the bed. The other end of the pressure probe is connected to a pressure transducer. More details about the second type of pressure measurement will be dealt with more extensively in section 2.9.

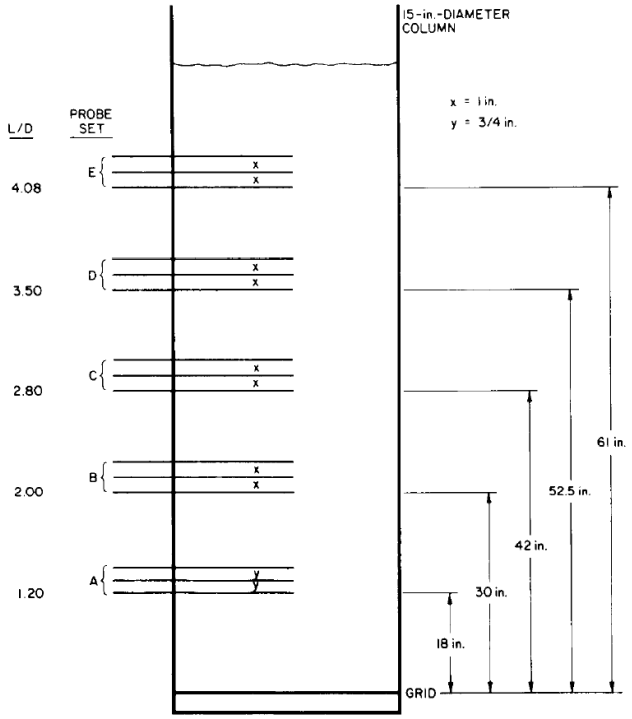

Figure 2.12: Pressure-probe configuration in the 15 inch diameter column [83]

One of the typical works on invasive pressure measurement has been conducted by Chan [83]. The configuration of his pressure measurement is shown above in Figure 2.12. There were five sets of pressure probes in total used in his experiment. Each set consisted of three parallel pressure probes separated by equal intervals. The opening sides of all five sets of probes were positioned in the centre of the bed. Bubble rising velocity was determined by any set of probes when a bubble was travelling through two adjacent probes.

As the pressure inside a bubble is assumed uniform, the corresponding probe-to-probe pressure drop detected by two adjacent probes is zero (a schematic diagram can be seen in Figure 2.13).

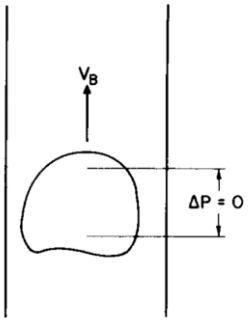

Figure 2.13: Uniform pressure inside a bubble [83]

The bubble travelling time span was calculated starting from the point when the top surface of the bubble touched the lower probe until the moment when the surface met the higher probe, so that interval between two probes means the bubble rising velocity can be readily determined. Meanwhile, bubble size (bubble pierced length) can be calculated with the aid of bubbling rising velocity and the distance between adjacent probes. This approach gave new insight into characterising bubble behaviour by means of the pressure fluctuation measurements.

However, this method for characterising bubble size and bubble rising velocity firstly depends on the condition that the bubble size should be significantly larger than the interval between adjacent probes otherwise the theory described above will not be valid. On the other hand, the internal gas solid two phase flow patterns will be unavoidably disturbed by the intrusion of the pressure probes. For instance, the bubbles may be broken or split due to the sudden contact with pressure probes.

2.6.2 Fibre optic probes

Fibre optic probes have been developed significantly [10, 18, 20, 21, 49, 84-86] and utilized widely in the area of fluidized beds in the last few decades. Their popular utilization largely benefits from the fact that they are simple to fabricate, are able to produce high signal-to-noise ratios and can create high accuracy if the probes are carefully designed [19, 87]. They were applied in both low flow regimes, such as the bubbling regime, and high flow beds, such as circulating fluidized beds [19]. Although, in the early stages, fibre optic probes were employed to determine local solid particles movements and the particle concentration [88, 89], they have more recently been applied to

characterize bubble features such as bubble size, bubble frequency, bubble rising velocity and bubble size distribution [21, 85, 90-93].

From the point view of a measuring principle, there are normally two critical components composing the fibre optic probes, namely, emission and detection fibres. Generally, two types of fibre optic probes have been utilized by previous researchers. The first type is based on fundamental forward light scattering whilst the second type is based on backscattering to a fibre optic system [19, 42, 49, 87].

One of the earliest reports of using the principle of the first type of optic probes was that by Yasui and Johanson [84]. They used a tungsten filament lamp as a light source which was coupled to a metal tube and a glass prism was chosen as the detector probe. Two such probes are separated by a certain short distance with one above another. The bubble rising velocity was calculated based on the time lag during which bubbles passed the two probes from the lower probe to the higher one and their separation distance. The corresponding bubble size (actually bubble chord length) was estimated as the product of the bubble rising velocity and the time length of the light pulse transmitted by each bubble. Consequently, the bubble size, bubble frequency and bubble rising velocity in ambient pressure fluidized beds have been successfully studied [85]. Although at that time, fibres were not the light transmitting media, the principles for extracting bubble characterization were widely adopted by their succeeding investigators.

An example of using the first type of fibre optic probes is the research conducted by Kage *et al* [51, 52]. A schematic drawing of their experimental fibre optic rig can be found in Figure 2.14. The primary purpose was to measure the frequency of bubble generation at the orifice of the distributor. The probes were placed 40 mm above the gas distributor to make sure the bubble generation frequency could be measured directly without being influenced by the continuous jetting flow flown from the distributor. A tungsten-halogen lamp was used as a light source. When there is a bubble emerging between the tips of the ‘source’ and ‘detector’ fibres, the detector probe can sense the light which is projected from the tip of the optic source fibre (the bubble phase is essentially optically clear). On the contrary, there would be no projected light to detect if the dense phase (or emulsion phase), instead of bubbles, engulfs the space between the two probes as the dense phase is not transparent to light.

Kage *et al* [51, 52] then examined three peak frequencies derived from the power spectral density function from the signal of pressure fluctuation

measured at the bed plenum position. A relatively good agreement has been found between one of the peak frequencies (called Fg) and the bubble generation frequency measured by the fibre optic probes.

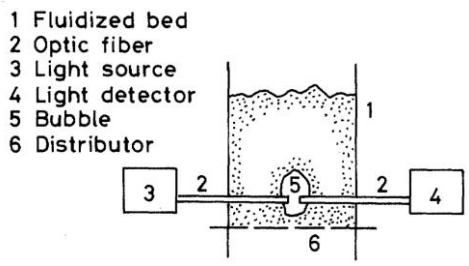

Figure 2.14: Outline of the fibre optic probe [52]

The second type of fibre optic probe has more advantages than the first type as it is simpler and less intrusive due to the nature of its configuration (normally intermingled or arranged in rows) [19, 42, 87]. Therefore, this type of fibre optic probe has been widely applied and received much attention from former scholars. Among those fellows, Pugsley [42] verified the usage of electrical capacitance tomography techniques in a cone shaped circulating fluidized bed by means of a cross-optical fibre probe which was believed to have no blind region and the measurement volume is well defined (less than 2 mm^3). However, no bubble parameters have been studied by them.

Rüdisüli *et al.* [21] utilized optical probes to investigate bubble characterization including bubble size and bubble rising velocity. A bubble linking algorithm was developed by them based on regression techniques. A schematic representation of their in-house designed fibre optic probes is shown in Figure 2.15. These reflective optical probes were used to measure bubbles feature in a fluidized bed. When the light is emitted from the ‘source’ probe, the ‘sensor’ probe can detect the reflected light if there are solid particles appearing within the measurement volume, as indicated in Figure 2.15. This principle is slightly different as depicted in the previous type in Figure 2.14.The amount of reflected light virtually depends on the concentration of the dense phase as the voids or bubbles are not able to reflect. Therefore, according to the measured intensity of the reflected light, the bubble fraction or concentration at the tip of the probes can be attained via the transferred voltage signal.

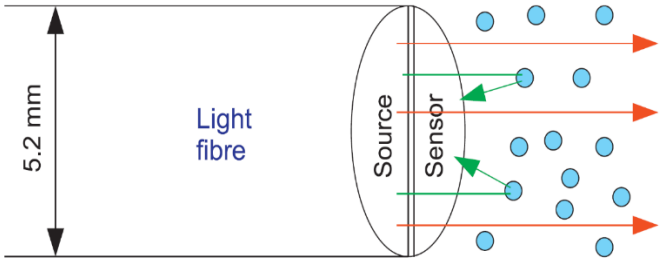

Figure 2.15: Schematic representation of the fibre optic probes in-house designed by Rüdisüli *et al.* [21]

Despite the fact that fibre optic probes have frequently been considered as a helpful approach to measure local voidage or bubble behaviour in fluidized beds [19]; there are still several issues which prevent their use in applications either in lab-scale beds or industrial plants. For the foremost, the nature of intrusion to the internal flow pattern cannot be eliminated completely which unavoidably disturbs the fluidized bed hydrodynamics. Furthermore, well-defined measurement volume (i.e. the probe size versus the solid particle size) and proper calibration procedure are always difficult to reach, which limits the accuracy of the fibre optic probes conventionally. Finally, it is still hotly debated and under scrutiny as to whether the fibre optic probes can bear harsh conditions such as high temperatures and high operating pressures which are common in industrial surroundings though some attempts have been made [94].

2.6.3 Capacitance probes

The original concept of bridging the dielectric constant distribution of two distinct fluid flow phases (such as gas solid systems) to the volume fraction of one phase distributed within another was initially introduced by Maxwell [95]. Capacitance probes which have been utilized by a large number of scholars to investigate the internal fluid flow processes within gas solid fluidized beds in the past few decades followed the above theory.

The principle can be summarized as follows [10, 40]. The capacitance value of a gas solid mixture (i.e. the emulsion phase of a gas solid fluidized bed) is intensely linked with the concentration of the solids in the mixture. If there is a change in the solids fraction (suppose a bubble appears) around a certain local position in the bed, a capacitance probe, which is placed around that specific location, can detect the change by measuring the corresponding capacitance value of the mixture material. The capacitance value will then be converted into a voltage signal which can be further interpreted via appropriate procedures. As the gas-solids fluidized beds are largely of a non-conductive

property (solids normally are silica sand, cracking catalysts, etc.), therefore, capacitance probes gained popular usage, especially in laboratory scale beds [96].

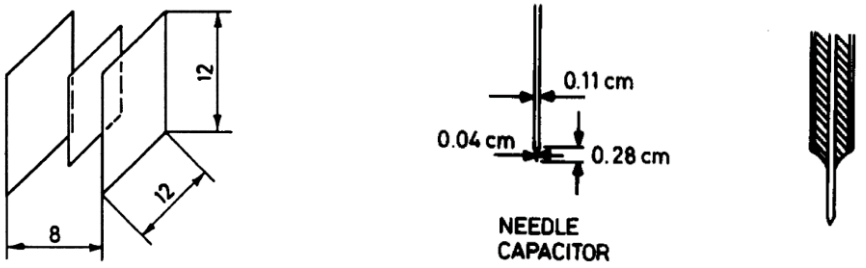

(a) (b)

Figure 2.16: (a) Geometry of the capacitance probe (dimensions in mm) used by Morse and Ballou [22]; (b) A needle type capacitance probe [24]

The concept was first put to use by Morse and Ballou [22] who used a parallel plates capacitor to study the uniformity of fluidization with a bed of fine particles and obtained quite useful qualitative findings. The geometry drawing of their capacitance probe is shown in Figure 2.16(a). Following Morse and Ballou, Geldart and Kelsey [97] employed a similar type of capacitance probe to investigate the events occurring in freely bubbling fluidized beds. They also addressed an inherent problem of the capacitance probe in interpreting the results.

In order to minimize the local disturbance to the fluid hydrodynamics, Werther and Molerus [23, 24] conducted a series of meticulous studies on the proper design of a capacitance probe comprising several factors, e.g. as little disturbance to the bed as possible, rapid response of measurement and sufficient mechanical strength, etc. Subsequently they proposed a needle type capacitance probe, which is schematically presented in Figure 2.16(b). They also introduced some classic approaches to deriving bubble characterization, for example, bubble size (pierced length) and bubble frequency. Figure 2.17 shows the principle suggested by them to estimate the bubble rising velocity. The tips of the two probes were separated by a small distance. The cross correlation techniques were utilized to derive the time lag during which the bubble traverses from the lower probe to the upper one. The corresponding bubble rising velocity was obtained by associating it with the known distance.

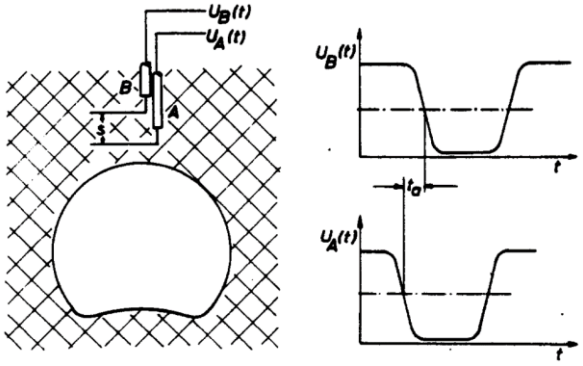

Figure 2.17: Measurement of the rise velocity of a single bubble [24]

However, when Hage *et al* and Grace *et al* [9, 98] carried out research on fluidized beds utilizing the similar capacitance probes configuration, they encountered some difficulties. Those problems may be explained by the following issues. Firstly, the capacitances are conventionally determined by balancing a bridge circuit. One difficulty may stem from the fact that the capacitances of the probe body and cables themselves can be larger than the values measured by the probe itself. Secondly, 'stray capacitances' may occur around the adjacent electrical surfaces, which would interfere with the proper measurement of the probes. Finally, the miniature property of the minimized capacitance probes can possibly produce capacitance values which are far smaller than the detectable range of traditional bridges, which consequently may create drift or instability [18, 19].

To overcome the aforementioned problems, Riley and Louge [99] initially introduced a guarded capacitance probe whose principle is shown in Figure 2.18. By using the guard circuit, the measurement circuit can be immunized largely from the stray capacitances. This arrangement was then adopted by Hage and Werther [100]. They constructed a new type of capacitance probe, called the water cooled needle capacitance probe, by integrating the guarded probe and needle probe configuration. Through the application of this newly designed probe, their measuring system utilized both in laboratory and industrial fluidized bed combustors, exhibiting higher resolution and stability compared with previous probes.

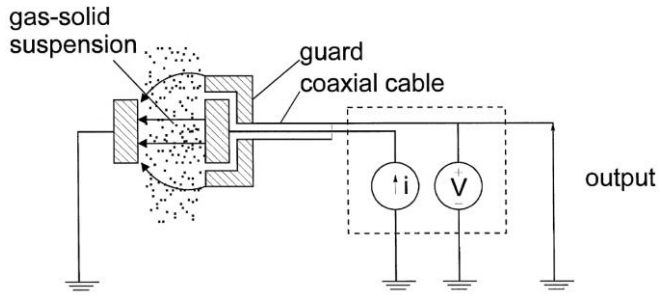

Figure 2.18: The principle of the guarded capacitance probe [18]

Despite the fruitful achievements the capacitance probes can bring about in studying local bubble properties in gas-solids fluidized beds, it is recognized by many researchers [25, 40, 101] that the disturbances and inferences induced by the intrusion of the probes cannot be avoided completely. According to Rowe and Masson [25, 101] who studied the effect of the intrusion with X-ray techniques by comparing nine different probes which were used by their preceding investigators, it was concluded that a probe can disturb bubble characterization. The quantity of properties measured with intrusive probes is different from those measured in a probe-free bed. It was observed that the probes have a tendency to attract bubbles towards them and elongate and accelerate bubbles in different degrees. The influence exerted on small bubbles was found to be significantly larger than those on larger bubbles. On the other hand, the intrusion nature can be eliminated completely by a measuring technique called electrical capacitance tomography which utilizes similar permittivity mixture measurement theory as capacitance probes to determine the solids fraction within two phase flow. This will be introduced in detail in section 2.8.

2.7 Non-intrusive measuring approaches

By looking at the concept, a fluidized bed is a quite simple device which only needs a source of upward flowing gas and a bed of solid particles sitting on a distributor [102]. But the advantages of fluidized beds, for example, high gas-solids mixing capability, high heat and mass transfer rates, are so powerful that fluidized beds have been utilized in many process applications as mentioned in section 2.1. However, the internal fluid flow processes are inherently fully three-dimensional. When the gas velocity is intermediate, bubbles or slugs (appearing in deep beds normally) can dominate the hydrodynamics within the fluidized beds. The behaviour of bubbles is truly complex during the process of their formation, growth, coalescence, splitting and bursting on the bed surface[26].

Therefore, many sophisticated techniques have been developed during recent decades, apart from some traditional temperature and pressure measurements, which are normally routine measurement approaches in industrial applications. In the previous section, some novel measurement techniques, such as fibre optic probes and capacitance probes, have been introduced.

However, all the previously mentioned conventional measurement methods suffer from some serious shortcomings. Firstly, the three-dimensional nature cannot be studied easily due to the fact that probes are often inserted at a local position. Such a 'point-based' measuring manner cannot rightfully reflect a three dimensional picture of the fluidized beds. Moreover, as indicated in section 2.6.3, those probes always introduce unavoidable intrusion which have been confirmed and will interfere with the internal characteristics of the beds. Hence, it is understandable that a great deal of non-invasive measuring techniques have been developed which can visualize, qualify and quantify the internal three dimensional fluid flow processes of fluidized beds. In this part, several non-invasive investigative techniques, such as optical photography, X-ray and Gamma-ray, will be reviewed in a detailed and critical fashion.

2.7.1 Optical Photography

Bubbles in fluidized beds are not always observable, either in large industrial scale or laboratory scale beds. Even in the latter case, bubbles can only be intermittently observed when they travel upwards along the bed wall surface. Otherwise the bubbles are immersed in the three dimensional tubular bed although the material of the bed is transparent in most cases [10].

However, visual observation will be possible if the fluidized bed is formed in a two dimensional manner, as indicated in Figure 2.19(a). High frame-per-second photographs or videos can also be taken to assist direct observation by the naked eye. The two-dimensional column normally has a rectangular cross section and consists of two parallel transparent plastic plates separated by an appreciably narrow distance (normal range 10 to 25 mm) [45]. It can be treated as a vertical slice from a three-dimensional bed system [10]. The effects of light reflection are largely eliminated by the parallel wall compared with the true three dimensional convex wall [45].

Many previous researchers utilized this two-dimensional fluidized bed by means of cine photography or video imaging and have drawn a large quantity of academic achievement in characterising bubble behaviours such as information on bubble rising, bubble coalescence, etc. Geldart and Cranfield

[103] employed two sets of two-dimensional fluidized beds with a width of 2 cm and 5 cm respectively, and studied bubble rising velocity, bubble shape and bubble size with large particles presenting in the beds. A significant difference was found in the gas distribution between the dense and bubble phases compared with the conventional two phase theory of fluidization. Arena *et al.* [104] made use of a thin, two-dimensional riser with transparent walls to investigate the solids flow structure by means of a motion analysis system which is capable of capturing 2000 frames per second. The two dimensional system was used by Hailu *et al.* [105] to measure the through flow velocity of gas inside a rising bubble by injecting single bubbles with light tracer particles and the results were in agreement with the theory prediction proposed by Davidson and Harrison [82].

Although there are many useful qualitative conclusions which have been drawn from two-dimensional systems in respect of bubble behaviour, it still cannot be ignored that the two dimensional beds cannot, to some extent, truly reflect the internal complex flow structures happening in three-dimensional systems. This may stem from some different mechanisms inherently between these two systems such as the rising velocities of isolated bubbles, bubble coalescence properties and bubble shape and wake characteristics [45]. Therefore, Rowe and Everett [70] studied the effect of transiting from 2D to 3D fluidized beds. The thickness of the two-dimensional bed was increased from 14 mm (a two dimensional column) to 0.30 m (a fully three dimensional column). They have concluded that with the increasing width of the bed, an obvious change has been found in bubble properties although the change was less significant when the bed width was increased beyond 0.10 m.

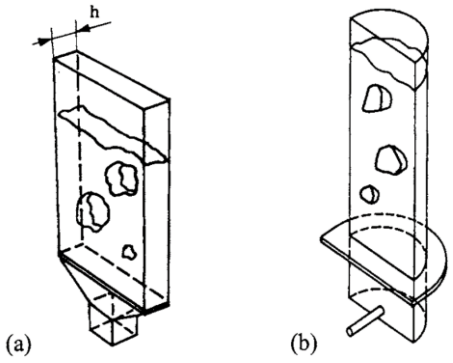

Figure 2.19: Schematic diagram of : (a) two dimensional column; (b) semi-cylindrical column [45].

A semi-cylindrical column was proposed to counteract this significant difference between two-dimensional and three-dimensional systems, as shown in Figure 2.19(b). The semi-cylindrical column is composed of a half

piece of a three-dimensional cylindrical pipe and a piece of flat plate which is similar to that used in the two dimensional column. This was successfully used by Whiting and Geldart *et al* [106, 107] to study the fluid flow processes within a spouted fluidized bed. However, to what extent would the semi-cylindrical be able to represent a full three-dimensional bed was doubted by many researchers. Rowe *et al*. [108] found that the properties of grid jets suffered from amendments caused by the flat surfaces compared with the full three-dimensional bed under the same operating conditions. The findings of Rowe *et al*. [108] accordingly gave rise for concern regarding the reliability and accuracy of measurements using semi-cylindrical columns and stimulated further developments of experimental instruments in measuring essential parameters in fluidized beds without changing the intrinsic three-dimensional geometry.

2.7.2 X-ray

In earlier stages, X-ray techniques were firstly introduced into the medical area as an imaging tool when examining human organs [40]. It was then applied to industrial processes, i.e. gas solid fluidized beds because the fluidized beds normally have a simple geometry (circular mostly) and have two distinct phases (gas solids in the majority) which exhibit clear different physicochemical properties [102, 109, 110]. When compared with other traditional measurement techniques, X-ray has some major advantages. An important advantage is that this method is totally non-invasive as there are no components of the X-ray facilities being inserted into the bed. Another merit of X-ray techniques is that images can be captured in a high temporal and spatial resolution and individual component of the bed structure can be analysed. In addition, the facilities can withstand harsh operating conditions such as high temperatures and pressures.

The measuring principle of X-ray, which is similar to medical X-ray transmission techniques, can be summarized as follows. The photons of X-ray have very high energy, when they are emitted from X-ray tubes (normal source arrangement), they can penetrate small solid particles as they have significantly small wavelets compared with particle size. However, their energy during this process will be attenuated. According to the attenuation which occurs whilst the X-ray penetrates across a specific level of the bed, an image can be reconstructed through proper algorithms [28]. The earliest preliminary investigation of gas solid fluidized beds by means of X-ray was conducted by Grohse [111]. He successfully obtained the effect of the mode of gas

distribution to a solid bed on the bed behaviour although there were no pictoral images produced due to limits he encountered in using X-ray.

After Grohse's preliminary research, X-ray techniques were then extensively utilized by many scholars within gas-solids fluidized beds. A schematic diagram of the UCL X-ray apparatus employed by Rowe and Yates and their co-workers [25, 62, 63, 68-71, 78, 101, 108, 112-117] is shown in Figure 2.20. They have investigated bubble behaviour in a freely bubbling regime. One of the typical images of an isolated bubble has been shown earlier in Figure 2.7. Rowe and his co-workers [63, 68] have studied bubble growth, bubble shape, bubble spitting (with and without the presence of internal heat exchanger tubes) and the effect of gas distribution. Yates and his co-workers [114-116] have been devoted to investigating the effect of the elevated temperature and pressure on bubble behaviour in gas-solids fluidized beds. The techniques for deriving bubble size and bubble rising velocity have been evolved from manual drawings to a Hewlett-Packard digitizer and Bioscan Optimas software, which facilitated the data interpreting process extensively.

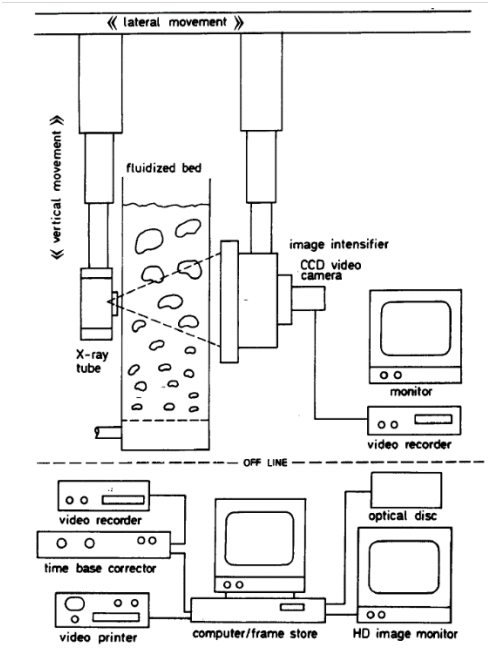

Figure 2.20: Schematic diagram of the UCL X-ray apparatus [102].

Kai and his co-workers [109, 110] have used X-ray systems and studied the bubble shape and structure by observing the interface between the bubble and emulsion phases in a fluidized catalyst bed. With the assistance of image processing techniques, they have reconstructed pseudo three-dimensional images of the bubbles, a typical image of which is shown in Figure 2.21. A conclusion has been drawn by them that the bubble shape is not perfectly spherical but a more complicated pattern.

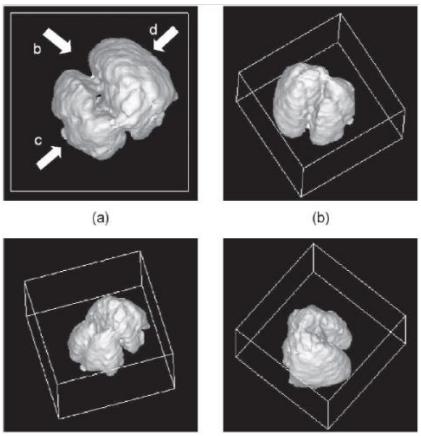

Figure 2.21: Pseudo 3-dimensioinal representation of an ascending bubble viewed from the top [109].

Although the X-ray techniques have eliminated the invasiveness obstacle which probes may introduce in measuring the internal hydrodynamics of bubbles, they still have some natural limitations as any measurement technique may have. Firstly, despite the unambiguous information which can be obtained from X-ray measurements, it has been acknowledged that the X-ray techniques are always confined to small laboratory scale fluidized beds. For large scale beds or industrial scale applications, X-ray techniques are commonly replaced by small volume probes from the point of view of practical operation [101]. Secondly, sufficient space must be provided to accommodate the facilities and this cost may be one issue which could limit progress.? Finally, they also demand operators who must have been trained in skills to handle and manipulate the X-ray facilities under strict conditions concerning health and safety issues, such as the potential hazard of radiation.

2.7.3 γ-ray

Similar to X-ray techniques, γ-ray was regarded as one of the best options in studying the complex fluid flow patterns within gas solid fluidized beds as a non-invasive measurement instrument. No parts of the γ-ray facilities have to physically interfere with the internal bed components. From the point view of measuring fundamentals, they are all involved with energy attenuation of photons [28]. The major difference comes from the fact that the photons of γ-rays come as a result of spontaneous decay of atomic nuclei whilst the photons of X-rays are created in the so-called X-ray tubes [45]. Nevertheless, γ-ray has attracted much attention for application in both industrial and laboratory scales.

The γ-ray techniques were firstly introduced into industrial applications in paper manufacturing and oil processing areas. After that, fluid catalyst

crackers (FCC) initially successfully employed the γ-ray techniques to quantitatively investigate solid concentration and distribution in fluidized systems. Martin *et al*. [118] employed γ-ray in FCC risers and obtained true tomographic images and a three-dimensional solid density map, which is presented in Figure 2.22.

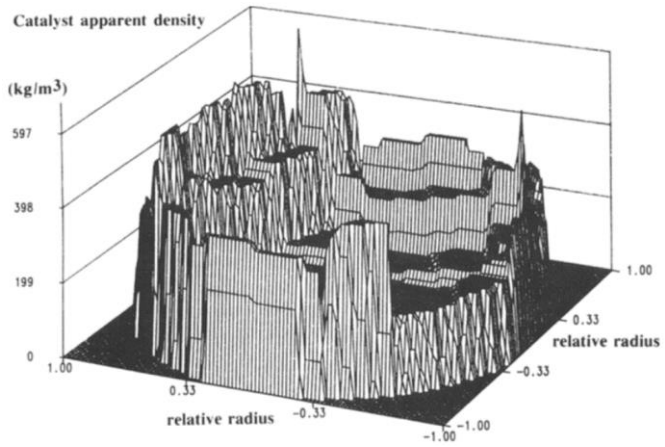

Figure 2.22: Catalyst density map in a 1.2 metre diameter FCC riser determined by γ-ray tomography [118]

There was also a great deal of investigations which utilized γ-ray on laboratory-scale fluidized beds. Baumgarten and Pigford [119] studied gas bubble sizes and frequencies with the help of density gauge-type apparatus under different operating conditions. Tomograms of the voidage distribution in the vicinity of the jet region with different gas distributors have been produced by Seville et al. [120]. The results are comparable with those predicted by widely used correlations [13]. Simons *et al*. [121] up-dated the γ-ray facilities used by Seville *et al*. [120] *a*nd succeeded in reconstructing higher resolution images with shorter scan times and larger beds dimensions.

However, several disadvantages of γ-ray techniques still exist and hinder its useful application in multi-phase diagnostic processes. The obvious one is its nature of time-averaged measurement fashion as a significant duration of time may be required to obtain a high resolution image involving the rotation of scanners. This period can span from a few minutes to hours depending on different application configurations. Moreover, well trained personnel are needed to meet the high standards of health and safety protocol concerning the potential hazards of radiation. Last but not least, the fiscal factor has to be given careful consideration when choosing to use the expensive γ-ray facilities, especially for lab-scale beds.

Considering all the measurement techniques introduced in sections 2.6 and 2.7, it is necessary to choose one specific technique with a dedicated consideration in terms of critical factors, for instance, physical properties of the components of gas solid two phase flow, the expense of purchasing relevant equipment, precision or resolution of the desired measurement results etc. [40]. In the following sections, two non-intrusive measurement techniques, namely, electrical capacitance tomography (ECT) and pressure fluctuation measurement, which are employed in the experiments conducted in this thesis, will be reviewed in a detailed manner.

2.8 Electrical capacitance tomography (ECT)

Electrical capacitance tomography (ECT) can provide qualitative and quantitative data in monitoring a multi-phase fluid flow system by measuring the electrical capacitances between sets of electrodes placed around a process vessel [29, 40]. The principle of the ECT techniques originates from the basic fundamentals of the capacitance probe which has been reviewed in section 2.6.3. Fundamentally, ECT and electrical resistance tomography (ERT) are in the same family of electrical impedance tomography (EIT). However, the ERT will not be introduced here and instead a book written by Wang [122] is recommended for reference. A typical diagram of an ECT system utilized in fluidized beds, which includes sensing system, data acquisition system and image reconstruction and display system, is shown in Figure 2.23. While the capacitance probes need to be inserted inside of the process vessel, the ECT sensor is simply positioned circumferentially of the vessel without invading it.

Being different from the inherent nature of point wise measurement of the capacitance probe, ECT can provide a cross-sectional image of the sensing domain, which gives a more comprehensive picture of the internal fluid flow processes. Moreover, ECT has an outstanding advantage of being non-invasive (it does not involve the rupture of the walls of the vessel) and non-intrusive (it does not interfere with the internal hydrodynamic characteristics of the fluid process), which is one of most desirable features of routine measurement instruments applied either in laboratory scale or industrial scale fluidized beds [30, 31]. Additionally, ECT has the advantage of being simple to construct, fast in measurement speed, of low cost and able to withstand harsh operating conditions, i.e. high temperatures and pressures.

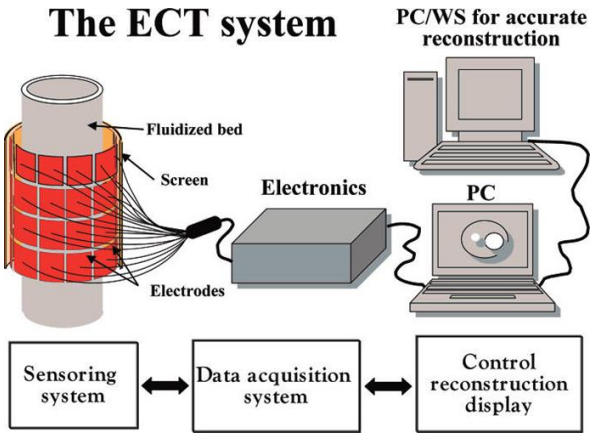

Figure 2.23: Diagram of an ECT system including sensor, data acquisition, and computer for reconstruction [123].

As a consequence, in recent years, there has been an increasing amount of literature on ECT study [26, 32, 33, 40, 45, 124, 125]. Some of them were involved with developing the ECT system to make the image clearer and the data capture rate faster [126-129]; some dealt with the lab-scale investigations in different types of multi-phase flow systems [6, 14-17, 44, 125, 130-136]; some tried to apply it into industrial applications, such as water/oil, gas/oil, and gas/solid flows [41, 137, 138].

It was acknowledged that [19] this sophisticated non-invasive and non-intrusive technique was pioneered nearly at the same time as at the US Department of Energy's Morgantown Energy Technology Center (METC) by Halow et al. [34, 139, 140] and at The University of Manchester Institute of Science and Technology (UMIST) by Huang et al. [35, 36, 141-143]. The basic idea was to reconstruct the two-dimensional distribution of effective dielectric constant of an object or multi-phase fluid processes using capacitance measurements with several pairs of electrodes. Due to the fact that the ECT system used in the experiments conducted in this thesis is largely based on the configuration proposed by UMIST, the following sections, which will introduce the fundamentals and image reconstruction algorithms of the ECT system, therefore, are established on the UMIST type of ECT.

2.8.1 Introduction to ECT

In general, the primary target of an ECT system is to reconstruct an image of the dielectric properties of an object positioned in a vessel (normally in circular shape) by measuring its electrical capacitance values between all possible measuring electrode pairs in a non-invasive and non-intrusive manner. A cross-sectional view of an ECT sensor enclosing eight measuring electrodes is presented in Figure 2.24.

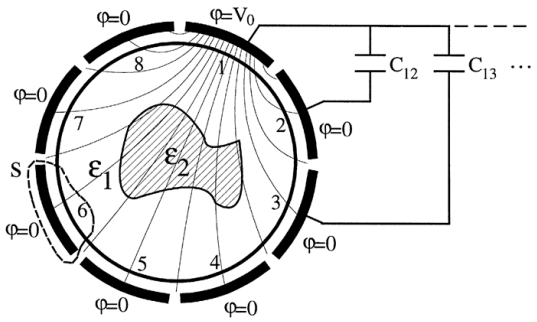

Figure 2.24: Schematic representation of the measurement principle of an ECT system [40]

As shown in Figure 2.24, the measuring protocol can be described as follows. Electrode 1 is excited with a voltage of Vo and all the remaining electrodes are set with a voltage of zero. The capacitance values between electrode 1 and all the remaining seven 'detector' electrodes will be measured. Then, electrode 1 will be 'silent' with a voltage of zero and electrode 2 will be 'excited' alternatively as the 'source' electrode. Therefore, the capacitance values between electrode 2 and all the remaining electrodes will be measured. This measuring pattern continues until all the electrodes are excited. In practice, due to the symmetrical nature of the geometry of electrodes distribution and possible self-capacitance, there are L=N(N-1)/2 independent measurements in total if there are N electrodes [29, 31, 40]. Therefore, there are 28 independent measurements for an 8-electrode sensor and 66 independent measurements for a 12-electrode sensor, respectively. Electrodes are distributed in an equal interval and attached to the circumference of the vessel. The electrodes are made of copper, whose fabrication process will be dealt with in depth in Chapter 3.

For an ECT system, the frequency of the imposed electric field is conventionally excessively low and the value of it is normally in the magnitude of 1 MHz. Therefore the corresponding wavelength of electromagnetic radiation can be simply calculated as below.

$$\lambda = \frac{c}{f} = 3 \times \frac{10^8}{10^6} = 3 \times 10^2 (m) \qquad (2.17)$$

Here c is the speed of electromagnetic propagation in vacuum and f is the frequency. Hence the corresponding wavelength λ is quite large compared with the dimensions of the normal object space (typical vessel diameter is in the range of 1 cm to 1 metre). Consequently, the electrical potential distribution within the measuring domain between all electrodes pairs can be described by the electrostatic field theory [31, 40].

The spatial distribution of the permittivity and the measured capacitances within the measurement domain can be related by the theory derived from Maxwell's equation. According to Gauss's law, the electric flux density $\boldsymbol{D}\ (\boldsymbol{r})$ is expressed as below.

$$\nabla \cdot \boldsymbol{D}\ (\boldsymbol{r}) = \rho_v(\boldsymbol{r}) \qquad (2.18)$$

where ρ_v represents the volume charge density, $\nabla\cdot$ is the divergence operator. For an ECT system, only one electrode is excited at one time, all the remaining electrodes are always at virtual earth potential as illustrated in Figure 2.24. Therefore, the total electric flux which is calculated over all the electrode surfaces is zero. Under such circumstances, the volume charge density is also zero. Because $\boldsymbol{D}\ = \varepsilon(\boldsymbol{r})\boldsymbol{E}(\boldsymbol{r})$ and $(\boldsymbol{r}) = -\nabla\varphi(\boldsymbol{r})$, where ∇ is the gradient operator, hence:

$$\boldsymbol{D}\ (\boldsymbol{r}) = -\ \varepsilon(\boldsymbol{r})\nabla\varphi(\boldsymbol{r}) \qquad (2.19)$$

here $\varepsilon(\boldsymbol{r})$ is the spatial permittivity distribution, $\boldsymbol{E}(\boldsymbol{r})$ is the electric field intensity and $\varphi(\boldsymbol{r})$ is the electric potential distribution.

Poisson's equation can be derived as below by introducing Equation (2.19) into Equation (2.18).

$$\nabla \cdot [\varepsilon(\boldsymbol{r})\nabla\varphi(\boldsymbol{r})] = 0 \qquad (2.20)$$

In case of the two-dimensional electric field $= (x, y)$, the capacitance measured between one pair of electrodes can be formulated as follows:

$$\mathrm{C} = \frac{Q}{V_0} = \frac{\oint_s\ \varepsilon(x,y)\nabla\varphi(x,y)ds}{V_0} \qquad (2.21)$$

where V_0 is the potential difference between the excited electrode and the detector electrode, Q is the total charge and s is the closed line as indicated in Figure 2.24.

2.8.2 Image reconstruction algorithms

There are two general terms, namely, forward problem and inverse problem, involved during the process of image reconstruction. The forward problem is a process of calculating the capacitance values of all the possible pairs of electrodes for a given distribution of permittivity (equivalent to the concept of a dielectric constant) inside a sensor, which can be mathematically expressed in Equation 2.22. The inverse problem is about the derivation of an image aiming to resemble the true permittivity distribution by means of the measured finite sets of capacitance values [40] and the process can be formulated as shown in Equation 2.23.

$$\boldsymbol{C} = \boldsymbol{F}\,[\varepsilon(\boldsymbol{r})] \qquad (2.22)$$

$$\varepsilon(\boldsymbol{r}) = \boldsymbol{F^{-1}}[\boldsymbol{C}] \qquad (2.23)$$

where $\boldsymbol{C}$ is termed as all possible independent capacitance measurements, $\varepsilon(\boldsymbol{r})$ is the given material permittivity distribution within the measurement domain, $\boldsymbol{F}$ is the *a priori* knowledge of the relationship between the measured capacitance values and the permittivity distribution [31].

On one hand, due to the non-linear nature of the governing Poisson partial differential Equation 2.20, there is no analytical solution to the above mentioned inverse problem. On the other hand, as described above in section 2.8.1, the frequency of an ECT system is generally low and the electrical field is governed by Equation 2.20. In electrostatic fields, it is well known that the electric flux lines will be deflected, i.e. being bent, when they encounter an interface of different permittivity. This is fundamentally distinct from the X-ray techniques, as mentioned in section 2.7.2, where the source lines pass directly through the object. Hence the electrical field within an ECT system is referred to as the 'soft field' [35]. The well-developed image reconstruction algorithms for X-ray will no longer be applicable to the ECT system and new algorithms need to be put forward to implement the image reconstruction task.

2.8.2.1 Linear back projection algorithms (LBP)

As demonstrated earlier, the changing rate of the measured capacitance values caused by the change of permittivity distribution is of non-linear nature according to the Equation (2.20). Furthermore, due to the number of unknowns (pixels in the desired image, normally 812) in the reconstructing process being much larger than the knowns (only 28 independent capacitance measurements with an eight-electrode sensor), the inverse problem is inherently ill-posed.

A simple linear back projection algorithm was initially proposed by Huang et al. [36, 142] to tackle this non-linear characterization. They demonstrated the image reconstruction algorithm with an eight-electrode ECT sensor. They also discovered that with a change in permittivity distribution, the measured capacitance value changed accordingly in different degrees at different locations in the sensor domain. For example, in some areas, one pair of measured capacitance changes positively with the dielectric increment whereas elsewhere it changes negatively or has very limited change.

To simplify the process, they assumed that any change in a measured capacitance results from a homogeneous change in the permittivity over the entire positive sensing area [36]. Hence they derived the positive areas of the

sensitivity distribution of the 28 measurements by simulating a process of moving a dielectric bar inside the sensor by virtue of the finite element method (FEM), which is shown in Figure 2.25. Although there are should be 28 sensitivity areas matching the 28 independent capacitance measurements, the four sensitivity areas obtained are enough as the others can be derived by rotation due to the symmetrical properties of the sensor.

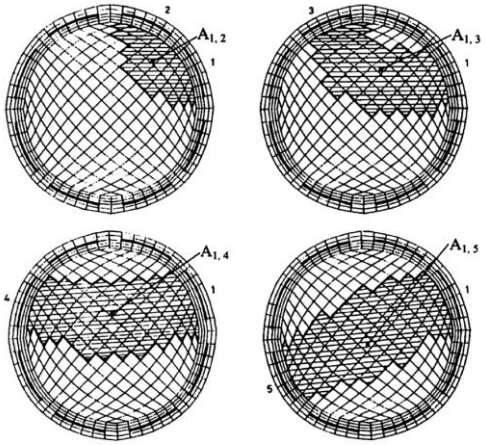

Figure 2.25: Positive sensitivity areas (shaded zones) [31]

The grey level in each pixel, as shown in Figure 2.25, of this linear algorithm is calculated from the following equations:

$$G(p) = \sum_{i=1}^{7} \sum_{j=i+1}^{8} S_{i,j}(p) C_{i,j}^{n} \qquad (2.24)$$

Here the element of sensitivity matrix is calculated as follows:

$$S_{i,j}(p) = \frac{\delta_{i,j}(p)}{\sum_{i=1}^{7} \sum_{j=i+1}^{8} \delta_{i,j}(p)} \qquad (2.25)$$

where δ has the value of 1 if pixel p is inside of the sensing area $A_{i,j}$ of electrode pair i-j and has the value of zero otherwise:

$$\delta_{i,j}(p) = \begin{cases} 1; & if \quad p \in A_{i,j} \\ 0; & if \quad p \notin A_{i,j} \end{cases} \qquad (2.26)$$

The results calculated from the denominator of Equation 2.25 actually act as a ‘weighting factor’ in situations where a given pixel belongs to more than one sensitivity area. $C_{i,j}^{n}$ is the normalized capacitance and is expressed as:

$$C_{i,j}^{n} = \frac{C_{i,j} - C_{i,j(low-\varepsilon)}}{C_{i,j(high-\varepsilon)} - C_{i,j(low-\varepsilon)}} \qquad (2.27)$$

where $C_{i,j}$ is the measured capacitance; $C_{i,j(low-\varepsilon)}$ is the measured capacitance when the sensor is full of the material with lower permittivity; $C_{i,j(high-\varepsilon)}$ is the measured capacitance when the sensor is full of the material with higher permittivity.

This simple linear back projection algorithm gave satisfactory results when tested against a two component flow, especially for a stratified flow [31, 36].

However, it is necessary to point out that the $S_{i,j}(p)$ is fundamentally determined by the unknown distribution due to the non-linear relationship between the measured capacitance and the permittivity distribution. In order to improve the image quality, Xie et al. [35] employed FEM methods and acquired the capacitance sensitivity map, from which four typical pairs are diagrammatically shown in Figure 2.26 for an eight-electrode sensor. In mathematical form, they are expressed as follows.

$$\delta_{i,j}(p) = [\frac{1}{\beta(p)}] \frac{C_{i,j}(p) - C_{i,j(low-\varepsilon)}}{C_{i,j(high-\varepsilon)} - C_{i,j(low-\varepsilon)}} \qquad (2.28)$$

where $\beta(p)$ is the fractional area of the pixel with respect to the pipe cross-sectional area.

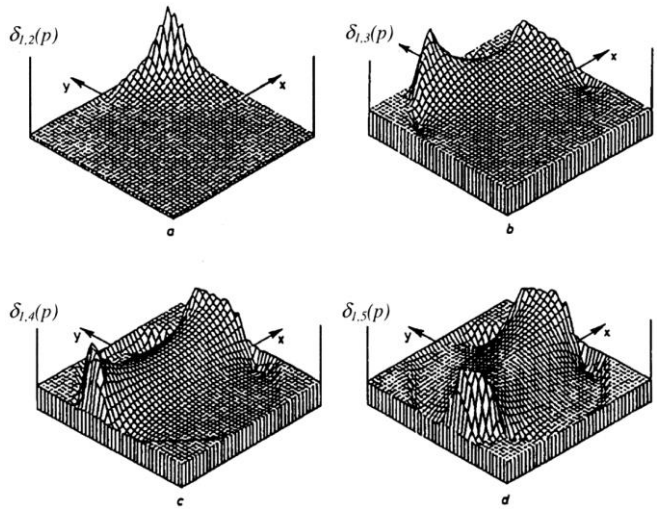

Figure 2.26: The capacitance sensitivity distribution for four pairs of electrodes: (a) adjacent electrodes, $\delta_{1,2}$; (b) a pair separated by one electrode, $\delta_{1,3}$; (c) a pair separated by two electrodes, $\delta_{1,4}$; (d) diagonally separated electrodes, $\delta_{1,5}$. [40].

Linear back projection algorithms have been proved to be simple and fast in reconstructing ECT images. However, they are approximate due to the linearization of the non-linear problem [29, 30, 127]. The images produced by LBP methods are subject to blurring and the factual sharp boundaries of two components within a two phase fluid flow, to some extent, are smeared [127]. To rectify this kind of problem, an iterative algorithm has been proposed by Yang [127].

2.8.2.2 Iterative LBP algorithms

The iterative techniques proposed by Yang [127] are based on the LBP algorithms and a flow chart of the iterative procedure is presented in Figure 2.27. The general process can be summarized as follows. Initially, the measurements of the independent capacitance values, C^n as shown in the Figure 2.27, are implemented. An initial image, G_0 , will be obtained based on the measured capacitance values by means of the conventional linear back projection process as demonstrated in section 2.8.2.1. Then the permittivity distribution for each pixel will be re-assigned based on the initial image and thereafter a forward problem is implemented with the re-assigned permittivity distribution, which gives rise to the calculated capacitance ξ. The capacitance error is, therefore, obtained from the measured capacitance C^n and the calculated capacitance ξ.

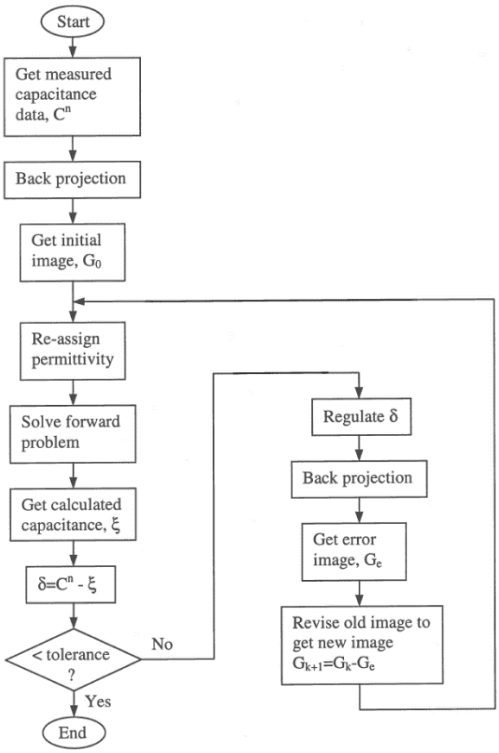

Figure 2.27: Flow chart of iterative procedure [31].

An ‘error image’ is subsequently reconstructed by means of the back-projection algorithm. The error image represents, to some qualitatively trustworthy extent, the difference between the current image and the true image. It is then added to the existing image. This procedure is repeated over and over again until a satisfactory image is achieved, viz. the difference between measured capacitance and calculated capacitance is within tolerance.

Generally, the iterative LBP algorithms are able to produce better quality images compared with the conventional LBP methods. The blurring effects can be removed significantly as confirmed by Yang, Dyakowski and Wang [31, 40, 127]. Although a great deal of effort has been devoted to producing better images, such as the algebraic reconstruction technique (ART), model-based algorithms (MOR), artificial neural networks [144], the iterative LBP methods are still the fastest and most robust, as demonstrated by McKeen and Pugsley [145] and Makkawi and Wright [14].

There are some drawbacks to the aforementioned reconstruction techniques, for example, the MOR algorithm was only applied to rather simple stratified phase distributors and artificial neural networks need to undergo a heavily time-consuming training process [33, 146]. Therefore, in Chapter 6, bubble characteristics within a bubbling fluidized bed will be tested against the iterative LBP methods together with the conventional LBP methods.

2.8.3 Applications of ECT in gas-solids flows

The ECT system, in certain cases, is an attractive tool in imaging gas-solids flow both at laboratory scale and industrial applications because of its simplicity and high-speed capabilities. Therefore, since the emergence of ECT techniques, it has been evolved significantly and been applied widely in multi-phase flow applications, especially in gas-solids flows, such as the pneumatic conveying process, circulating fluidized beds and bubbling fluidized beds.

In respect of pneumatic conveying applications, Brodowicz et al. [33, 147] were one of the first authors to investigate a flow map for a pneumatic conveyor by means of an ECT system. Cross-sectional slices were obtained from an 8-electrode ECT system which was integrated into the experimental plant which included a horizontal glass pipe with an internal diameter of 80 mm and external diameter of 96 mm. Later, the flow instabilities within a dense pneumatic conveying system were studied by Jaworski and Dyakowski [6]. In order to extensively investigate the three dimensional and unsteady nature, such as ‘slugs’ and ‘plugs’, exhibited in the dense pneumatic conveying process, they utilized a high-speed camera and a twin-plane ECT system. Different types of data have been extracted, such as the internal structure of the flow instabilities and their associated propagation velocity and frequency feature. Figure 2.28 gives a comparison of plug results obtained using a high speed camera and ECT images.

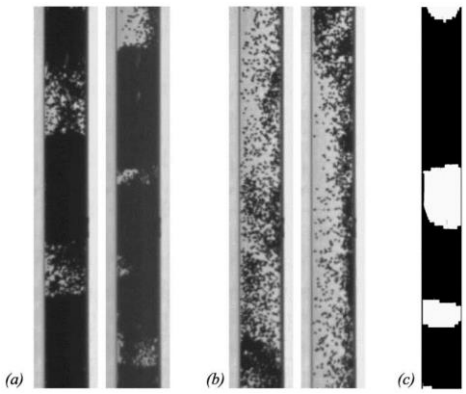

Figure 2.28: (a) Photographs of the plugs travelling upwards along a vertical channel; (b) Materials dropping downwards in between the trains of plugs; (c) Tomographic visualization obtained by thresholding of tomographic images for upward travelling plugs [6].

The dynamics of gas/solids flow within a circulating fluidized bed riser whose internal diameter is 14 cm has been investigated by Pugsley et al. [42]. They have also validated the utilization of the ECT system against a fibre optic probe. The reconstructed images from both methods showed good agreement was achieved when the gas superficial velocities were more than 0.25 m/s. They also demonstrated that the ECT system worked better in dense beds, which had good consistency with the results obtained by Dyakowski et al.[33]. Moreover, annular flow was observed by Wang and Dyakowski et al. [31, 33] by means of cross sectional images which provided the solids concentration profile. A significant discrepancy between the time averaged solids distribution and instantaneous images identified that the average solids distribution exhibited a higher degree of axial symmetry.

Fluidized beds with low superficial gas velocities, such as bubbling fluidized beds and slugging fluidized beds, have attracted enormous attention and studies conducted using ECT techniques as the ECT has the non-intrusive capability to observe the internal complex two phase flow.

One of the most seminal studies is the one conducted by Makkawi and Wright [16]. They carried out an experimental study in a cold conventional fluidized bed which had a 15 cm diameter. Several flow regimes including single bubble, slugging bed, turbulent flow and fast fluidization regime has been distinguished by the ECT measurements. The corresponding velocities such as minimum fluidization velocity, minimum slugging velocity and turbulent transition velocity has been identified by means of different analysis methods such as standard deviation, amplitude and solid fraction fluctuation, and power spectral and probability distribution. Figure 2.29 presents the standard

deviation of average solid fraction against a wide range of superficial gas velocities at two different levels.

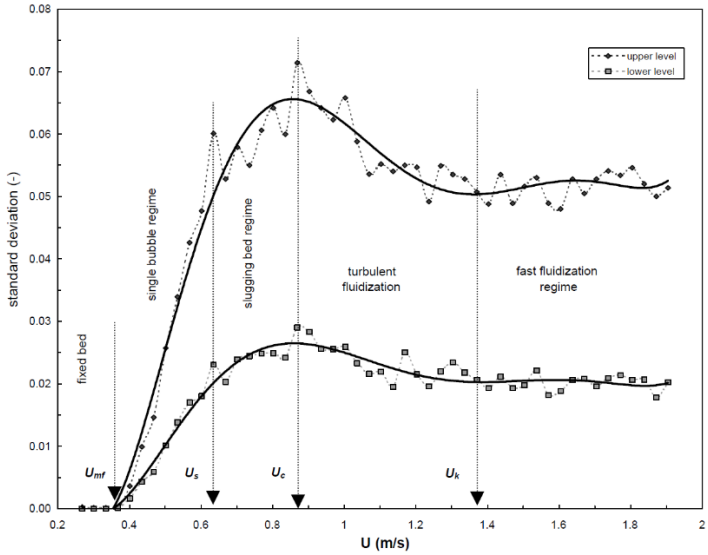

Figure 2.29: Standard deviation of average solid fraction against a wide range of superficial gas velocities at two different levels [16]

Wang et al. [44] also observed the different flow patterns which occurred in bubble flow beds and slug flow beds and rough demarcation velocity was proposed by observing gas bubbles in the vicinity of an air distributor plate. Wang [31] also demonstrated the average solid fraction measured by ECT and differential pressure transducers. In the bubbling regime and slugging regime, relatively good agreement has been achieved with a maximum discrepancy of 14.9%. In order to investigate the internal flow structure in a square-shaped fluidized bed, a square-shaped ECT sensor has been developed by Liu and Yang [38, 148] and promising results have been obtained in terms of bubble behaviour and concentration distribution of solids.

Bubble behaviour in the bubbling regime is a critical factor or parameter in describing the hydrodynamic characteristics of the bed. The main feature of the bubble behaviour such as bubble size, bubble rising velocity and bubble frequency has been widely studied using advanced ECT techniques. The following section will deal with these in depth.

2.8.4 Bubble characteristics study in bubbling fluidized beds using ECT

Recently, a considerable amount of literature has been published around the theme of bubble behaviour in fluidized beds as the characteristics of the bubbles, to a large extent, influence or determine the gas-solids mixing intensity and the mass and heat transfer rates. ECT has been developed over

several decades and been devoted to imaging flow morphology of multi-phase flows of the non-homogeneities, especially in fluidized beds. In the following sections, bubble size, bubble rising velocity and bubble frequency studied by the ECT techniques, will be reviewed critically.

2.8.4.1 Bubble size

One of the earliest studies on bubble size determination by virtue of the ECT techniques was the investigation conducted by Halow et al. [34, 139, 140] although the ECT system was slightly different to the one developed at UMIST. Halow et al. observed that voids (bubbles) in the experimental results rarely exhibited the circular cross-section of spherical cap bubbles. Figure 2.30(a) shows an image of the voidage cross-section of a wall-attached bubble. They derived the fontal bubble diameter by using the average cross sectional voidage data and by considering a distinct two-phase assumption and a hemispherical bubble shape.

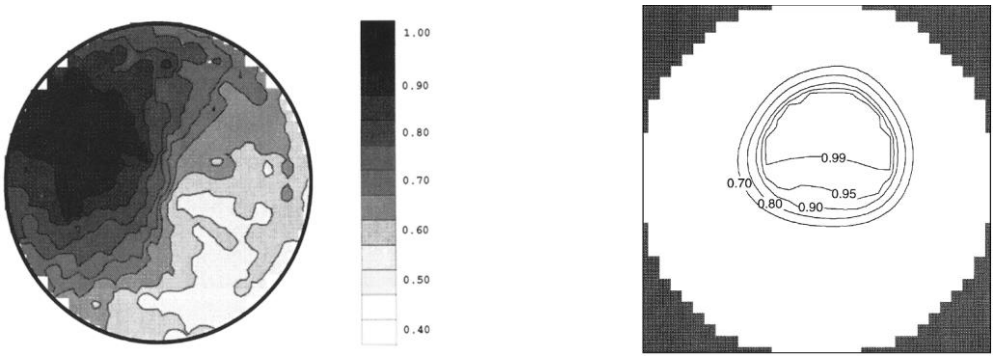

(a) (b)

Figure 2.30: (a) Voidage cross-section of a wall-attached bubble [140]; (b) Voidage contours showing a typical bubble within the cross-section of the ECT sensor [149]

McKeen and Pugsley [149] utilized a new method to calculate bubble diameters, which made use of the actual ECT voidage contours available from the tomographic images. One example is shown in Figure 2.30(b). A voidage contour of 0.80 was chosen to define the bubble boundary. The results were compared with the two dimensional CFD simulation results and two sets of empirical correlations.

Wang [31] extracted bubble diameters from a thousand tomograms and compared the results with several empirical correlations. As he demonstrated, the ECT system he employed was sensitive enough to measure an increase in bubble diameters caused by the increase in gas superficial velocity. From the time sequence of images of particle concentration distribution both for

bubbling fluidization and slugging regime, Wang et al. [44] concluded the mean bubble diameter for a bubbling fluidization was in the range 0.5 -1.5 cm and for a slugging regime in the range 1.5 - 4.7 cm within a 150 mm diameter vertical bed. A correlation for bubble length has also been proposed. The bubble length can be calculated from:

$$L_b = n\Delta\tau v_b + l_{el} \qquad (2.29)$$

where n corresponds to the number of images, v_b is the bubble rising velocity and l_{el} is the electrode length. Hence, the bubble length for bubbling fluidization was in the range 3.7 - 5.7 cm and slug flow in the range 4.8 - 8.5 cm.

Additionally, Chandrasekera et al. [43] measured bubble diameter by means of an ECT system. Two measuring assumptions have been made by them. One is that the measured bubble diameter was defined as the diameter of a circular bubble with equivalent cross sectional area to the measured one. Another is that the measured bubble diameter was calculated as the equivalent spherical diameter of a bubble with the same cross-sectional area, assuming that the bubble has a hemispherical shape. The measured bubble diameters were compared with three sets of empirical correlations.

However, there are many limitations for the above mentioned bubble size measurements. Despite that Halow et al. [139, 140] measured the frontal bubble diameter by means of average cross sectional voidage, they were aware that there were some limitations to the approach as the emulsion phase cannot realistically be characterized by a uniform voidage. The bubble sizes are still to be confirmed with empirical correlations. McKeen and Pugsley [149] have noted the limitations of the methods Halow et al. [34, 139, 140] employed, but they just picked up an arbitrary voidage contour of 0.80 to define the bubble boundary from the open literature without giving any experimental validation. Moreover, Wang [31] estimated bubble sizes in fluidized beds and compared them with correlations but how the bubble sizes were determined – in particular the bubble boundary defined as a “cut-off” grey level value distinguishing gas and solid phases – is not clear. In addition, three arbitrary bubble size boundary values (0.4,0.5 and 0.6) were used by Chandrasekera et al. [43] to estimate bubble sizes in single bubbling fluidized beds.

Hence, it is evident that, no systematic study on bubble size estimation, especially cut-off value determination, has yet been performed. In Chapter 6,

a systematic study of the influence of bubble boundary value (cut-off value) on bubble size estimation will be fully investigated.

2.8.4.2 Bubble rising velocity

Besides bubble size, bubble rising velocity is another critical parameter in describing bubble behaviour in bubbling fluidized beds. Several researchers [14, 16, 17, 149] extracted bubble rising velocity by means of a twin-plane ECT sensor and cross correlation techniques, which will be introduced in detail in Chapter 6. Figure 2.31 shows an example of the estimated bubble rising velocity, which was obtained by utilizing the known separated distance between two ECT sensor planes and the time lag (a bubble traverses from the lower plane to the upper plane) derived from the cross correlation techniques.

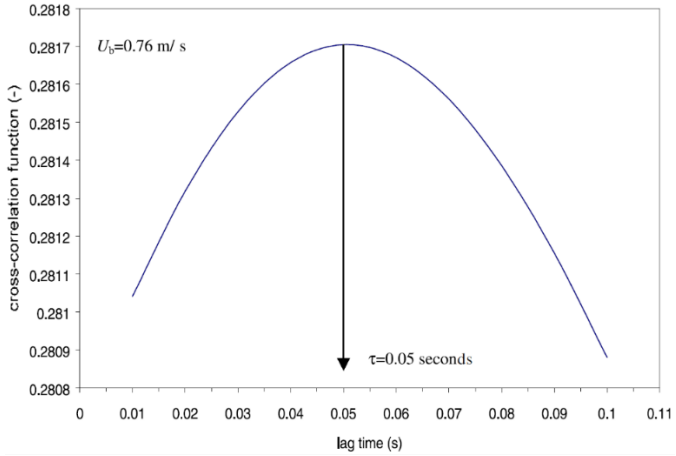

Figure 2.31: Estimated bubble rise velocity from tomography measurement by cross-correlation method [17].

In addition, Makkawi and Wright [14] proposed another mathematical method for determining bubble rising velocity, which is expressed as follows.

$$U_b = \frac{1}{N-1}\sum_{i=1}^{N}\frac{\Delta x}{\Delta t_i} \qquad (2.30)$$

where $\Delta t_i = t_{b2} - t_{b1}$ and t_{b2} and t_{b1} represent time when a bubble peak passes through the upper and the lower level planes, respectively. Δx stands for the distance between the centre of the two measuring planes. Relatively good agreement has been achieved by comparing the results derived from the above Equation 2.30 and the results obtained from cross correlation techniques up to the point of onset to turbulent fluidization. Wang [31] calculated bubble rising velocity by utilizing the same concept but without giving detailed explanation as the above Equation 2.30 did.

However, all the bubble rising velocities are derived based on the averaged cross sectional solid fraction values. As there are normally 812 pixels in the

reconstructed images, the influence of bubble location on the bubble rising velocity values cannot be identified from the available data in the literature. It is necessary to conduct such studies and in the present study, Chapter 6 will deal with this extensively.

2.8.4.3 Bubble frequency

Bubble frequency can be regarded as the number of bubbles which appeared in the bubble flow beds in a specified time interval of a measured sample. To be specific, in ECT raw data, the bubble frequency was defined as the number of the local minima values of the averaged or local pixel-based solid fraction within a limited time interval. Wang [31] calculated bubble frequency at three different gas superficial velocities in a bubbling regime, however, without giving any convincing explanation regarding the method of deriving them.

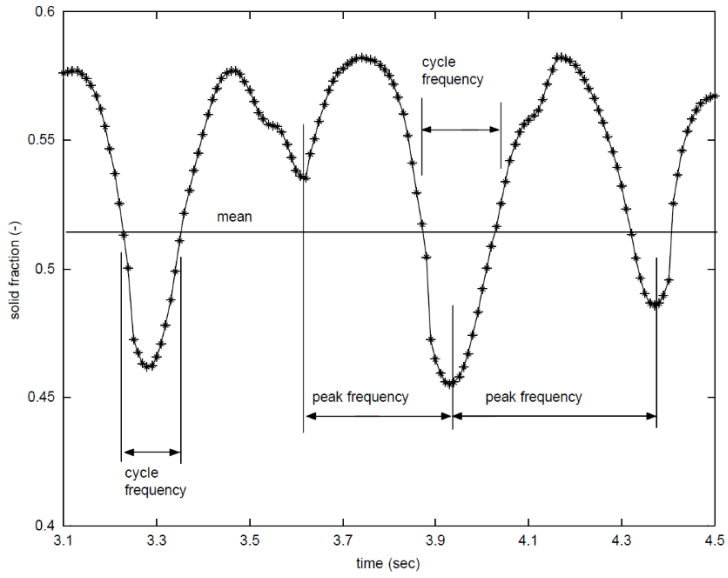

Figure 2.32: Calculation method for the cycle and peak frequency taken from a typical time series measurement of solid fraction fluctuation [16]

The concept of the bubble frequency was extended by Makkawi and Wright [16] who proposed a simple algorithm to calculate the number of bubble peaks or cycles in a 20 second measurement sample. The bubble peak frequency was defined at a point when the solid fraction reached a minimum value together with transition of the vicinity line slope from negative to positive. The bubble cycle frequency was defined as half of the total number of times when the signal passed over its mean. A schematic illustration of these two concepts is presented in Figure 2.32. The main difference between the defined peak frequency and cycle frequency is that the peak frequency had no connection with the mean value of the solid fraction curve.

Bubble frequency can be interpreted from the dominant frequency in the power spectral density (PSD) function, which has been studied by several researchers [16, 48, 150, 151] and will be covered in depth in Chapter 7. As demonstrated by Makkawi and Wright [16], the dominant frequency obtained from the PSD function had good agreement as the results acquired from the bubble cycle frequency (depicted in Figure 2.32).

2.9 Pressure fluctuation measurement

Apart from temperature, pressure is another quantity chosen to characterize the fluid dynamic behaviour of gas-solids fluidized beds and it is routinely measured both in laboratory scale beds and industrial plants [8, 46-48]. The benefit of using pressure is that it has the advantages of being easily measured and has the ability to withstand harsh operating conditions (such as elevated temperature and pressure), which is common in industrial surroundings. On top of that, the instruments used in the pressure measurements, such as pressure transducers or pressure taps, are robust, relatively cheap and essentially non-intrusive. Therefore, the distortion of the flow in the vicinity of the measurement point could be minimized or even eliminated effectively [8].

Normally the pressure measurements can be classified into two general categories: one is for time averaged pressure drop measurement and another is for time series pressure signal measurement. The first type of pressure measurement has been illustrated in section 2.6.1, where pressure drop measured in a bubbling fluidized bed can be extrapolated to extract the linear distribution of bed expansion across the bed by means of Equation 2.17. The second type is the time series pressure fluctuation which is recorded with an adequately high frequency enabling a large amount of information about the internal fluid dynamics of the fluidized bed being extracted.

However, unlike the time averaged pressure drop, the interpretation of the time series pressure fluctuation signal is not straightforward at all [8, 46]. It is believed that the pressure fluctuations largely stem from bubble motion within the bed. But the exact origin of the pressure fluctuations is not entirely clear yet, although many attempts have been made by numerous previous researchers [51, 52, 152-155]. The major obstacle in understanding the characteristics of the pressure fluctuation signal is probably on account of its intrinsically non-local nature. Hence, dissimilar to the local measurements performed by optical probes and capacitance probes which have already been

introduced in sections 2.6.2 and 2.6.3, respectively, the evaluation process on the pressure fluctuation signal is much more complex [46].

A considerable amount of literature has been published on the origin of pressure fluctuations in gas-solids fluidized beds. These studies resulted in a general conclusion that the pressure fluctuation can be caused by serval different events inside the beds [8]. The events may include, for example, generation of bubbles just above the distributor [52] , bubble coalescence [156], bubble bursting at the bed top surface [157], bubble passage and fluctuation in the gas fluid flow, etc. [8]. Moreover, a conflicting conclusion has been drawn among those scholars regarding the origin of pressure fluctuation. Bubble formation and coalescence were regarded as the primary source of pressure fluctuations by van der Schaaf et al. [27]. On the contrary, several other investigators [156, 158, 159] claimed that the main origin of pressure fluctuation come from the phenomena closer to the tope surface of the beds. The pressure fluctuation may measure the deflection of the surface due to both gas molecules and solid particle collisions. The former could be sound waves or hydrodynamic mass motion, hence pressure fluctuations could register more than gas-solid spatial distribution.

Nevertheless, the main approaches which were used to exploit the link between the characteristics of the time series pressure signal and the physical phenomena perceived in a fluidized bed, are conventionally categorized into four categories: (a) time domain analysis, (b) frequency domain analysis, (c) time-frequency domain analysis, and (d) state space analysis [8, 46, 48]. In spite of the usefulness of methods (c) and (d), such as wavelet analysis [160-162], correlation dimension [163, 164] and Kolmogorov entropy [165, 166], methods (a) and (b) are still the most robust and reliable approaches. Therefore, the time domain analysis and frequency domain analysis in gas-solids fluidized beds will be reviewed in the next section.

2.9.1 Time domain analysis in fluidized bed

The most direct analysis in the time domain must be the simple plotting of the pressure fluctuation signal (normally converted from a voltage signal) versus sampling time steps [8, 46]. A typical time series plot of pressure fluctuation in different flow regimes is shown in Figure 2.33. From a visual inspection on the time series plot, some qualitative feature can be obtained, such as time scale, possible low frequency trends and periodicities. Also, potential abnormities caused by data acquisition problems may be identified before further processing the signal. As discovered, the normal dominant frequencies

in a gas-solids fluidized bed are within a range of 1 ~ 5 Hz. Hence, a 10 second section signal will suffice for this purpose.

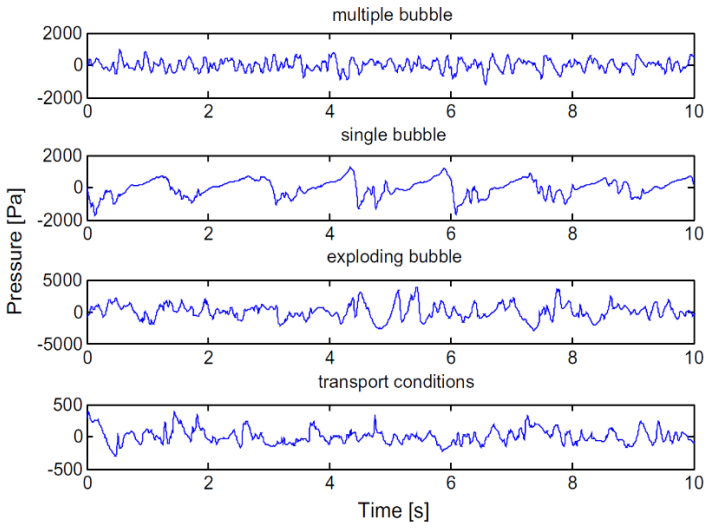

Figure 2.33: Time-series of the pressure fluctuations measured in different flow regimes [46].

Clearly, visual observation cannot help further with quantitative investigation. A widely applied time domain quantitative analysis approach is the so-called standard deviation, which characterizes the amplitude of the pressure fluctuation signal. The mathematical details of the standard deviation will be dealt with in more depth in Chapter 5. Standard deviation was often used to identify different flow regimes. Figure 2.34 presents a representative curve of standard deviation with increasing gas superficial velocity. The peak of the standard deviation curve was commonly regarded as the onset of the turbulent flow regime [167, 168]. However, there are very few studies concerning the demarcation of the bubbling regime and slugging regime by virtue of standard deviation. In Chapter 5, this will be studied extensively.

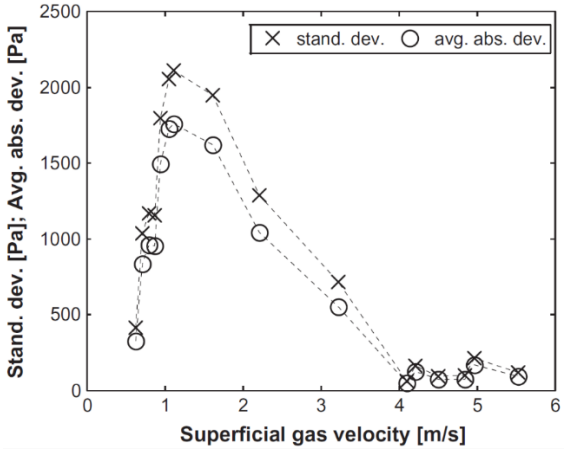

Figure 2.34: Standard deviation (marked by the cross symbols) with the increasing gas superficial velocity [46].

Excluding standard deviation, auto-correlation and cross-correlation functions were utilized to analyse the pressure fluctuation signal. The auto-correlation function of a pressure fluctuation signal, X(t), can be expressed as follows.

$$\emptyset_{xx}(\tau) = \lim_{T\to\infty} \frac{1}{T} \int_{-T/2}^{T/2} x(t)x(t+\tau)\, dt \qquad (2.31)$$

where $x(t)$ is the value of X(t) sampled at time t, and $x(t+\tau)$ sampled at time $t+\tau$. As auto correlation plays a vital role in analysing signals which may contain potential periodic components, Yutani et al. [96, 156] applied the auto correlation function to extract the bubble occurrence time steps. However, due to the equivalence to the power spectral density function (PSD, to be introduced in the next section), the auto correlation function is not frequently used in gas-solids fluidized beds [8].

The cross correlation function has been widely applied to extract rising bubble velocity by means of capacitance probes, optical probes and ECT measurements, which have been demonstrated in previous sections. It can also be utilized in interpreting pressure fluctuation signals. Fan et al. [156, 169] measured on line the rise velocities of bubbles, slugs and pressure waves in a gas solid fluidized bed with the aid of pressure transducers coupled with cross-correlation techniques. Although the results they obtained have been compared with other investigators, the method of measuring rising bubble velocity is still under scrutiny. Chapter 7 will examine this approach carefully by considering the pressure fluctuation measurement positions.

2.9.2 Frequency domain analysis in fluidized beds

Analysis in the frequency domain is a well-established tool for investigating pressure fluctuation signals measured in gas-solids fluidized beds [8, 46]. Extra information (especially frequency-related) can be obtained with the assistance of frequency analysis approaches, which is beyond the capacity of the time domain analysis.

The most frequently used method is the power spectral density function (PSD) which is derived from Fourier spectral analysis. The mathematical description of the PSD function will be covered in detail in Chapter 7. The Fourier spectral analysis can convert the time series pressure fluctuation signal into the frequency domain. Dominant frequencies of the PSD function were commonly used to characterize various physical phenomena observed in fluidized beds. Figure 2.35 exhibits a power spectral density function of the pressure fluctuation signal measured in plenum position by Kage et. Al [51, 52, 153]. Different peak frequencies were identified and linked to the frequencies

derived from other measurements such as fibre optic probes and a high speed camera.

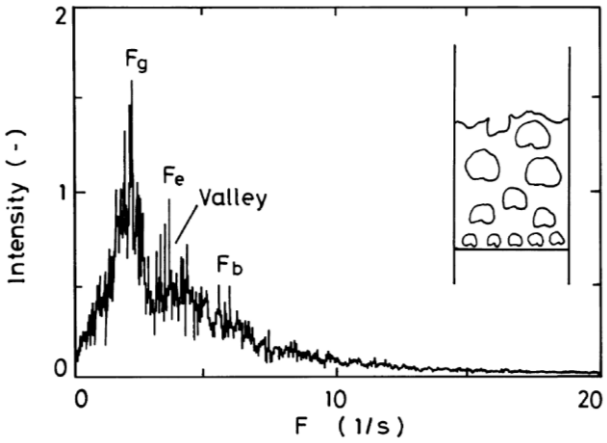

Figure 2.35: Power spectral density function and sketch of the fluidized bed formed by Group B particles [51].

In order to study the origin of pressure fluctuations, van der Schaaf et al. [27] initially proposed a method for decomposing the PSD function into different components, i.e. a coherent part and an incoherent part. The decomposed components were then associated with phenomena in fluidized beds which result in pressure fluctuations. Specifically and briefly, the coherent part contributes to the pressure propagating in the entire system whereas the incoherent part reveals the effect of local events in the bed (for example, gas voids and turbulence). Alberto and Rocha [170] studied the differentiation of states of typical fluidization regimes in a gas-solids fluidized bed utilizing the PSD function. Different flow regimes are identified and differentiated by the dominant frequency characteristics of the PSD function.

No doubt the time domain and frequency analysis in fluidized beds will give remarkable insight into the three dimensional fluid flow processes. In Chapter 7, the characteristics discovered from pressure fluctuation signals by virtue of time and frequency domain analysis will be compared closely with the corresponding findings from ECT measurements. The primary purpose of doing this comparative evaluation is to identify the advantages or disadvantages of the two non-intrusive measurement techniques in characterising the complex hydrodynamics of gas-solids fluidized beds.

2.10 Summary

Some basic fundamentals in respect of fluidization and fluidized bed flow regimes have been presented. The fundamental concept of the fluidization

and the classical two phase theory for depicting the fluidization phenomenon are stated in a detailed and understandable manner. A widespread classification criterion proposed by Geldart for classifying granular materials in fluidized beds is described. There are four groups in total for considering the particle to gas density difference and particle size.

With different gas superficial velocities, the packed solid materials in a fluidized bed can exhibit different flow regimes. Six different flow regimes, viz. fixed bed, bubbling regime, slugging regime, turbulent regime, fast fluidization and pneumatic conveying, together with their applications are reviewed. The characteristics of bubbles in a bubbling regime are described in detail. These features include bubble shape, bubble growth and coalescence, correlations for bubble size and correlations for bubble rising velocity.

Then three typical conventional instrumentation and measurement techniques are presented. The measuring capability, laboratory and industrial applications, advantages and disadvantages of them are demonstrated extensively. Being capable of avoiding direct interference to the internal fluid flow processes within a gas-solids fluidized bed, three representative non-intrusive measuring approaches, namely, optical photography, X-ray and Gamma ray, are introduced and evaluated. Each of the measurement techniques, either intrusive or non-intrusive, has its own advantages and limitations. Some factors such as cost, desired measurement accuracy or resolution, physical dimension and potential hazards have to be taken into careful consideration in the selection process.

Finally, two advanced non-intrusive measurement techniques are described and reviewed critically and thoroughly. They are electrical capacitance tomography (ECT) and pressure fluctuation measurement, respectively. Regarding the ECT technique, the theoretical background of the internal electric field is described. Two robust and fast image reconstruction algorithms are illustrated. The applications of the ECT in gas solid fluid flow especially in bubbling fluidized beds are shown. The latest progress in studying bubble characteristics in bubbling regime by virtue of the ECT technique is reported and some relative research gaps have been critically drawn. In respect of the non-intrusive pressure fluctuation measurement, two commonly used approaches, namely, time domain analysis and frequency domain analysis, in investigating pressure fluctuation signal are presented. The capabilities of the two methods in interpreting the complex hydrodynamics in fluidized beds are comprehensively evaluated.

Chapter 3
Numerical Simulation and Design of ECT Sensor

This chapter deals with four parts mainly. The first part is about the review of numerical simulation of electrostatic field within ECT sensor. The second part is about the COMSOL simulation of the proposed ECT sensor to establish the feasibility to be fitted with the current ECT system. The third part involves with the COMSOL simulation for plastic ball wall effect on the simulated capacitance values between measuring electrodes pairs before conducting any further plastic ball calibration process. The final part is about the design and constructing process of ECT sensor where some key issues and steps are addressed.

3.1 Review of numerical simulation of electrostatic field within ECT sensor

As aforementioned in the Aims and Objectives of the Study section of the Introduction, ECT measuring techniques will be used to study the internal flow processes within fluidized beds. Each project or research needs its own customized ECT sensor, which fits its physical experimental apparatus. Without exception, in this project, a customized ECT sensor needed to be designed and fabricated for experimental purposes. However, prior to the fabrication of a customized ECT sensor, it was necessary to conduct a numerical simulation to ensure the sensor was compatible with the ECT measuring unit used in the present study, which was purchased from Process Tomography Ltd., Cheshire, UK.

In previous studies, the reasons for using numerical simulation can normally be summarised as being two-fold. One is that it is much more cost effective than a trial-and-error approach, i.e. an initial design will be modified given that it cannot produce the expected results or it does not work as anticipated with the corresponding experimental rig, which is inevitably costly. Another reason for using numerical simulation or the advantage of numerical simulation on an ECT sensor lies in the fact that it is efficient in dealing with the complex mathematics which are involved in the fundamentals of ECT techniques.

For example, the electrostatic field distribution of two different materials within a 2D ECT sensor is governed by the Poisson's equation of 2.20 [171].This equation is still very difficult to solve within a specific ECT sensor which may have complicated geometry or boundary conditions although it might be the simplest equation in the sense of mathematics. Therefore, a finite element

method (FEM) is normally applied to solve this type of equation for an ECT sensor to eventually obtain the capacitance values for each effective unique measuring electrode pair. One of the advantages of FEM is that a complex geometry can be discretized into different elements, which generally have the shape of triangles and quadrilaterals in two dimensional domains and tetrahedra, pentahedra or hexahedra in three dimensional domains [172].

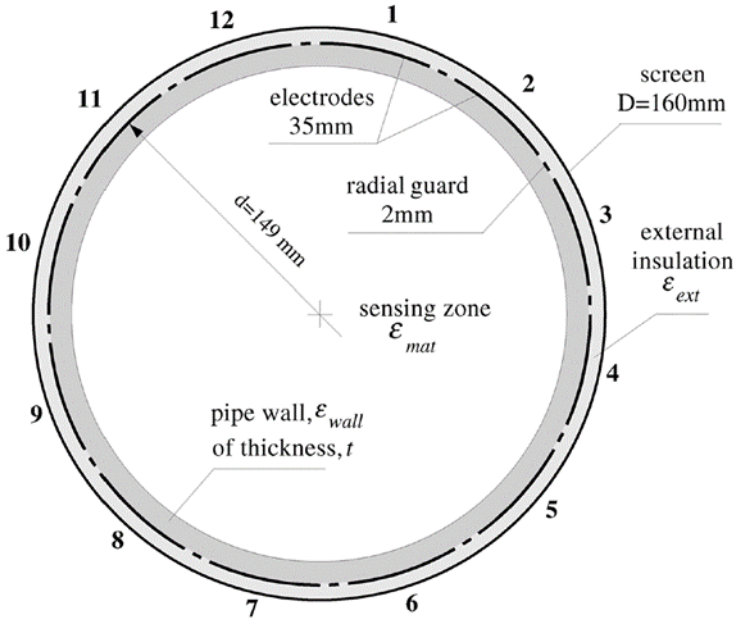

Figure 3.1: Schematic diagram of an example of a 12 electrode ECT sensor geometry used in numerical simulation [132]

Flores et al. [173] successfully utilised the FEM method to simulate a 12 electrode ECT sensor which has applications in the oil industry. To investigate and validate the potential performance of an ECT sensor for media of high permittivity (i.e. water), Jaworski and Bolton [132] conducted numerical simulations using a commercial software produced by the Ansoft Corporation's Maxwell 2D Field Simulator, (which uses an iterative finite element method (FEM) with adaptive mesh generation). Mohamad et al. [174] also carried out numerical simulation for the purpose of investigating a new differential excitation protocol in a 12-electrode ECT sensor. The results of the simulation are verified with their experimental data. Moreover, in order to seek which type of ECT sensor (three types of ECT sensors have been defined as follows - Type 1: with earthed ring guards; Type 2: with driven segmented guards and Type 3: without guards) is suitable for imaging a blast furnace, a three dimensional numerical simulation has been carried out by Yan et al. [172]. Accordingly, based on the previous successful studies on numerical

simulation within an ECT sensor, simulation work in the present research will be described in detail in the following sections.

3.2 COMSOL simulation of proposed ECT sensor

In section 3.1, three different FEM software packages in total were mentioned, except the FEM software package used by Yan et al. [172] was developed by themselves, commercial software was applied by others. For example, FEMLAB was used by Flores [173], Maxwell 2D Field Simulator was the case for Jaworski [132] and COMSOL Multiphysics was utilized by Mohamad [174]. However, COMSOL Multiphysics is intrinsically the succeeding version of FEMLAB after 2005.

In most cases of ECT systems, the frequency of electrical signal which is used to generate the electrical field in the sensing area has an order of 1 Mhz. The corresponding wavelength of electromagnetic radiation (in the order of hundreds of metres) is greater than the sensor size by several orders of magnitude (normally a sensor has a diameter between 1 cm and 1 metre). Therefore, under such circumstances, the electrical field distribution within an ECT sensor can be treated as an electrostatic field [40]. Moreover, there is a specialized module called AC/DC in the COMSOL Multiphysics software, which is ideal for simulation of electrostatic fields. Hence, COMSOL Multiphysics was chosen for future numerical simulation execution.

COMSOL Multiphysics is a finite element analyser, solver and simulation software/FEA software package for various physics and engineering applications, especially coupled phenomena, or Multiphysics [174]. The embedded AC/DC Module is used by engineers and scientists to understand, predict, and design electric and magnetic fields in static, low-frequency and transient applications. It can perform simulations in a two dimensional or three dimensional manner.

Although, in the case of the current study, the proposed customized ECT sensor is inherently of three dimensional nature, a two dimensional numerical simulation can be permitted instead of conducting the time-consuming and computing capability demanding three dimensional simulation. Firstly, a two dimensional model is representative of the transversal section of the ECT sensor body [173]. Secondly, a set of driven guard electrodes are normally placed at both ends of the measuring electrodes. By means of this arrangement, to a large extent, it eliminates the electrical field deformation which may occur at the edges of measuring electrodes and ensures the

electric field is uniform in the longitudinal direction. Therefore, the three dimensional effects could be neglected [132, 173] and a two dimensional numerical model is appropriate to investigate the internal electrostatic field distribution of an ECT sensor.

The general process of the 2D simulation can be summarised as follows:

a) Geometry generation;
b) Materials and boundary condition assignments;
c) Physical condition assignments;
d) Computing and results process.

3.2.1 Geometry of the 2D numerical model

In all the experiments conducted in this thesis, a 59 mm internal diameter acrylic pipe with a wall thickness of 3 mm was used as the main body of the laboratory-scale fluidized bed, which will be described in full detail in Chapter 4. An eight electrode ECT sensor was designed and simulated in the present study and its detail will be illustrated in section 3.4. A 2D geometry generated by COMSOL Multiphysics (version 4.4; Electrostatics Field AC/DC module) is presented in Figure 3.2.

As is shown in Figure 3.2, eight measuring electrodes are equally distributed circumferentially and the numbering of them starts conventionally at around three o'clock in the anti-clockwise direction [175]. For each measuring electrode, there is one corresponding accompanying radial guard electrode whose functionality has already been mentioned in an earlier section. An earthed outer copper screen is wrapped around the outline of the ECT sensor to give immunity from the external electrical interference. The space between the outer screen and measuring electrodes is known as the insulating area. It can normally be occupied by an insulating material and in the present numerical model it is filled with air purely for the purpose of simplicity.

3.2.2 Materials and boundary condition assignments

The primary aim of simulating the ECT sensor was to obtain capacitance values between measuring electrodes and the remaining detecting electrodes and examine whether the capacitance values are within the detectable range of the ECT system used in the experiment. This problem can be referred to as a forward problem. A forward problem is the process of finding out the output response of an ECT system providing the permittivity distribution is known.

Therefore in the materials set-up section, the information of permittivity for different materials is applied primarily.

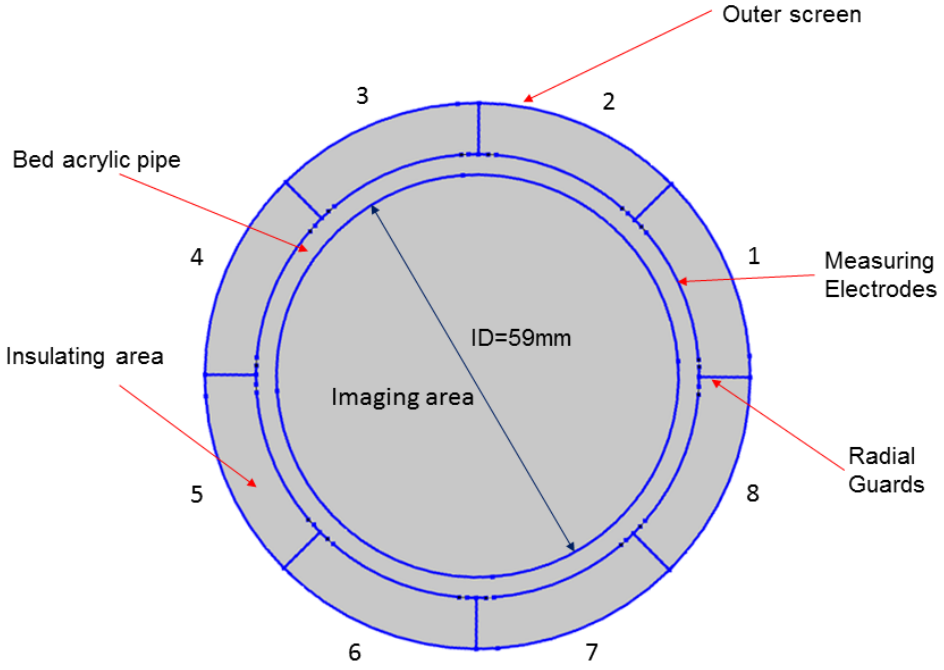

Figure 3.2: Geometry of the 2D numerical simulation

As silica sand will be used as the fluidization granular material in the present study, two extreme operating conditions were simulated. Firstly, the imaging area within the pipe, as shown in Figure 3.2, is fully occupied by air (relative permittivity of 1 is applied); and then, only silica sand (relative permittivity of 3.0 is applied, which is the ratio of absolute permittivity of silica sand to the absolute permittivity of air) fills the imaging area. All other material settings remain the same in these two conditions. For example, the fluidized bed pipe wall uses the relative permittivity of 2.7 (values for acrylic material); the insulating area uses the relative permittivity of 1 (values for air); all the measuring electrodes, radial guard electrodes and outer screen are copper.

3.2.3 Physical condition assignments and computing

As illustrated earlier, the internal electrical field distribution can be modelled as an electrostatic field. Assuming that there is no free charge involved in the simulated domain, the electrical potential and the distribution of the relative dielectric permittivity are governed by Poisson's equation [35]:

$$\nabla \cdot [\varepsilon_0 \varepsilon_r(x,y) \nabla \varphi(\mathrm{x},\mathrm{y})\,] = 0 \tag{3.1}$$

where $\varphi(\mathrm{x},\mathrm{y})$ and $\varepsilon_r(x,y)$ are the two dimensional potential and dielectric constant (permittivity) distribution, respectively, ε_0 is the free-space permittivity.

The physical boundary conditions imposed by this type of measuring technique are of Dirichlet type. In practice, for a 2D numerical model, the physical boundary conditions are summarised as follows. When one of the measuring electrodes is 'excited' (or 'fired'), i.e. the voltage on it is V_0, all the remaining measuring electrodes, radial guard electrodes and the outer screen are kept at zero potential. These are shown in the following equational forms.

$$\varphi_{excited} = V_0 \tag{3.2}$$

$$\varphi_{rest} = 0 \tag{3.3}$$

This measuring protocol will be repeated alternately until all the unique measuring electrodes have been completed as an 'excited' electrode. The 2D model will be used to simulate the proposed real sensor. To achieve this aim, the so-called forward problem has to be resolved by solving $\varphi(\mathrm{x},\mathrm{y})$ in Equation (3.1). A way to calculate $\varphi(\mathrm{x},\mathrm{y})$ is by means of the finite element method (FEM). In this method, an approximation of the potential distribution can be obtained in the sensor at a finite set of points corresponding to the nodes of the triangular mesh which is the normal mesh shape in 2D simulation in the finite element method [173]. The relationship between capacitance and permittivity distribution is governed by the following equation [130]:

$$C = \frac{Q}{V_0} = \frac{\oint_S \varepsilon_r(x,y) \nabla \varphi(x,y) ds}{V_0} \tag{3.4}$$

where Q is the electric charge on each detector electrode; S is a closed curve surrounding the detector electrode. Once the potential distribution is obtained by the FEM method, the resulting capacitance between any pair of electrodes can be expressed as C_{i-j} (i, j =1,2,…,8). These capacitances are later obtained by solving Equation 3.4 with the boundary conditions of (3.2) and (3.3) for eight times [132].

In the practical computing implementation in COMSOL Multiphysics software, the exciting voltage applied to the measuring electrode is 1 V and zero V is applied to all the remaining measuring electrodes which remain as 'detectors'. Figure 3.3 shows an example of the potential distribution when electrode No.1 is ''excited'' and the remaining electrodes work as ''detectors''. As there are eight measuring electrodes of the ECT sensor, 28 independent

measurements were performed. Accordingly, a matrix of the capacitance values obtained can be derived.

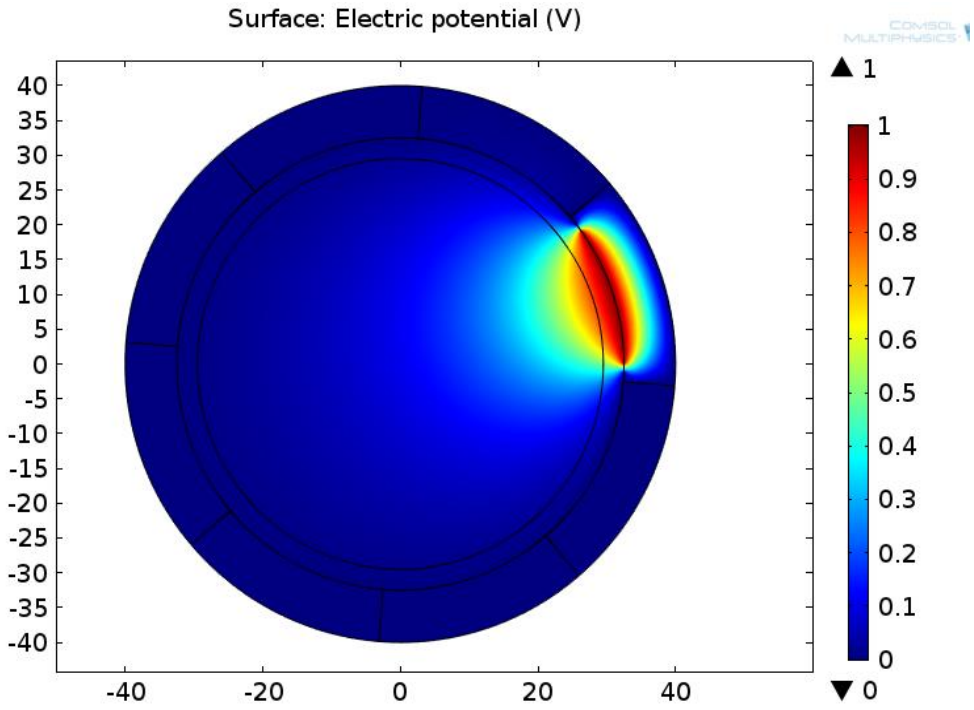

Figure 3.3: Typical electrical potential distribution when electrode No.1 is 'excited' by 1 V.

3.2.4 Results

Once the computing, as outlined in section 3.2.3, is executed, simulated capacitance values for each pair of electrodes under the two aforementioned extreme conditions are obtained and presented in Figure 3.4. Since the electrostatic field within the circular ECT sensor cross section is symmetrical, only electrode pairs of 1-2, 1-3, 1-4 and 1-5 are shown here.

It is worth noting that the initial capacitance value obtained is in F/m due to the nature of the 2D numerical simulation. However, the unit of simulated capacitance values in Figure 3.4 and Table 3.1 is in fF, which is converted by considering the proposed length of the measuring electrode of the ECT sensor is 10 mm which can be found in the sensor arrangement in section 3.4.1.

In Figure 3.4, it can be readily observed that the capacitance values between adjacent electrodes (pair 1-2) are much higher than pairs of the opposite electrodes (pair 1-5), which can be explained by Equation (3.4) whether the imaging area is full of air or silica sand material [176]. Also the values, when the pipe is full of silica sand, are significantly higher than the empty pipe. The

higher permittivity of silica sand contributes to this difference. To further distinguish the capacitance values between pairs 1-4 and 1-5 as they all belong to the region from 0 fF to 20 fF, the original simulated capacitance values are shown in Table 3.1.

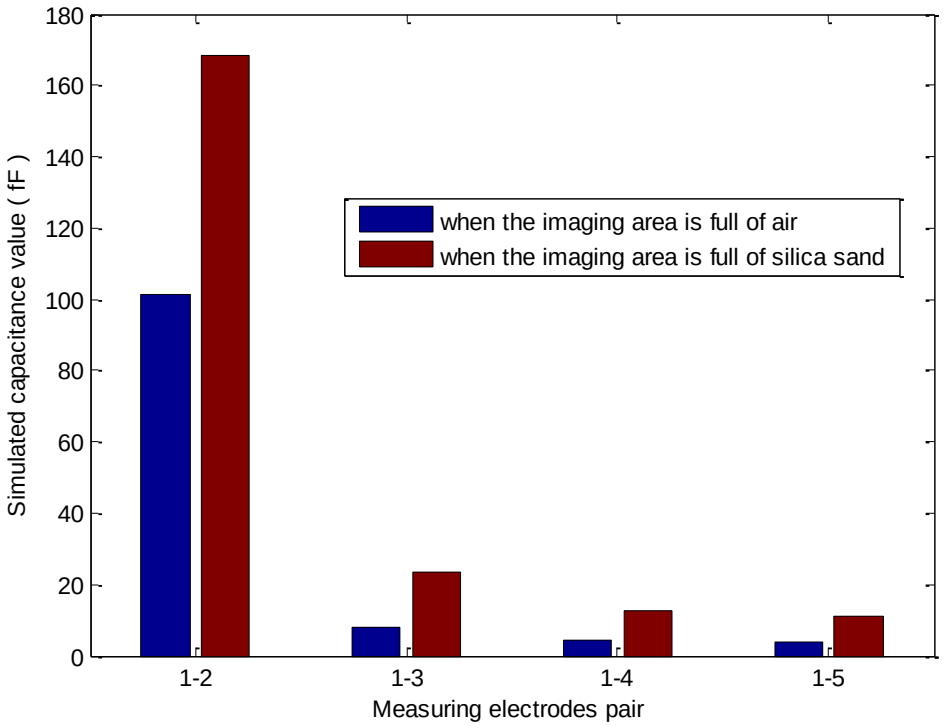

Figure 3.4: Simulated capacitance results for each measuring electrodes air under two extreme conditions.

Table 3.1 Simulated capacitance values (units converted into fF by considering the 10 mm-long measuring electrodes)

Pairs	Capacitance with air (fF)	Capacitance with silica sand (fF)
1-2	101.39	168.46
1-3	7.87	23.28
1-4	4.31	12.87
1-5	3.63	10.86

As the measurement range of the ECT system is 0.1 fF – 2000 fF, the simulated capacitance values from Table 3.1 are all within the above range. The simulation results demonstrate that the proposed ECT sensor with 10 mm

measuring electrodes mounted along a 59 mm acrylic pipe is compatible and feasible to be used with the PTL300E ECT system.

3.3 COMSOL simulation for plastic ball wall effect

3.3.1 Overview

Given a 32 x 32 pixel ECT image, a cut-off value of a specific pixel needs to be identified so as to estimate the size of a bubble appearing in the bubbling regime. As reviewed in Chapter 2, the bubble size estimation by means of ECT measurements is still being argued and it is worth noting that no systematic study has been performed so far especially on the cut-off value determination process.

In the following sections from section 3.3.1 to section 3.3.3, the primary research objective is to identify the most appropriate cut-off value to fulfil an accurate bubble size estimation. The initial idea was to use the ECT system to image a plastic ball to obtain a reference cut-off value and then estimate a bubble size by virtue of the cut-off value obtained and then evaluate it against empirical correlation estimation. The major advantage of choosing a real three dimensional plastic ball is that it is expected to be able to significantly eliminate the distortion which could be caused by using a cylindrical tube phantom as previous researchers have done since in real bubbling regime, the bubbles are always in three dimensional spherical shape, as already discovered and reviewed in Chapter 2.

Information of plastic balls applied in the present study are summarized and given in Figure 6.1 and Table 6.1 However, it can be readily observed that the wall thickness of each plastic ball is not exactly the same for all five plastic balls. This is perhaps caused by market availability and fabrication tolerance when making the balls. Therefore, it is vital to carry out an investigation of the wall effect on ECT measurements to eliminate any potential uncertainty which may cause inaccuracy or data deviation in deriving the reference cut-off values. Numerical simulation is a cost-effective approach and it will be covered in the next section.

To fulfil the task of investigating the wall effect on ECT measurement, a three dimensional numerical simulation was performed to seek the wall effect on the simulated capacitance values from each pair of measuring electrodes. The simulation work was implemented using the COMSOL Multiphysics software version 4.4 as utilized in section 3.2 in designing the customized ECT sensor. The relative governing electrostatic field equations and meshing process will

not be repeated here and instead, the physical model and simulated results will be given as follows.

3.3.2 Three-dimensional model building

The numerical simulation was carried out in a three-dimensional model due to the plastic balls being three dimensional in reality. In order to unambiguously demonstrate the established three-dimensional model, Figure 3.5 (a) presents the drawing from the COMSOL software and Figure 3.5 (b) shows a section view of the three-dimensional model where different components are shown to assist the illustration of the established numerical model.

The plastic balls will be imaged by the ECT system in the packed bed state as shown in Figure 3.5. The plastic balls were placed symmetrically in the test domain. Two conditions will be considered in the simulation. One is when the plastic ball wall material is set as the real polypropylene whose permittivity value is 2.2. Another condition is when the plastic ball wall material is regarded as the same material of the mixture of silica sand and air. The difference in the simulated capacitance values will be checked under these two conditions where simulation will be done for the five different plastic balls. Nevertheless, the permittivity value of the mixture of silica sand and air need to be decided in the first place. Therefore, the corresponding pseudo mixture effective permittivity of silica sand and air of the packed bed is derived by the following equation, the Maxwell Garnett Equation:

$$\left(\frac{\varepsilon_{eff}-\varepsilon_m}{\varepsilon_{eff}+2\varepsilon_m}\right)=\delta_i\left(\frac{\varepsilon_i-\varepsilon_m}{\varepsilon_i+2\varepsilon_m}\right) \tag{3.5}$$

where ε_{eff} is the effective dielectric constant of the medium (in this case, the mixture of the silica sand and air), ε_i is one of the inclusions (air), value = 1; ε_m is one of the matrix (silica sand), value = 3.0; δ_i is the volume fraction of the inclusions, value = 0.4. The resulting effective permittivity for the mixture of air and silica sand is 2.1. As for other physical properties, the measuring electrodes were set as copper material and the bed pipe used 2.7 as its permittivity value.

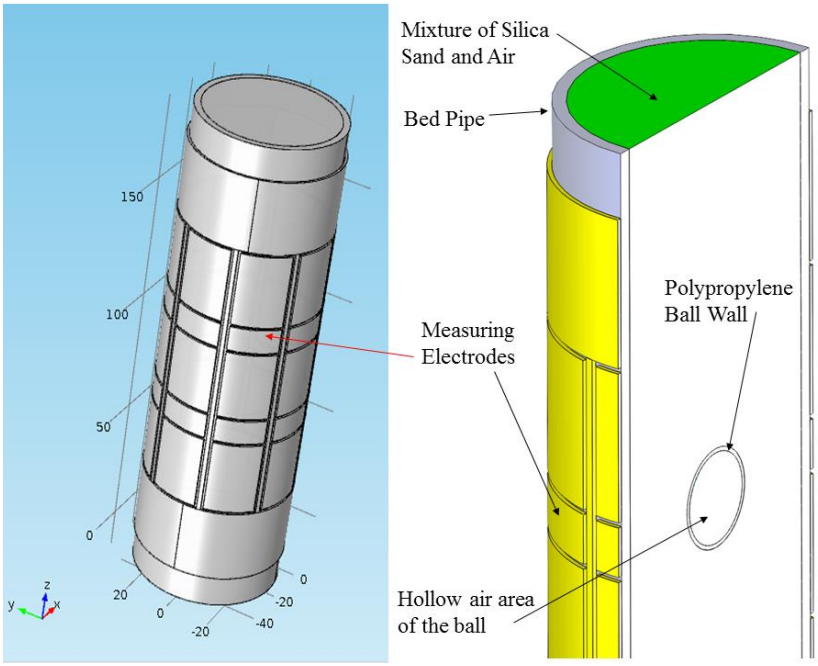

Figure 3.5: Schematic drawing when a plastic ball is put inside the packed bed: (a) three-dimensional model in COMSOL software; (b) section view of the model.

3.3.3 Simulated results and conclusions

The simulated capacitance results are derived from the surface integral of the electrical charge density over the corresponding measuring electrode area. One set of results for the 40 mm outer diameter ball is shown in Figure 3.6. Due to the symmetrical nature of the sensor area, only results for measuring electrode pairs between No. 1 and No. 2, No. 1 and No. 3, No. 1 and No. 4, and No. 1 and No. 5 are given. It can be observed without difficulty that the simulated capacitance values from the above mentioned two conditions have no obvious difference by looking at the four pairs of results. Clearly, the simulated capacitance between the adjacent pair of No.1 and No. 2 has the largest value while the one derived from the opposite pair of No. 1 and No. 5 has the smallest value, which is expected considering the fundamentals of the electrostatic field distribution. The largest percentage difference (0.1%) for the case of the 40 mm plastic ball occurs at pair No.1 and No. 4. Overall, based on the numerical simulation results for the five different plastic balls, the largest percentage difference of the results obtained under two extreme conditions is approximately 0.3%. This fairly small value indicates that the existence of the varied plastic ball wall would have a truly limited effect on the measured capacitance value and thus the proposed reference cut-off derivation process can be executed with confidence in the following sections.

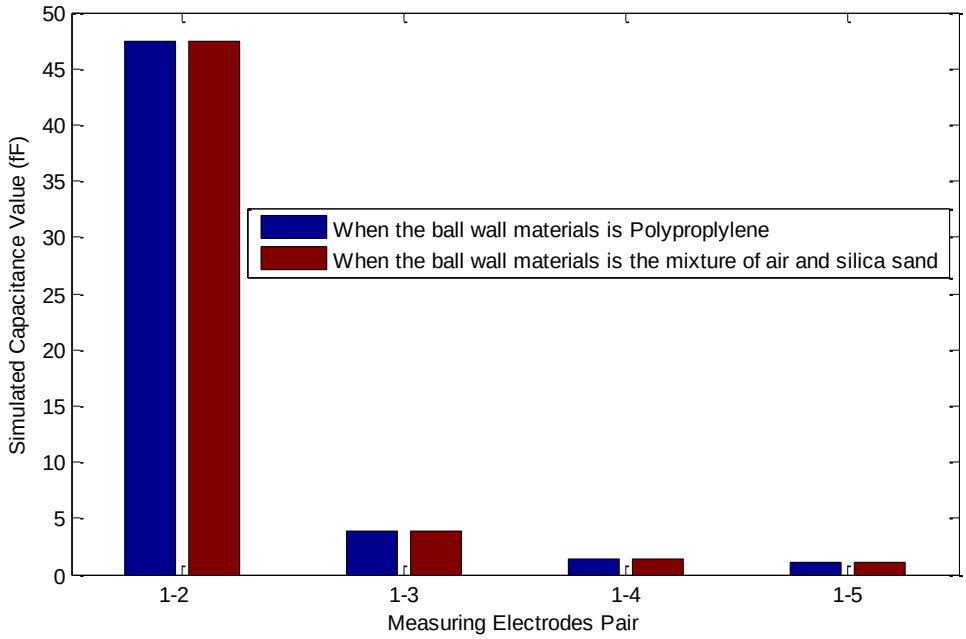

Figure 3.6: Simulated capacitance value for different measuring electrode pairs of the 40 mm outer diameter ball.

3.4 Design of ECT sensor

Once the numerical simulation has been finished, the next step is to design the customized ECT sensor which fits the proposed experimental rig. There are many aspects to consider in respect of the design process. In the following sections, some key components of the ECT sensor will be discussed, such as layout of the ECT sensor, number and length of measuring electrodes, driven guard electrodes and earthed screens, etc. Key steps in fabricating the sensor, such as the etching and potting process, will be briefly described.

3.4.1 Layout of proposed ECT sensor

A schematic layout of the proposed ECT sensor is shown in Figure 3.7. It was produced by Eagle software (version 7.2.0) that is a professional and easy to use software for printed circuit board (PCB) fabrication techniques, which will be described in section 3.4.2. It should be highlighted here that the proposed ECT sensor has two measuring planes (referred to plane 1 and plane 2, respectively), which is known as a twin-plane ECT sensor. The purpose of such a design is to derive the bubble rising velocity by means of cross correlation techniques, which will be introduced in Chapter 6.

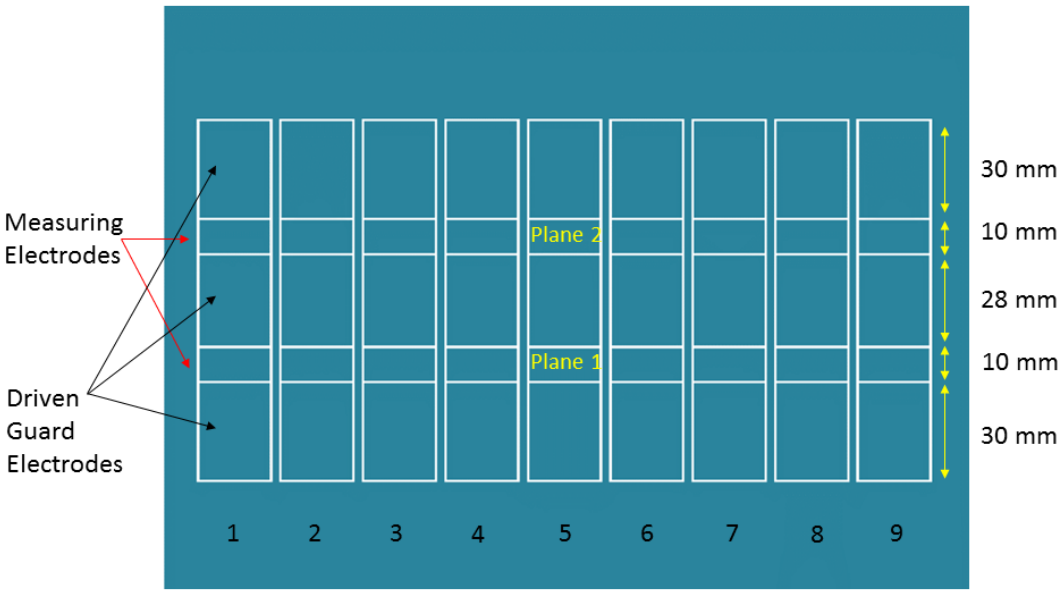

Figure 3.7: Layout of the proposed ECT sensor

3.4.1.1 Number of measuring electrodes

Before deciding any other issues in designing an ECT sensor, the number of measuring electrodes needs to be determined first. The process of choosing the number of electrodes is truly a trade-off between axial and radial resolution, sensitivity and image capture rate. The existing PLT300E system can be used with sensors having 6, 8 or 12 electrodes [175].

With a small number of measuring electrodes, a smaller number of data acquisition channels is required and less independent inter-electrodes measurements are executed. There are N(N-1)/2 possible unique capacitance measurements per image for an ECT sensor with N measuring electrodes. For example, choosing 6 electrodes will reduce the number of individual capacitance measurements to 15 compared with choosing 12 electrodes which need to measure 66 times. This will significantly improve the data acquisition rate. However, with the reduced number of independent capacitance measurements, a good quality image is not really expected.

Similarly, if the number of electrodes is increased, the number of independent measurements increases and the resolution of the image obtained will be improved. Under such circumstances, more measurements will be required to collect data for each image, and therefore the speed of data capture will be reduced as the number of electrodes is increased.

The number of 8 measuring electrodes was chosen for the present study after considering image capture rate (in the experiments 200 frames per second was used preferably) and image resolution issues. It needs to be clarified that, in Figure 3.7, the number 1 and number 9 electrodes will be cut into half respectively and form the 'real' number 1 electrode via soldering in the fabrication process.

3.4.1.2 Length of measuring electrodes

It is well known that the image produced by an ECT system is derived from the inter-electrode capacitance values. From the fundamental point view of capacitance, these values are averaged over the length of the measuring electrodes and hence the length of the measuring electrode cannot be infinitely long.

In the determining process, two factors are considered: (1) the minimum detectable inter-electrode capacitance values; (2) the feasibility of imaging bubbles as small as possible in fluidized beds. The first aspect has been validated by numerical simulation with 10 mm long measuring electrodes. As for the second issue, ideally the shorter the measuring electrodes the smaller the bubbles that can be detected. However, short electrodes produce low values of capacitance which may be insufficient to be able to reconstruct an ECT image. Also, the spatial resolution of the ECT sensor has to be considered (approximately 10% of the vessel cross sectional size). To ensure all the values within a reasonable range, 10 mm was chosen as the length of the measuring electrodes.

3.4.1.3 Driven guard electrodes

If the length of measuring electrodes is comparably smaller than the diameter of the fluidized bed, the electric field lines may spread axially at both end of the measuring electrodes. The purpose of mounting the driven guard electrodes is to maintain a parallel electric field distribution across the sensor in the region of the measuring electrodes by eliminating these three-dimensional effects in electrical field distribution [175]. This was achieved by exciting the guard electrodes in the same manner as the corresponding measuring electrodes (the same exciting voltage is applied to driven guard electrodes and measuring electrodes) [40].

As shown in Figure 3.7, the driven guard electrodes at both ends have the same length of 30 mm and the middle one has a length of 28 mm due to the 1 mm gaps which are used to separate measuring electrodes and driven guard electrodes.

3.4.1.4 External or internal electrodes

There are normally two methods for placing of electrodes, namely, externally or internally to the vessel wall. As for the external arrangement, in this case, the ECT sensor is both non-intrusive and non-invasive, which is the desired feature of the present study. However, the wall thickness of the bed pipe may introduce additional capacitance that is in series with the internal capacitance. This issue can be easily removed by the internal arrangement. But this demands some special insulated liner to support the electrodes, which is very difficult to design and construct from a mechanical viewpoint.

By considering the non-intrusive and non-invasive characteristics of the ECT sensor, the external electrode mounting type was used. Moreover, the current wall thickness is 3 mm, which is in the recommended range between 2 and 4 mm as suggested by Yang[171] .

3.4.1.5 Earthed screens and resistors

In order to prevent external noise signals or variations in the stray capacitance to earth which would otherwise predominate and corrupt the measurements, an earthed screen was used around the measuring electrodes. There are three classic types of earthed screens used in the present design: (1) outer screen; (2) two axial earthed screens; (3) radial screen. The screens of types of (2) and (3) are shown in Figure 3.8 and the screen type of (1) is shown in Figure 3.9 (a).

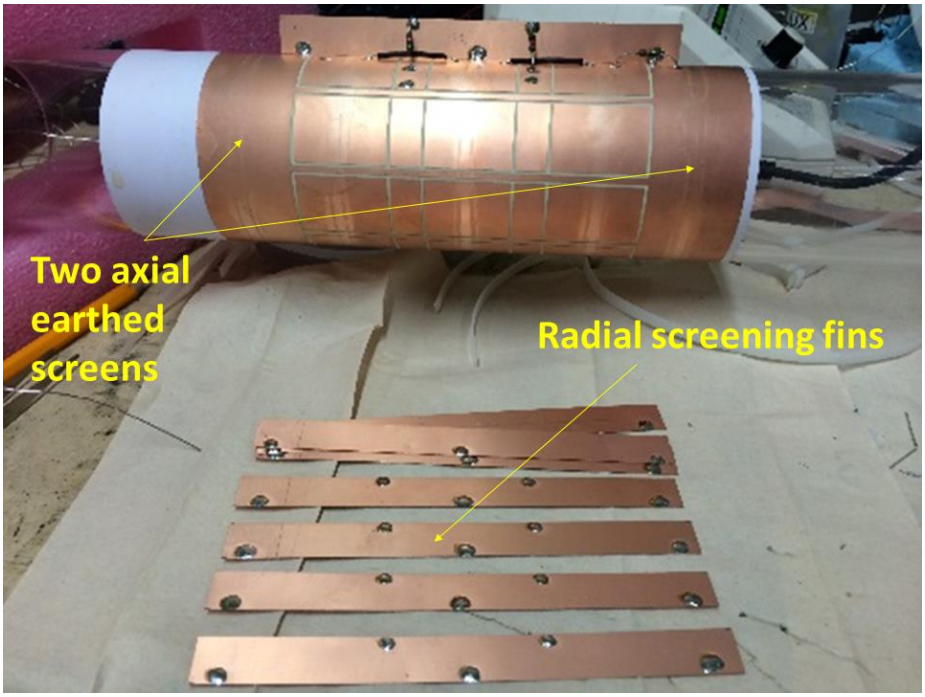

Figure 3.8: Two axial earthed screens and radial screening fins

Due to the presence of dielectric materials, such as silica sand in the present study, the motion of them could probably establish an electrostatic charge which could accumulate on the measuring electrodes [175]. There is a high probability of building high voltages between the electrodes and earth. Consequently, these voltages could harm the sensitive electronic circuitries which are embedded in the capacitance measuring unit (CMU). Therefore, some action was needed as a precaution.

Practically, this was done by soldering discharge resistors between each individual measuring electrode, driven guard electrode and earthed screen. The value of the discharge is recommended to be in the range of 100 K – 10 M Ohm. It is worth noting that these discharge resistors should be integrated within the ECT sensor itself not in the CMU.

As shown in Figure 3.9 (b), resistors with a value of 500 K Ohm are used in the present sensor and there are 24 resistors used for connecting two planes of measuring electrodes, driven guard electrodes and earthed screens. A sample of soldering resistors is shown in Figure 3.9 (b).

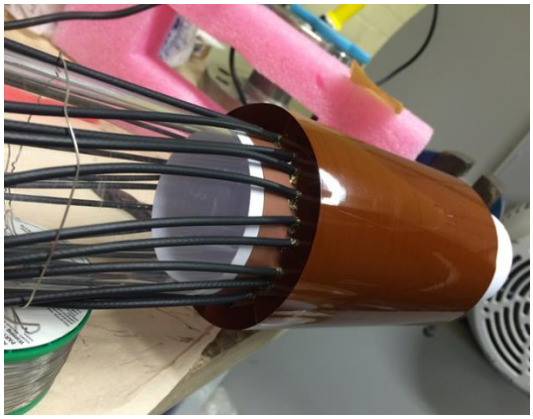

(a)

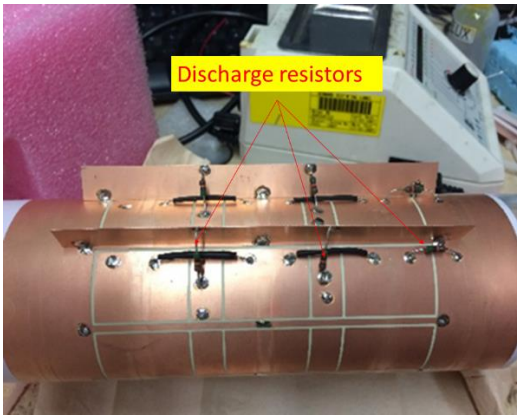

(b)

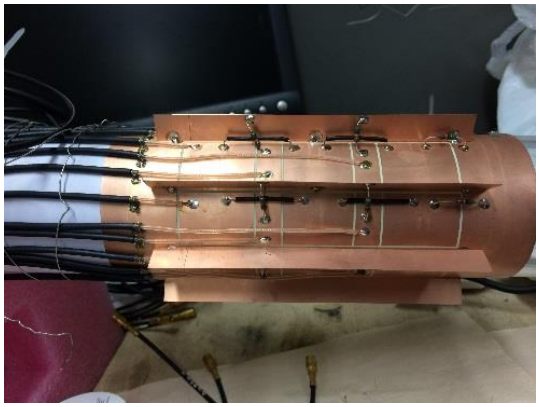

(c)

(d)

Figure 3.9: (a) Outer screen; (b) Discharge Resistors; (c) Coaxial cables soldered to measuring electrodes, driven guard electrodes and earthed screens; (d) End cap.

3.4.2 Fabrication of ECT sensor

Firstly, a single-sided copper sheet was etched according to the layout of the ECT sensor (as shown in Figure 3.7) by means of the PCB etching technique, which is a relatively cheap and precise method of electrode design [132]. The No. 1 and No. 9 sets of electrodes were cut in half along their axial middle line, wrapped around the acrylic pipe with two pieces of 80 gsm paper underneath (as shown in Figure 3.8) and were soldered together to form a new set of electrodes.

Then, a series of soldering work was carried out, e.g. three sets of driven guard electrodes were axially soldered via two sections of insulated wires to ensure they are were the same potential level; eight radial screening fins were soldered axially in between adjacent electrodes (examples can be found in Figure 3.8 and Figure 3.9 (b)); 24 coaxial cables (with SMB plugs at the end and connected to SMB sockets on the PLT300E ECT hardware system) were

soldered with two planes of measuring electrodes and all the driven guard electrodes individually (see Figure 3.9 (c)).

Finally, the outer screen, made from a piece of copper sheet was wrapped around the sensor leaving a gap around 1.5 cm between the sensor sheet and the external outer pipe, which was made from a section of acrylic pipe with an outer diameter of 100 mm and wall thickness of 3 mm. An end cap which was made of an aluminium plate was mounted on top of the sensor with coaxial cables running through it. As there were 24 coaxial cables which needed to go through the top end cap, 24 holes were drilled on it (see Figure 3.9 (d)). However, the bottom cap was not drilled. Both the end caps and the outer screen were soldered together to be earthed.

Figure 3.10: Photograph of the completed twin-plane ECT sensor.

A high level of mechanical stability is normally required for an ECT sensor. Because any small movement between electrodes or earthed screens would significantly change the values of inter-electrodes, which will directly alter or distort the quality of further reconstructed images. Hence, in the present design, two bags of 250 g Potting Compounds (RS Stock No.160-8497) were used to consolidate the connections inside of the sensor. The completed ECT sensor is shown in Figure 3.10.

3.5 Summary

The brief review of numerical simulation within an ECT sensor is presented. COMSOL Multiphysics has proved to be one of the most appropriate software packages for simulating electrostatic field distribution using the finite element method and was chosen for the present numerical simulation process.

A 2D numerical simulation model has been built based on an AC/DC module embedded in COMSOL Multiphysics. Geometry and physical boundary conditions are specified and the basic theory behind the electrostatic field distribution is illustrated. The simulation results demonstrate that the proposed ECT sensor with 10 mm measuring electrodes mounted along a 59 mm acrylic pipe is compatible and feasible to be used with the PTL300E ECT system.

Numerical simulation was conducted to investigate the plastic ball wall effect on the simulated capacitance of each measuring electrode pair. The simulated results suggested that the plastic ball wall would have very limited influence on the measured capacitance values.

The general design and fabrication process of the customized twin-plane ECT sensor is described. Some key components of the ECT sensor are discussed in detail, such as how to determine the number and length of the measuring electrodes, how to choose the external or internal electrodes arrangement, and how to select driven guard electrodes and discharge resistors, etc. Then key steps in fabricating the sensor, such as the etching and potting process, are briefly outlined. Finally, a completed twin-plane ECT sensor is presented.

Chapter 4
Experimental Set-up

In order to investigate fluid flow processes using a gas-solids fluidized bed, a set of experimental rigs were designed and built. A detailed illustration of the experimental set-ups, including the ECT measurement test rig and the pressure fluctuation measurement rig respectively, will be dealt with in this chapter. After that, the experimental setup for plastic ball calibration will be introduced, which involves the arrangements of the suspension of the plastic ball in the bench-scale fluidized bed and plastic ball measurement positions.

4.1 ECT experimental test rig

To investigate the fluid flow processes within a laboratory scale gas-solids fluidized bed, a customized measurement apparatus was developed to fulfil this aim. A schematic drawing and a photograph of the experimental rig are shown in Figure 4.1 and Figure 4.2, respectively.

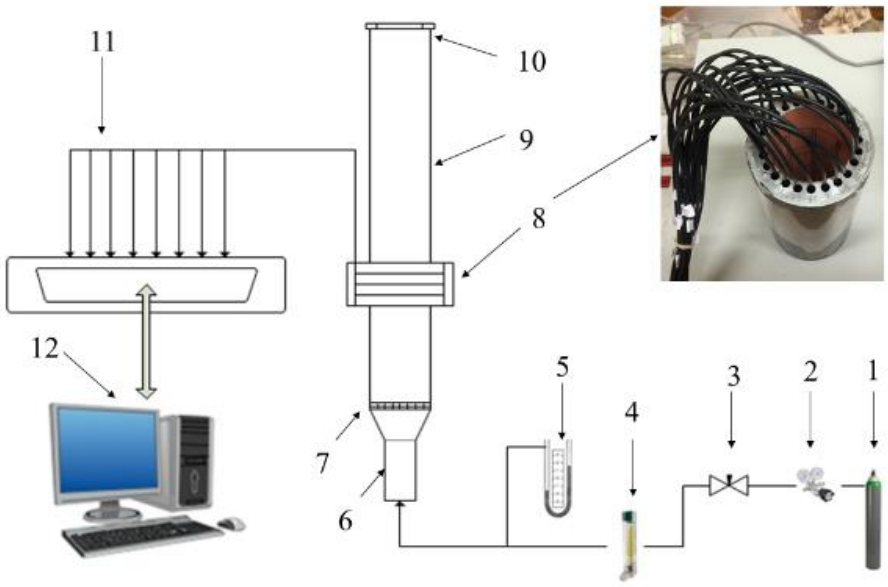

Figure 4.1: Schematic diagram of the ECT measurement rig

The corresponding components relating to the numbers as shown in Figure 4.1 are stated as follows: 1. Compressed air cylinder; 2. Air regulator; 3. Needle valve; 4. Flowmeter; 5.U-shaped manometer; 6. Plenum. 7. Air distributor; 8. Twin plane ECT sensor; 9. Fluidized bed; 10. Top cap; 11.

Capacitance Measurement Unit (CMU); 12; Host PC. It is worth noting only main parts are labelled in the below Figure 4.2.

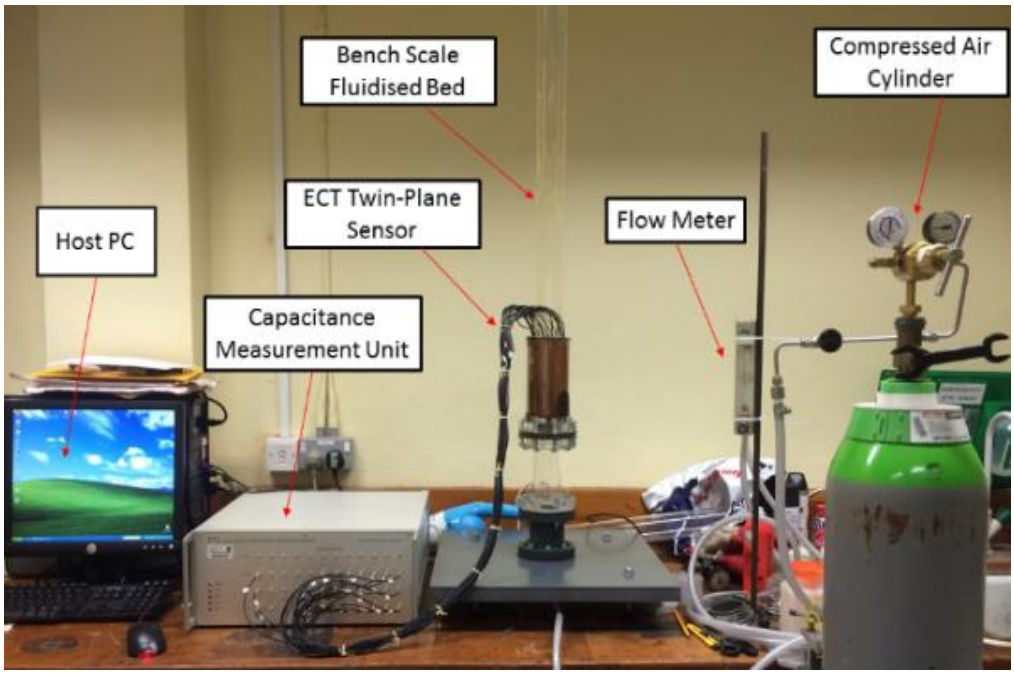

Figure 4.2: Photo of the ECT measurement rig in the B25 lab, chemistry building, at the University of Leeds

4.1.1 General description of the rig

The laboratory scale gas-solids fluidized bed measurement system presented in Figure 4.2 is mainly composed of two sections, viz, the fluidized bed system including associated auxiliary components (such as the air cylinder, flow meter, bed plenum, air distributor and bench-scale bed pipe etc.) and the ECT measuring system. The whole measurement rig was operated at room temperature and atmospheric pressure.

Generally three sub-systems are included in the ECT measurement system which is similar to the one schematically reviewed in Figure 2.23. The sub-systems are the sensing system, data acquisition system and image reconstruction and display system. The sensing system is actually the customized twin plane ECT sensor whose detailed information was introduced in Chapter 3. As for the data acquisition system and image reconstruction and display system, more information will be provided together the fluidized beds system (including auxiliary components) in the following sections.

4.1.2 Description of the ECT measurement system

The ECT measurement system used in the experiments is the PTL300E system, which was commercially provided by Process Tomography, Ltd., Cheshire, UK. The PTL300E system is a computer-controlled twin-plane ECT measurement system with the capability of recording and observing inter-electrode capacitance values and reconstructed image data at either one or two measurement planes [177]. Without exception, compared with any other kind of ECT measurement system, it consists of the sensing system, data acquisition system and image reconstruction and display system. These three components are described as follows.

The sensing system is composed by the aforementioned customized twin-plane ECT sensor. Since a detailed design and fabrication process has been demonstrated in Chapter 3, only a completed conceptual diagram is presented below in Figure 4.3 for illustration purposes. Relative dimensions are also shown below.

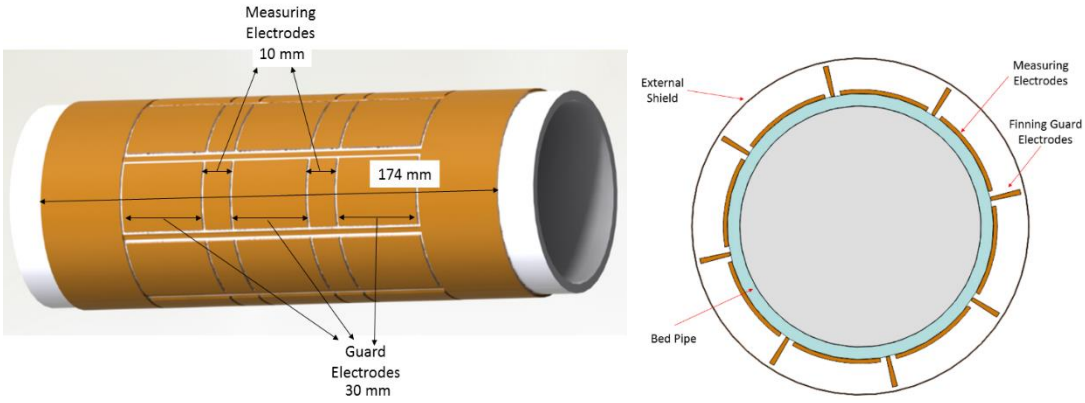

Figure 4.3: Arrangement of the twin-plane ECT sensor [178].

The data acquisition process is completed by the DAM200E Capacitance Measurement Unit (CMU), which can measure inter-electrode capacitances in the range of 0.1 to 2000 fF. The unit can be seen in Figure 4.2. In the front panel of the CMU, there are four sets of 12 X SMB miniature coaxial connecters where two sets are allocated for plane 1 and plane 2 measurement electrode channels and the other two sets for plane 1 and plane 2 driven guard electrode channels. For future reference, plane 1 is defined as the lower level plane and plane 2 is the upper level plane as the compressed air flows upwards through the fluidized bed vertically. The CMU was connected to the host PC via a LAN 10/100 Mb/s Ethernet connector located on the rear panel of the CMU. The measurement protocol, in which one measurement electrode

in each measuring electrode plane and the corresponding driven guard electrode is set to be a source electrode and all the remaining electrodes are maintained at virtual earthed potentials, as described in Chapter 2 and Chapter 3, is utilized by the DAM200E CMU. Consequently, in the present study, 28 measurements in total for each time step were implemented for the eight-electrode twin-plane ECT sensor.

The tasks of image reconstruction and display are mainly executed by the PTL ECT32v2 software. This is a comprehensive suite of programs enabling the PTL300E system to be configured, calibrated, and utilized to record inter-electrode capacitance data files and to reconstruct them into image files at user-defined speeds. The maximum image capturing speed in all the experiments conducted was kept at 200 frames per second (fps). It can also permit the PTL300E system to display and playback the captured capacitance and permittivity image data [177]. In the present study, the ECT32v2 software was embedded in the host PC running on the MS operating system (Windows XP) as shown in Figure 4.2.

The primary objective of the ECT system is to obtain images of the distribution of a mixture with two different permittivity values inside ECT sensors. From the permittivity distribution, it is possible to acquire the distribution of the relative concentration fraction of the two components over the cross-section of the vessel [175]. A typical reconstructed ECT permittivity image utilizes a square grid of 32 x 32 pixels to display the distribution of the normalized composite permittivity of each pixel. For a circular-shaped sensor, 812 effective pixels in total are applied to approximate the cross-section of the sensor, which is shown in Figure 4.4. In the present study, since the inner diameter of the bench scale fluidized bed is 59 mm, the equivalent physical area of each pixel is approximately 3.37 mm^3. The raw ECT image data can be viewed either in a quantitative manner by looking at individual normalized permittivity value of each pixel as demonstrated in Figure 4.4, or in a qualitative way in the form of a coloured (Red-Green-Blue) image as illustrated in the Figure 4.5.

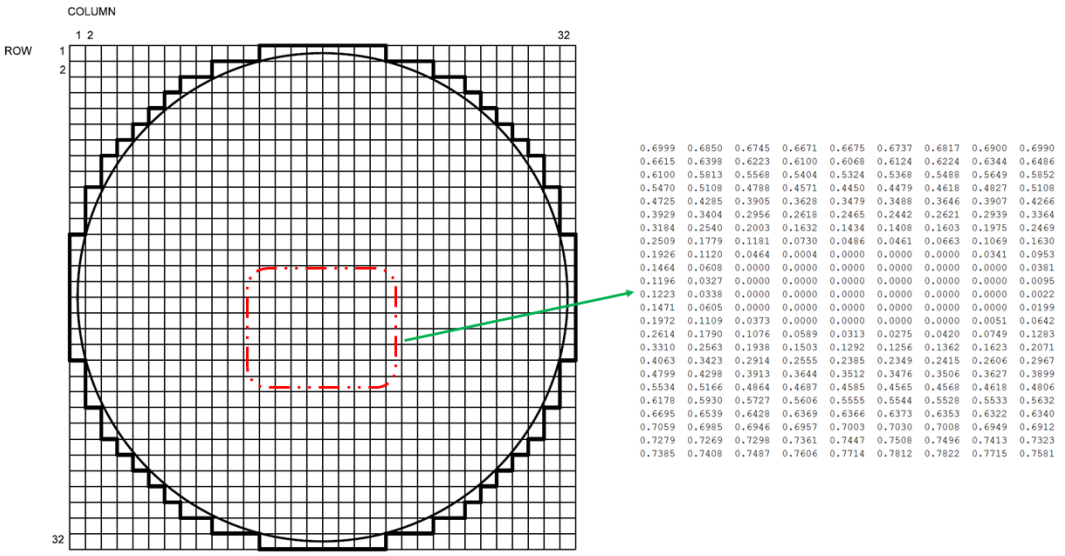

Figure 4.4: A 32 x 32 image format used in the ECT system and a standard set of normalized permittivity values.

A representative operating window of the ECT32v2 displaying twin-plane permittivity images is presented in Figure 4.5. The data was obtained when gas superficial velocity was at 8.87 cm/s while a gas bubble was traversing plane 2. The corresponding normalized capacitance values for each inter-electrode (marked as red bars in the box under the plane 2 image) can be found in the Figure 4.5.

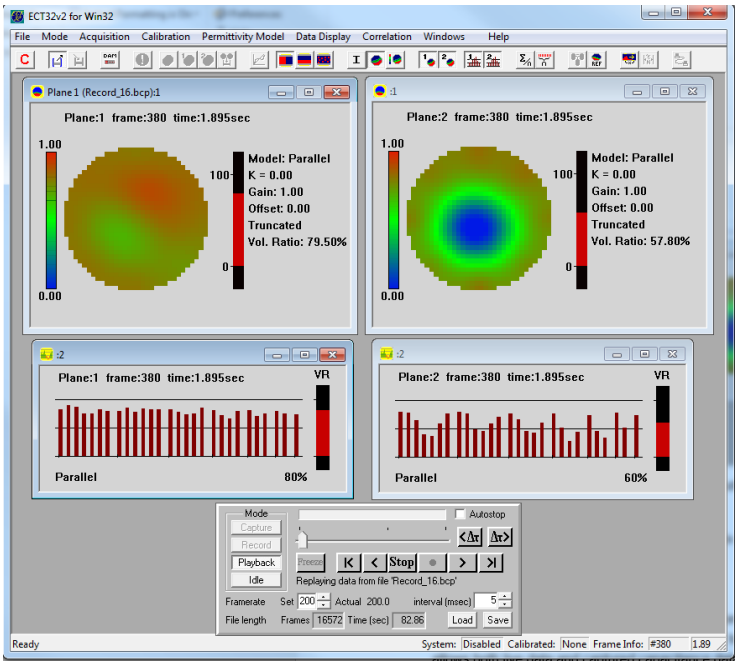

Figure 4.5: A screenshot of the ECT32v2 software operating interface

Prior to data recording, the ECT system requires calibration as described in Chapter 2. The calibration process often involves the measurement of two extreme operating conditions by filling the vessel with the lower and higher

permittivity materials in turn. In the present study, this was done first by positioning the twin-plane ECT sensor at a desired vertical level around an empty bed and recording the corresponding calibration data. Then, unload the sensor and load the silica sand (whose properties will be introduced in the next section) from the top opening of the bed pipe to the desired static bed height. Put the sensor in the previous location around the packed fluidized bed, record and save the calibration data for both cases. Although recorded calibration data can be used repeatedly for conditions using the same materials, it is still recommended to conduct the calibration process in-situ prior to each run of experiments [179].

In addition to the ECT32v2 software, some supplementary software was provided to facilitate the interpretation of ECT raw image data, such as, IU2000, which is able to produce a range of enhanced ECT images from data files captured using the ECT32v2 software; Plot3d, which is useful for displaying images obtained from the ECT32v2 software in a two or three dimensional form. Besides the software provided by Process Tomography Ltd., several sets of programming codes based on the MATLAB software were developed to interpret the image data to study the bubble behaviour. These will be illustrated in the following sections where appropriate.

4.1.3 Granular materials

As mentioned in the review section, silica sand with a surface mean diameter of 276 microns and density of 2650 kg/m^3, which belongs to Group B according to Geldart's classification criterion, are used throughout the experimental work due to its popular property of being easily fluidized and its wide application in the process industry. The silica sand particles were dried before being loaded into the bed in a laboratory oven in the Materials Laboratory of the School of Civil Engineering. Its size distribution, which was obtained by means of the Mastersizer 2000 analysis in the School of Chemical and Process Engineering, can be found in Figure 4.6.

The Mastersizer 2000 instrument utilizes the Mie theory to predict the way light is scattered by spherical particles and to deal with the way light passes through assuming that some specific information about the particle, such as its refractive index and absorption index are known (in this case, 1.544 and 0.1 are the refractive index and absorption index, respectively, for silica sand). As each size of particle holds its own characteristic scattering pattern, the size

of particles with specific scattering patterns were calculated by the Mastersizer 2000 instrument which is shown in Figure 4.7.

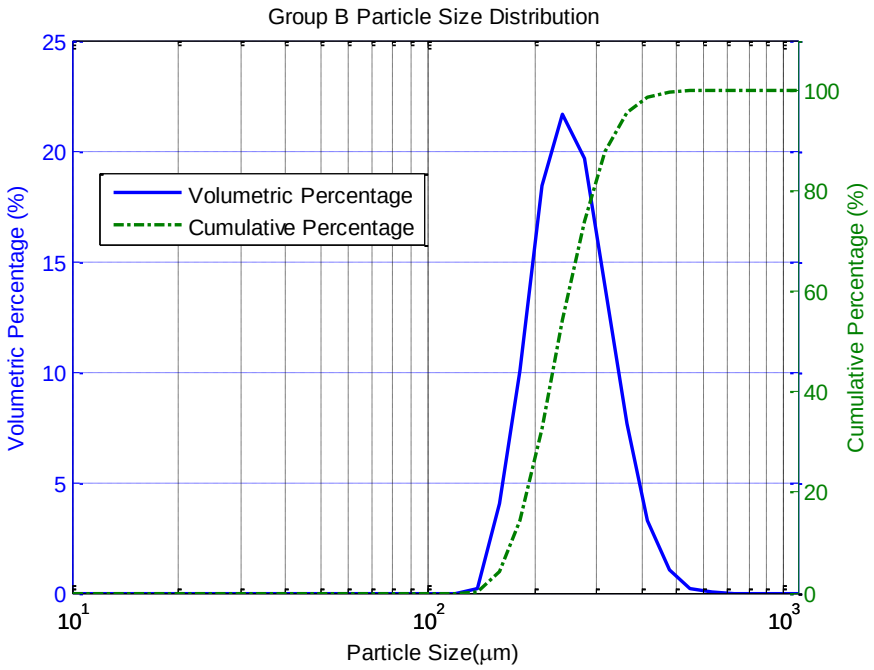

Figure 4.6: Silica sand size distribution [178]

Figure 4.7: The Mastersizer 2000 instrument in the Materials laboratory, School of Chemical and Process Engineering.

4.1.4 Air distributor feature

In the process of fluidization, it is common practice to keep the air flowing upwards evenly with contact solid particles in order to have stable fluidization and prevent any non-fluidized regions. To achieve this, an air distributor (also called a grid) should be inserted at the bottom of the fluidized bed to ensure

the air is distributed uniformly over the cross section of the bed [1]. Another functionality of the air distributor is to support the weight of solid particles mechanically in the bed. As for how to choose an air distributor, it is really a trade-off between popular use, mechanical feasibility and cost [4].

Generally, there are two types of air distributors, e.g. porous and perforated distributors. The porous distributor has prevailed in fluidized beds applications for a long time. However, the popularity in the use of the porous type has declined due to two reasons. One is that the commercially provided porous plates often have various thickness or degrees of permeability which consequently results in some areas having a large flow rate whereas elsewhere blockages can easily occur. Moreover, it is very time consuming to improve or rectify these problems. Another reason is that it is normally costly because of the fragile features and difficulty caused in machining work of this type [1].

Comparing with the porous distributor, the perforated one has relative more popular applications as they can be easily fabricated and inexpensive[4]. They are normally plastic plates where small holes are drilled or punched on them. In the design process, the size of the hole and its distribution pattern are the two most concerned factors.

As for the size of the holes, two competing points need to be considered. Smaller holes, especially if the size is smaller than 1 mm, are very difficult and expensive to fabricate. However, a better performance is usually given by a large number of small holes than a small number of large holes having the same cross-sectional area [1]. The conventional size of the small holes in experimental laboratory-scale fluidized beds is between 1 mm and 6 mm. Considering all the above mentioned factors, a 1 mm hole size was chosen.

Regarding the holes distribution pattern, there are normally two patterns, namely, square and triangular pitch patterns. Triangular pitch, which is shown in Figure 4.8, was chosen as it can produce more holes per unit area as indicated by Yang [4]. A governing correlation of triangular pitch pattern is shown in Figure 4.8. L_h is the pitch size and N_d is the hole density with the unit of holes per unit area of the bed.

In the present study, the air distributor is made from PVC material. The air distributor was fabricated in the mechanical workshop in the Faculty of Engineering. A schematic diagram of the air distributor is presented in Figure 4.9. The thickness is 8 mm, which is designed to sufficiently support the weights of silica sand packed at 170 mm height.

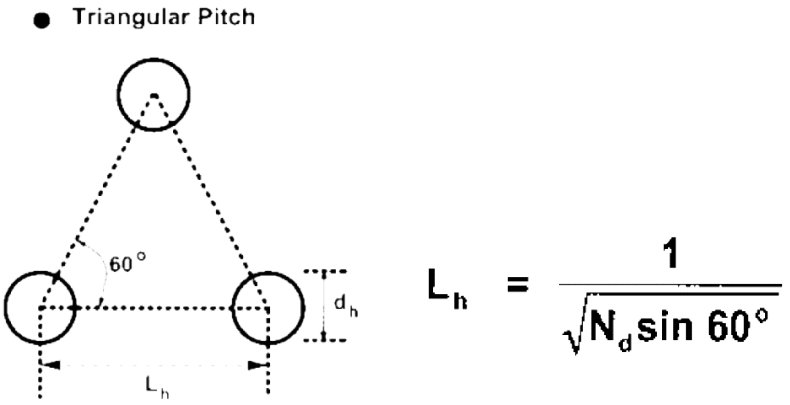

Figure 4.8: Triangular pitch pattern and governing equation [4]

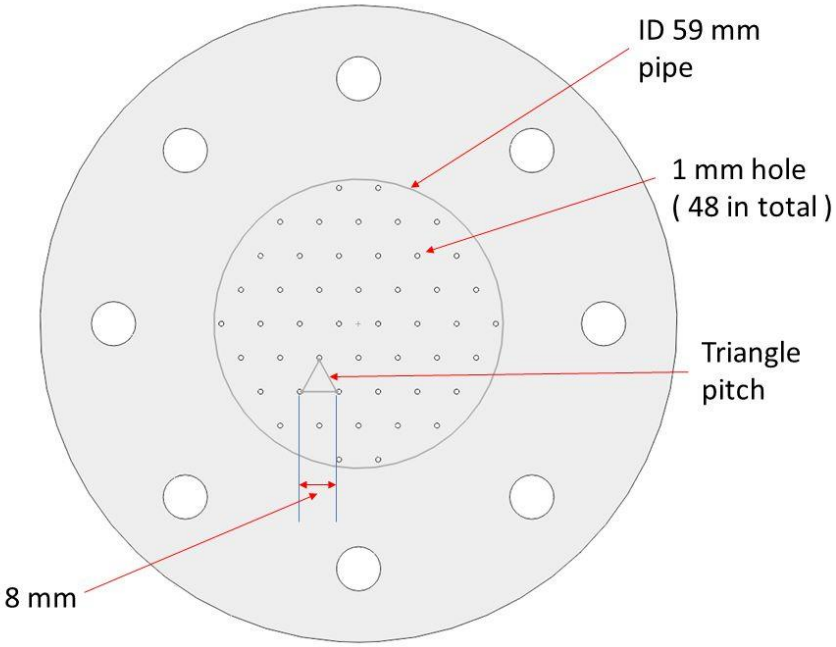

Figure 4.9: Layout of the air distributor

4.1.5 Auxiliary components

4.1.5.1 Flow meter and U-shaped monometer

In order to monitor and control the flow rate of the compressed air which was used to fluidize the silica sand, a float type of oxygen flow meter was installed in the air supply loop (as shown in Figure 4.2) with a conversion factor provided from the company of about 1.51 by considering the operating pressure and density difference between oxygen and air. A small constant increment step of the fluidizing velocity was kept at 1 litre per minute, which is equivalent to 0.42 cm/s of air superficial velocity when the ECT data or

pressure fluctuation data was continuously recorded. Although measurements were only concerned the bubble behaviour study, in order to examine the fluctuation characteristics of the solid fraction signal, a few measurements before the onset of minimum fluidization velocity were also conducted.

An U-shaped water monometer was connected to the air plenum to monitor the pressure drop across the bed. On one hand, it is an easy, inexpensive and reliable approach to obtain the pressure information; on the other hand, the results acquired from it can be used to compare and re-affirm the results measured with the pressure transducers.

4.1.5.2 Pipe components and air supply

Experiments were carried out in a cold conventional fluidized bed. The bench scale fluidized bed was composed of a 1 metre long acrylic pipe with an internal diameter of 59 mm and wall thickness of 3 mm. The 1 metre length of the acrylic bed pipe was designed to prevent any perturbation which may occur on the inside of the fluidized bed [13]. The transparent acrylic pipe enabled direct visual observation of the gas solid contact along the pipe wall at the top of the bed surface, which is useful for qualitative analysis and a pre-judgement of the internal flow regimes. The air distributor was sandwiched by flanges between the pipe and a 15 cm long plenum which was also made of acrylic material.

Beneath of the plenum, a cone-shaped PVC pipe was fabricated and used to connect the plenum and the pipe supply loop. The major functionality of the cone-shaped pipe and the plenum was to distribute the upward flowing air as evenly as possible to avoid any potential flow vortex and eventually to prevent de-fluidization regions from occurring. The cone-shaped PVC pipe was connected to a thick square PVC plate sitting on four adjustable feet. The plate has a thickness of 20 mm and 50 cm by 50 cm for length and width, which was used as the base of the whole fluidized bed.

Ambient air was supplied by a compressed air cylinder which was supplied by BOC Ltd. A regulator was mounted on top of the cylinder to monitor the output pressure and a needle valve was connected immediately after the regulator to act as the isolation valve and to control the flow rate of the air to be introduced to the bed.

To prevent silica sand from being entrained out of the top opening of the fluidized bed and causing any air pollution to the laboratory surroundings when the bed was operated at relatively high superficial velocities, a

customized top cap was designed and fabricated in which a layer of fine mesh was embedded.

Before conducting any experiments, a leakage test must have been done to ensure all connections were properly sealed. Otherwise, a small leakage may have great proportional influence on minimum fluidization velocity [1]. To locate the points or areas of leakage, the soap bubble method was utilized as it is the most simple and reliable approach although there may be other methods, such as the use of special emission detectors. The examined points or areas included the fluidization column, needle valve joints, flow meter connections with air supply hose loop and air distributor joints with both sides flanges.

4.1.6 Main operating conditions and operating procedures

According to the experimental rig described, the main operating conditions and general operating procedures for ECT measurements are summarized as follows in Table 4.1.

Table 4.1: ECT measurements operating conditions

Parameters	Specific Conditions
Static bed height	170 mm
Particle type	Group B Silica sand with mean diameter of 276 microns and density of 2650 kg/m^3
ECT sensor	Twin plane, eight measuring electrodes (1 mm long), 200 fps sampling rate
Fluidized bed	59 mm ID, 3 mm wall thickness, 1.5 m long in total
Distributor	Perforated PVC plate, 48 holes of 1 mm diameter with an open area of 1.38%

Main operating procedures:

1) Assemble all the essential parts including the fluidized bed pipe, air distributor, flanges; connect ECT sensor with the CMU; power on the host PC and the CMU; check the horizontal degree of the rig using a spirit level.

2) ECT calibration with lower permittivity materials (an empty pipe in this case); load silica sand to a height of 170 mm; ECT calibration with higher permittivity materials.
3) Release the air from the compressed air cylinder gradually via the needle valve.
4) Turn the ECT32v2 software on and switch it to the Data Capture Mode at a sampling rate of 200 fps for 80 seconds for each superficial velociy; increase the superficial velocity steadily with an incremental step of 1 L/MIN on the oxygen flow meter; take record of the readings from the flow meter, U-shaped monometer and ECT images data.
5) Slightly step up the superfiical velocity to a desired value, repeat Step 4 until all the data have been collected; shut down the gas supply.
6) Dismount the twin ECT sensor, disassemble the rig, discharge silica sand and clean the fluidized bed pipe.

4.2 Experimental Rig of Pressure Fluctuation Measurements

4.2.1 Description of the principle of the rig

Pressure fluctuation signals recorded by pressure transducers at high sampling rates are very useful in interpreting the bubble characteristics either in time domain or frequency domain analysis as reviewed in Chapter 2.

An experimental rig was built to measure the pressure fluctuation in a laboratory scale fluidized bed which is shown below in Figure 4.10. Ideally, a replica of the ECT measurement rig as depicted in Figure 4.2 was desired but with a different the test sections for pressure taps. Under such a design, all other parameters can be kept the same as the ECT measurements and hence, a comparative study can be accomplished between ECT measurements and pressure fluctuation measurements under the same operating conditions.

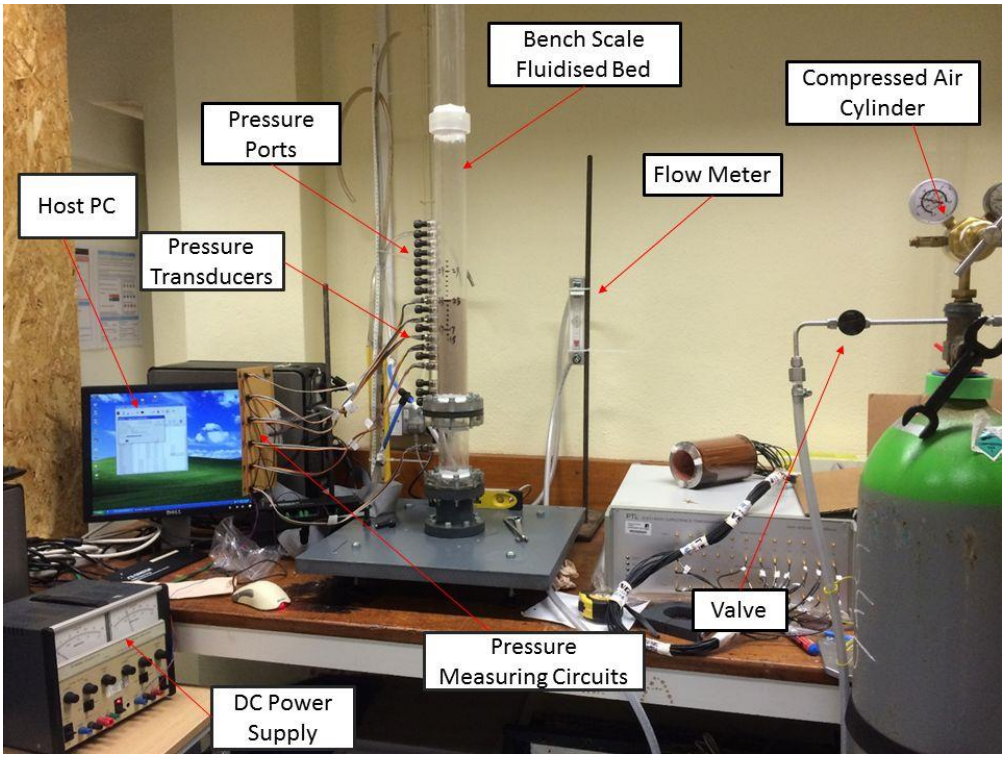

Figure 4.10: Arrangement of the pressure fluctuation measurement rig.

4.2.2 Pressure transducers and data acquisition system

According to a pre-calculation of average pressure drop across the bed with a static bed height of 170 mm, three types of pressure gauge transducers, namely, PX72-0.3GV, PX72-0.8GV, PX72-1.5GV, from Omega Engineering Limited, Manchester, UK, were selected to measure the pressure fluctuation at different locations. PX72-0.3GV types have a measurement range from 0 to 0.3 psi, which were used to measure the pressure fluctuation at the upper location of the bed to obtain as accurate data as possible. Based on a similar consideration, PX72-0.8GV with a measurement range from 0 to 0.8 psi was used to measure the lower part of the bed and PX72-1.5GV with a measurement range from 0 to 1.5 psi one was used to measure pressure fluctuation at the plenum location.

There are six transducers used in total during the pressure fluctuation measurement at six different measurement locations which will be introduced in Figure 4.13. All the pressure transducers were calibrated against a U-shaped water monometer priori to data acquisition. One of the calibration curve (with pressure transducer of PX72-0.3GV) is shown in Figure 4.11 for the purpose of illustration. The direct output voltage is in milivolts unit.

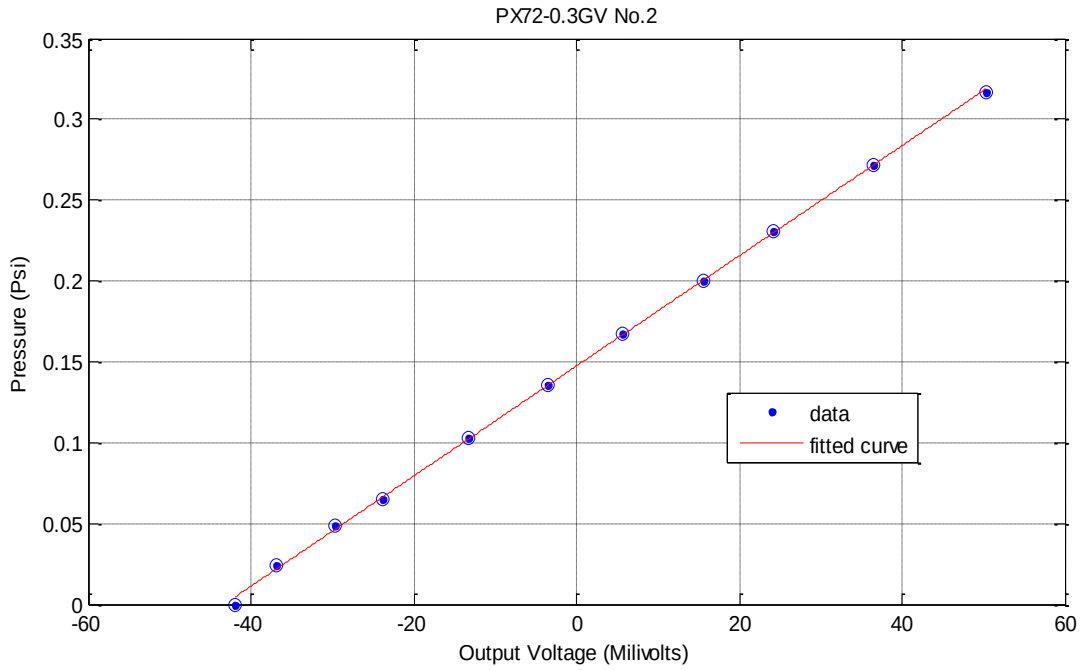

Figure 4.11: Pressure transducer (PX72-0.3GV) calibration curve

The recorded pressure fluctuation data were collected at a sampling rate of 200 Hz by a DAQ card (DaqTemp Model 14A) from Omega Engineering Limited, Manchester, UK. To determine dominant frequencies in a bubbling fluidized bed, a sampling rate at 20 Hz is considered adequate as the crucial fluidized bed frequency is conventionally below 10 Hz [8]. Hence, the sampling rate of 200 Hz is more than enough for data analysis. On the other hand, the equivalent 200 Hz sampling rate was chosen for the ECT measurements whose image capture rate was 200 fps. By doing this, comparative study between ECT and pressure fluctuation measurements was made possible.

It is always beneficial to make a lengthy data record by which the accuracy of some parameters' calculation will be improved, for example, the power spectral density. However, by doing this, extra labour expense or time consumption caused by calculation may occur. To maintain the above factors at a relatively reasonable level, 80 seconds were used in all experimental runs. All the pressure transducers were calibrated at 10 Volts, which was provided by a DC power supply as shown in Figure 4.10.

4.2.3 Pressure probes and their distribution

In most cases, the pressure transducers are not able to contact directly with the fluidized beds and instead they normally connected with each other via a probe or tube. In the present study, as shown in Figure 4.12, a modified tube boss (marked in red) was used to act as a probe which connected the bed pipe (marked in green) and the pressure transducer (marked in black). The tube boss was fabricated using transparent acrylic material since it has been demonstrated that the materials of the probe have no influence on the recorded pressure data [46].

Normally the probe diameter is in the range between 2 and 5 mm. Smaller size will result in dampening of the signal and a much larger diameter probe will increase resonance effects and introduce disturbance to the internal local hydrodynamics [46]. Hence in the present study, 2.6 mm was chosen for the tube boss internal diameter because by doing so, it was possible to match the transducer opening which is 2.6 mm in diameter. Accordingly, the diameter of the hole drilled through the bed wall was also kept at 2.6 mm to ensure all the three parts had a consistent pressure signal passage. In order to obtain pressure fluctuation data in a non-intrusive manner, all the tube bosses were placed flush with the bed wall as demonstrated in Figure 4.12.

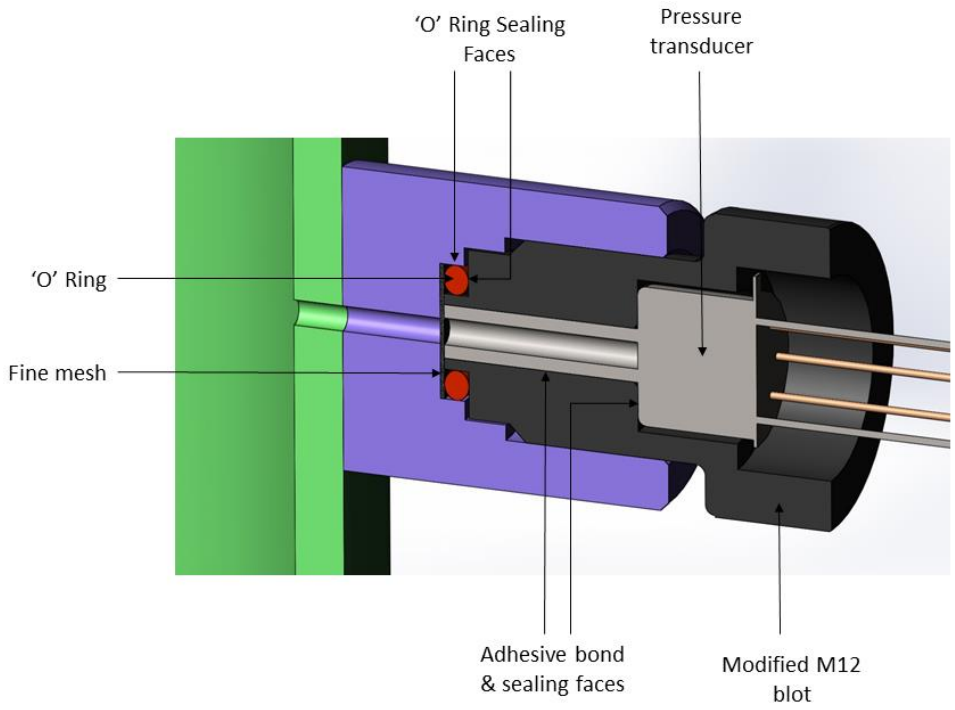

Figure 4.12: Schematic diagram of pressure probe design

The total length of the tube boss was approximately 1 cm which is far less than 20 cm which was recommended by Ommen et al. [46, 50] as the maximum length for a probe for high frequency data capture.

A layer of fine mesh was placed at the inlet of the pressure transducer to prevent any silica sand from contaminating the pressure transducer. As long as the mesh was open enough, it had no significant influence on the pressure fluctuations [46]. One O-ring was attached for each pressure transducer next to the fine mesh to, on one hand, mechanically stabilize the position of the fine mesh, on the other hand, to partially assist improvement of the condition of the seal between the pressure probe and pressure transducer.

Pressure fluctuations were measured simultaneously via six pressure transducers which were distributed axially along the bed pipe, as presented in Figure 4.13. In order to have a comparative study between ECT measurement and pressure fluctuations, two pressure taps were drilled at the equivalent levels of plane 1 (88.5 mm) and plane 2 (128.5 mm) in the ECT experimental rig, respectively.

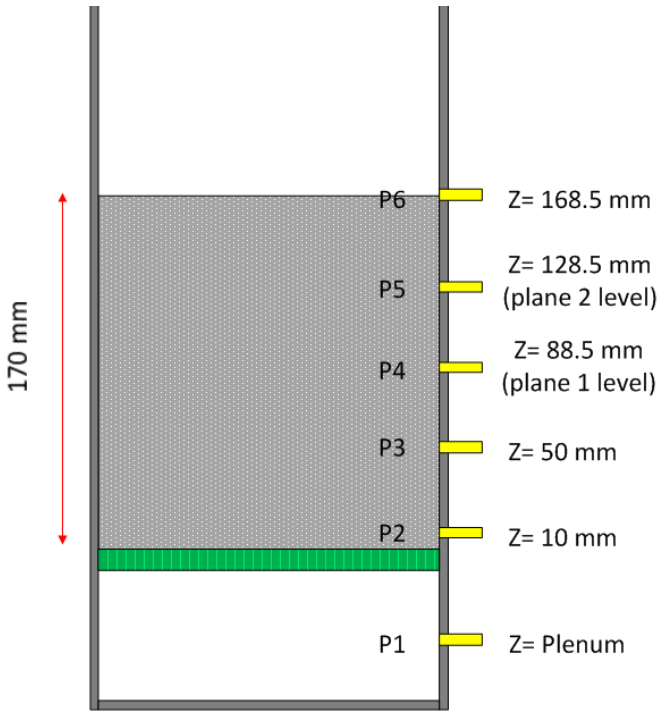

Figure 4.13: Pressure fluctuation measurement location distribution.

4.2.4 Auxiliary components

A PCB board was simply designed and fabricated to facilitate the pressure fluctuation measurements. An on-site photo is shown in Figure 4.14. As can

be seen from the figure, six eight-pin DIP sockets were soldered in a row numbered from 1 to 6 upwards vertically (which corresponds directly to the pressure probes location distribution in Figure 4.13). Pressure transducers were electrically connected with the PCB board via six multi-core cables (shown in Figure 4.10).

Apart from the above mentioned components, all other parts which were used to form the pressure fluctuation measurement test rig in Figure 4.10 were the same as the ECT measurement used in Figure 4.2, such as the air distributor, plenum, flow meter, compressed air cylinder, etc.

Prior to data recording, leakage tests must be done. The same soap bubble approach was utilized to detect any leakage points or surfaces. Unlike the process in ECT measurements, leakage tests in pressure fluctuation measurements are more vital as any tiny leakage would corrupt the recorded pressure data. The main testing areas are the joints between the pressure probes and the bed pipe wall, between pressure probes and pressure transducers.

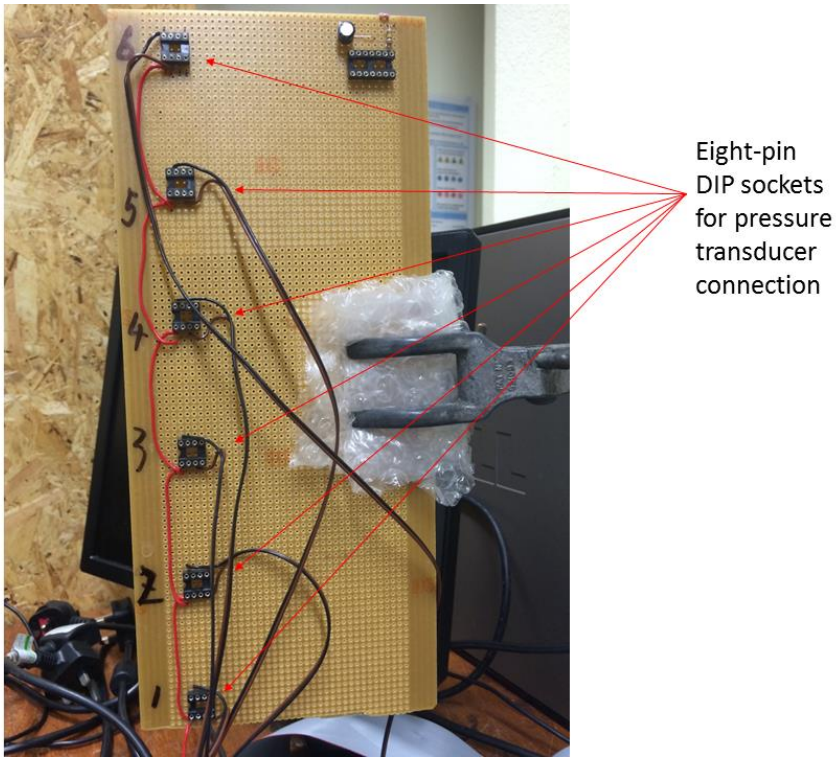

Figure 4.14: PCB board for pressure transducer connections.

4.2.5 Main operating conditions and operating procedures

According to the aforementioned, all the aspects of the pressure fluctuation measurement test rig, the main operating conditions and operating procedures are summarized in Table 4.2:

Table 4.2: Pressure fluctuation measurements operating conditions

Parameters	**Specific Conditions**
Static bed height	170 mm
Particle type	Group B with mean diameter of 276 microns and density of 2650 kg/m^3
Pressure ports used	Six in total cf. Figure 4.12
Fluidized bed	59 mm ID, 3 mm thickness, 1 m long
Pressure transducers	2 of PX72-0.3GV, 3 of PX72-0.8GV and 1 of PX72-1.5GV; Operating voltage: 10 V.
Pressure probes	2.6 mm diameter, 1 cm long, made of acrylic
Sampling rate and duration	200 Hz, 80 seconds

Main operating procedures:

1) Assemble all the necessary parts including fluidized bed pipe, air distributor, flanges; connect the Daq card between host PC and the PCB board; check the horizontal degree using a spirit level.
2) Install pressure transducers, connect them individually with the PCB board via multi-core cables.
3) Load silica sand to a height of 170 mm.
4) Finalize the assemblage; release the needle valve to introduce air; start recording using the provided data acquisition software.
5) Increase the superifical velocity gradually once the previous data was recorded for 80 seconds.
6) Repeate step 5 until all the desired operating conditions have been completed.
7) Stop air supply; dissemble the test rig; dismount all the pressure transducers; discharge silica sand and clean the fluidized bed pipe.

4.3 Experimental setup for plastic ball calibration

4.3.1 Overview

Five plastic balls have been introduced in Chapter 3 and the numerical simulation of the plastic ball wall effect on the simulated capacitance values has been carried out as well. The conclusion was that the plastic ball wall would have very limited influence on the measured capacitance values. In the present section, the experimental setup for plastic ball calibration will be introduced, which involves the arrangements of the suspension of the plastic ball in the bench-scale fluidized bed and plastic ball measurement positions.

4.3.2 Arrangement of the plastic balls

Taking the sensitivity map of the ECT system as mentioned in review section 2.8.2 into account, it is needful to consider the location of the plastic balls when conducting the calibration process as the ECT sensor is sensitive in a different way for the permittivity change at different locations. In the present study, two typical locations were considered namely, near centre and near corner of the fluidized bed pipe cross section. Each plastic ball was imaged at both locations. Figure 4.15 shows an image of when a plastic ball of No.5 was placed near the wall of the bed pipe.

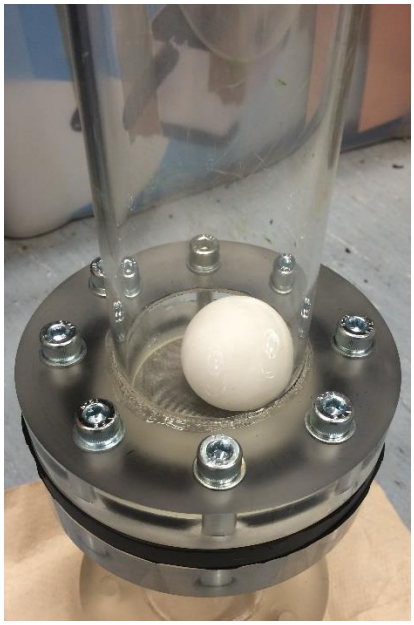

Figure 4.15: Image of a plastic ball placed near the wall of the bed pipe.

In the plastic ball calibration process, in order to image the plastic balls when they occupied most of the sensor volume, the balls were pierced through the

central lines by a piece of very thin fishing line (5LB, 0.20 mm) and the line was knotted at both ends of the plastic balls to ensure the balls were attached to the fishing line properly [178]. For the purpose of moving the plastic balls freely, the fishing line goes through an ‘anchor’ which was modified from an M3 screw with a pierced ‘cap’ and was tapped into the PVC air distributor. Therefore, by holding both ends of the fishing line, the plastic balls can be moved freely up and down so that an image of the moment when the balls take the most of the sensor volume as indicated in Figure 3.6 can be captured by the ECT system.

4.4 Summary

This chapter deals mainly with three issues, which are the ECT experimental test rig, experimental rig of pressure fluctuation measurements and experimental setup for plastic ball calibration.

In the section covering the experimental set-up for ECT measurements, a general description of the ECT experimental rig, which is composed of two sub-sections namely, the fluidized bed system and the ECT measurement system, was given. Then, a detailed description of the ECT measurement system followed where the capacitance measurement unit (CMU) together with the associated operating software were introduced in a comprehensive fashion. A graph of silica sand size distribution which was obtained by means of the Mastersizer 2000 instrument was described. Following that, the feature of the air distributor and some auxiliary components in the experimental rig were outlined. Some main operating conditions and a simplified operating procedure were given.

As for the experimental set-up for pressure fluctuation measurement, an overall layout of the whole rig was described first. Subsequently, the characteristic of pressure transducers and the data acquisition system were presented. A schematic description of the design and spatial distribution of the pressure probes were described. Some essential auxiliary components which facilitate the pressure fluctuation measurement were also mentioned. After that, the main operating conditions and operating procedures were summarized.

Last, experimental setup for the plastic ball calibration process was introduced, which includes the arrangement of the plastic ball measurement locations and the plastic ball suspension approach.

Chapter 5 Determination of minimum fluidization velocity and minimum slugging velocity

5.1 Overview

The state of incipient fluidization is one of the main features of a fluidized bed and the minimum fluidization velocity provides the pivotal information that is needed in designing and developing a variety of fluidization reactors [180]. Additionally, as the bubbling regime is the major focal bed state of the present study, it is needful to demarcate the lower boundary of the bubbling regime (with the incipient fluidization) and the upper boundary (with slugging regime), which will be discussed in section 5.2 and 5.3, respectively.

In the following sections, estimation of the minimum fluidization velocity estimation and the minimum slugging velocity via different approaches (some of which have been reviewed and mentioned in Chapter 2), will be presented. The performance of these approaches will be summarized and evaluated by comparing the results derived from the results obtained from existing empirical correlations.

5.2. Determination of minimum fluidization velocity (U_{mf})

The most fundamental theoretical approach for identifying the minimum fluidization velocity is the one solving Equations (2.8-2.10). However, there is a need to know the bed voidage, ε, at minimum fluidization. The voidage is inevitably dependent of particle size, particle distribution and particle shape, which are not easy to measure. Practically, measurements of pressure drop across the bed were regarded as the most simple and reliable approach to perceive the minimum fluidization velocity [180-183]. There are some other statistical methods developed in measuring the minimum fluidization velocity. Therefore, the primary aim of this section is to identify the value of minimum fluidization velocity by means of the ECT and pressure fluctuation measurements and to evaluate the performance of them.

5.2.1 Pressure drop

Pressure drop data in the bed were obtained by averaging the pressure fluctuation signal in the sampling time interval of 80 seconds. The minimum fluidization velocity was estimated using the plot of bed pressure drop versus

the gas superficial velocity which is presented in Figure 5.1. The main process can be generally described as follows.

The bed was firstly fluidized forcefully by increasing the gas superficial velocity. Then, the gas superficial velocity was decreased gradually and the corresponding pressure drop across the bed at different vertical heights was recorded. The minimum fluidization velocity was then determined at the point where two fitted curves (one is the sloping fixed bed pressure drop line versus gas superficial velocity and the other is the nearly horizontal fluidized bed pressure drop line versus gas superficial velocity) were intercepted.

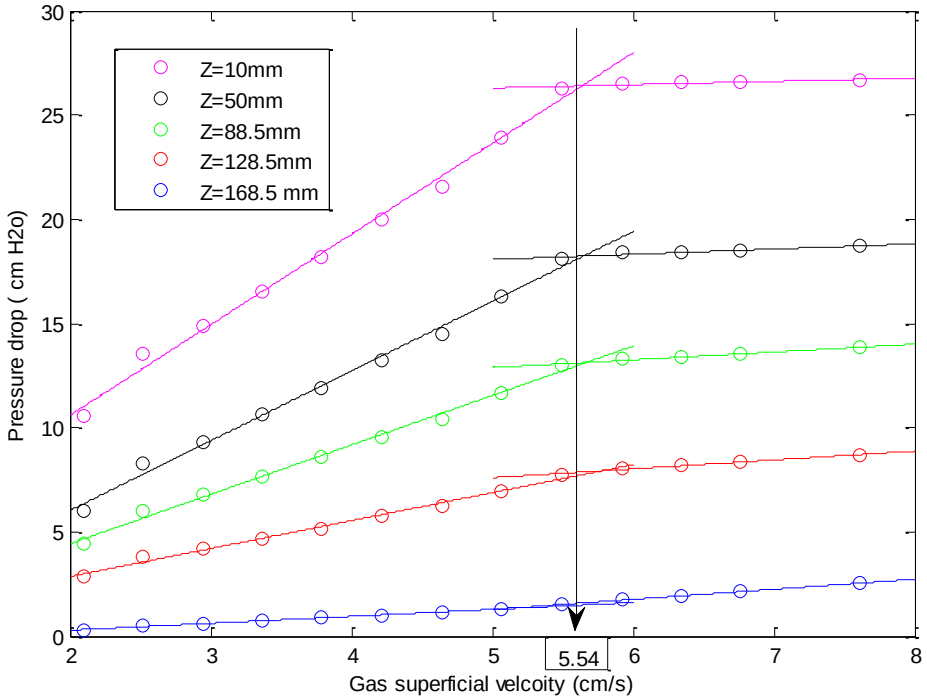

Figure 5.1: Pressure drop against gas superficial velocity at different bed heights.

By observing Figure 5.1, the pressure drop shows a logical pressure drop gradient where lower height has higher pressure drop due to more solid particles above that point. The estimated minimum fluidization velocities have good agreement at five different locations (as described in Figure 4.13), measurements above the air distributor, viz, Z=10 mm, Z=50 mm, Z=88.5 mm, Z=128.5 mm and Z=168.5 mm. When the superficial velocity was higher, the pressure drop across the bed was nearly horizontal, indicating the bed was fully fluidized. When the gas superficial velocity was decreased gradually after the minimum fluidization velocity, the pressure drop fell quickly in an almost linear curve, as shown in Figure 5.1. The estimated minimum fluidization velocity values for the five different heights vertically upwards are 5.64 cm/s, 5.65 cm/s, 5.67 cm/s, 5.78 cm/s and 4.99 cm/s, respectively. Except the one

at Z=168.5 cm height, all the other four locations had very similar results. This phenomenon may be attributed to the fact that the location is too close to the fixed bed surface of the bed (170 mm) and the pressure drop may not be so obviously detected or the pressure drop may have no manifest difference with varied gas superficial velocity with limited bed expansion height at relatively low gas superficial velocities. The value of the averaged minimum fluidization velocity from these five different heights is estimated at 5.54 cm/s which is marked on the X-axis.

It is worth noting that the pressure drop versus gas superficial velocity measured at plenum position was plotted in Figure 5.2 to attempt to estimate the minimum fluidization velocity. The pressure drop at the plenum location was measured simultaneously by the pressure transducer and by the U-shaped water monometer in the pressure experiments. As indicated by the raw results, the readings from both methods fitted well. To avoid repeating data presentation, only measurements obtained via the pressure transducer are shown in Figure 5.2. The data points are marked by the magenta colour in Figure 5.2 and the fitted curves (sloping fixed bed pressure drop line and horizontal fluidized bed pressure drop) have a similar trend as the other five positons shown in Figure 5.1. The pressure drop values are much higher than the five different positions above the air distributor due to the pressure difference caused by the introduction of the air distributor. It was found that the interception point of the two fitted curves at the plenum position has a comparable value, 5.62 cm/s, with the ones discovered in Figure 5.1. The error between the value estimated from the plenum position and the averaged value from five in-bed positions was calculated as 1.4%. Since the measured gas superficial velocity is in two decimal digits, one decimal digit would be sufficient for the error percentage expression as more decimal digits could not bring more accuracy in practical measurements or even are not measureable.

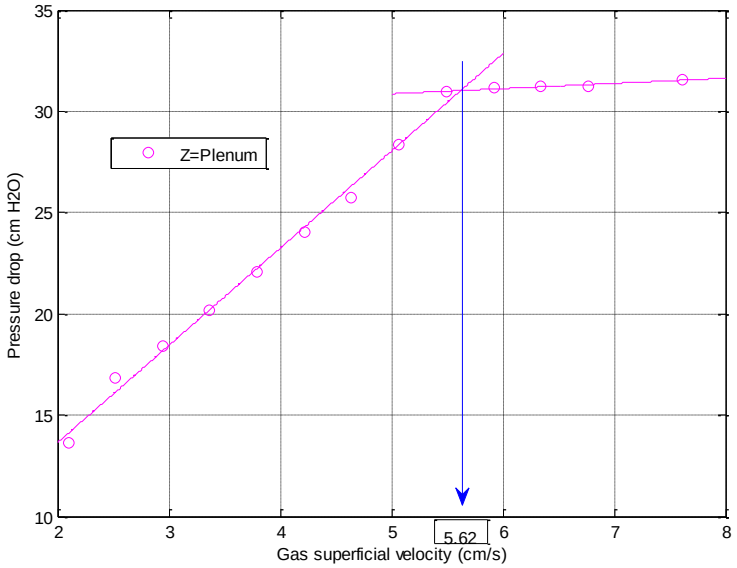

Figure 5.2: Pressure drop against gas superficial velocity at the plenum position.

It demonstrates that the data of pressure drop versus superficial velocity from the plenum position displays a consistent result as indicated by the pressure drop versus superficial velocity at the other five locations. It hints that the minimum fluidization velocity can be determined directly from pressure measurement in the plenum position which is much more convenient and effective, especially in industrial operating plants. Because it will significantly avoid any possibility of particle blockage and of contamination via abrasion on the pressure sensors, which could not fundamentally take place in the plenum location measurement. The results found here concur with the findings from Makkawi and Wright [16] although they assumed a sudden sharp decrease in the pressure drop when decreasing the gas superficial velocity as an indication of the transition from bubbling to fixed bed because in their experimental experience, the sloping and flattening in the pressure drop curve could not be achieved.

Due to the reliability of this method for predicting minimum fluidization velocity, the averaged value, 5.54 cm/s, from the measurements at the five different heights above the air distributor will be taken as the reference value against other values which are to be estimated by other approaches which will be discussed in the following sections.

5.2.2 Standard deviation of pressure fluctuation

As reviewed in Chapter 2, standard deviation is one of the most essential time domain parameters in describing bubble behaviour by means of pressure

fluctuation measurements. The definition of it is given below [48]. The amplitude of the signal, x, is expressed by the standard deviation (square root of second-order statistical moment):

$$\sigma = \sqrt{\frac{1}{N-1}\sum_{n-1}^{N}(X(n) - \overline{x})^2} \qquad (5.1)$$

with the average $\overline{x}$,

$$\overline{x} = \frac{1}{N}\sum_{n=1}^{N} x(n) \qquad (5.2)$$

Standard deviation has been regarded as one of the effective approaches to estimate the minimum fluidization velocity [183, 184].

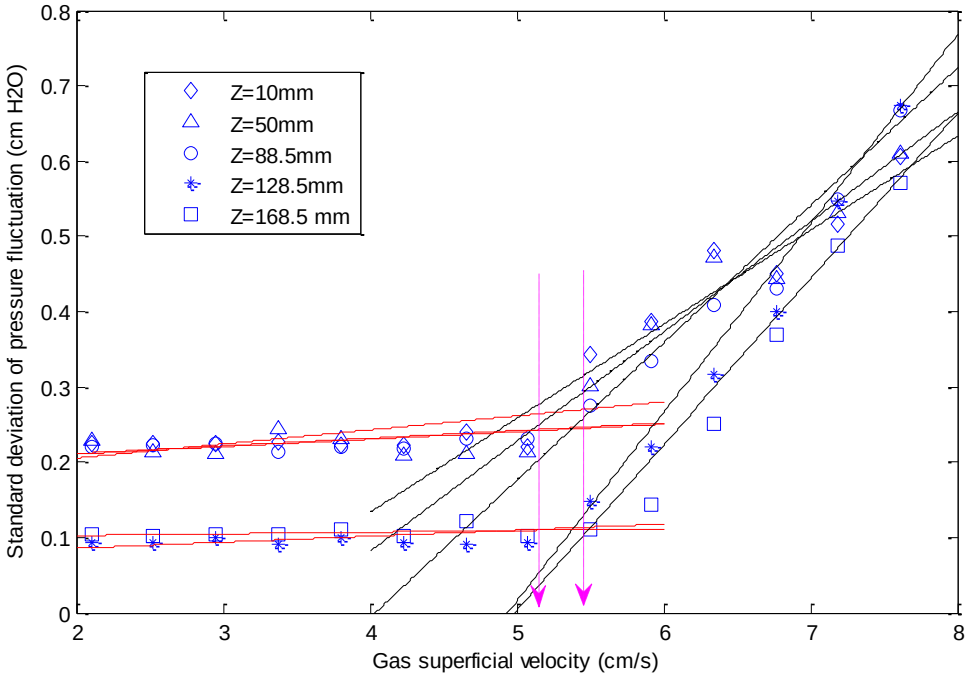

Figure 5.3: Standard deviation of pressure fluctuation at different in-bed locations at various gas superficial velocities.

Standard deviation of pressure fluctuation at the five different locations above the distributor is plotted in Figure 5.3 against various gas superficial velocities. The fitted curves according to the data points before and after the onset of bubbling regime are drawn in the figure. Normally, the interception points between the X-axis and fitted curve under bubbling regime are regarded as the onset point of the minimum fluidization as indicated by some previous researchers [185] [183, 184].

However, with the current experimental results, if those points were taken as the minimum fluidization velocity, the values would be much underestimated. As indicated in Figure 5.3, the interception points between the X-axis and fitted

curve under bubbling regime would be mostly less than 4 cm/s giving a very high relative error of 27.8% compared with a value of 5.54 cm/s which was estimated using the pressure drop approach. Therefore, in the present study, the interception points between two fitted curves (flat curve under fixed bed and sloping line under bubbling regime) are taken as the points where minimum fluidization velocity occurred. The reason behind this may be explained by the fact that the pressure fluctuation data under the fixed bed state must be taken into account when identifying the minimum fluidization velocity using data under bubbling regime. Otherwise, the information loss may result in the underestimation of the onset point of the minimum fluidization state. Accordingly, the calculated minimum fluidization velocity from these five different heights above the gas distributor are 5.03 cm/s, 5.11 cm/s, 5.37 cm/s, 5.39 cm/s and 5.49 cm/s, respectively. The corresponding averaged value of them is 5.28 cm/s which gives a relative error of 4.6% compared with the reference value of 5.54 obtained from the pressure drop approach.

By looking at the five values obtained from five corresponding measurement locations, it can be found that the value of 5.03 cm/s, which is estimated at Z=10 mm, gives the highest error compared with the reference value of 5.54 cm/s, which agrees well with the conclusion drawn by Hong et al.[185] that the measuring height of pressure fluctuation should not be too close to the gas distributor in order to get reliable results. Comparatively, the results derived from higher positions, such as Z=128.5 and Z=168.5, give much smaller errors, 2.7 % and 0.9 %, respectively.

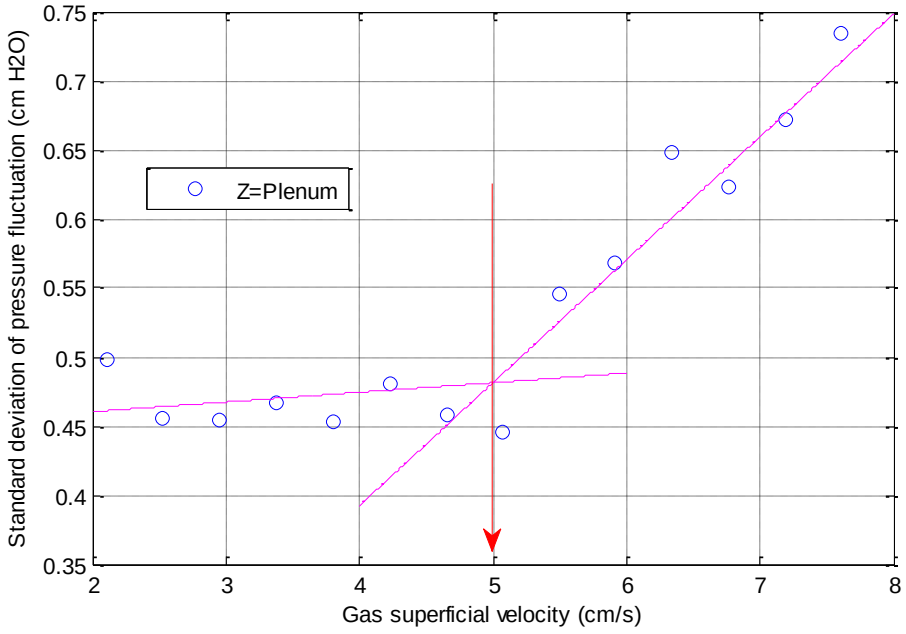

Figure 5.4: Standard deviation of pressure fluctuation at the plenum position at various gas superficial velocities.

Similarly, in order to seek the performance of the standard deviation of pressure fluctuation measured at the plenum position in predicting minimum fluidization velocity, the original data points and the corresponding fitted curves are presented in Figure 5.4. It can be observed that the absolute standard deviation values are much larger than the ones shown in Figure 5.3 owing to the higher absolute pressure drop within the plenum position. Furthermore, the estimated minimum fluidization velocity was obtained at 5.0 cm/s using the same method as utilized in Figure 5.3. The relative error between this value and the values estimated from standard deviation of pressure fluctuation measured at five different heights above the air distributor is 5.3%. The relative error between this value and the one obtained from the pressure drop approach is 9.7%. It reveals that the pressure fluctuation measurement at the plenum position can be used to determine the minimum fluidization velocity as the pressure fluctuation measurements at five different heights above the gas distributor do. The advantage of it has been demonstrated in section 5.2.1.

It is clear that the standard deviation of pressure fluctuation can be used to estimate the minimum fluidization velocity within a limited error range compared with results achieved from the pressure drop approach. Moreover, unlike the pressure drop approach, this method avoids the need to de-fluidize the bed by decreasing the gas superficial velocity from a vigorous fluidization state. Hence, without disrupting the process of the operational bubbling fluidized beds, the minimum fluidization velocity can be found just by changing the gas superficial velocity given that the pressure fluctuation signal is properly recorded. This approach would be much more useful and effective in industrial applications where continuous operations are much desired, with consideration of the financial cost and operating productive efficiency. Moreover, the pressure fluctuation measurement at the plenum positon gave an advantage of significantly preventing potential pressure sensor clogging and erosion brought about by the reaction between the solid particles and gas phase in some specific chemical reactors.

5.2.3 Standard deviation of ECT volume fraction

Utilizing the standard deviation of pressure fluctuation to predict the minimum fluidization velocity is quite a simple and reliable method, which could be much favoured in industrial applications due to its merit as described in the previous section. The ECT system has quite a high sampling rate, for example, 200 fps in the present study. The time series data captured via the ECT system also

exhibited similar fluctuation characteristics. This section is endeavouring to examine the performance of the standard deviation of ECT volume fraction in predicting the minimum fluidization velocity.

The volume fraction can be defined as follows. As introduced in section 4.1.2, the ECT system is able to obtain images of the distribution of permittivity inside the customized ECT sensor for any arbitrary mixture of different dielectric materials. Regarding a two-phase mixture, such as air and silica sand in the present study, the distribution of the relative concentration of the two different materials can be derived from the fast captured ECT image data. As illustrated in Figure 4.4, the value of each effective pixel stands for the normalized permittivity value. This value is related to the fraction of the higher permittivity material (silica sand phase in this case) present at that specific pixel position. The volume fraction is defined as the percentage of the volume of the sensor occupied by the silica sand material. The volume of the sensor is the product of the cross-sectional area over the finite sensor length. It can be expressed in mathematical form as below [177].

$$\text{Volume fraction} = (1/\mathrm{M}) \sum_{i=1}^{\mathrm{M}} (P_{(i)}/P_k) \tag{5.3}$$

where M is the total number of effective pixels, $P_{(i)}$ is the value of the i th pixel, and P_k is the value of the i th pixel when the sensor is filled fully with silica sand (normally 1).

Accordingly, the standard deviation of the volume fraction measured at plane 1 and plane 2 are plotted in Figure 5.5 and Figure 5.6 respectively, in order to avoid the appearance of data superposition. By observing Figure 5.5, the standard deviation of the volume fraction experienced an obvious jump at the lower superficial velocities between 2 cm/s and 3 cm/s. This may be strongly related to the particle movements and re-arrangements of the position between particle and particle and between particle and gas phase with the introduction of the compressed air flow from the bottom of the bed. Afterwards, the standard deviation approached the X-axis as indicated in the Figure 5.5.

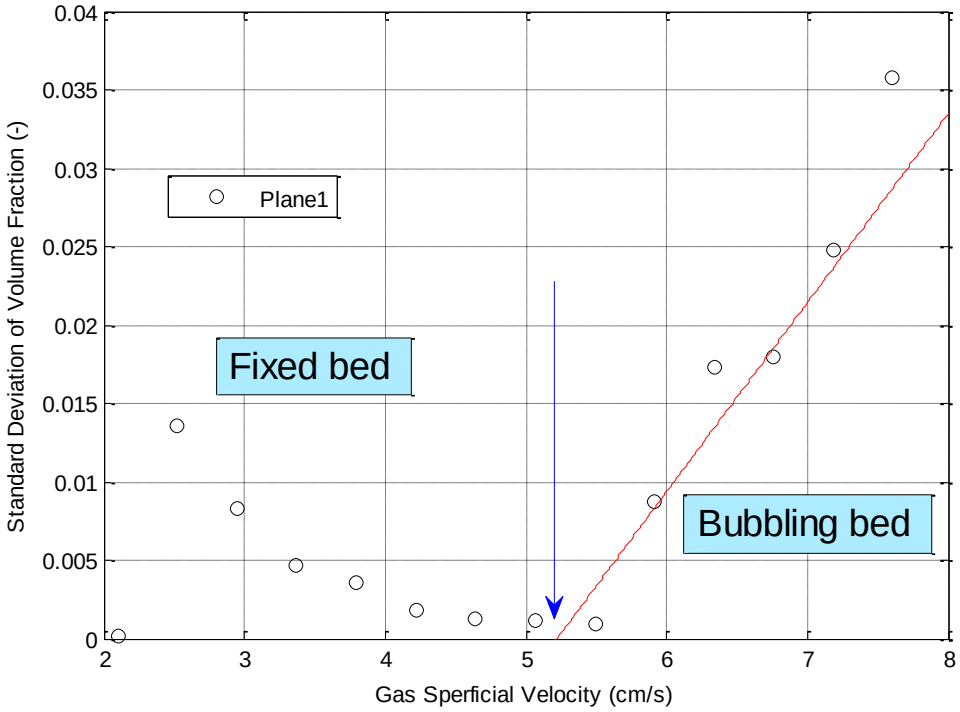

Figure 5.5: Standard deviation of averaged volume fraction measured at plane 1 location at various gas superficial velocities

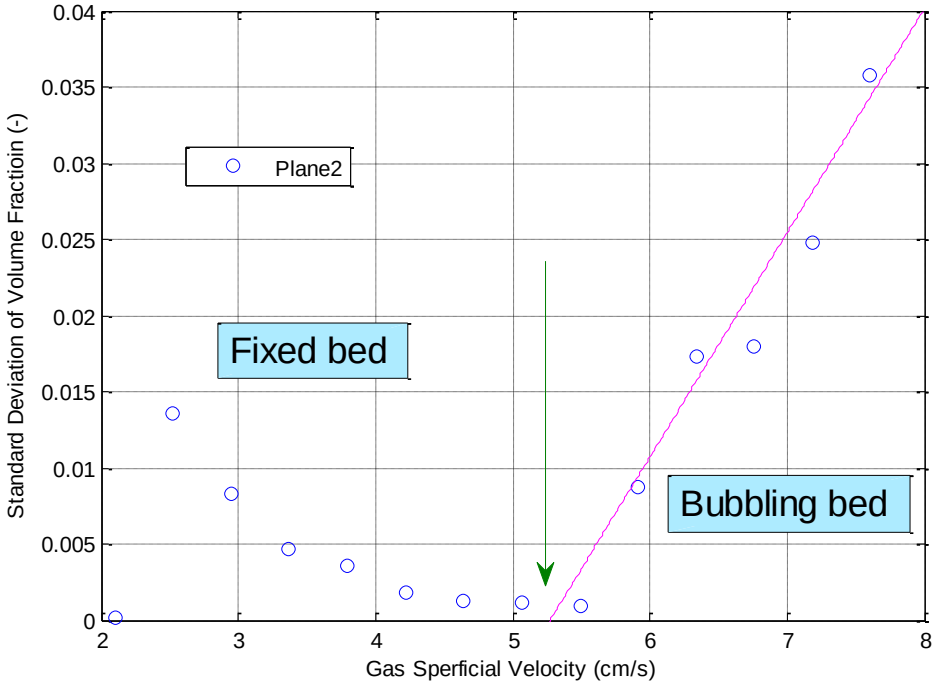

Figure 5.6: Standard deviation of averaged volume fraction measured at plane 2 location at various gas superficial velocities

The applicability of using ECT data to predict the minimum fluidization velocity has been demonstrated previously by Makkawi and Wright [16]. However,

they did not provide the information of the standard deviation of volume fraction in the fixed bed state. As shown in Figure 5.5, if the interception point between the X-axis and the fitted curve in bubbling regime is taken as the incipient of the minimum fluidization, the corresponding minimum fluidization velocity is 5.22 cm/s yielding a relative error at 5.8%.

Moreover, the two fitted lines at bubbling regime for both plane 1 and plane 2, shown in Figure 5.5 and Figure 5.6, respectively, have nearly the same line slopes of 0.012 and 0.014. Hence they are unlikely to coincide, which is in contrast with the findings of some authors [16]. In the present study, they are likely to be parallel instead of coinciding at the lower gas superficial velocities. In Figure 5.6, the gas superficial velocity of the interception point between the X-axis and the fitted curve at bubbling regime is 5.27 cm/s, giving a relative error of 4.9%.

Therefore, the standard deviation of the averaged volume fraction captured by the ECT system has been proved to be able to effectively predict the minimum fluidization velocity.

5.2.4 U_{mf} calculated by an empirical correlation

Over the last few decades, much attention have been devoted to bringing up empirical or semi-empirical correlations to estimate the minimum fluidization velocity as precisely as possible with the aim of preventing repeating tedious experimental work. The Equation (2.11) proposed by Wen and Yu [59] has been recognized as one of most extensively accepted empirical correlations. According to the empirical correlation, the calculated minimum fluidization velocity is 5.96 cm/s. All the physical properties used in Equation 2.11 are adopted from Table 4.1 and 4.2.

5.2.5 Summary of determined U_{mf}

As demonstrated in the previous sections, different fluidization velocity values have been obtained by means of different approaches, such as time averaged pressure drop, standard deviation of pressure fluctuation, standard deviation of ECT volume fraction and empirical correlation estimation. It is necessary to summarize and evaluate the performance of them. Hence, the summarized minimum fluidization velocity via different methods are shown in Table 5.1.

Table 5.1: Summary of determined U_{mf} via different approaches

No.	Approach used	U_{mf} (cm/s)	Error(%)
1	Pressure drop versus gas superficial velocity measured at five different heights above air distributor	5.54	/
2	Pressure drop versus gas superficial velocity measured at plenum position	5.62	1.4
3	Standard deviation of pressure fluctuation measured at five different heights above air distributor	5.28	4.6
4	Standard deviation of pressure fluctuation measured at plenum position	5.0	9.7
5	Standard deviation of averaged volume fraction measured by ECT at plane 1 level	5.22	5.8
6	Standard deviation of averaged volume fraction measured by ECT at plane 2 level	5.27	4.9
7	Empirical correlation [59]	5.96	7.6

It can be observed from Table 5.1 that all the results of the minimum fluidization velocity obtained from the seven different approaches gave relatively good agreement with each other. All the errors are calculated compared with the No.1 result. The biggest discrepancy lies in the result obtained from the standard deviation of pressure fluctuation measured at plenum position with a relative error percentage of 9.7% compared with the result obtained from pressure drop versus gas superficial velocity measured at five different heights above the air distributor. The result derived from the pressure drop versus gas superficial velocity measured at plenum position gives the best agreement with the No.1 result. Moreover, the results derived the standard deviation of averaged volume fraction measured by ECT at plane 1 level and plane 2 level give a quite good agreement. This consolidates the fact that the data captured from the ECT system is able to provide a fairly accurate estimation of the minimum fluidization velocity. It is somewhat surprising that the overall results of the minimum fluidization velocity estimated from the standard deviation of the ECT volume fraction data gave

a very good consistency compared with the ones obtained from the standard deviation of the pressure fluctuation results at different measurement heights.

5.3 Determination of minimum slugging velocity (Ums)

The minimum slugging velocity is one of the most crucial parameters in describing the onset of the slugging regime. In the present study, once the minimum fluidization velocity has been determined (discussed in the previous section 5.2), it is necessary to identify the minimum slugging velocity. The reason for doing this can be two-fold. On one hand, the ratio of the bed height to the bed diameter is about 2.89, which is noticeably larger than the precondition (normally 2, as introduced in section 2.4.3) for the existence of slugging regime. Considering the research emphasis of the present investigation is on characterizing bubble behaviour in bubbling regime, it is needful to demarcate the boundary between bubbling regime and slugging regime. On the other hand, there are several methods developed to predict the transition from bubbling regime to slugging regime. It is necessary and helpful to evaluate the performance of them for future reference.

In the following sections, the approaches of standard deviation of pressure fluctuation, standard deviation of ECT volume fraction, pseudo-3D image analysis and empirical correlation will be utilized to estimate the minimum slugging velocity.

5.3.1 Standard deviation of pressure fluctuation

Standard deviation of pressure fluctuation has been proved to reasonably predict the minimum fluidization velocity as described in the previous section 5.2. Further, the standard deviation of pressure fluctuation was often used to determine the transition velocity from bubbling regime to turbulent regime. It has been widely reported and acknowledged that the maximum point of the standard deviation of pressure fluctuation as a function of the gas superficial velocity implies the transition velocity (normally symbolized as U_c) [168]. There were only a very few studies reported in the open literature undertaking such work [186]. Hence, this section is seeking to find the applicability of using the same set of standard deviation of pressure fluctuations to estimate the minimum slugging velocity. Figure 5.7 presents the standard deviation of

pressure fluctuation measured at five vertical locations above the air distributor and plenum position as a function of the gas superficial velocity. The raw data is the same set of data as used in Figure 5.3, however, instead, Figure 5.7 plots the standard deviation in a wider range of the gas superficial velocity from 2 cm/s to nearly 13 cm/s.

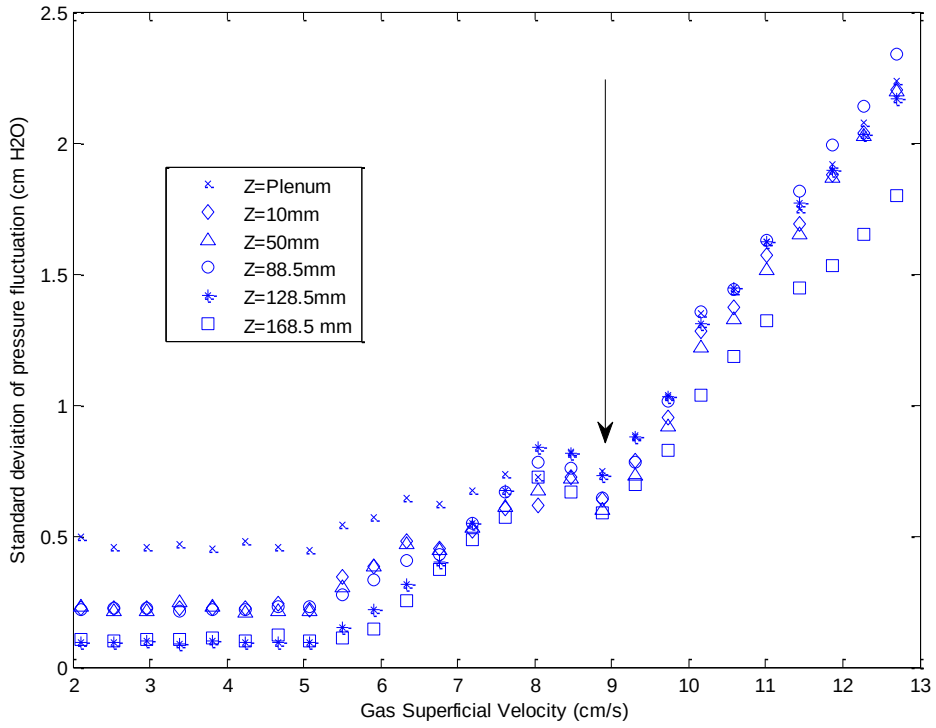

Figure 5.7: Standard deviation of pressure fluctuation measured at five vertical locations and plenum position at various gas superficial velocities.

Figure 5.7 reveals that there is a pronounced trend of increasing the standard deviation for all of the six measurements. In a closer look, this phenomenon can be described and unfolded in a multi-stage manner. Before the minimum fluidization velocity of 5.54 cm/s, which is already determined in section 5.2.1, the standard deviations in general are extremely small except the measurement at plenum position where perhaps the larger absolute pressure contributes. The bed is still in a fixed bed state at this stage. When the gas superficial velocity is larger than 5.54 cm/s, the standard deviation increased significantly in an almost linear fashion until the gas superficial velocity reached 13 cm/s. This is understandable as the bed has entered the fluidization state and it is worth noting that, at this stage, the standard deviation measured at plenum position is consistent with the ones measured at five different heights above the gas distributor.

However, during the process, it can be observed readily in Figure 5.7 that there is an obvious drop point of the standard deviation when the gas superficial velocity is at around 9 cm/s as marked by an arrow. Here, this point is defined as the onset of slugging regime and the corresponding gas superficial velocity of 8.89 cm/s is regarded as the minimum slugging velocity. Nevertheless, this finding is inconsistent with the conclusion drawn by Qiu et al. [186] where they just simply presented a figure of standard deviation with varied gas superficial velocity without any proper explanation. In Figure 5.7, the dramatic drop in the standard deviation at U_o = 8.89 cm/s could stem from the evolution of gas bubbles. When the bed is at bubbling regime, the bubble size increases gradually and the standard deviation of the pressure fluctuation increases accordingly. However, when the bed is approaching slugging regime, the bubbles are growing large enough to be converted to slugs. Although the size of bubbles is expanded, the increasing rate is probably decreasing due to the size of bubbles and slugs being constrained by the bed diameter (in the present case, 59 mm ID). Once the bed is in slugging regime, the slugs grow slightly in a limited space and the bed is approaching the turbulent flow regime where the bed is in a significantly chaotic state resulting in higher values of standard deviation of the pressure fluctuation.

To further investigate the performance of other approaches in predicting minimum slugging velocity in the following sections, the above value of the minimum slugging velocity obtained from standard deviation of pressure fluctuation measurements will act as a reference.

5.3.2 Standard deviation of ECT volume fraction

This section seeks to find the minimum slugging velocity by using the standard deviation of ECT data as the standard deviation of ECT volume fraction has already been evaluated to be able to estimate the minimum fluidization velocity as indicated in section 5.2.3. Figure 5.8 and Figure 5.9 present the standard deviation of the volume fraction at plane 1 level and plane 2 level, respectively. Being different as shown in Figure 5.5 and Figure 5.6, the data shown here were expanded to the gas superficial velocity up to 12 cm/s. By observing these two graphs, it can be seen that generally the standard deviation was increasing after the minimum fluidization velocity which is in line with the trend as discovered in the standard deviation of pressure fluctuation measurements as shown in Figure 5.7. However, after further observation, there is a tendency change around one point on the standard deviation data

evolution. In order to identify the incipient point of the slugging regime, the curve fitting effort was accomplished before and after that point. As suggested in Figure 5.8, the slopes of the fitted lines before and after the point (pointed by an arrow) are different with values of 0.014 and 0.016, respectively. Moreover, there is a steep increase in standard deviation before and after that point.

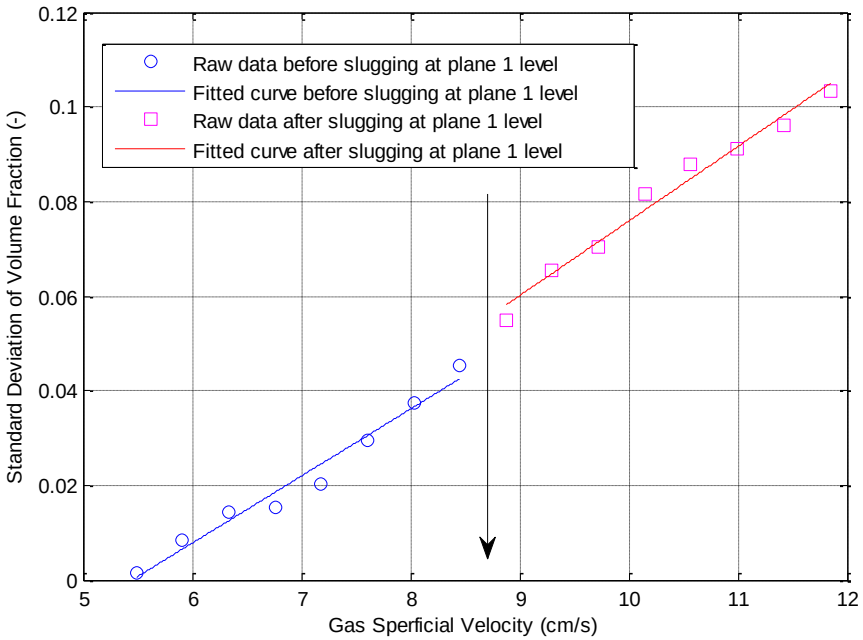

Figure 5.8: Standard deviation of averaged volume fraction measured at plane 1 location at various gas superficial velocities

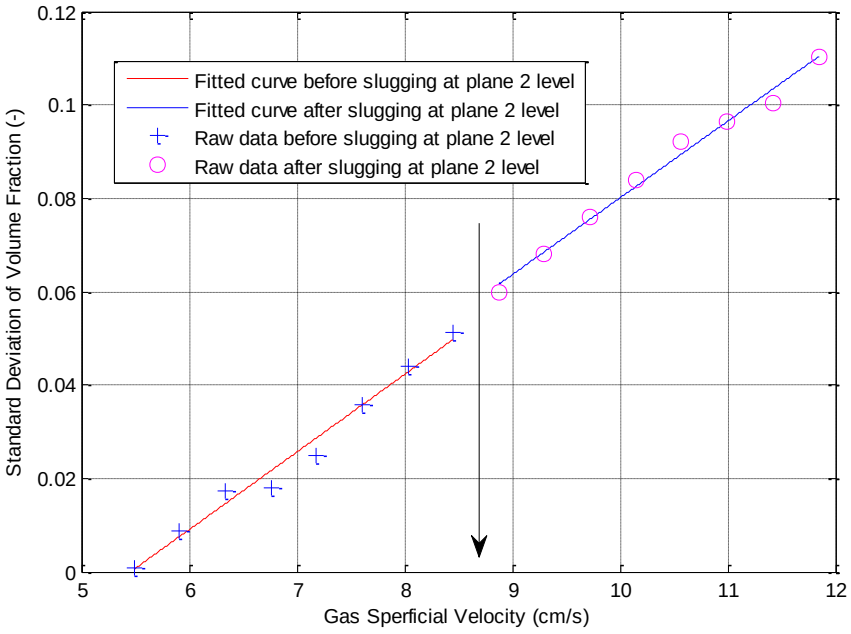

Figure 5.9: Standard deviation of averaged volume fraction measured at plane 2 location at various gas superficial velocities.

This combined information above indicates a regime change from bubbling regime to slugging regime. Therefore, the point is referred to as the starting point of slugging regime and the corresponding gas superficial velocity is defined as the minimum slugging velocity whose value was calculated at 8.66 cm/s. The relative error between this value and the one (8.89 cm/s) estimated by the standard deviation of pressure fluctuation is only 2.6%. The same trend can be recognized in Figure 5.9 for plane 2 level standard deviation data although the difference between the two fitted curves is not discernible as shown at the plane 1 level. The corresponding minimum slugging velocity is the same as predicted at the plane 1 level due to the fact that the same data capture protocol was conducted simultaneously for both ECT planes.

According to the above discussion, a conclusion can be drawn here that the standard deviation of the averaged volume fraction captured from ECT measurements can not only effectively predict the minimum fluidization velocity but also estimate the minimum slugging velocity.

5.3.3 Pseudo-3D ECT image analysis

In the ECT measuring system, the normalized permittivity values converted from the measured capacitance values are expressed in a 32 x 32 pixel format. One such typical image is presented in Figure 5.10 where two distinct phases are marked and a bubble appears near the corner of the bed when the gas superficial velocity is at 8.03 cm/s. However, the data can be rearranged in a pseudo-3D format to allow further analysis from the original data [14, 187]. If a number of such 2D image slices measured at a different time step but in the same location are stacked, the pseudo-3D image can be constructed. Figure 5.11 shows the reconstructed pseudo-3D images by using the central data set (where i=16, j=1,2,3,..,32 as indicated in Figure 5.11) when the gas superficial velocity ranges from 5.91 cm/s to 9.72 cm/s. The construction process was aided by MATLAB software. Results for both planes are presented under a specific gas superficial velocity.

The X-co-ordinate denotes relative radial position compared to the bed diameter. The Y-co-ordinate denotes time in seconds. There are 600 frames (which has an equivalent time interval of 3 seconds as the sampling rate is set at 200 fps) used in total for each operating condition. The physical fluid flow direction is from the bottom to the topside. The red colour in the images means the area is full of silica sand whilst the blue colour means the area is full of air and the green colour indicates the area is partly occupied by silica sand.

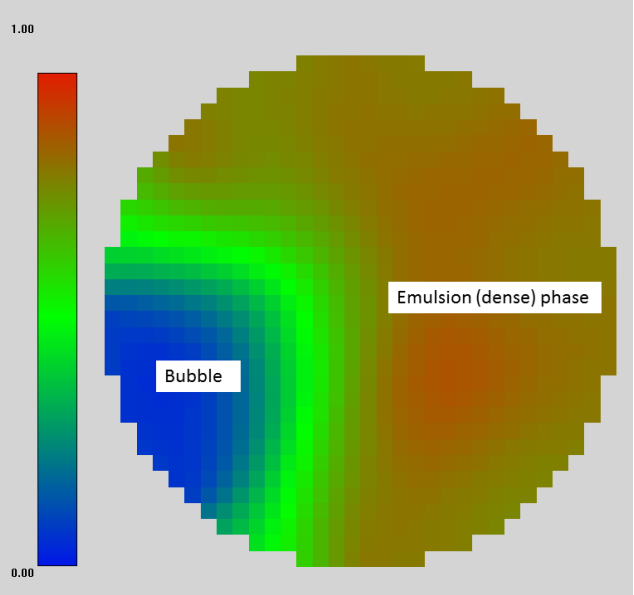

Figure 5.10: A typical two dimensional 32x32 ECT image.

This section attempts to detect the transition gas superficial velocity from bubbling regime to slugging regime. When the gas superficial velocity is at 5.91 cm/s, the size of bubbles which appeared was fairly small compared to the bed diameter. It is worth noting that the size of bubbles appearing at the plane 2 measurement position seemed smaller than the ones at plane1.

This phenomenon is probably caused by a situation where the bubbles changed radial locations slightly when they were travelling from the lower plane 1 to the upper plane 2. Moreover, when the time step is at about 2 seconds, a distinct bubble can be noticed in both planes. It is possible to identify the time lag while the bubble was travelling from plane 1 to plane 2 and therefore, the bubble rising velocity can be extracted via suitable techniques, such as cross correlation techniques, which will be introduced and discussed in more detail in Chapter 6.

With the increase of the gas superficial velocity from 5.91 cm/s to 8.03 cm/s, the size of bubbles increased gradually. At the same time, the number of bubbles increased as well, which can be evidenced by the image data presented at gas superficial velocities of 7.61 cm/s and 8.03 cm/s. Notwithstanding, the number of bubbles decreased slightly when the gas superficial velocity was at 8.45 cm/s and decreased significantly at 8.89 cm/s where the appearance of bubbles exhibited a characteristic of periodicity. This is in line with the findings from Liu et al. [39]. It was reported by them that the slugging regime occurred in a seemingly periodical manner and this phenomenon can be explained well by image data at plane 2 measurement level when superficial velocity is at 9.72 cm/s.

By focusing on the aspect of bubble size, the size of the bubbles when the gas superficial velocity is at 8.87 cm/s is comparable with the bed diameter especially the one which appeared at 1.5 seconds at the plane 2 measurement level. With further increase in the gas superficial velocity, the size of bubbles increases appreciably. For example, when the gas superficial velocity is at 9.30 cm/s, the bubble appeared at 0.5 seconds at plane 2 level having already grown into a slug which is actually a square-nosed slug as indicated in Figure 2.4 in section 2.4.3.

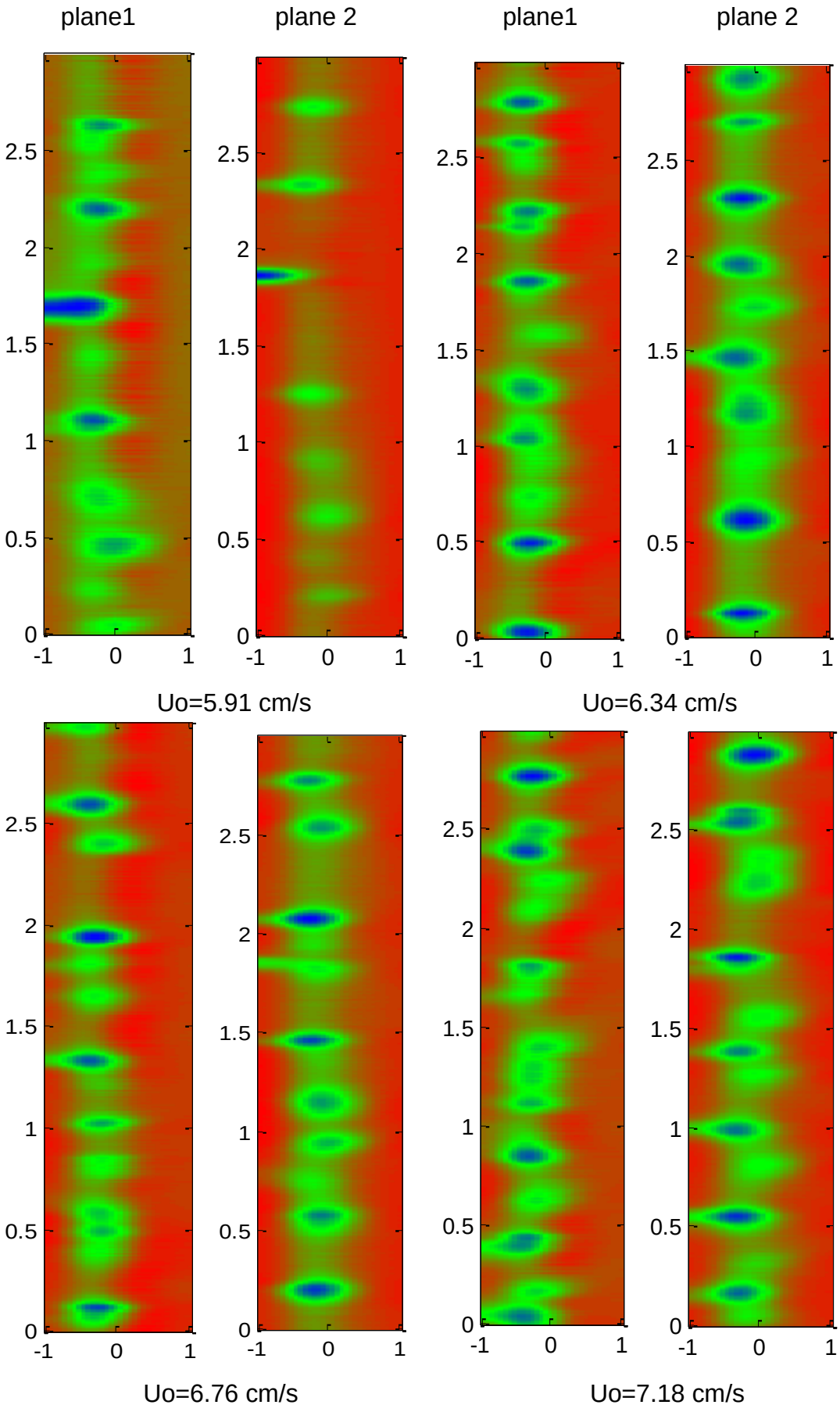

Figure 5.11: Pseudo-3D image analysis at various gas velocity (continued)

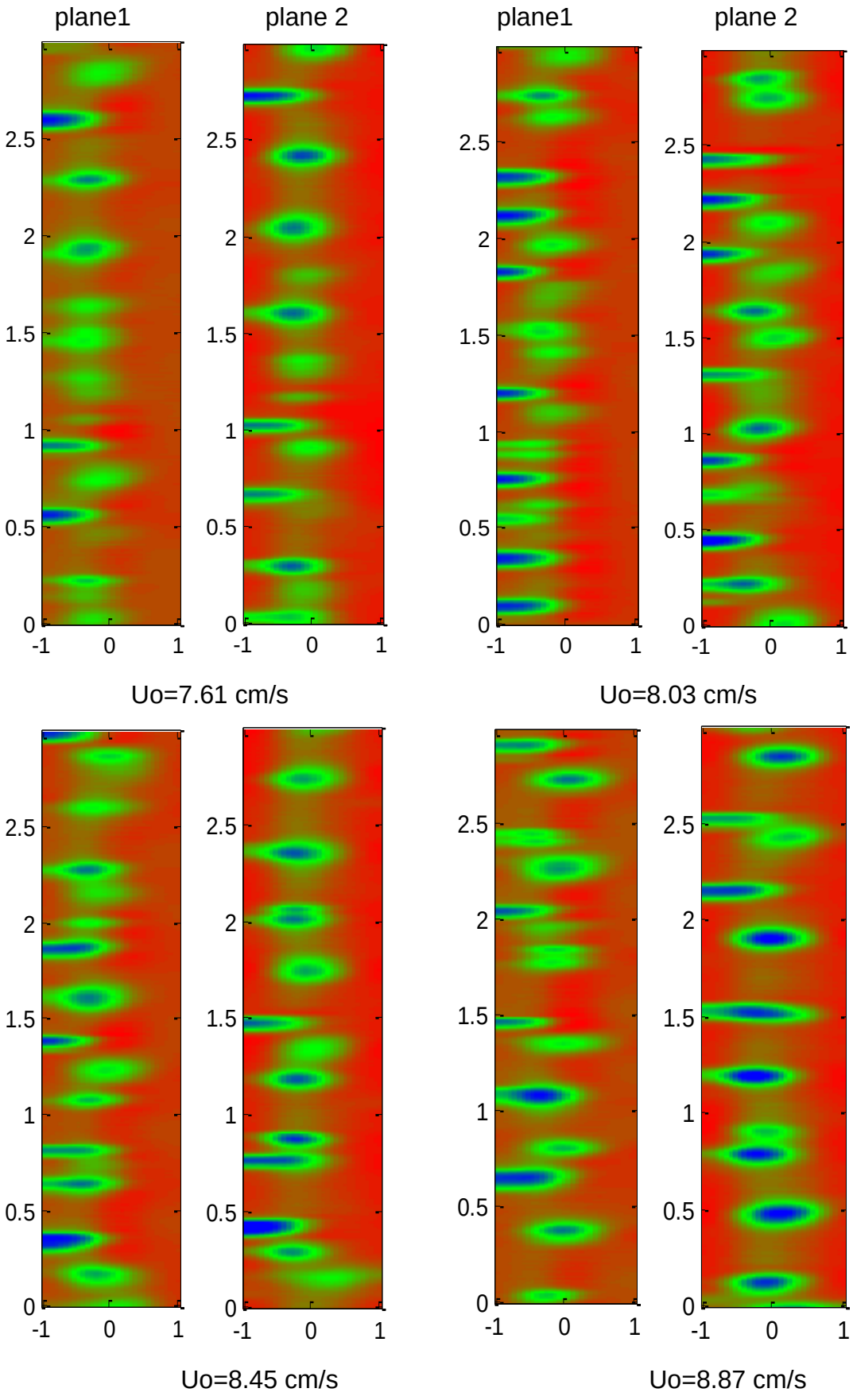

Figure 5.11: Pseudo-3D image analysis at various gas velocity (continued)

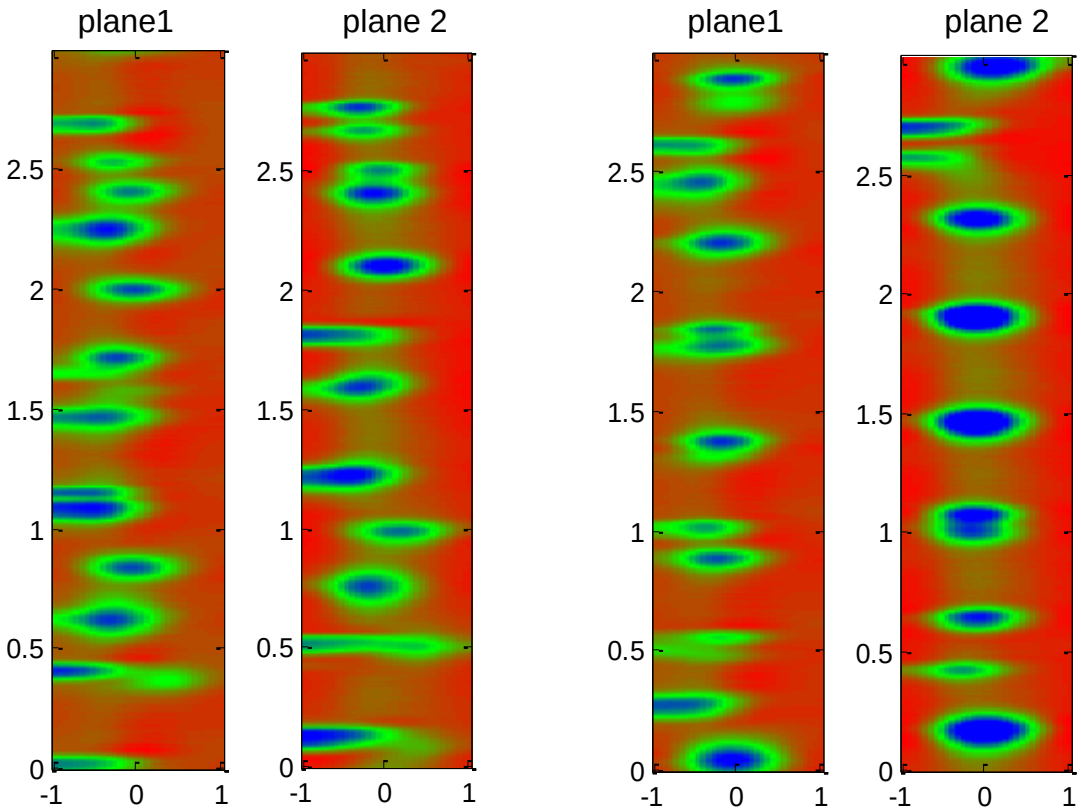

Figure 5.11: Pseudo-3D image analysis at various gas velocities

Consequently, considering all the above discussions, the onset of slugging regime is defined as the point when the gas superficial velocity is at 8.87 cm/s. The relative error of this value compared with the one predicted from the standard deviation of pressure fluctuation is only 0.2%. Actually, with further increase in gas superficial velocity, the size of slugs increased significantly which was evident when the gas superficial velocity was at 9.72 cm/s at plane 2 level. Therefore, the minimum slugging velocity discovered from the pseudo-3D ECT image analysis supports the findings from the standard deviation of pressure fluctuation.

5.3.4 Empirical correlation calculation

Numerous studies have been devoted to arrive at a suitable empirical correlation to estimate the minimum slugging velocity as precisely as possible. Stewart and Davidson [60] were one of the earliest investigators involved in such work. A correlation put forward by them has been accepted and referenced as a guideline in estimating the minimum slugging velocity though reasonable results sometimes can only be obtained in a very high ratio of bed

height to bed diameter via this correlation [188]. Nevertheless, the correlation agrees approximately with the data of several scholars in the open literature. The mathematical expression of the empirical correlation for estimating the minimum slugging fluidization velocity is as follows:

$$U_{ms} = U_{mf} + 0.07\sqrt{gD} \qquad (5.4)$$

where U_{mf} is the minimum fluidization velocity; g acceleration due to gravity; D diameter of the fluidized bed;

Accordingly, the calculated minimum slugging velocity is 10.82 cm/s. The corresponding relative error of this value compared with the one obtained from the standard deviation of pressure fluctuation is 17.8%. This value is fairly high compared with the previous relative errors as calculated by means of the standard deviation of ECT volume fraction and pseudo-3D ECT image analysis approaches. The large discrepancy may be linked to a circumstance that this correlation has no connections with some essential parameters in composing the bed operating conditions, such as particle size, size distribution and bed height as discussed by Baeyens and Geldart [189]. In spite of that, the results derived from the empirical correlation calculation can still be a reference for further investigation.

5.3.5 Summary of determined U_{ms}

Several different values of the estimated minimum slugging velocity have been obtained in the previous sections by virtue of various approaches, such as standard deviation of pressure fluctuation, standard deviation of ECT volume fraction data, pseudo-3D ECT image analysis and empirical correlation calculation. It is necessary and beneficial to carry out a summary and comparison of them to evaluate the performance of the different methods as conducted in section 5.3. Table 5.2 presents a summary of the determined minimum slugging velocity via different approaches.

Table 5.2: Summary of determined U_{ms} via different approaches

No.	Approach used	U_{ms} (cm/s)	Error(%)
1	Standard deviation of pressure fluctuation measured at five different heights above air distributor and plenum position	8.89	/
2	Standard deviation of averaged volume fraction measured by ECT at plane 1 level	8.66	2.6
3	Standard deviation of averaged volume fraction measured by ECT at plane 2 level	8.66	2.6
4	Pseudo-3D ECT image analysis	8.87	0.2
5	Empirical correlation [60]	10.82	17.8

It is surprising to find that the smallest relative error of the estimated minimum slugging velocity comes from the pseudo-3D ECT image analysis which is essentially a qualitative approach compared with others. At a moderate level, the results obtained from the standard deviation of the ECT volume fraction data from both ECT planes have magnificent agreement with the result estimated from the standard deviation of pressure fluctuation. As discussed in section 5.3.4, the result obtained from the empirical correlation calculation gives the largest deviation. A possible cause of this situation may emerge from the absence of several essential parameters in the empirical correlation.

5.4 Summary

This chapter deals mainly with two topics, which are the determination process of the minimum fluidization velocity and determination process of the minimum slugging velocity.

Different approaches have been utilized to estimate the minimum fluidization velocity due to the importance of it in defining the boundary between the fixed bed state and the bubbling regime. Four general methods were adapted which include the conventional and reliable approach of using pressure drop, the standard deviation of pressure fluctuation, the standard deviation of ECT

volume fraction and the empirical correlation calculation. The performance of these four different approaches were summarized and evaluated.

In order to estimate the minimum slugging velocity which is vital in distinguishing the threshold between bubbling regime and slugging regime, four methods namely, the standard deviation of pressure fluctuation, the standard deviation of ECT volume fraction, pseudo-3D ECT image analysis and the empirical correlation calculation, were applied. The performance of these methods was summarized and assessed and it revealed that the results derived from the standard deviation of averaged volume fraction measured by ECT at both planes can give a good prediction. Additionally, pseudo-3D ECT image analysis provides a quite convincing estimation though it is an inherently qualitative approach.

Chapter 6
ECT Measurement Results

6.1 Overview

Few writers have been able to draw on any systematic research into the determination process on the threshold (a cut-off value in ECT image pixel) of distinguishing bubble phase and emulsion phase in estimating bubble size in ECT measurement. Moreover, bubble rising velocity obtained from ECT measurement is still not fully understood on a pixel by pixel basis. Bubble behaviour in the spatial domain across a 32 x 32 ECT image has not been extensively studied.

Hence, this chapter aims to shed light on some of the essential aspects of bubbles in bubbling regime applying ECT measurements.

Specifically, this chapter is mainly concerned with three issues. The first one is presenting the reference cut-off values in determining bubble diameter by virtue of the plastic ball calibration process. Then, the bubble diameter in bubbling regime is estimated with two different image reconstruction algorithms at various gas superficial velocity under three different methods which include individual cut-off values, linear fitted curves and second-order fitted curves of original cut-off values. Lastly, bubble rising velocity study by means of four different approaches (including cross-correlation via averaged volume fraction, mathematical calculation analysis, cross-correlation via local pixel solid fraction and statistic average approach using original 32 x 32 images) will follow. The performance of these four different approaches will be evaluated.

6.2 Plastic ball calibration results

6.2.1 Overview

Figure 6.1 and Table 6.1 give an image for five different plastic balls made of polypropylene and their specific detailed information which includes internal and external diameter, weight, wall thickness and internal cross sectional area, respectively. The external diameter ranges from 10 mm to 40 mm, which were chosen by considering the laboratory-scale fluidized bed diameter (ID 59 mm).

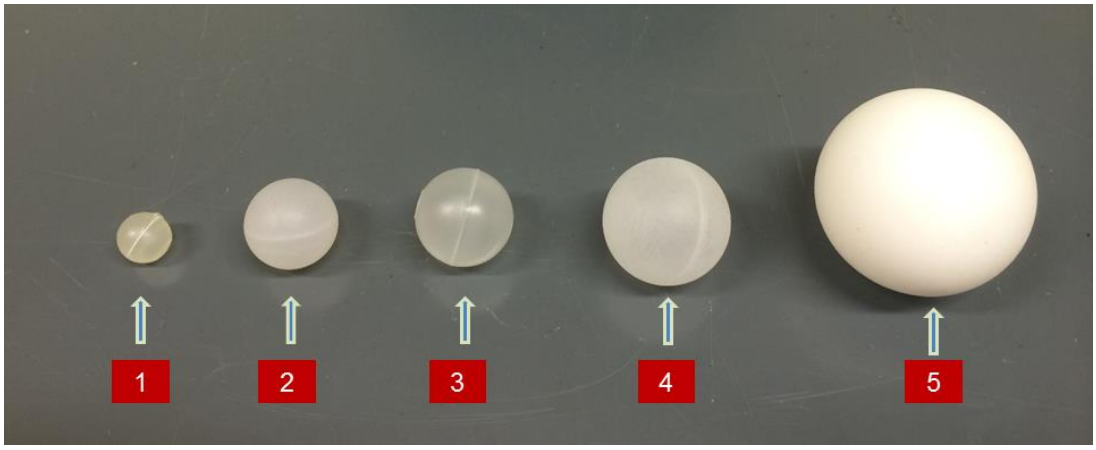

Figure 6.1: Image of five different plastic balls

Table 6.1: Specification of the five different plastic balls

No.	External Diameter (mm)	Weight (g)	Wall Thickness(mm)	Internal Hollow Diameter (mm)	Internal cross section area (mm2)
1	10	0.275	1.2	7.6	45.34
2	18.4	1.355	1.6	15.2	181.36
3	20	0.92	0.84	18.32	263.46
4	25.4	2.25	1.3	22.8	408.07
5	40	2.7	0.38	39.24	1208.72

The experimental setup of the plastic ball calibration has been introduced in Chapter 4 and the numerical simulation of the plastic ball wall effect on the simulated capacitance values between different measuring electrodes pairs has been carried out in Chapter 3. In the following section, the iterative step will be evaluated and chosen to reconstruct the original images from ECT measurements. After that, all the reference cut-off values derived from the plastic ball calibration process will be summarized in Table 6.1.

6.2.2 Determination of the image reconstruction algorithm

It has been reviewed and acknowledged that the linear back projection (LBP) algorithm has been developed and regarded as the simplest and most commonly used image reconstruction algorithm. The main advantages of this algorithm are that it has low computing demands and has fast response in the image reconstruction process. However, due to the nature of approximation as indicated in section 2.8.2, the images derived via this kind of method exhibit relatively low quality with regard to accuracy. The iterative LBP algorithm has

been recognized as an improved image reconstruction algorithm and it has the capability to produce images of better quality, for example, sharper boundaries between bubbles and the emulsion phase in the bubbling regime. The fundamental aspects of the iterative LBP algorithm has been reviewed in Chapter 2 and illustrated by McKeen and Pugsley [145] in a simpler manner. Therefore, the details of this information will not be repeated here again. However, the iterative step is still unknown in respect of obtaining the most appropriate ECT images. Hence, to investigate how many iteration steps need to be implemented to achieve fairly accurate and reliable ECT images, images which were produced via different iteration steps are presented in Figure 6.2. Additionally, the corresponding averaged volume fraction information is given below each image.

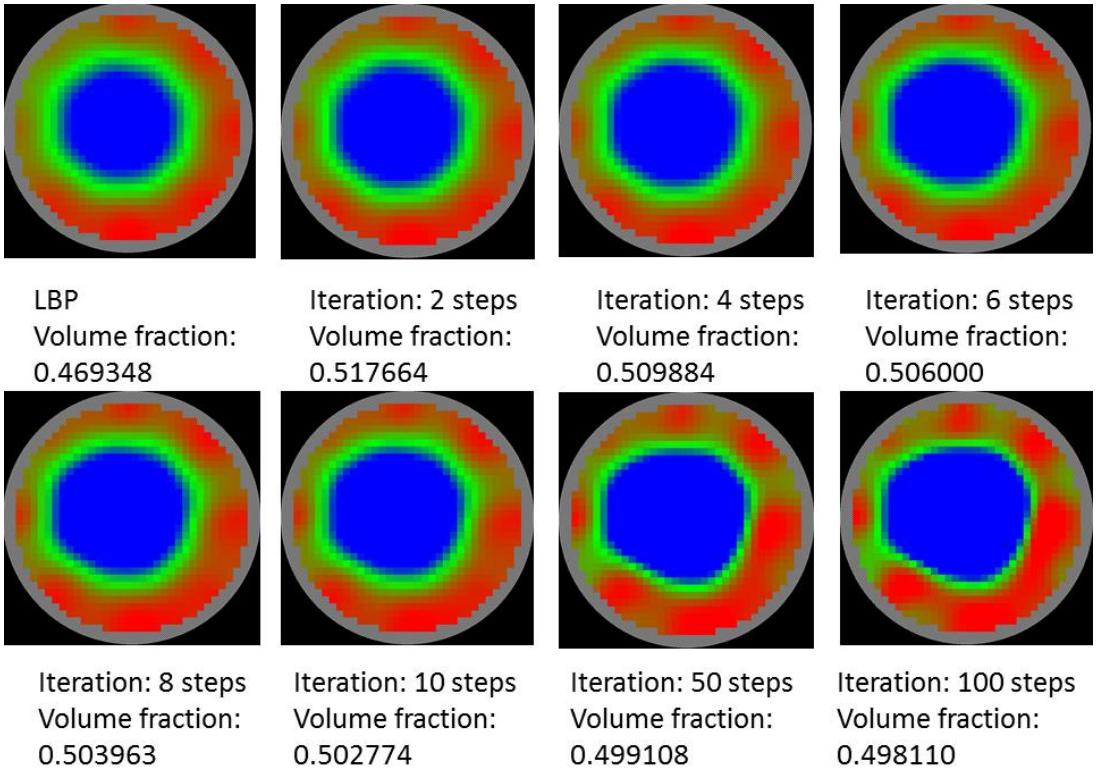

Figure 6.2: Images of a plastic ball for different iterative steps

All the images presented in Figure 6.2 are based on the 40 mm outer diameter plastic ball. It can be seen that the image produced by the LBP method has a very blurred boundary. With the increased iterative steps, the boundary between the internal hollow air area and the surrounding mixture of silica sand and air becomes sharper and sharper especially when the iteration step is at 100. Meanwhile, the volume fraction was first increased and then decreased slightly. Nevertheless, the iterative step cannot be increased without limitation. When the iterative is at 50 steps, the shape of the plastic ball is no longer and

the change rate of the volume fraction becomes insignificant. Therefore, by ensuring the boundary is sharp and the shape of the internal air area is not distorted too much, the images reconstructed by 10 step iteration will be chosen, analysed and compared with the results via the LBP method. The parallel permittivity model in the ECT system was chosen since it has been regarded as having good accuracy based on a phantom test [145].

6.2.3 Calibration Results

Once information of the location of the five different plastic balls and the image reconstruction algorithms have been determined, the next step is to extract the cut-off values based on the calibration process. The main procedure for deriving cut-off values is summarized in Figure 6.4.

Table 6.2: Cut-off value derived for five different plastic balls

Cut-off value derived from plastic balls						
No.	Outer Diameter (mm)	Internal Hollow Diameter (mm)	Near Centre		Near Wall	
			LBP	Iteration 10	LBP	Iteration 10
1	10	7.6	0.9394	0.9000	0.9200	0.9000
2	18.4	15.2	0.7700	0.7540	0.6999	0.6700
3	20	18.32	0.7687	0.7700	0.6646	0.6400
4	25.4	22.8	0.6300	0.6482	0.4948	0.4600
5	40	39.24	0.5835	0.5383	0.4441	0.4293

Initially, a 32 x 32 pixel image was obtained when a plastic ball occupied the biggest area of the ECT sensor [178]. The circular cross sectional area in the image has 812 effective pixels. The area is seen as the equivalent area of the internal area of the fluidized bed pipe (ID 59 mm). The ratio of the plastic ball hollow area to the fluidized bed internal area is calculated. Then, the corresponding pixel number which the plastic ball hollow area equivalently holds is calculated. After that, the number of pixels in the image was counted starting from the lowest grey level until the cumulative number of pixels equals the pixel number the plastic ball has. The largest value of these counted pixels is taken as the cut-off value for distinguishing the solid and air phases. This process is repeated for the five plastic balls at two locations. The derived cut-off values are summarized in the Table 6.2.

In order to examine the effectiveness of the ‘cutting-off’ process, two images when the No. 5 plastic ball was placed in the centre of the bed, generated under 10 iterative LBP method, are displayed in Figure 6.3. The first image shows the original image of the ball whilst the second image presents the processed image after the ‘cutting off’ process.

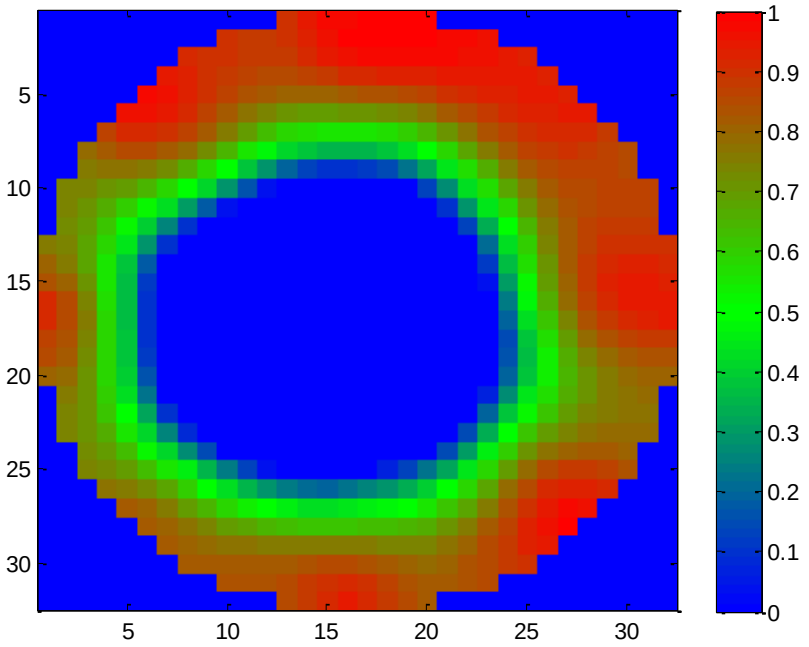

(a)

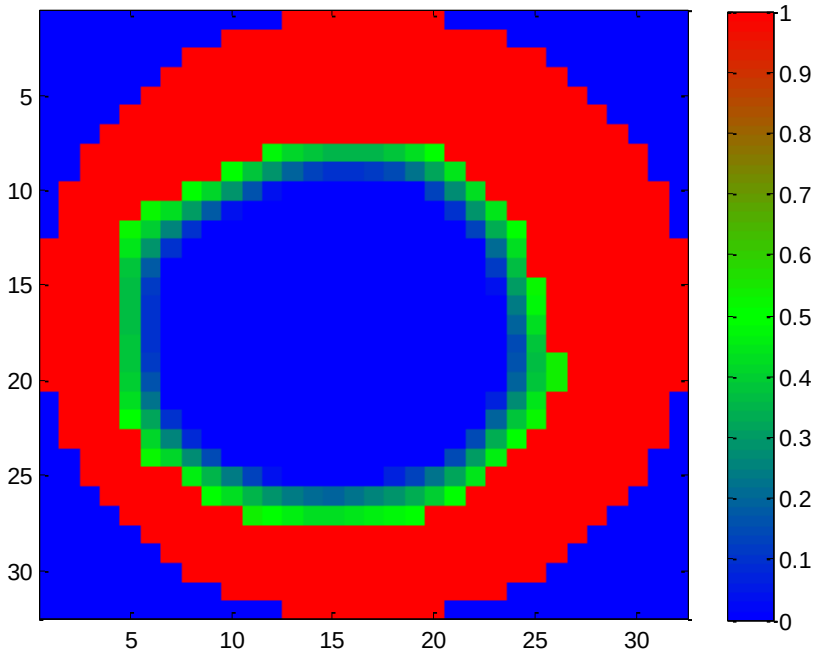

(b)

Figure 6.3: Images when the No. 5 plastic ball was placed near centre of the bed. (a) : before cutting-off and (b): after cutting-off process.

It can be found that these two images give generally the same pattern of the No. 5 plastic ball qualitatively. Moreover, the second image demonstrates a sharper boundary between plastic ball hollow area and the packed bed materials. This is attributed to a fact that all the pixels whose volume fraction value are less than the cut-off value are assigned as 0 (blue colour) whereas the ones whose volume fraction values are larger than the cut-off are set as 1(red colour). Moreover, during the process of deriving the cut-off of No.5 plastic ball near centre with 10 iterative LBP method, the pixel number difference is only 1 between the theoretical equivalent pixels numbers of the ball hollow area to the bed cross-sectional area and the calculated pixel numbers, which re-affirms the confidence of the derived cut-off value of 0.5383 as shown in Table 6.2.

6.3 Bubble size estimation results for LBP

With the derived cut-off values as shown in Table 6.2, the diameter of the real bubbles which are the bubbles experimentally appearing in fluidized beds can be estimated. The process of determining bubble diameter is summarized in Figure 6.4. It is somewhat a ‘reverse’ procedure of the process of deriving cut-offs. Firstly, a 32 x 32 image is acquired when a real bubble in the bubbling regime occupies most of the sensor volume. Then, add up the number of pixels whose grey level values are below a given cut-off value. Calculate the cross sectional area according to the ratio of the summed total pixel number for a real bubble to 812. The equivalent diameter of that area is taken as the real bubble’s diameter. This process is repeated 20 times as there are 20 cut-off values using different image reconstruction algorithms in different locations as shown in Table 6.2.

In this section, the bubble diameter is estimated under the LBP image reconstruction algorithm. Three different methods will be utilized as introduced in section 6.1.

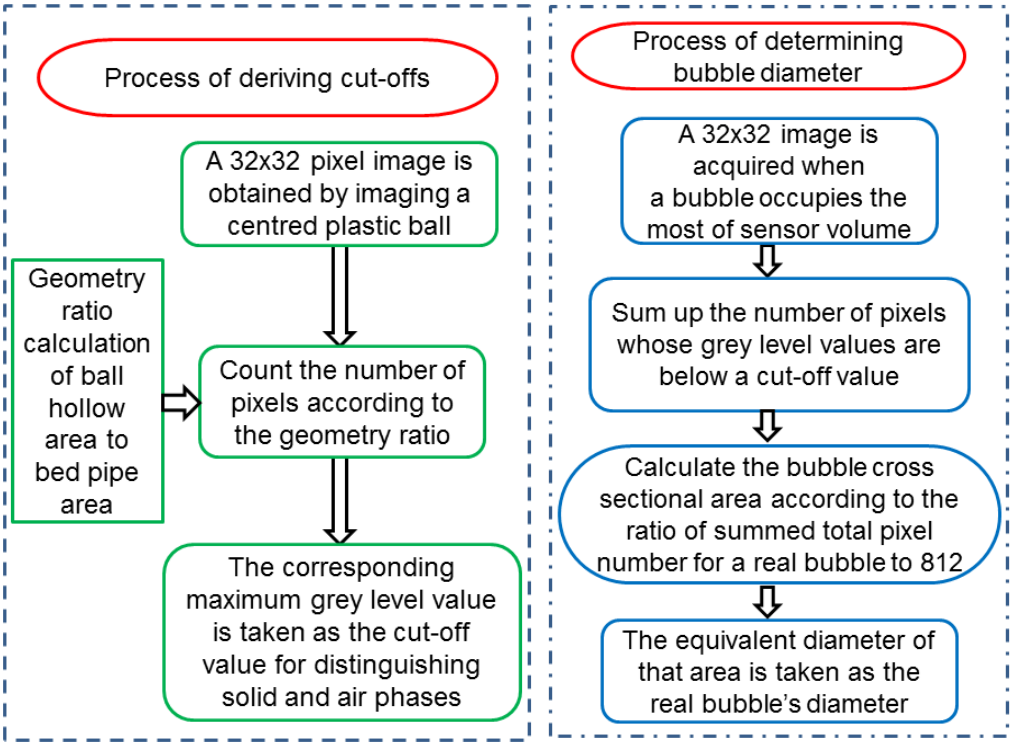

Figure 6.4: Flow charts for the process of deriving cut-off values and the process of determining bubble diameter.

6.3.1 Individual cut-off values method

The bubble diameters estimated by using individual cut-off values with LBP algorithms are compared with the results estimated by the five widely used empirical correlations which have already been summarized in Table 2.1. Figure 6.5 shows the comparison of results in which (a) represents the results obtained by the cut-off values near centre; (b) represents the results obtained by the cut-off values near wall. All the bubble diameters are measured at the ECT plane 1 level.

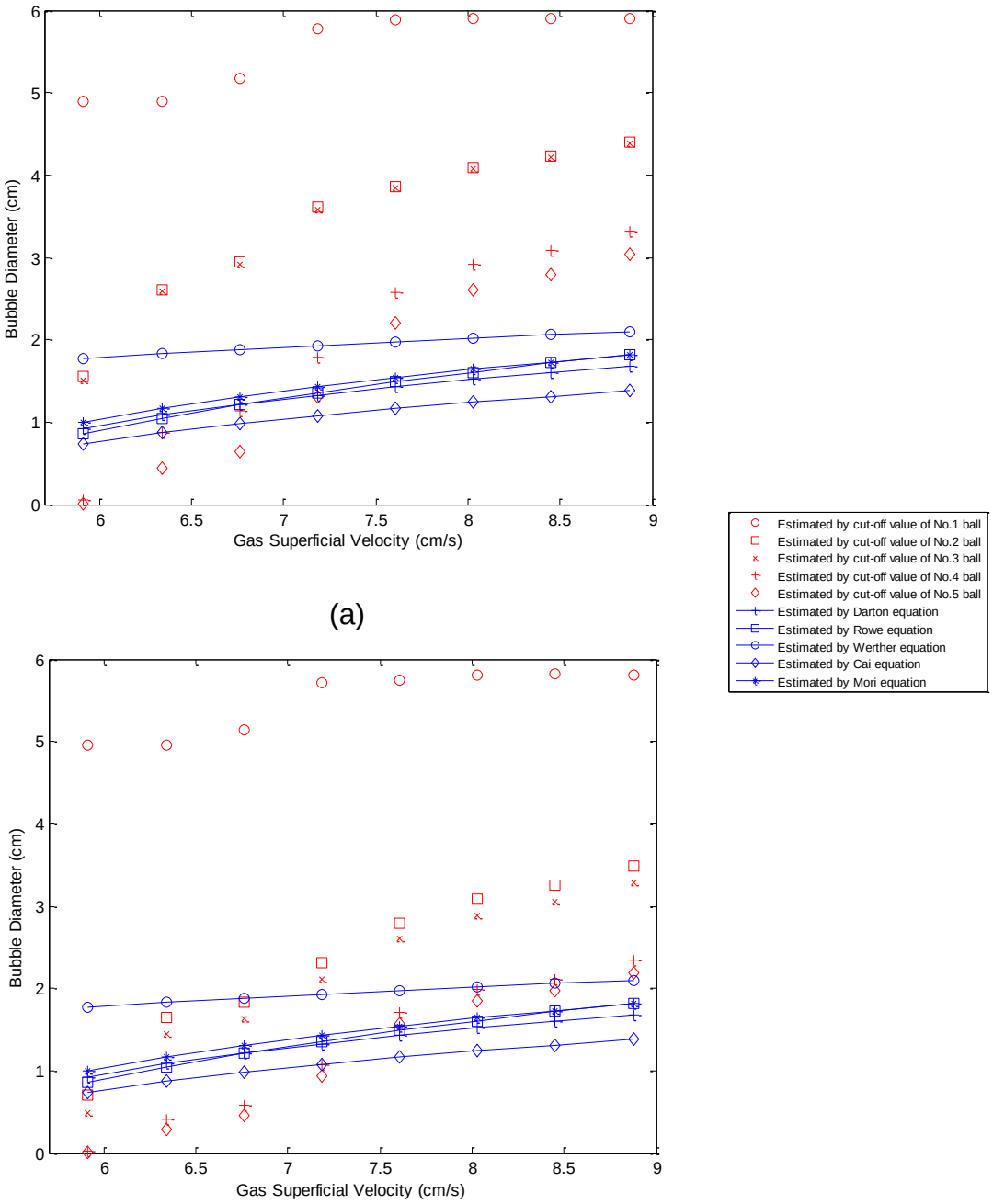

(a)

(b)

Figure 6.5: Bubble diameter estimated with cut-off values from LBP, (a) near centre, (b) near wall.

By observing Figure 6.5, it is interesting to discover a good agreement amongst the results obtained from the five different widely accepted empirical correlations. An apparent discrepancy can be identified between the bubble diameters obtained by using cut-off values derived from No. 1 plastic ball either near centre or near wall and the bubble diameters estimated from five empirical correlations. This may be attributable to the fact that the internal diameter of the No. 1 plastic ball is about 7.6 mm, which is mostly in the

magnitude as the spatial resolution (normally 5% to 10% of the vessel diameter) of an ECT system. Moreover, the No. 1 plastic ball is so small that the cut-off values derived from it may not be valid since the size of the ball is probably not comparable with the size of real bubbles in a fluidized bed.

Nevertheless, the results obtained with cut-off values from No. 4 and No. 5 plastic balls have a relatively good consistency with the empirical correlation results and the results near wall performed better than the ones near centre in which case the results when the gas superficial velocity is lower than 7.3 cm/s show a better fitting with empirical correlation results than the data when the velocity is between 7.3 cm/s and 8.9 cm/s. The stronger sensitivity near wall of the ECT measurement system may contribute to that phenomenon. The bubble diameters obtained with cut-off values near centre from No. 2 and No. 3 plastic balls had poor agreement compared with the empirical correlation results whereas a better association was found on the results near wall. The results achieved with cut-off values from No. 2 and No. 3 plastic balls are very close to each other which was expected since the original plastic ball internal diameter (15.2 mm and 18.32 mm, respectively) is close.

6.3.2 Linear fitted curve method

In order to discover the effect of cut-off values on the estimated size of bubbles in the bubbling regime, a linear curve fitting was implemented considering a limited number of plastic balls. There is probably some relation or connections among cut-off values themselves. Hence, in this section, the size of real bubbles is estimated via a linear fitted curve of cut-off values instead of using individual cut-off values. Figure 6.6 shows the linear fitted curves with cut-off values near centre and near wall. It can be seen that the two curves have a similar sloping trend where the cut-off values decrease with the increased internal hollow diameter. The size of the real bubbles was obtained according to the fitted curves of cut-off values within a certain degree of confidence.

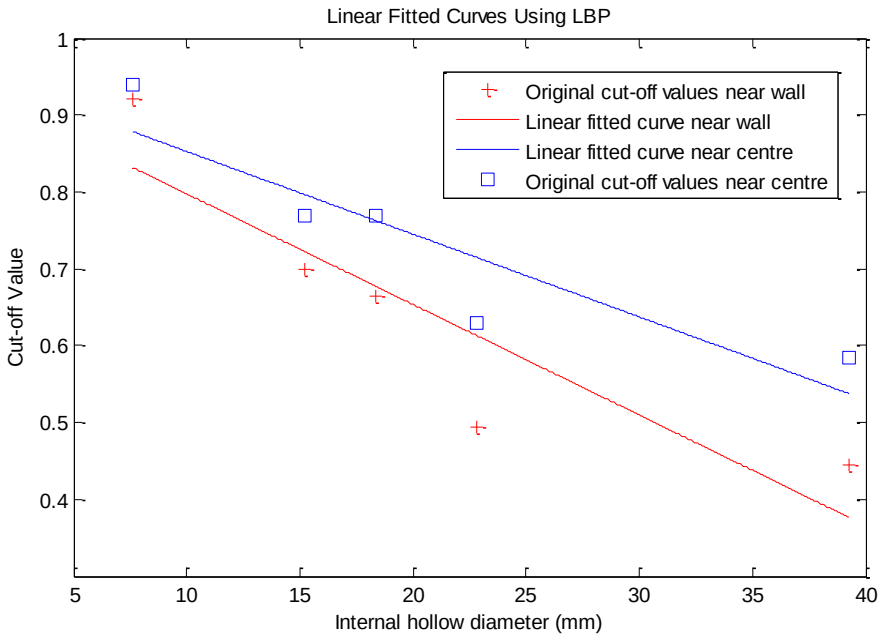

Figure 6.6: Linear fitted curves for cut-off values using the LBP algorithm

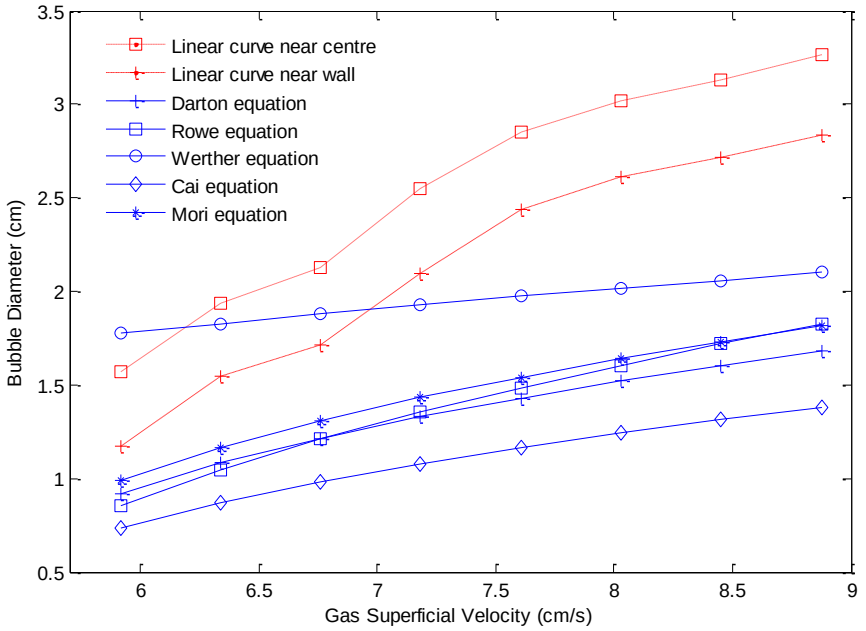

Figure 6.7: Bubble diameter derived from the linear fitted curves of cut-off values using LBP algorithm

The results obtained are presented and compared with the results estimated from the five empirical correlations in Figure 6.7. It can be seen that the estimated bubble diameters from Werther's equation gives the best agreement with the results obtained with linear fitted curves of cut-off values especially when the gas superficial velocity is lower than 7 cm/s. The results acquired with the linear curve of cut-off values near centre is larger than the

ones obtained from the linear curve of cut-off values near wall. In addition, there is still quite a good fit between the results from the linear curve near wall and the results estimated from the other four empirical correlations at relatively lower gas superficial velocities.

6.3.3 Second-order fitted curve method

The results shown in Figure 6.7 demonstrate that the linear fitted curves of cut-off values have been proved to be effective in estimating the size of real bubbles in a gas-solids fluidized bed. The gradients of fitted curves of cut-off values agree well with a well-known finding that the size of bubbles increased mostly with the increasing gas superficial velocity within the bubbling regime. However, in Figure 6.6, some evident data deviation between the original cut-off values and the linear fitted curves can still be readily identified. For example, the original cut-off values of No. 1 plastic ball both near centre and near wall and of No. 4 plastic ball near wall have very large inconsistencies with the linear fitted curves. Furthermore, the estimated bubble diameters via these two linear fitted curves are still not a great fit with the empirical correlation results. To attempt to achieve a better cut-off data fitting and to further investigate the effect of the cut-off values on the process of estimating real bubble diameter, a second-order curve fitting was conducted. Figure 6.8 shows the second-order fitted curves with cut-off values near centre and near wall.

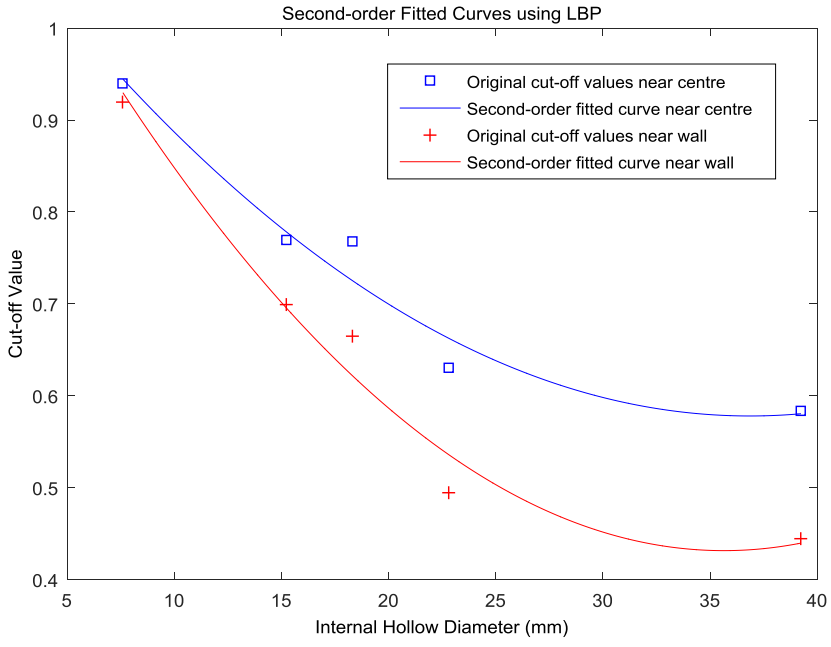

Figure 6.8: Second-order fitted curves for cut-off values using LBP algorithm

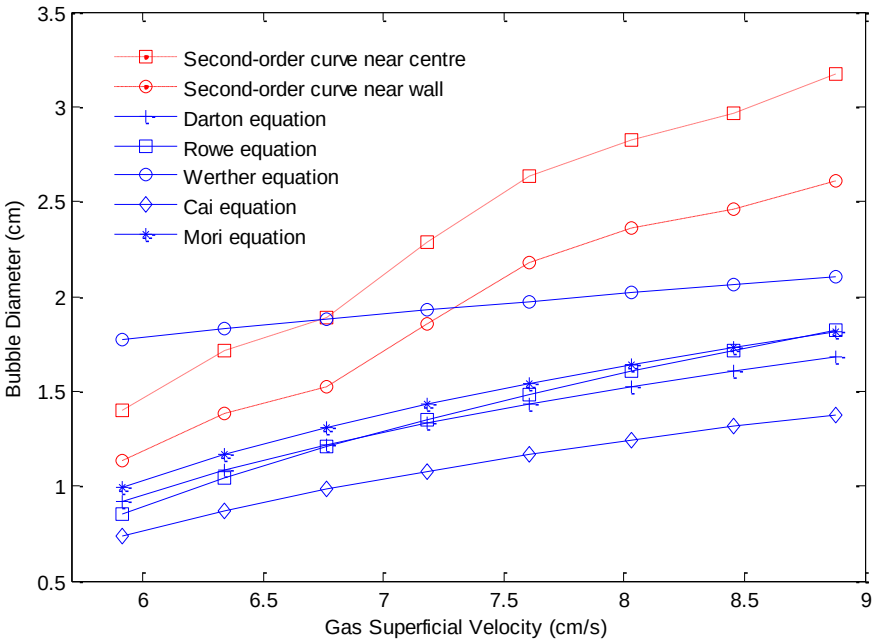

Figure 6.9: Bubble diameter derived from the second-order fitted curves of cut-off values using LBP algorithm

In Figure 6.8, a clearly better fitting between the fitted curves and the original cut-off values either near centre or near wall can be observed compared with the linear curve fitting results in Figure 6.6. More specifically, five original cut-off values near centre line were close to the second-order fitted curve as indicated in Figure 6.8. A similar general trend of the relationship between the cut-off value and the internal hollow diameter can be detected between the second-order curve fitting and the linear curve fitting.

The results for estimated bubble diameter via the second-order fitted curves are shown in Figure 6.9. There is a better fit between results obtained from the second-order curves and the results estimated from Werther's equation. Specifically, one data point when the gas superficial velocity is between 6.5 cm/s and 7 cm/s nearly coincides with Werther's equation result (1.88 cm) and the second-order curve near centre result (1.87 cm). Subsequently, the percentage error at that point improved effectively from 11.8% to 0.4%. As for the results from the second-order curve near wall, they have a significant superior agreement with the results obtained from Mori's equation than the results from the linear curve near wall with the averaged percentage difference increased by approximately 8% when the gas superficial velocity was below 7 cm/s. Notwithstanding, when the gas superficial velocity is more than 8 cm/s there is still a large discrepancy between the second-order fitted curve results near wall and the results estimated from Mori's equation.

6.4 Bubble size estimation results for iterative LBP

6.4.1 Individual cut-off values method

As indicated in section 6.2.2, 10 iterative steps were chosen for the iterative LBP algorithm to examine the image quality improvement compared with the conventional LBP algorithm. Figure 6.10 presents the estimated bubble diameter results with individual cut-off values from 10 iterative LBP compared with the five empirical correlation results.

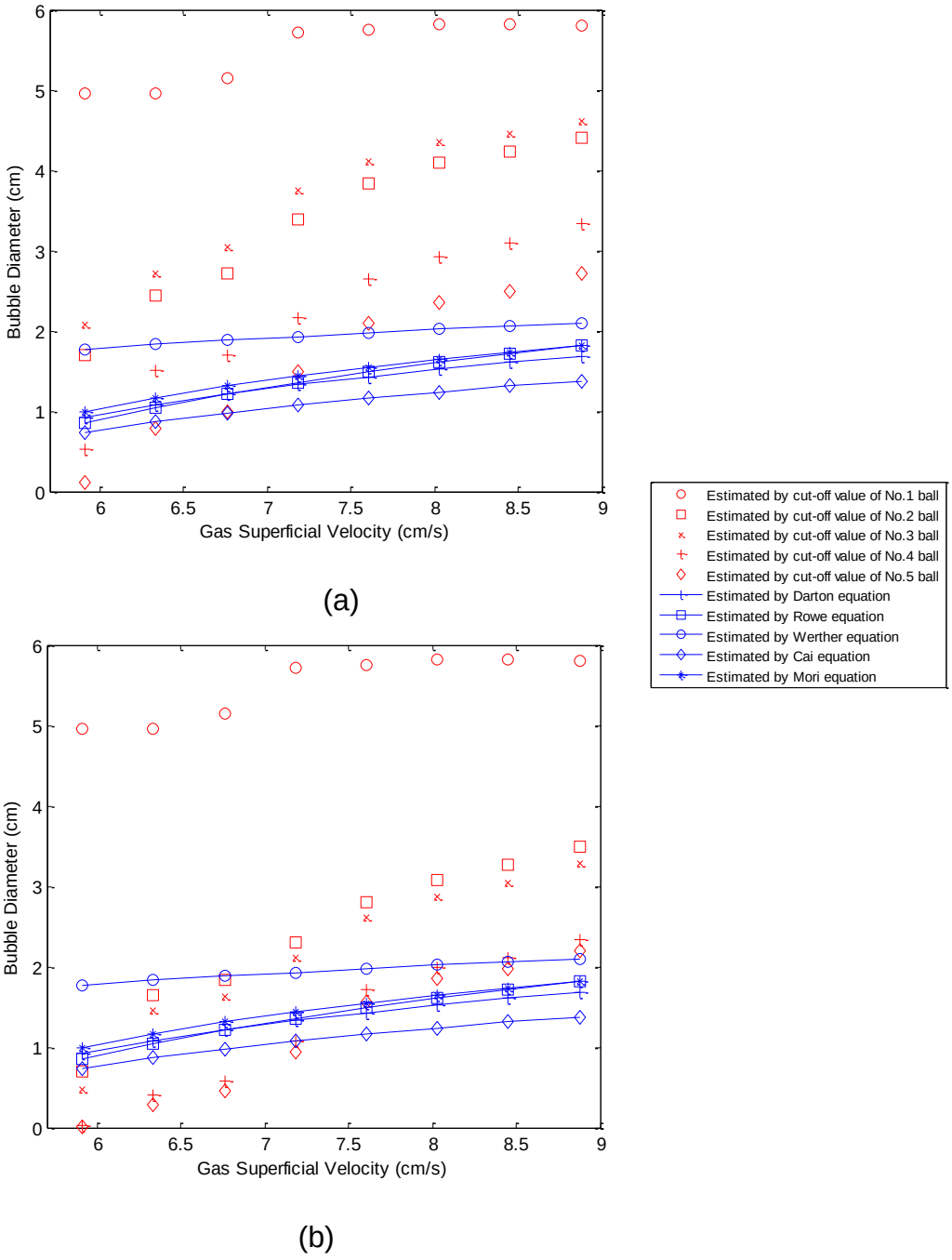

(a)

(b)

Figure 6.10: Bubble diameter estimated with cut-off values from 10 iterative LBP, (a) near centre, (b) near wall

The results obtained in Figure 6.10 demonstrate again that the estimated bubble diameters with cut-off values from the No. 1 plastic ball either near centre or near wall have a pronounced deflection with the results from all the five empirical correlations. It indicates that improved image reconstruction algorithms are unable to rectify or compromise the settled spatial resolution of an ECT measurement system as discussed previously in section 6.3.1.

However, it is interesting to find that the 10 iterative LBP algorithm aids in distinguishing the bubble diameters estimated with the cut-off values from the No. 2 and No. 3 plastic balls whilst the corresponding results are intertwined or overlapped in the case of LBP algorithm results in Figure 6.5. The data agreement is improved further between the results estimated with the cut-off values from the No. 4 and No. 5 plastic balls and the results obtained from the five empirical correlations when the gas superficial velocity is more than 7.5 cm/s. A further look at the results estimated with cut-off values from the No. 5 plastic ball near centre reveals that there is an enhancement on the percentage error from 26.2% to 17.4% when the gas superficial velocity is at 8.45 cm/s. Moreover, when the gas superficial velocity is at 7.6 cm/s, a magnificent improvement is identified on the percentage error from 10.7% to 5.9%.

6.4.2 Linear fitted curve method

Nevertheless, regarding the results shown in Figure 6.10, except the results obtained from Werther's equation, all the results estimated from the other four empirical correlations have very limited agreement with results estimated via the cut-off values from the No. 2 and No. 3 plastic balls at higher gas superficial velocities.

Similarly, for the purpose of identifying the effect of a wider range of cut-off values on the process of estimating bubble diameter and detecting any potential capability of the 10 iterative LBP algorithm in improving image quality, a linear curve fitting was carried out. The linear fitted curves are shown in Figure 6.11. A similar tendency can be readily seen that cut-off values decreased with the increased internal hollow diameter of the plastic balls compared with the linear curve fitting using the LBP algorithm in Figure 6.6. Cut-off values from the linear fitted curve near centre are larger than the ones from the linear fitted curve near wall. The estimated bubble diameter results, according to the two linear fitted curves, are presented in Figure 6.12.

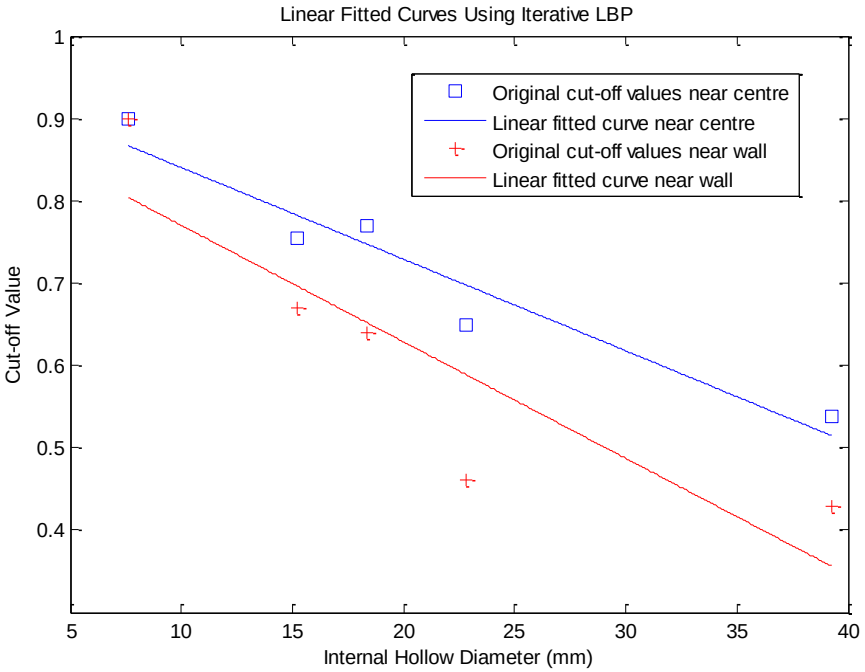

Figure 6.11: Linear fitted curves for cut-off values using 10 iterative LBP algorithm

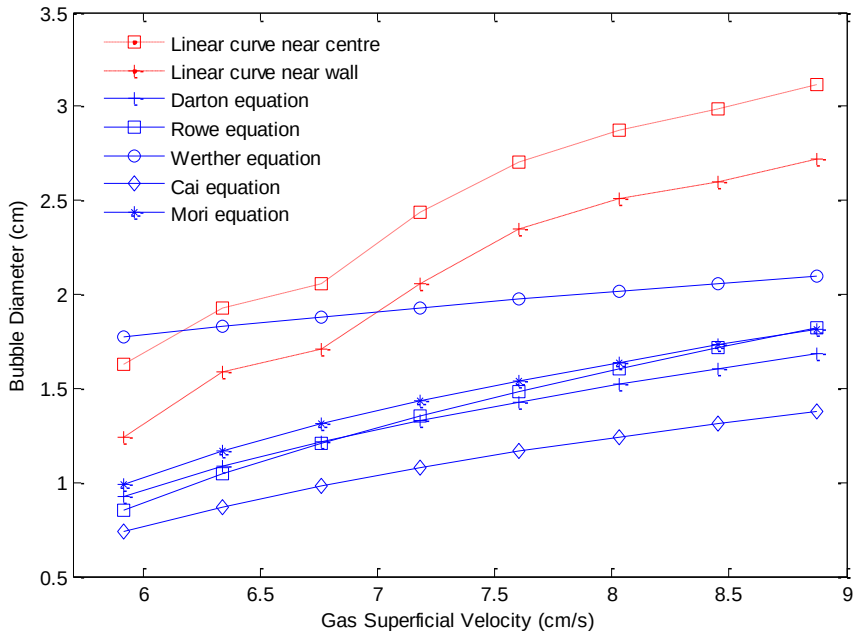

Figure 6.12: Bubble diameter derived from the linear fitted curves of cut-off values using 10 iterative LBP algorithm

As can be seen from Figure 6.12, the results of the estimated bubble diameter obtained from the linear curve, both near centre and near wall, demonstrate an overall consistency of the increasing trend with the increasing gas superficial velocity. In particular, the results fit well with the estimated bubble diameter by means of the empirical correlation of Werther whose results lie in

the middle between the results obtained from linear curve near centre and linear curve near wall when the gas superficial velocity was lower than about 7.2 cm/s. It reaffirms that the relation in Figure 6.11 between cut-off values and the internal hollow diameter of the plastic balls is reflected and justified reasonably by the results shown in Figure 6.12 that bubble diameter increases with the increasing gas superficial velocity within the bubbling regime.

In addition, by comparing the results estimated by means of the 10 iterative LBP algorithm in Figure 6.12 and the results obtained by virtue of the conventional LBP algorithm in Figure 6.7, it can be observed that the image quality is slightly improved and that can be reflected by the following observation. When the gas superficial velocities are at 6.34 cm/s and 7.18 cm/s, the percentage error between the bubble diameters estimated from the linear fitted curve near centre using the LBP algorithm are improved from 5.6% to 5.1% and from 24.3% to 20.8%, respectively.

6.4.3 Second-order fitted curve method

Although it has been concluded that the estimated bubble diameter with the linear fitted curve of cut-off values using the 10 iterative LBP algorithm reflects well on the relation between individual cut-off values and internal hollow diameter and the image quality is improved compared with the traditional simple LBP algorithm by some discovered promising results as discussed in the former section 6.4.2, the size of the estimated bubble diameters are still generally larger than the results obtained with the five empirical correlations.

Besides, the data deviation can still be recognized between the original cut-off values and the linear fitted curves as shown in Figure 6.11, especially between the original cut-off values of the No. 1 and No. 4 plastic balls and the linear fitted curve near wall. Therefore, a second-order curve fitting was executed in order to achieve better data fitting and to further scrutinize the performance of the 10 iterative LBP algorithm on the process of bubble diameter estimation.

The second-order fitted curves for cut-off values using the 10 iterative LBP algorithm both near centre and near wall are plotted in Figure 6.13. There are some better data fits which can be spotted plainly by comparing the original cut-off values with the second-order fitted curves and the linear fitted curves especially for the second-order fitted curve near wall. The corresponding estimated bubble diameter results are shown in Figure 6.14 and are compared with the results obtained from the five empirical correlations.

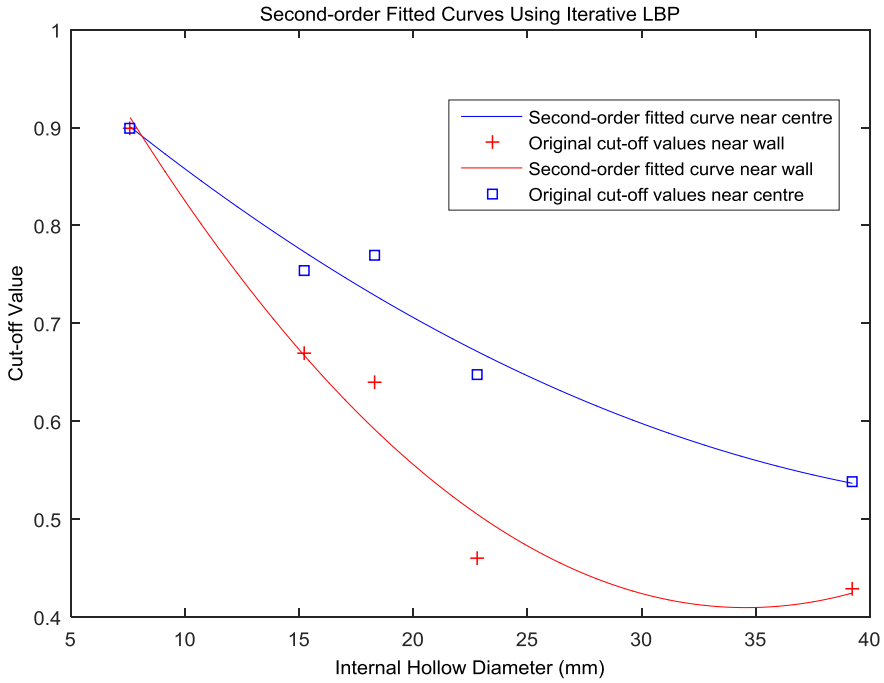

Figure 6.13: Second-order fitted curves for cut-off values using 10 iterative LBP algorithm

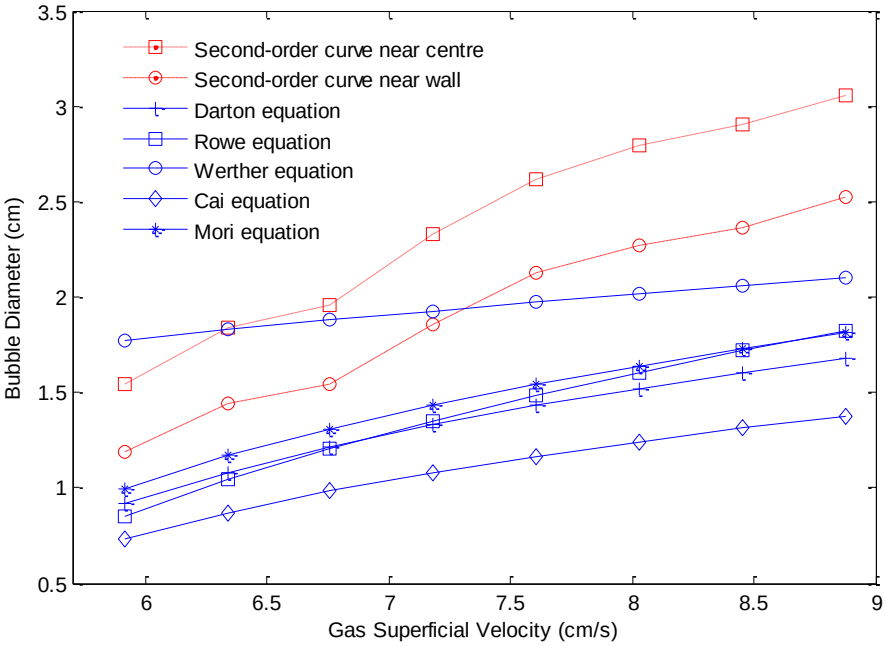

Figure 6.14: Bubble diameter derived from the second-order fitted curves of cut-off values using the 10 iterative LBP algorithm

A similar tendency between the estimated bubble diameter via fitted curves of cut-off values and the results obtained from empirical correlations as identified from Figure 6.12 and Figure 6.14 that bubble diameters increase constantly with increasing gas superficial velocity. The results from the fitted curves near

centre are all slightly larger than the ones from the fitted curves near wall. If a closer look is taken at Figure 6.14, some improvements can be located compared with the results obtained from the second-order fitted curves using the LBP algorithm in Figure 6.9 and the results obtained from the linear fitted curves using 10 iterative LBP algorithm in Figure 6.12.

Firstly, the results obtained from the second-order fitted curves near centre have a better agreement with the results estimated from Werther's equation than the results shown in Figure 6.9 when the gas superficial velocities are at 6.34 cm/s and 6.76 cm/s. The corresponding percentage errors are improved from 5.1% to 0.4% and from 8.6% to 4.1%, respectively. Secondly, the results obtained from the second-order curve near wall performed better than the ones obtained from the linear curve near wall compared with the estimated bubble diameter from Werther's equation when the gas superficial velocity is larger than 7.18 cm/s. The corresponding averaged percentage difference is enhanced from 19.7% to 11%. Thirdly, by comparing the results obtained between the estimated bubble diameter achieved from the second-order curve near wall using the 10 iterative LBP algorithm and Werther's equation with the ones between the estimated bubble diameter achieved from the second-order curve near wall using the simple LBP algorithm and Werther's equation in Figure 6.14 and Figure 6.12, it can be observed that the averaged percentage difference has improved fairly well from 14.9% to 11%.

Nonetheless, there are still some discrepancies existing between the results by means of either individual cut-off values or linear or second-order fitted curves of cut-off values and the results estimated from empirical correlations. This may stem from the fact that there are probably some unforeseen limitations in using empirical correlations since the operating experimental conditions in the present study inevitably have some differences with the ones utilized by previous investigators who proposed the empirical correlations. Alternatively, the bubble shape assumption of the spherical shape may not be entirely true for all the bubbles appearing in the bubbling regime as some researchers [43] have pointed out that bubbles with hemispherical shape possibly still exist in the bubbling regime.

By all means, the cut-off values derived from the plastic ball calibration have been showcased as being effective in estimating bubble diameter in bubbling regime in the gas-solids fluidized bed. Further conclusions regarding this will be summarized in the summary section 6.6.

6.5 Bubble rising velocity results

Besides of the bubble diameter, the bubble rising velocity is another key variable in determining the hydrodynamic characteristics of the bubbles in bubbling regime. As reviewed in Chapter 2, numerous investigations have endeavoured to come up with effective empirical correlations (some of the most popular ones have been summarized in Table 2.2 using different experimental techniques to estimate the bubble rising velocity in an ultimate accurate manner. The cross-correlation technique has been recognized as one of the most capable approaches in estimating bubble rising velocity applied in several conventional measurement techniques, such as capacitance probes [100] and optical probes [21]. Recently, it has been applied in the ECT measurement system to estimate bubble rising velocity [17].

However, very few studies have been found so far in the open literature to have compared the results obtained by means of the cross-correlation technique with the results calculated from the widely accepted empirical correlations. Also, the ECT data previously captured were almost in a sampling rate of 100 fps.

In this section, the cross-correlation technique is utilized to estimate the bubble rising velocity in the bubbling regime in order to evaluate the performance of the empirical correlations and to examine the ECT data quality captured at 200 fps. In addition, a detailed mathematical analysis will be carried out on the captured ECT data. Moreover, individual pixel-based axial bubble rising velocity will be estimated over the sampling time interval of 80 seconds. They will be presented in a three dimensional format by means of MATLAB programming to further analyse the hydrodynamic feature in the gas-solids fluidized bed. A new method based on the principle of identifying the similarity between two images will be introduced afterwards in an attempt to estimate the bubble rising velocity. Finally, all the results obtained will be compared and evaluated against the results calculated from the empirical correlations.

6.5.1 Cross-correlation via averaged volume fraction

The cross-correlation technique has been widely applied originally to identify the similarity of two signals in signal processing. The mathematical expression of it is presented in Equation (6.1). In order to estimate the bubble rising velocity in the ECT system, a discrete format is shown in Equation (6.2)

integrated with the signal of the averaged volume fraction obtained from the ECT measurement which has been reviewed and introduced in Equation (5.3) in Chapter 5.

$$R_{xy}(\tau) = \frac{1}{T}\int_0^T X(t)Y(t+\tau)dt \qquad (6.1)$$

$$R_{xy}(\tau) = \frac{1}{N}\sum_{i=1}^{N} x(t)\, y\ (t+\tau) \qquad (6.2)$$

where x(t) and y(t) are the upper and lower plane signals of the averaged volume fraction, N is the number of samples in the summation, τ is the time lag between the signals of the two measuring planes.

To further facilitate the illustration of the cross-correlation technique utilized with ECT measurement, Figure 6.15 showcases a schematic illustration of the cross-correlation technique in estimating the bubble rising velocity. The time series of averaged volume fraction for plane 1 and plane 2 in a time interval of 2.5 seconds (500 frames with sampling rate of 200 fps) are plotted in Figure 6.15. Bubbles are identified when the volume fraction is in the lowest values locally as marked in the figure. Suppose a bubble is travelling upwards through the centre of plane 1 at a time step of t_1 and through the centre of plane 2 at a time step of t_2, the time lag for the bubble passing through two planes is detected using the cross-correlation technique by identifying the largest cross-correlation coefficient value of the two signals [17]. Figure 6.16 demonstrates the normalized cross-correlation coefficients for various gas superficial velocity. The corresponding bubble rising velocity estimated by virtue of the cross-correlation technique at various gas superficial velocities is shown in Figure 6.17 and compared with the results calculated from the empirical correlations.

In order to evaluate the system error caused by applying the sampling rate using the cross-correlation techniques, it is necessary to conduct the following evaluation. According to previous work [190, 191] , the minimum acquisition time δ can be taken as twice the product of the minimum transit time of the fluid τ and the fractional discrimination k. By rearranging this, it gives the following:

$$k = \frac{\delta}{2\tau} \qquad (6.3)$$

The fractional discrimination is the sensitivity of a velocity measurement system based on its sampling speed. Here, in the present study, the distance between two measuring planes is 0.04 m, the sampling rate is 200 fps and the maximum gas superficial velocity is 8.87 cm/s. By applying Equation (6.3),

subsequently, the fractional discrimination of 0.006 or 0.6% is obtained. Compared with previous work [192], the system error in the present study is much more acceptable.

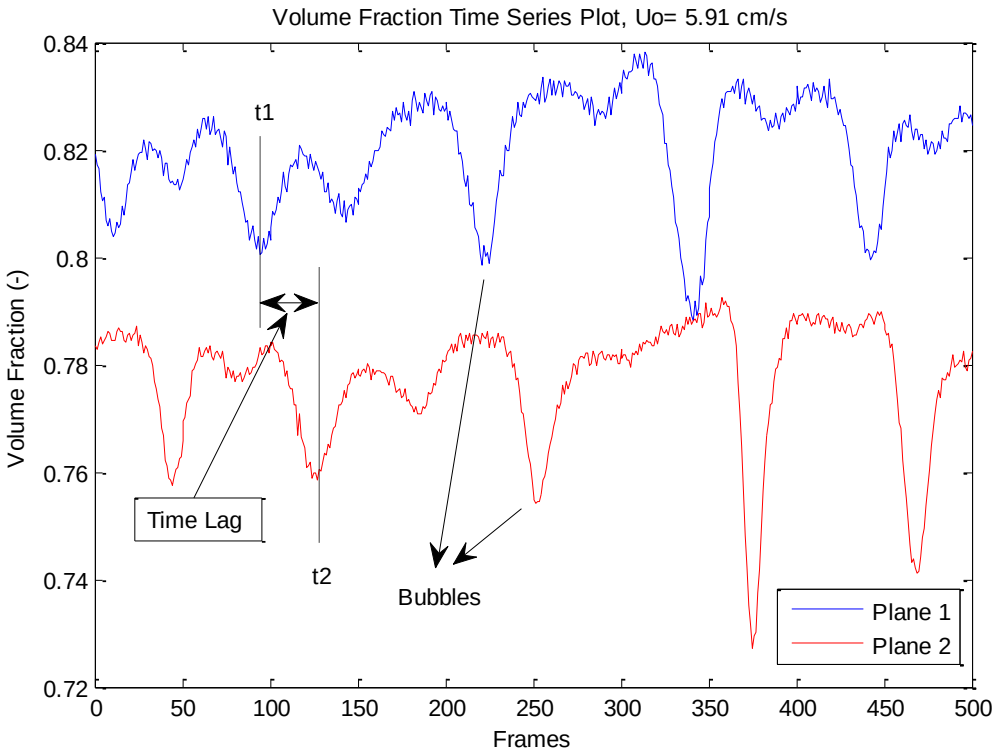

Figure 6.15: Schematic illustration of cross-correlation techniques in estimating bubble rising velocity

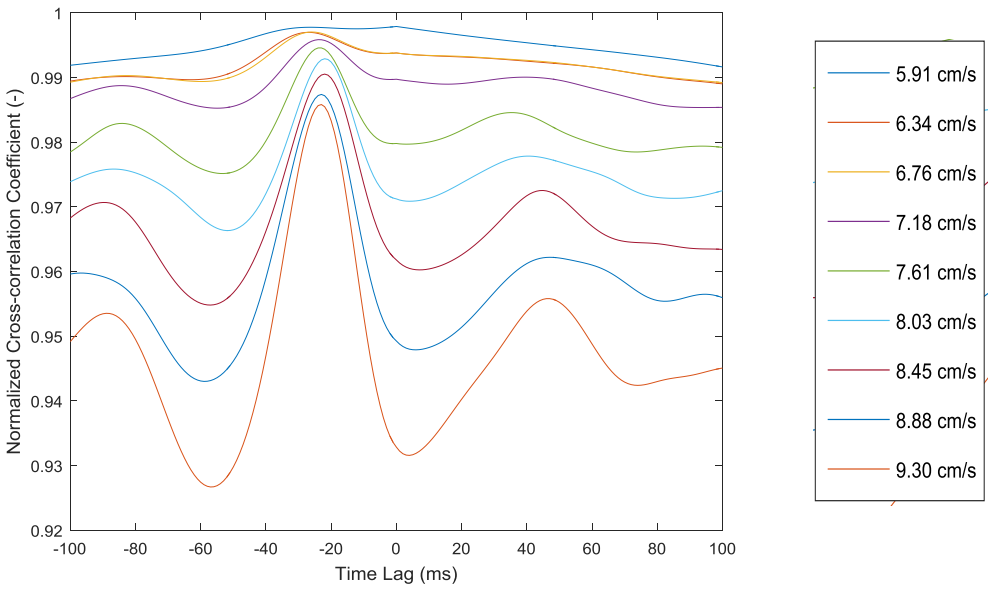

Figure 6.16: Normalized cross-correlation coefficients at various gas superficial velocity

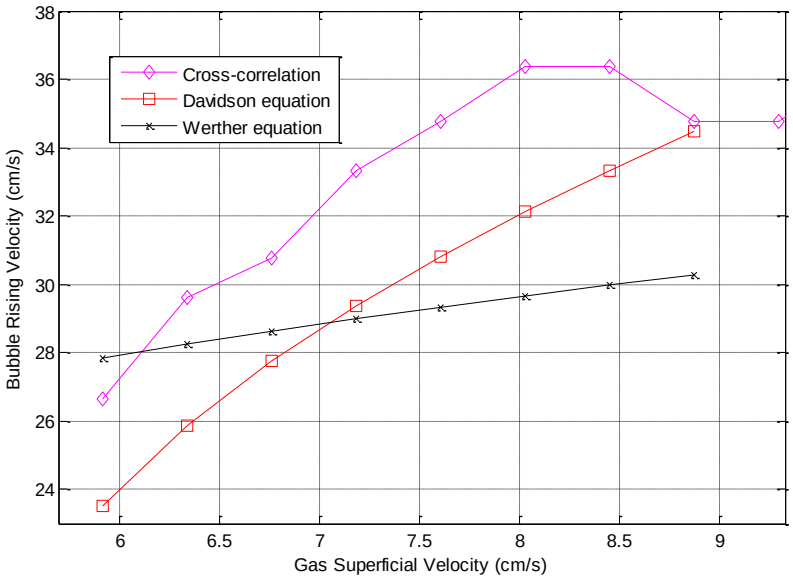

Figure 6.17: Comparison of bubble rising velocity results derived by means of cross-correlation techniques and empirical correlations

The results presented in Figure 6.17 demonstrate generally that the estimated bubble rising velocity via cross-correlation has a good increase tendency that the bubble rising velocity increases accordingly with the gas superficial velocity compared with the results of Davidson and Werther's empirical correlations.

However, the estimated bubble rising velocity had better agreement with Davidson's equation than Werther's equation. The percentage errors between the cross-correlation results and the results from Davidson's equation are all within 11.7% with the smallest values of 0.8% when the gas superficial velocity was at 8.87 cm/s. However, the largest percentage between the results from cross-correlation and the results from Werther's equation is around 18.4% occurring at a gas superficial velocity of 8.02 cm/s.

Furthermore, the estimated values of bubble rising velocity from Werther's equation are mostly lower than the results obtained from both the cross-correlation and Davidson's equation. The reason behind this phenomenon may stem from the original expressions of both equations. The term U_0-U_{mf} which appeared in Davidson's equation is absent from the Werther equation, as indicated in Table 2.2. Since the U_{mf} is constant, when the superficial velocity increases, the value of the term of U_0-U_{mf} is correspondingly increased [176].

6.5.2 Mathematical analysis via MATLAB codes

It is possible to extract the bubble rising velocity by mathematically analysing the averaged volume fraction data at both ECT measuring planes in a detailed manner [17]. The basic concept of the method and its mathematical expression is reviewed and shown in Equation (2.30) in Chapter 2. This information will not be repeated again here. Instead, a schematic graph is presented in Figure 6.18 which utilizes the same set of original data of Figure 6.15 used to showcase the illustration of the detailed mathematical approach in estimating the bubble rising velocity.

Two sets of 2.5-second long data of the averaged volume fraction measured at both planes are shown in Figure 6.18. The lowest points which are regarded as bubbles were picked out by means of a section of customized MATLAB codes. However, the bubbles will be used in Equation (2.30) only if their averaged volume fraction values are lower than the mean value over the sampling time interval of 80 seconds. By implementing this step, some uncertainties on the choice of bubbles, such as multi-bubbles and bubble coalescence, are expected to be effectively eliminated. Assuming a bubble appears at plane 1 at a time step of t_1 and at plane 2 at a time step of t_2, the time consumed for this process can be obtained straightforwardly and the rising velocity of this bubble is calculated by using a separation distance of 40 mm for both measuring planes. This process is repeated over the 80-second sampling time interval until an averaged bubble rising velocity is obtained.

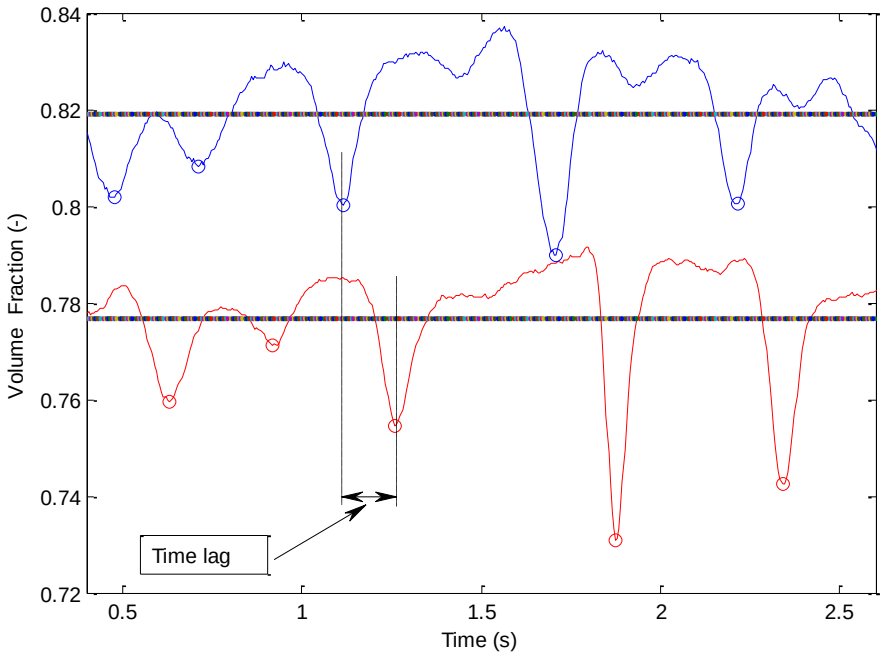

Figure 6.18: Schematic illustration of detailed mathematical approach in estimating bubble rising velocity

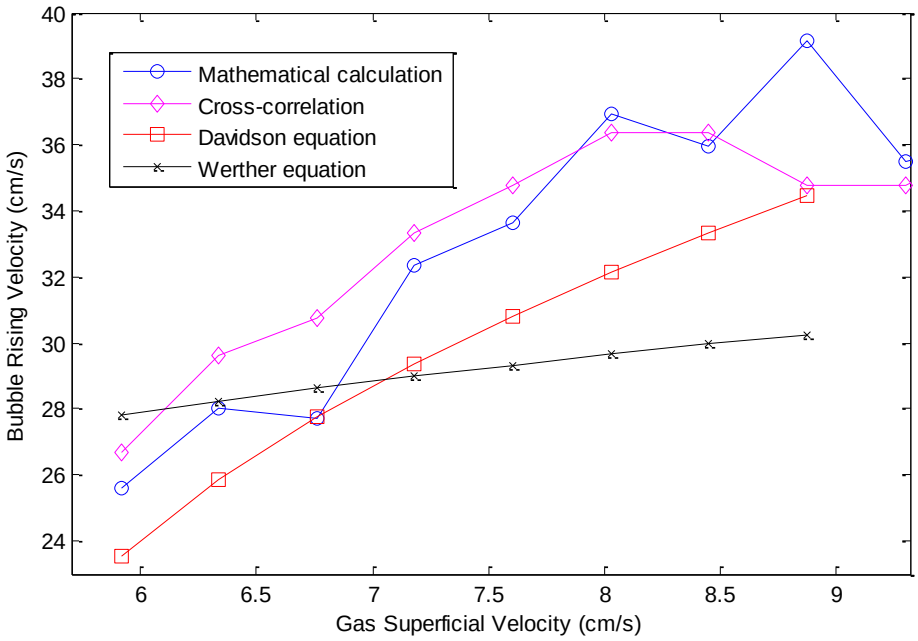

Figure 6.19: Comparison of estimated bubble rising velocity results

The estimated bubble rising velocity employing the detailed mathematical analysis method at various gas superficial velocity are presented in Figure 6.19. In order to evaluate its performance, the results obtained are compared with the ones estimated from cross-correlation and two empirical correlations.

Figure 6.19 shows a great consistency between the three sets of results of mathematical calculations, cross-correlation and Davidson equation. The percentage difference between the results of mathematical calculation and cross-correlation is within 11.1%. The smallest value (1.1 %) happens at the point when the gas superficial velocity is at 8.45 cm/s and the largest value is at the gas superficial velocity of 8.87 cm/s (11.1%). As for the results, comparison between mathematical calculation and Davidson's equation, the percentage difference is within 13.1%. The largest value occurs at gas superficial velocity of 8.02 cm/s whilst the smallest value is around 0.2% when the gas superficial velocity is at 6.75 cm/s.

The results obtained from the mathematical calculation and cross-correlation are plotted beyond the gas superficial velocity of 8.5 cm/s. This has been done intentionally to observe the trend of the bubble rising velocity beyond the slightly bubbling regime. The bubble rising velocity declines when the gas superficial velocity is larger than 8.5 cm/s where bubbles have probably evolved into slugs whose rising velocity might be slower due to the increased gas volume occupied. This is in support again of the conclusion drawn in Chapter 5 of the determination of the minimum slugging velocity of 8.89 cm/s.

6.5.3 Cross correlation via local pixel solid fraction

The fluid flow within the gas-solids fluidized bed is full of three-dimension and the behaviour of bubbles in the bubbling regime exhibit three dimensional features as well as was reviewed in Chapter 2. One of the critical parameters in describing bubble behaviour is the bubble rising velocity, which can be presented in a three dimensional fashion by virtue of ECT measurement. However, there are almost no studies in the present open literature pointing out the three dimensional profile of bubble rising velocity except one case which has been carried out within the application of ECT measurement on a pneumatic conveying process [6]. Therefore, in this section, the three dimensional profile of the bubble rising velocity in the bubbling regime will be investigated.

Local three dimensional profiles of the bubble rising velocity are derived by means of the cross-correlation technique within each pixel of the 812 effective individual pixels of the circular bed pipe cross section. The process is expressed in the following equation:

$$R_{xy},k(j)=\frac{1}{N}\sum_{i=1}^{N}x_k(i)\,y_k(i+j) \qquad (6.4)$$

where j=0,1,2,…,M; k=1,2,…,812; x(i) and y(i) are the upper and lower plane signals of local solid fraction, N is the number of samples in the summation, M is the number of samples in the cross correlation calculation, j is the number of delayed samples, and k is the pixel index.

The estimated three dimensional distribution profiles of the bubble rising velocity at various gas superficial velocities are plotted in Figure 6.20 (a), (b), (c), (d) and (e). X and Y co-ordinates denote the pixel index by row and by column, respectively. The Z co-ordinate represents the value of the axial bubble rising velocity at a specific pixel location.

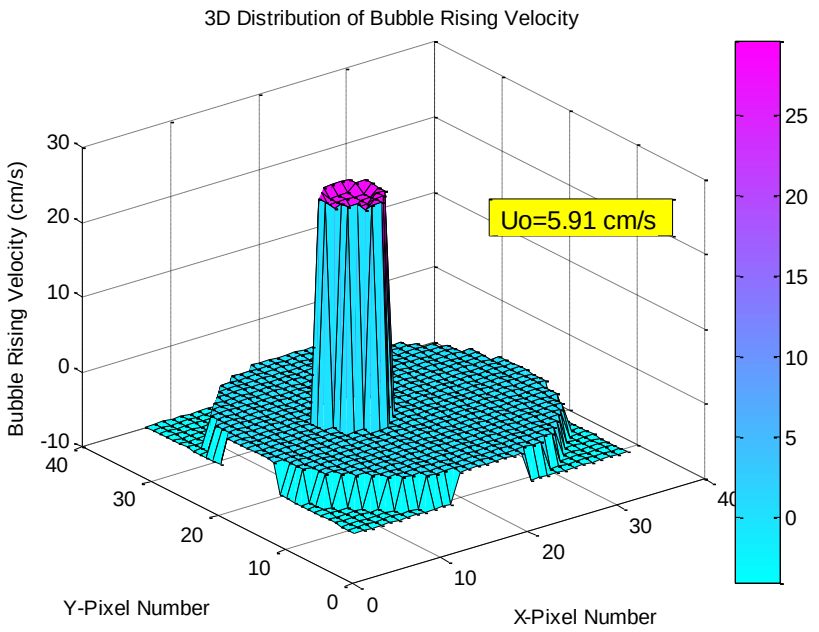

Figure 6.20 (a): Three dimensional distribution of bubble rising velocity on a pixel-by-pixel basis derived from the cross-correlation when the gas superficial velocity is at 5.91 cm/s

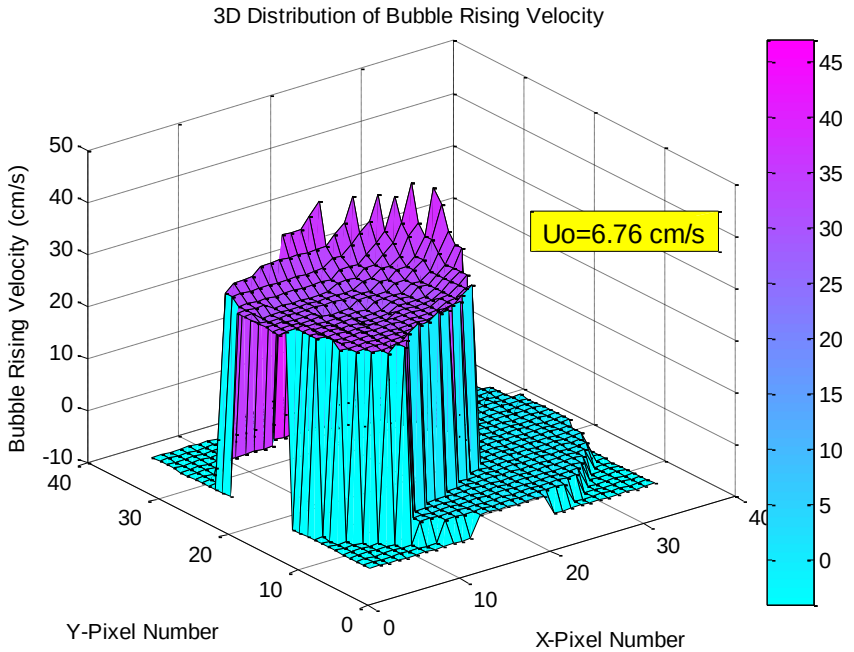

Figure 6.20 (b): Three dimensional distribution of bubble rising velocity on a pixel-by-pixel basis derived from the cross-correlation when the gas superficial velocity is at 6.76 cm/s

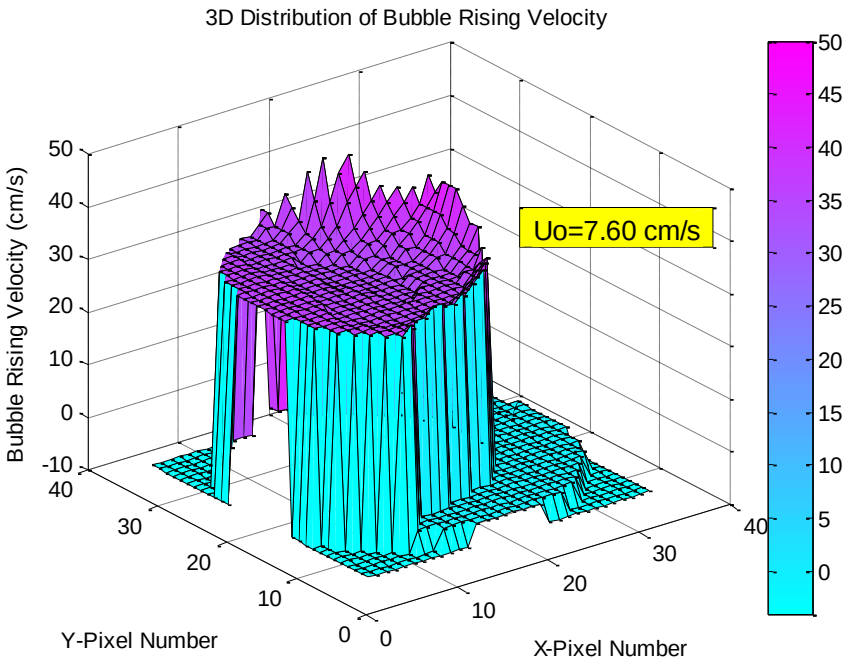

Figure 6.20 (c): Three dimensional distribution of bubble rising velocity on a pixel-by-pixel basis derived from the cross-correlation when the gas superficial velocity is at 7.60 cm/s

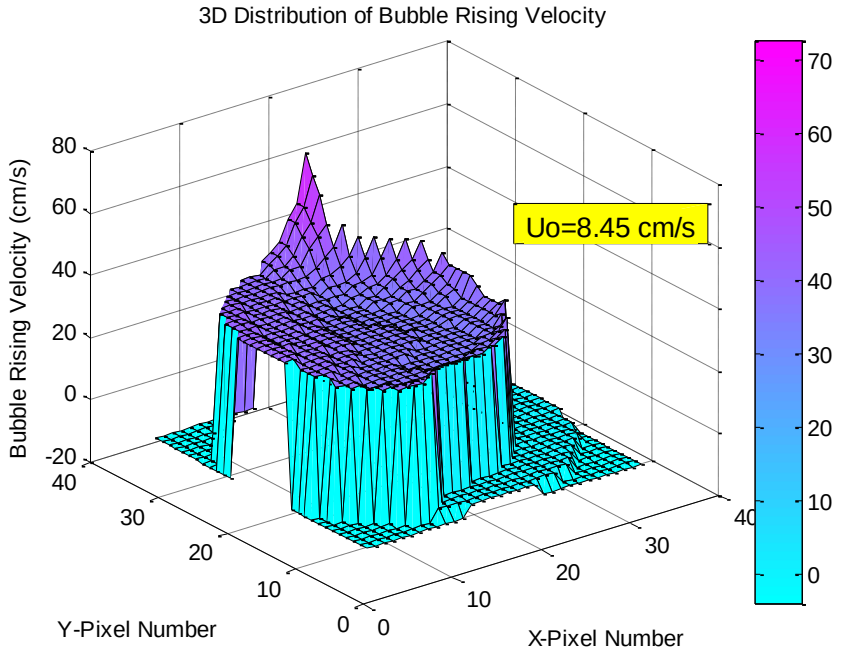

Figure 6.20 (d): Three dimensional distribution of bubble rising velocity on a pixel-by-pixel basis derived from the cross-correlation when the gas superficial velocity is at 8.45 cm/s

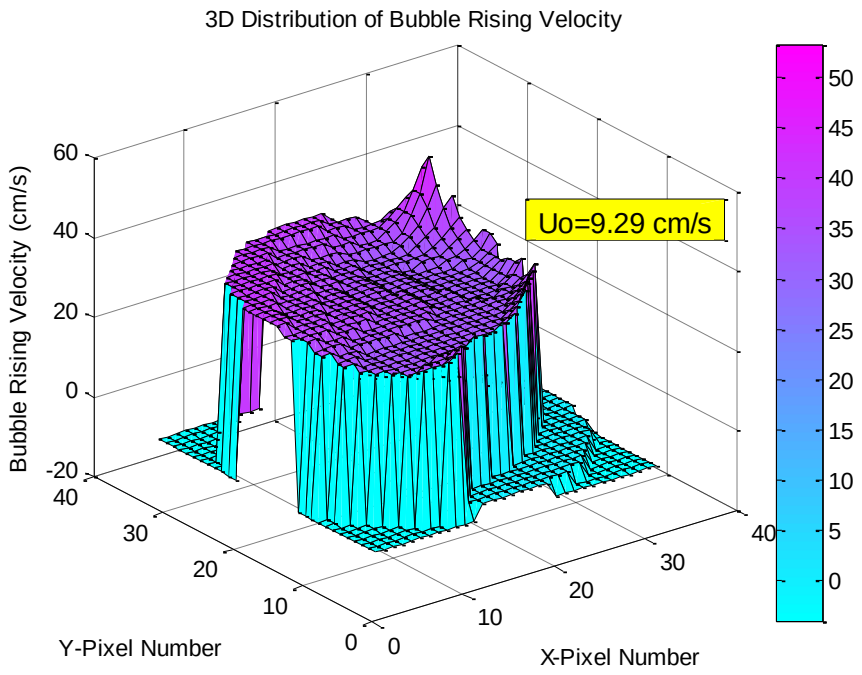

Figure 6.20 (e): Three dimensional distribution of bubble rising velocity on a pixel-by-pixel basis derived from the cross-correlation when the gas superficial velocity is at 9.29 cm/s

As it can be seen from Figure 6.20 (a), when the gas superficial velocity is low at 5.91 cm/s, the bubble rising velocity can only be extracted on limited pixels. This phenomenon can probably be explained as follows. The fluidization state at lower gas superficial velocities has not been developed or evolved completely. Hence, some areas, especially near wall, have bubbles appearing in a random fashion even with the evenly distributed upward flowing air. In addition, some bubbles may change the moving path in the translational direction. Subsequently, the bubble rising velocity cannot be detected by means of the cross-correlation technique since the similarity of the two signals is significantly weakened when a bubble is traversing from plane 1 to plane 2 at a specific pixel location.

By observing the three dimensional distribution of the bubble rising velocity in Figure 6.20 (b)-(e) where the gas superficial velocity was increased, more and more pixels are able to produce the bubble rising velocity estimated via the cross-correlation. This indicates that the fluidization state is fully developed. Also, there are gradients on the derived bubble rising velocity values, for example when the gas superficial velocities are at 6.76 cm/s and 7.6 cm/s. This demonstrates that bubbles appeared on the pixels near wall have larger rising velocities compared with the values in the central area pixels.

Moreover, if taking a look at the maximum bubble rising velocity on individual pixels at various gas superficial velocities, it increases with the increasing gas superficial velocity gradually from 29.62 cm/s to 61.53 cm/s. This finding is in line with the conclusions as discussed in the previous sections 6.5.1 and 6.5.2. In order to evaluate the performance of the three dimensional profile of the bubble rising velocity on a pixel-to-pixel basis, the averaged bubble rising velocity values based on the effective pixels within the 812 pixels are plotted in Figure 6.21 compared with the results obtained from the mathematical calculation, cross-correlation using the averaged volume fraction data and the empirical correlations.

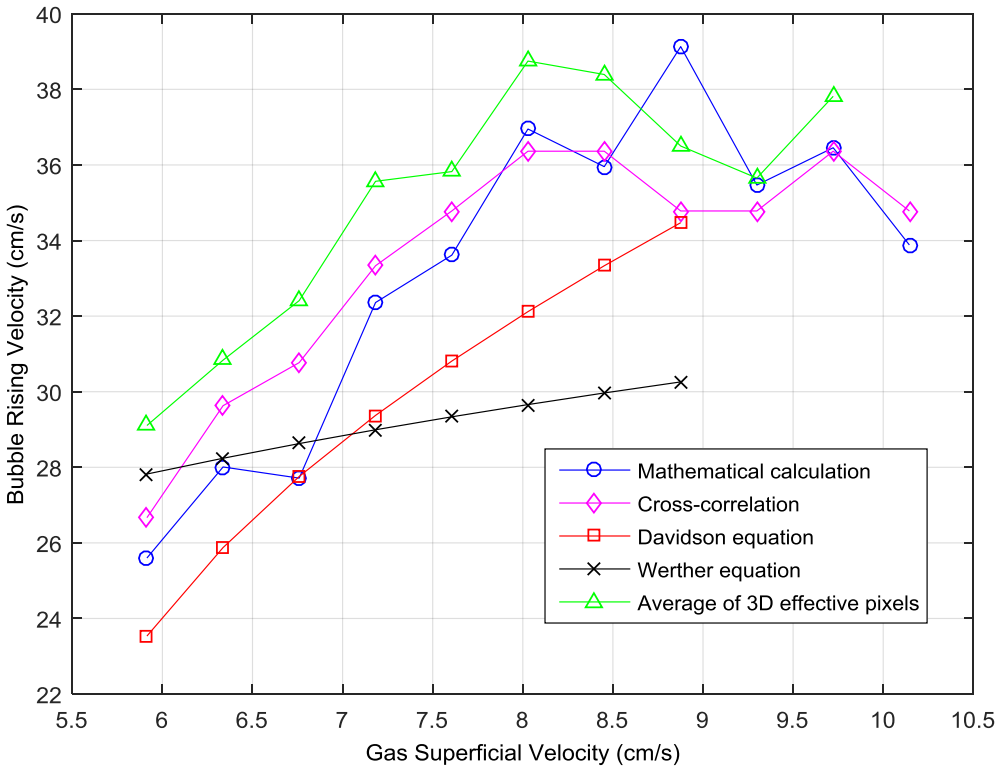

Figure 6.21: Comparison of the estimated bubble rising velocity results between mathematical calculation, cross-correlation, empirical correlations and the average of 3D effective pixels

The results shown in Figure 6.21 display good agreement between these five different approaches in deriving bubble rising velocity. Although the results obtained from the averaged value via the 3D effective pixels locations are slightly larger than the cross-correlation results using the averaged volume fraction, the percentage difference between them is in a really low range of 2.9% to 8.4%. It demonstrates again that the cross correlation via local pixel solid fraction is an effective approach in investigating bubble behaviour in a three dimensional manner.

6.5.4 Statistic average approach via MATLAB codes

Similarities between two digital photographs can be identified using a statistic average approach. The present section attempts to detect the bubble rising velocity by integrating the statistic average approach with two series of 32 x 32 pixel images measured by the ECT system at two different measuring plane locations. The mathematical expressions of the statistic average approach and the process of deriving the coefficients are as follows:

$$C_k = \sum_{i=1}^{M} \sum_{j=1}^{N} P(i,j)\, Q(i,j) \qquad (6.5)$$

$$C_\tau = \sum_{k=1}^{L} C_k \qquad (6.6)$$

where i, j are the index of pixels in the 32 x 32 images; M,N are the maximum pixel index values of 32; k is the time step, k = 1, 2, 3,…,16000; C_k is the statistic average approach coefficient at k time step; L is the total sampling length of 16000; C_τ is the summed statistic average approach coefficient when the time lag is at τ ; $P(i,j)$ and $Q(i,j)$ are the pixel grey levels for two measuring planes. Calculation with different time lag (in this case ± 0.25 s) is aided by a section of customized MATLAB codes. The statistic average approach coefficients obtained are normalized and the results are displayed in Figure 6.22 at different gas superficial velocities.

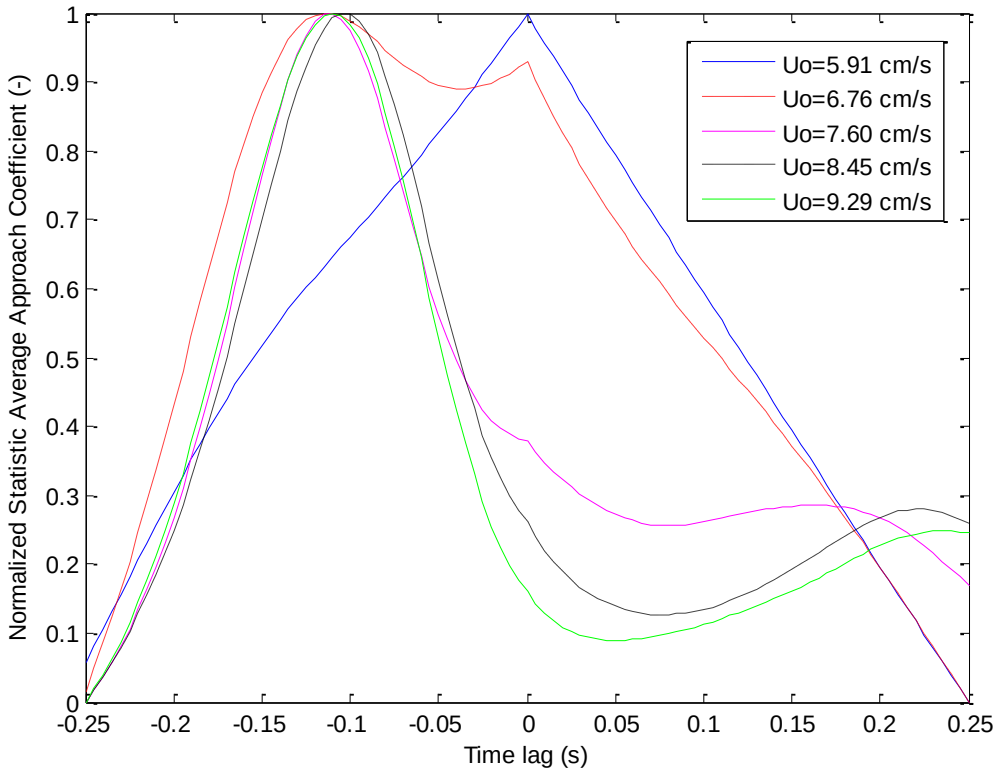

Figure 6.22: Statistic average approach normalized coefficients at different gas superficial velocities

From the coefficient results shown in Figure 6.22, it can be found that most of the maximum values of the statistic average approach occurred at negative time lags. This is understandable since the negative values of the time lags mean how many time lags are needed for the signal measured at plane 2 level to move backwards to obtain the most similarity with the signal measured at plane 1 level. It is worth noting that the maximum statistic average approach coefficient at the gas superficial velocity of 5.91 cm/s is at a time lag of zero. It indicates that the two sets of 32 x 32 images captured at both planes cannot be correlated. This may be attributable to the under-developed fluidization state at such low gas superficial velocities. Alternatively, it could be caused by the fact that the size of the bubbles is too small which was apparently undetectable. But overall, the maximum statistic average approach coefficients are attainable as shown in Figure 6.22. Therefore, the bubble rising velocity was estimated by considering the separation distance (40 mm) between the two measuring planes. The results obtained are plotted in Figure 6.23. Furthermore, for the purpose of evaluating the performance of the statistic average approach in deriving the bubble rising velocity, the results are compared with the aforementioned four methods.

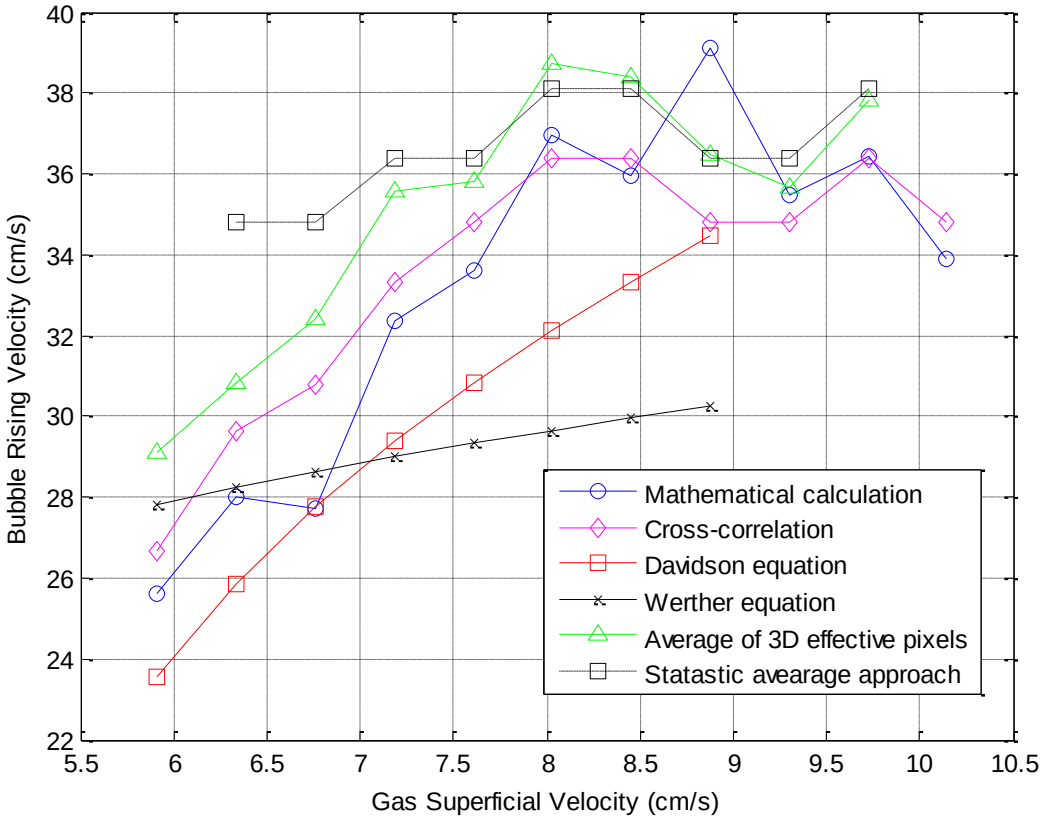

Figure 6.23: Comparison of the estimated bubble rising velocity results between five different approaches at various gas superficial velocities

Comparing with the results obtained from the other four approaches, the results estimated from the statistic average approach were larger, especially at lower gas superficial velocities. However, when the gas superficial velocity was more than 7.5 cm/s, a good agreement could be seen between the results from the statistic average approach and the results estimated via the average of 3D effective pixels and the detailed mathematical calculation. The smallest percentage difference of results between the statistic average approach and the average of 3D effective pixels is 0.4% when the gas superficial velocity is at 8.87 cm/s while the smallest percentage difference of the results between the statistic average approach and the mathematical calculation is 3.1% at the gas superficial velocity of 8.03 cm/s. The statistic average approach has demonstrated its applicability for estimating bubble rising velocity although there are still some discrepancies with other approaches. The performance could be enhanced if the current sampling rate of the ECT system could be increased.

6.5.5 Closure

In section 6.5, bubble rising velocity has been studied extensively using four different approaches. The performance of each approach has been evaluated. The results obtained from the cross-correlation technique using the averaged volume fraction data have given a good agreement with the results calculated from the empirical correlation of Davidson.

The detailed mathematical calculation method shows a good data fit with the results obtained from both empirical correlations and the cross-correlation technique using the averaged volume fraction data. A three-dimensional profile of the bubble rising velocity has been obtained on a pixel-by-pixel basis by means of the cross-correlation technique. The results have revealed some aspects of the three dimensional characteristics of bubble behaviour. A newly proposed statistic average approach showcased its applicability and potential capability in deriving the bubble rising velocity by using two sets of the original 32 x 32 images.

6.6 Bubble size estimation via obtained bubble rising velocity results

As identified from the empirical equations for deriving bubble rising velocity in Table 2.1, there is a link between the two parameters of bubble diameter and bubble rising velocity. On one hand, the bubble rising velocity achieved by means of cross-correlation in Figure 6.17 shows a good agreement with the results obtained from the empirical equations. On the other hand, the pixel-based bubble rising velocity distribution profiles demonstrate a ‘trend’ with increased gas superficial velocity. As presented in Figure 6.20, when the gas superficial velocity is low, there is a small area of effective pixels having axial bubble rising velocity whist when the gas superficial velocity is increased, the area of effective pixels increases.

This section seeks to explore if the bubble size can be estimated by means of the obtained bubble rising velocity results. The first section is about the determination from the cross-correlation results. The second section is about the determination from the pixel-based velocity profile boundary.

6.6.1 Determination from the cross-correlation results

According to the two empirical correlations in Table 2.2, it is achievable to back-calculate the bubble diameter with the bubble rising velocity obtained by means of the cross-correlation results. The back-calculated bubble diameter are presented and compared with the results from the five bubble diameter empirical correlations in the following Figure 6.24.

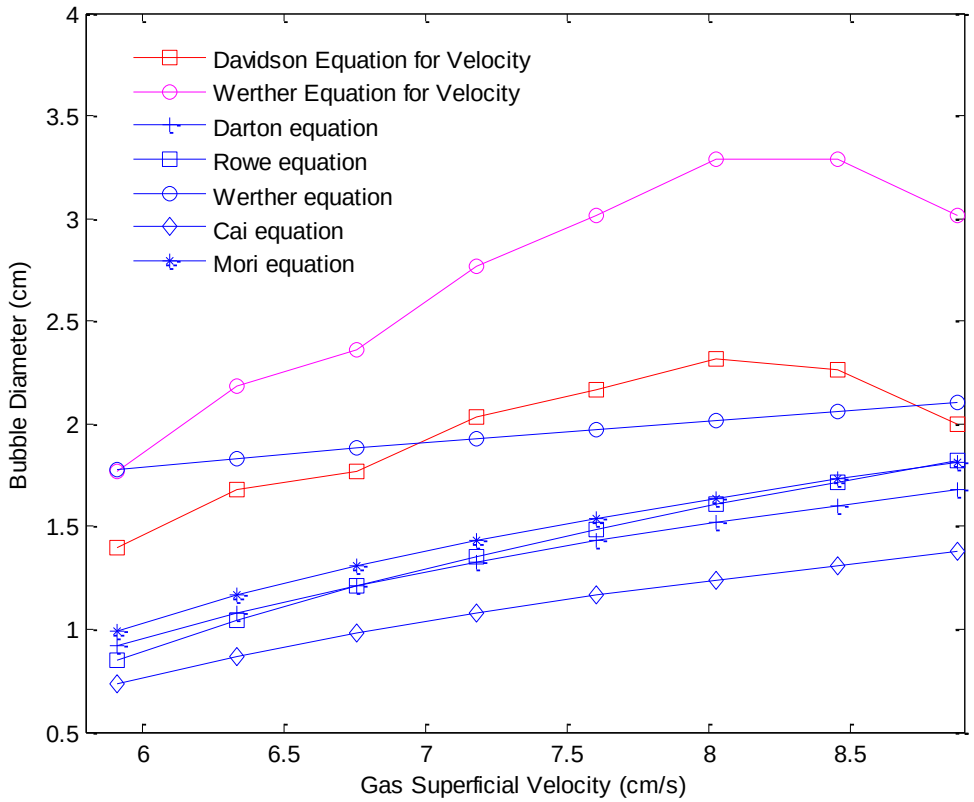

Figure 6.24: Comparison between the back-calculated bubble diameter and the results from the five bubble diameter empirical correlations

It is surprising to observe that the back-calculated bubble diameter results show a good trend with the five empirical equations. Moreover, the results back-calculated from Davidson equation gives a better agreement than Werther equation's back-calculation. It is also worth noting the back-calculated bubble diameter results has the best fit with the empirical equation results from Werther equation. When the gas superficial velocity is high, i.e. above 8.5 cm/s, the back-calculated bubble diameter decreases which may stem from the similar trend of the bubble rising velocity versus gas superficial velocity.

In summary, the back-calculated bubble diameter from the bubble rising velocity shows fairly well agreement with the five empirical equations. Furthermore, it reaffirms the effectiveness of deriving bubble rising velocity by means of the cross-correlation techniques.

6.6.2 Determination from the pixel-based velocity profile boundary

This section attempts to derive the bubble diameter by means of the pixel-based velocity profile boundary as shown in Figure 6.20. The equivalent bubble diameter was calculated by the similar process in Figure 6.4. The obtained bubble diameter results is shown and compared with the results from other five empirical equations in Figure 6.25.

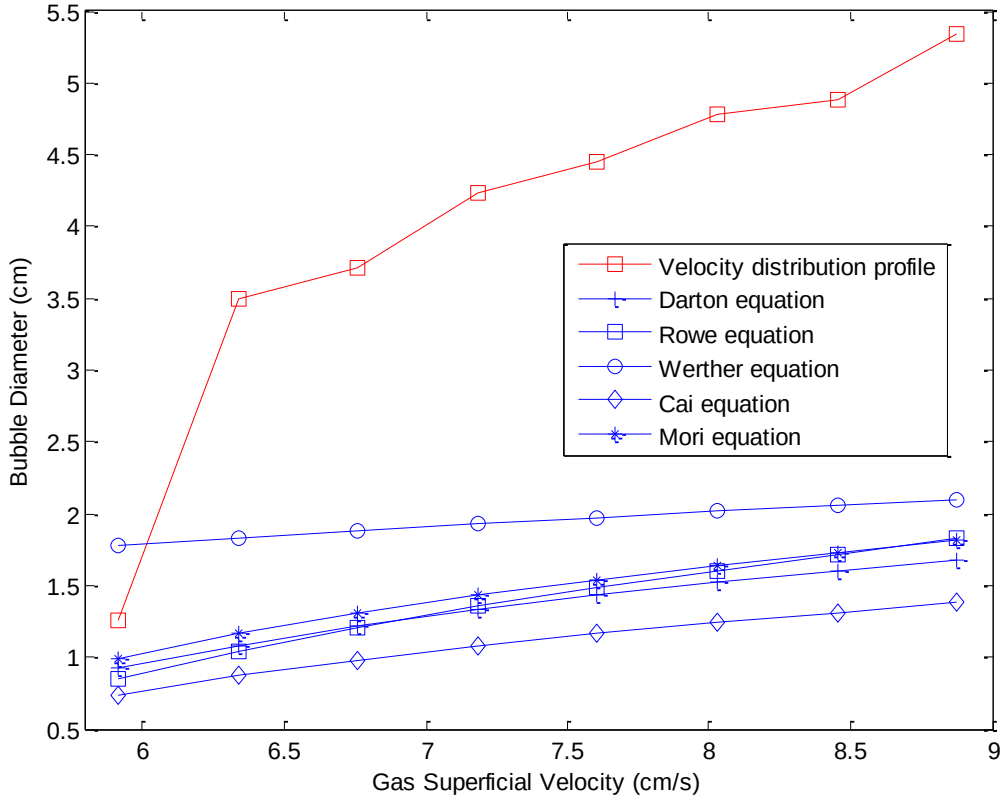

Figure 6. 25: Comparison between the derived bubble diameter via velocity distribution profile boundary and the results from the five bubble diameter empirical correlations

It is clearly seen that except the result when the gas superficial velocity is at 5.91 cm/s, all the derived bubble diameter results deviate much away from the five empirical equations results. To some extent, this demonstrates the results derived from the pixel-based velocity profile boundary are not promising.

6.7 Summary

Firstly, the 10 iterative LBP algorithm was chosen to extract bubble diameter in order to compare the results with the conventional LBP algorithm. All the reference cut-off values derived from plastic ball calibration process with two different measurement locations and two algorithms are provided.

Bubble diameter obtained by means of individual cut-off values suggested that the cut-off values from No. 1 plastic ball were not able to produce reasonable bubble diameter estimation. Instead, the cut-off values from No. 4 and No. 5 plastic balls present a better agreement of the estimated bubble diameter compared with the results calculated from the five widely used empirical correlations, especially that of Werther. Linear and second-order curve fittings were carried out to further examine the effect of the cut-off values obtained from the plastic ball calibration process on the estimation process of bubble diameter in bubbling regime. Results obtained from the linear fitted curves of cut-off values demonstrate a reasonable agreement with the results calculated from Werther's equation using both the LBP algorithm and 10 iterative LBP algorithm. In general, results estimated from the second-order fitted curves showed a better data agreement than the linear fitted curves compared with the five empirical correlation results. The estimated bubble diameter using cut-off values near wall showcase better performance than the cut-off values near centre either individual cut-off values or the linear or second-order fitted curves.

The cross-correlation technique was applied to predict the bubble rising velocity by using the averaged volume fraction data. The results showed a good consistency compared with two empirical correlations, especially the one of Davidson. The results of bubble rising velocity obtained from the detailed mathematical analysis demonstrate a good fit compared with the results acquired by means of the cross-correlation and empirical correlations. Three dimensional distributions of the bubble rising velocity were investigated by means of the cross-correlation technique on a pixel-to-pixel basis. The averaged bubble rising velocity on the 3D effective pixels were compared with three other approaches and good agreement was achieved. A newly introduced statistic average approach was examined to derive the bubble rising velocity by using two sets of original 32 x 32 images captured at both ECT measuring planes. It demonstrated its potential capability in estimating the bubble rising velocity by comparing with the other four different methods.

Chapter 7
Comparative Study Between ECT and Pressure Fluctuation Measurements

This chapter aims to present an extensive comparative study between the ECT and pressure fluctuation measurements. The primary purpose of the study is to examine and identify the advantages and drawbacks of each technique in acquiring different types of hydrodynamic information connected with gas-solids fluid flow. The ultimate target is to establish an informed choice for further research when it comes to determining different measurement approaches in deriving specific data.

Specifically, this chapter starts by dealing with the qualitative signal amplitude comparison analysis measured by both methods. The data of the averaged volume fraction at both ECT measuring planes measured by the ECT system and the data of the pressure fluctuation at both two equivalent locations of plane 1 and plane 2 measured by pressure transducers will be chosen for comparison. Then, dominant frequency by means of the power spectral density function which is one of the widely used approaches in the frequency analysis domain will follow. After that, information of the solid concentration and bubble rising velocity derived from both methods will be studied in the last two sections. Finally, a comprehensive summary to compare and evaluate the two measurement techniques will be provided.

7.1 Signal Amplitude Results

7.1.1 Amplitude measured by ECT

The amplitude of averaged volume fraction at various gas superficial velocities measured at both plane 1 and plane 2 levels are plotted in Figure 7.1 and Figure 7.2, respectively. The X-axis denotes the sampling time in seconds and the Y-axis denotes the value of the averaged volume fraction which has been explained in Chapter 5 in Equation 5.3.

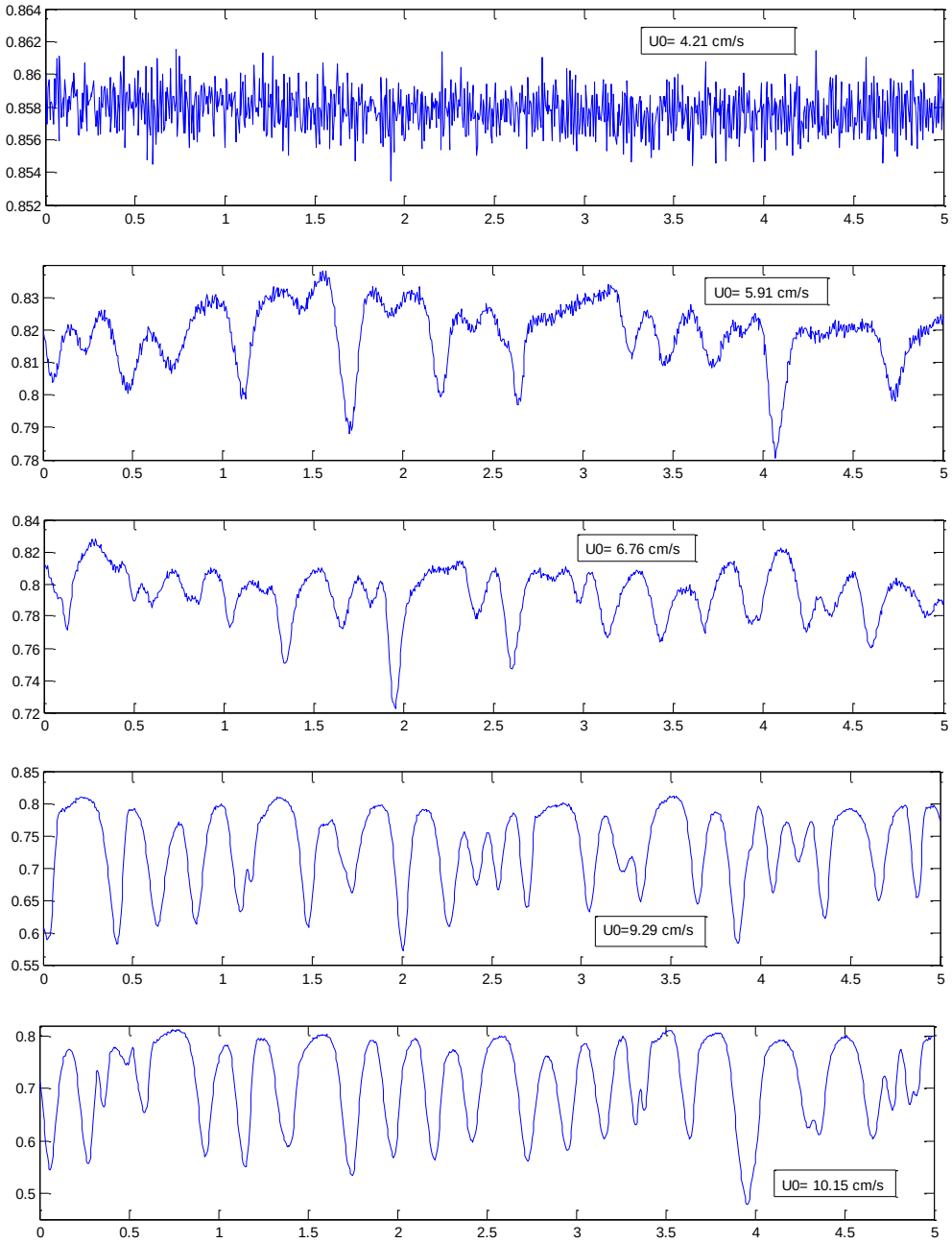

Figure 7.1: Time series plot of amplitude of averaged volume fraction at ECT plane 1 level

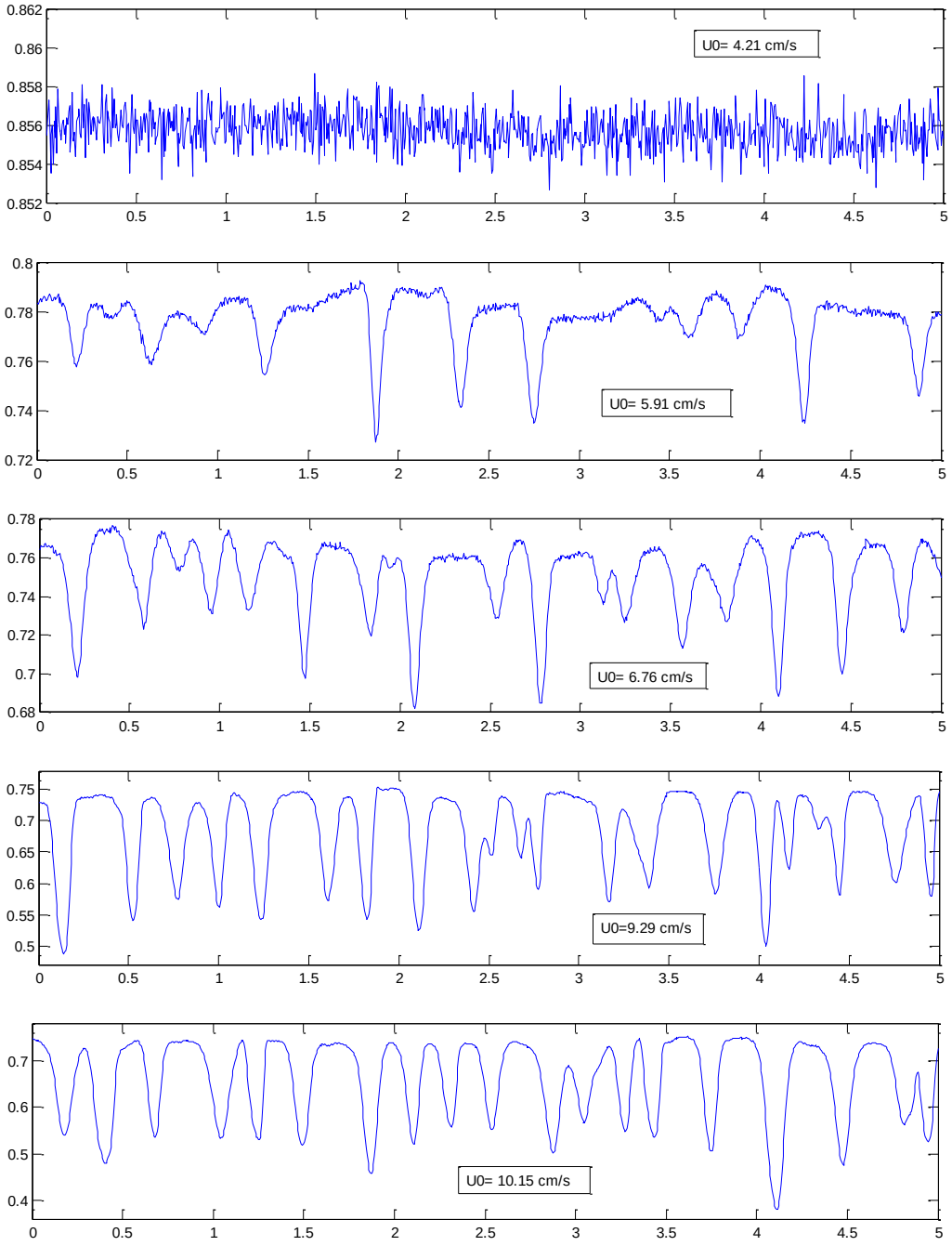

Figure 7.2: Time series plot of amplitude of averaged volume fraction at ECT plane 2 level

As can be seen in Figure 7.1, the amplitude of the averaged volume fraction at the plane 1 level varies significantly at the five different gas superficial velocities. The amplitude is small and fluctuates being constrained around the value of 0.858 due to the bed still being in the fixed bed state. Once the bed is at the gas superficial velocity of 5.91 cm/s, the amplitude expands significantly into a wider range of 0.78 to 0.83. The indications of single

bubbles are visible as valleys in the curves of the averaged volume fraction. The number of bubbles were increasing, which is evidenced by the further expanded amplitude of the averaged volume fraction and by the increased number of valleys at a gas superficial velocity of 6.76 cm/s. The amplitude increases further into the range of 0.57 to 0.82 when the gas superficial velocity is increased to 9.29 cm/s. Moreover, the plot exhibits a periodical movement, which suggests the bed is already in the slugging regime. Higher gas superficial velocity at 10.15 cm/s helps produce more and larger slugs signified by the more intense periodical movement.

The information of the amplitude at the ECT plane 2 level as presented in Figure 7.2 reveals larger amplitudes at various gas superficial velocities compared with the plane 1 results. In addition, averaged volume fraction at the lowest points of valleys are lower than the plane 1 results and this indicates the size of bubbles is larger than the ones which appeared at the plane 1 level. Similarly, the slugging regime can also be spotted transparently with the more obvious periodical movement at higher gas superficial velocities, such as 9.29 cm/s and 10.15 cm/s, respectively.

7.1.2 Amplitude measured by pressure fluctuation

The amplitude of pressure fluctuation at various gas superficial velocities is plotted in Figure 7.3 and Figure 7.4. The X-axes represent the sampling time in units of seconds and the Y-axes represents the pressure in units of pascal. Figure 7.3 shows the plot measured at pressure port 4 (Z = 88.5 mm indicated by Figure 4.13) which is equivalent to the ECT plane 1 level while Figure 7.4 shows the plot measured at pressure port 5 (Z = 128.5 mm indicated also by Figure 4.13) which is equivalent to the ECT plane 2 level.

In Figure 7.3, the pressure fluctuates in a very limited range of 1270 pa to 1310 pa when the bed is in the fixed bed state (gas superficial velocity of 4.21 cm/s). With the increased gas superficial velocity at 5.91 cm/s, the amplitude expands into a wider range of 1300 pa to 1420 pa. Bubbles can still be detected at a moderate level by the local pressure fluctuation valleys although the pressure fluctuation signals are of complex nature as they might originate from the local pressure change or from the pressure propagation of faraway measurement locations (i.e. pressure port 3 or port 2). The evidence of bubbles is becoming clearer when the bed is at a gas superficial velocity of 6.76 cm/s accompanied by a larger amplitude range of 1250 pa to 1450 pa. When the gas superficial velocity was increased to 9.29 cm/s, the amplitude

of pressure fluctuation increased extensively into a range of 1300 pa to 1590 pa and meanwhile, slugs were detectable by the periodical change of the pressure fluctuation curve. The periodical change is intensified at a gas superficial velocity of 10.15 cm/s. The amplitude is increased to a larger range.

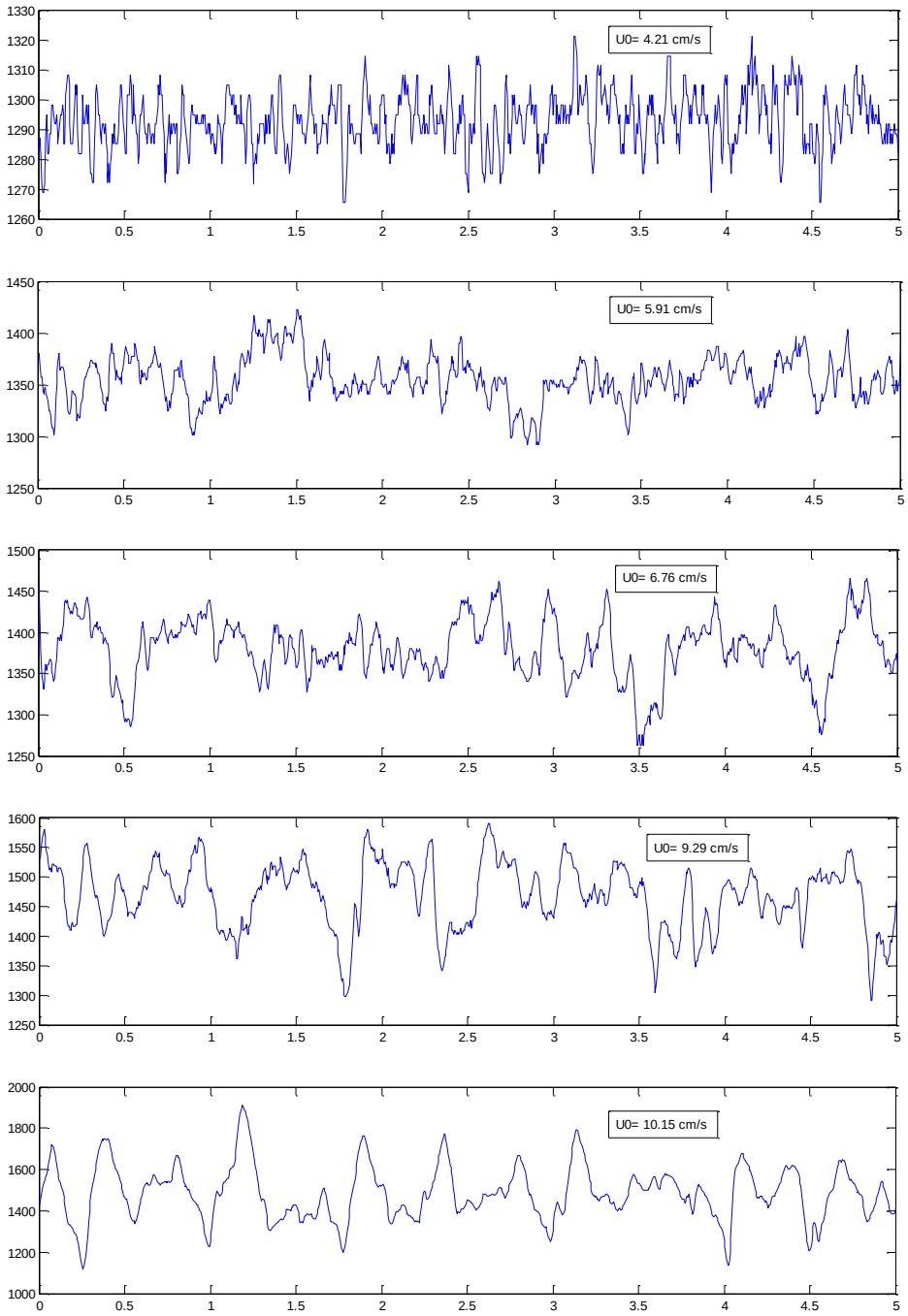

Figure 7.3: Time series plot of amplitude of pressure fluctuation at port 4 (equivalent to ECT plane 1 level)

By observing the amplitude of pressure fluctuation at port 5 as shown in Figure 7.4, the amplitude range at a gas superficial velocity of 4.21 cm/s is small and

is similar to the one shown in Figure 7.3. However, the absolute values (around 675 pa) are smaller than the one measured at port 4 (1290 pa). This is understandable since the bed height above port 5 is lower than port 4. The results measured at port 5 are more recognizable than the ones at port 4, such

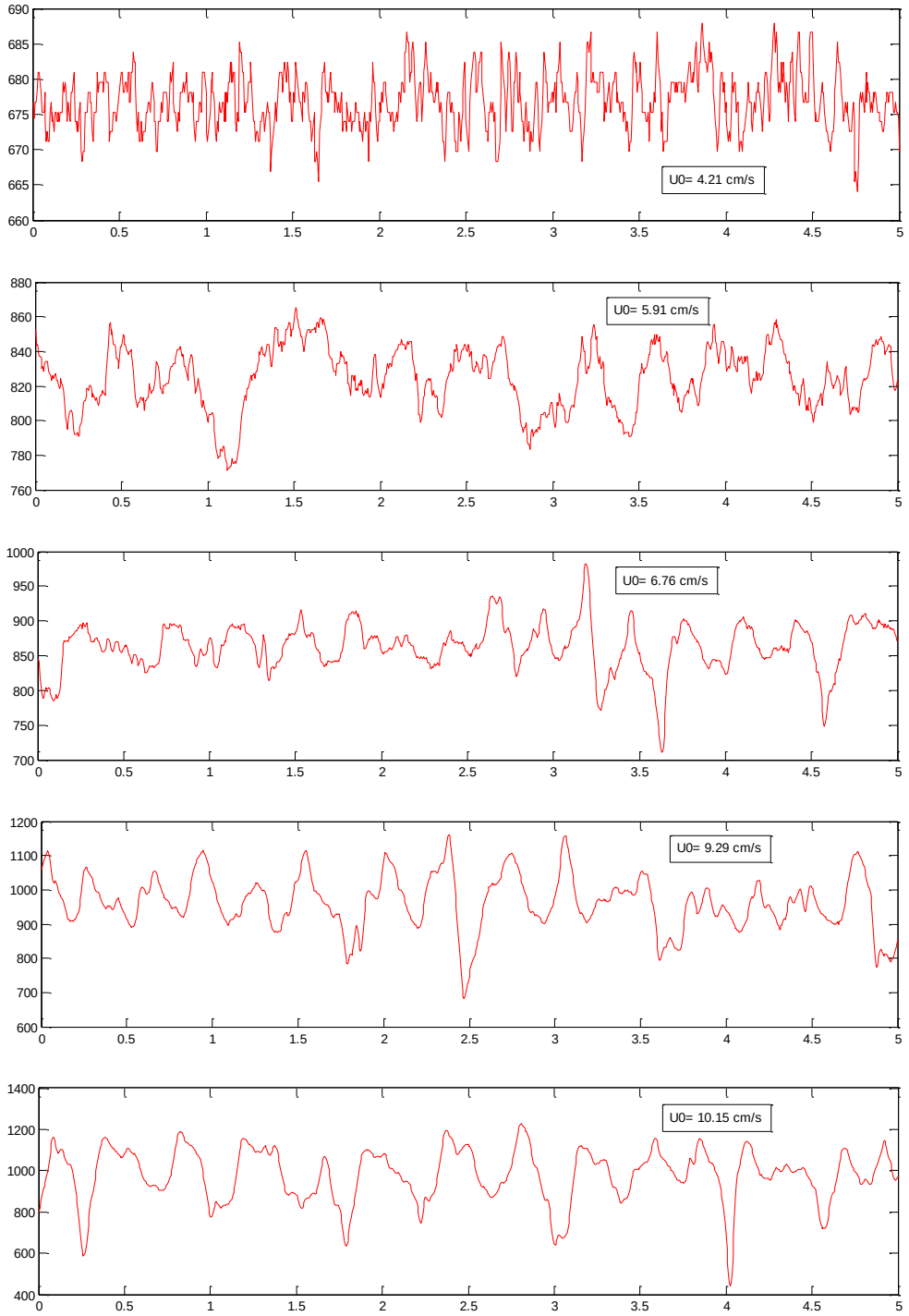

Figure 7.4: Time series plot of the amplitude of pressure fluctuation at port 5 (equivalent to ECT plane 2 level)

as the bubbles and slugs indicate (local signal valleys of and periodical movement of the pressure fluctuation). This can be explained as the bubbles

or slugs take more fractions of the gas-solids two phases as they expand, grow or coalesce while they travel upwards to higher positions.

7.1.3 Comparison between ECT and pressure fluctuation

The average volume fraction measured by the ECT system and the pressure fluctuation measured by the pressure transducers are the most direct data types obtained for both methods. Although the units of both data types are not comparable inherently, they can still be compared in a qualitative manner.

In the plots of the averaged volume fraction as shown in Figure 7.1 and Figure 7.2, three fluidization states (fixed bed, bubbling regime and slugging regime) can be recognized by the qualitative analysis on the amplitude of the averaged volume fraction at various gas superficial velocities. In addition, data measured at a higher level (ECT plane 2) gives a clearer indication of the different flow patterns. The amplitude plotting of the pressure fluctuation measured at port 4 and port 5 shown in Figure 7.3 and Figure 7.4 can do a similar job to the signal of the averaged volume fraction. By seeing the amplitude change at both measurement levels, three recognizable flow regimes (fixed bed, bubbling regime and slugging regime) can be differentiated at various gas superficial velocities. Similarly, the amplitude at the port 5 measurement location demonstrates a more explicit indication. However, unlike the straightforward data presentation of ECT measurements, it has to be admitted that pressure fluctuation signals are much more complex and inexplicit in interpreting the occurrence time steps of bubbles. The transducers may measure the deflection of the surface due to both gas molecules and solid particle collisions. The former could be sound waves or hydrodynamic mass motion, hence pressure fluctuations register more than gas-solid spatial distribution. ECT, however, is insensitive to the gas motion.

Hence, a good consistency can still be seen here by comparing the amplitude analysis obtained by the two methods. The amplitude plots can still give useful and supplementary information in the sense of qualitative analysis. The analysis demonstrates again these two non-intrusive measurement techniques are valid and effective in describing bed behaviour. This is vital either in laboratory scale or industrial scale fluidization applications.

7.2 Dominant Frequency Results

Power spectral density (PSD) is one of the most commonly used parameters in frequency domain analysis in gas-solids fluidized bed investigation as reviewed in Chapter 2. The dominant frequency derived from the PSD is effective in characterizing bubble behaviour [16, 186]. Hence, this section aims to demonstrate and evaluate the dominant frequency results obtained from ECT and pressure fluctuation measurements.

The most popularly used non-parametric method in estimating the PSD is Welch's power spectral density estimate. To reduce the variance in estimating the PSD, the original signal is divided into segments. The length of the segment really depends on the competing factors of frequency resolution and variance. The mathematical expression is as follows [8]:

$$P_{xx}(f) = \frac{1}{N}\sum_{i=1}^{N} P_{xx}^{i}(f) \qquad (7.1)$$

where N is the number of segments and $P_{xx}^{i}(f)$ is the power spectral estimate of each segment. In the present study, the PSD estimation was facilitated by MATLAB software. The number of segments chosen was eight by default with a 50% overlap.

7.2.1 Dominant frequency from ECT measurements

Power spectral density (PSD) of the averaged volume fraction measured by the ECT system is presented in Figure 7.5 at various gas superficial velocities ranging from 5.91 cm/s to 12.69 cm/s. To simplify data presentation, only measurements at plane 2 level are showcased.

Figure 7.5 shows that a broad band of power spectra is observed when the gas superficial velocity is low at 5.91 cm/s. This phenomenon indicates the bed in a bubbling regime with many small bubbles, which is in line with the conclusions drawn by Qiu et al. and Makkawi and Wright [16, 186].with the increasing gas superficial velocity, the magnitude of the power spectra is increasing accordingly. Meanwhile, the band of the power spectra becomes narrow and sharp. More specifically, when the gas superficial velocity increases to 10.99 cm/s and 12.69 cm/s, the dominant frequency of the PSD is already obvious to see. At this stage, slugging regime dominates the gas-solids fluidized bed.

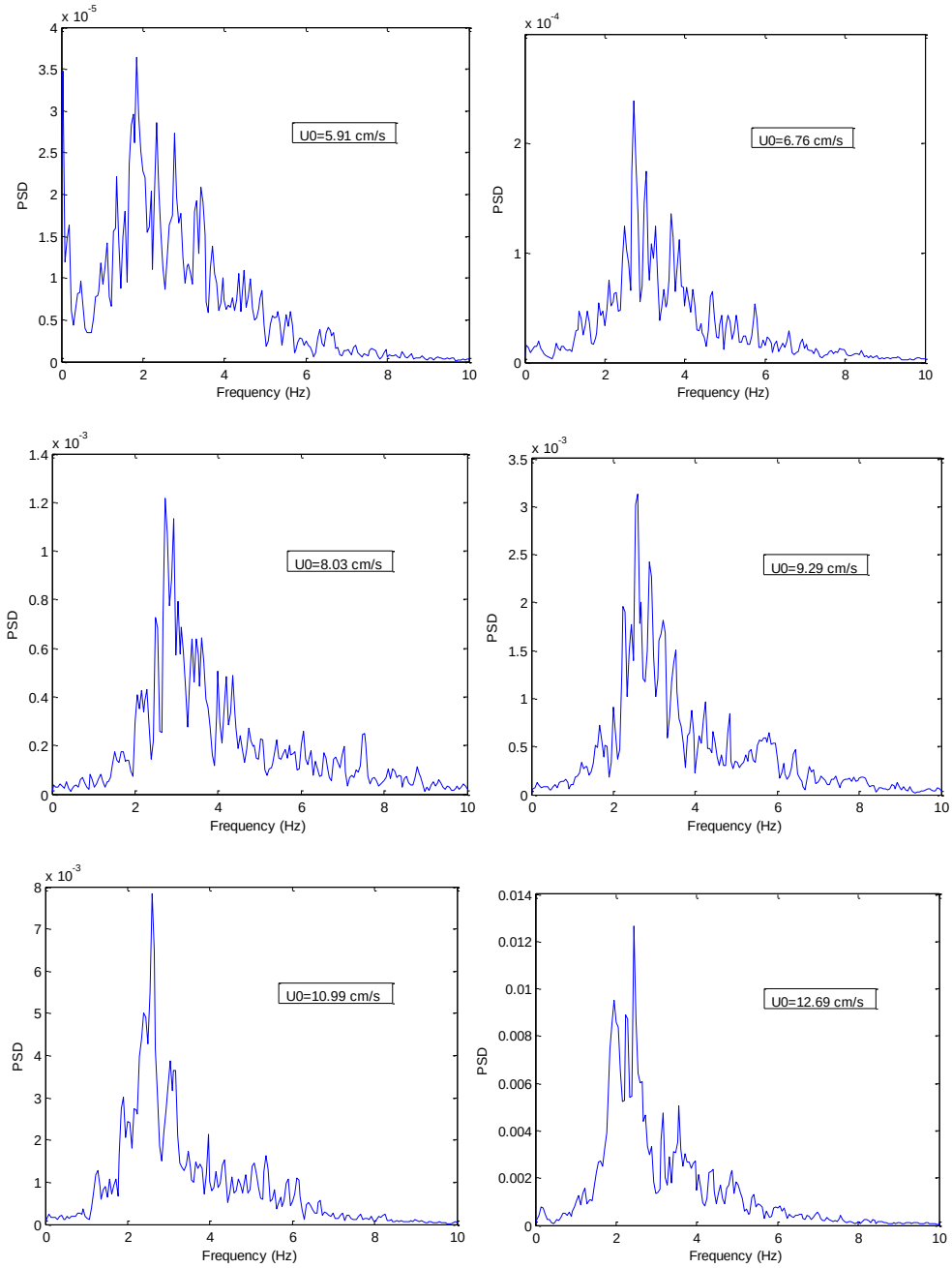

Figure 7.5: Power spectral density (PSD) obtained from ECT measurements for various gas superficial velocities

In order to further investigate the functionality of the power spectral density function, the dominant frequency are extracted for both ECT measuring planes and they are plotted in Figure 7.6 and Figure 7.7, respectively.

In Figure 7.6, the trend of the dominant frequency curve with various gas superficial velocities shows that a point (targeted by the arrow) can be recognized to demarcate the bubbling regime and slugging regime. Initially, the dominant frequency increases significantly at the very early stage of the bubbling regime and then decreases gradually until the gas superficial velocity

is around 9 cm/s. This may be caused by the reduction in bubble numbers due to the bubble growth and bubble coalescence. After that point, the dominant frequency fluctuates slightly. The exact gas superficial velocity is 8.89 cm/s, which agrees outstandingly with the previous conclusion drawn in Chapter 4. Moreover, the results shown in Figure 7.6 are in support of one previous finding [186]. It demonstrates that the dominant frequency obtained from the PSD is capable of characterizing the bubble behaviour.

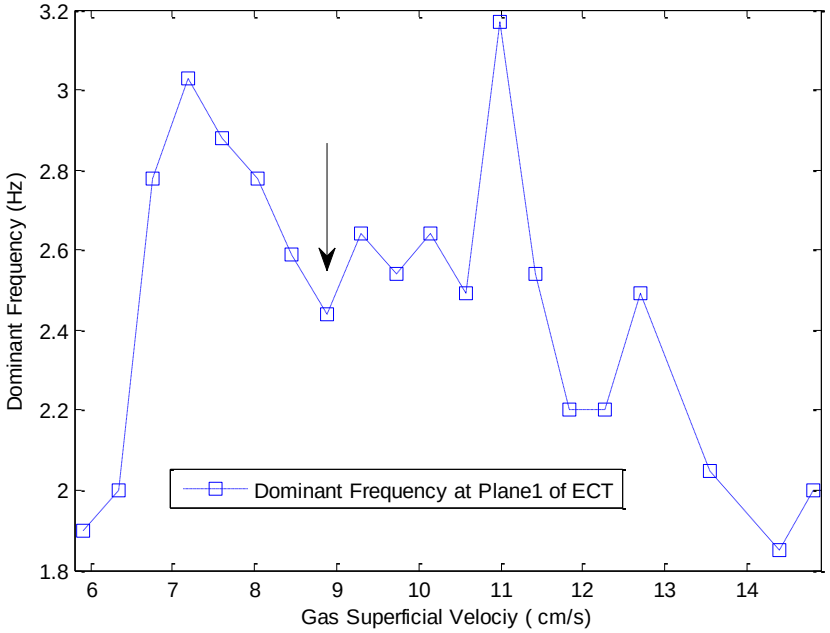

Figure 7.6: Dominant frequency at plane 1 of ECT

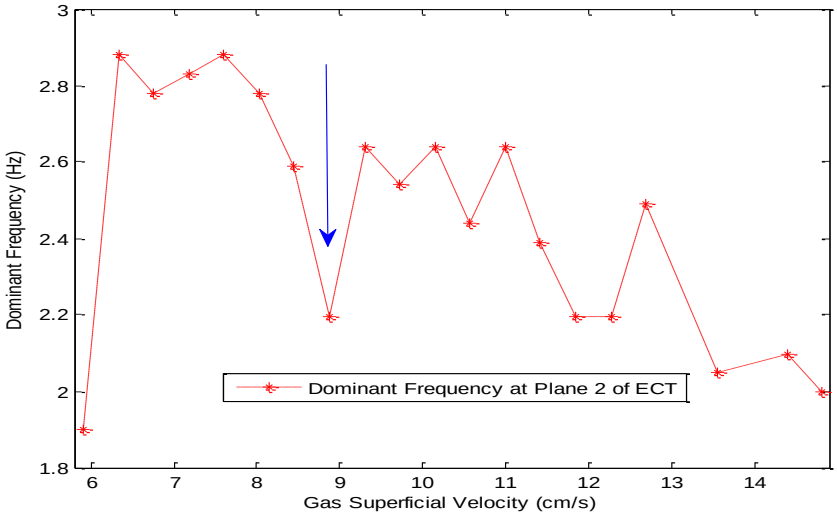

Figure 7.7: Dominant frequency at plane 2 of ECT

The conclusions drawn from the data presented in Figure 7.6 are further confirmed and supported by the results obtained at ECT plane 2 level as

shown in Figure 7.7. A similar point can be identified by observing the dominant frequency curve with the increasing gas superficial velocity, the point derived from Figure 7.7 is at 8.89 cm/s as well due to the simultaneous data capture protocol employed.

7.2.2 Dominant frequency from pressure fluctuation

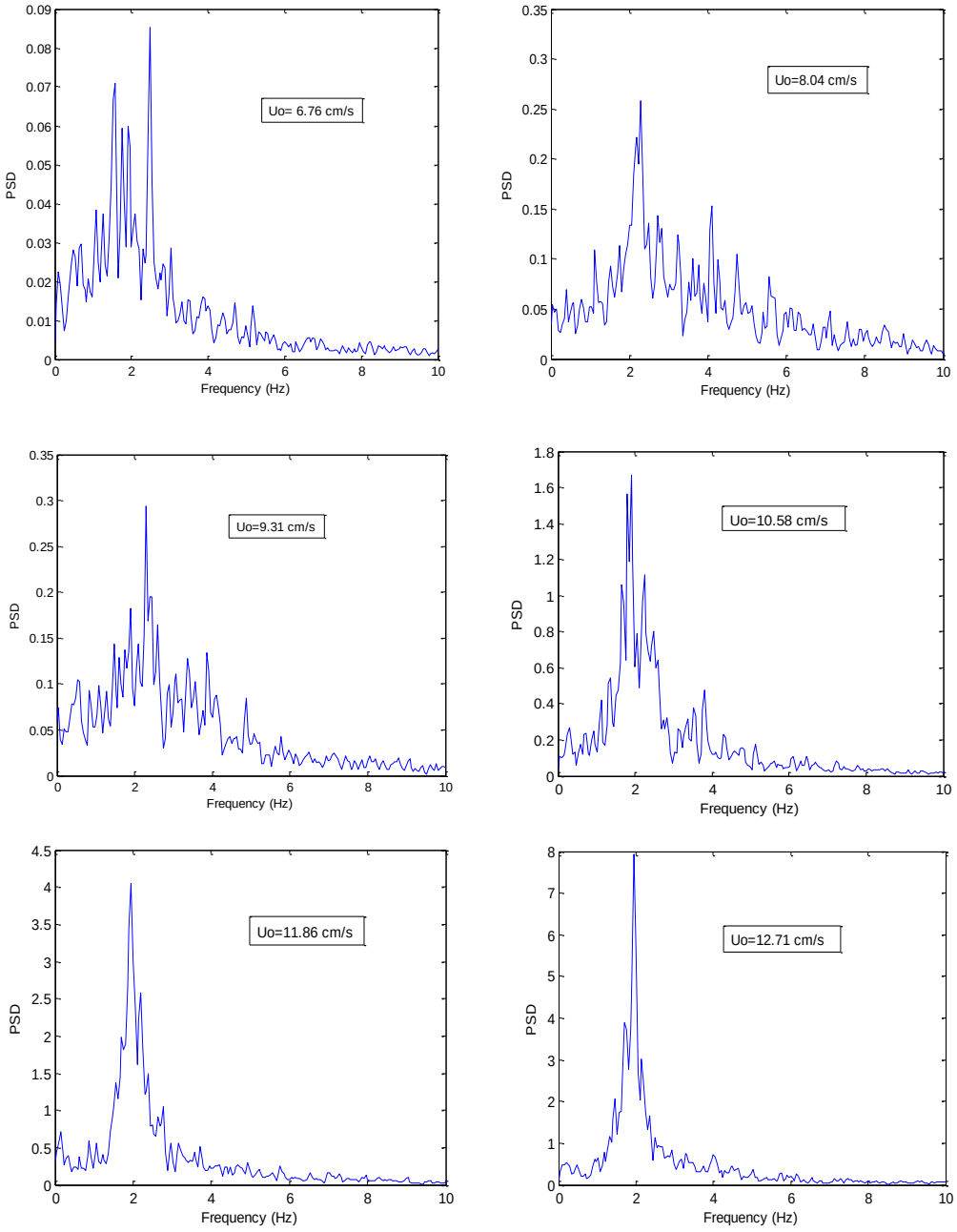

Figure 7.8: Power spectral density (PSD) obtained from pressure fluctuation measurements for various gas superficial velocities

Power spectral density obtained from pressure fluctuation at various gas superficial velocities is presented in Figure 7.8. The measurements taken at ECT equivalent plane 2 level is shown to reflect the data shown in Figure 7.5. It can be seen from Figure 7.8 that the wide band of the PSD exists until the gas superficial velocity is increased to 8.04 cm/s. Once the bed is in slugging regime, the dominant frequency of the PSD becomes sharp and clear and the band of the power spectral is narrow. The magnitude increases with the increased gas superficial velocity.

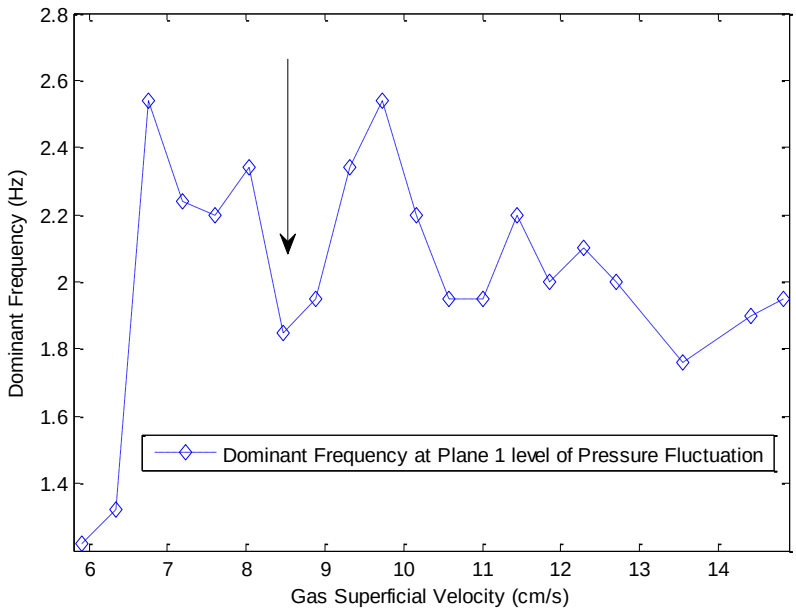

Figure 7.9: Dominant frequency at plane 1 of pressure fluctuation

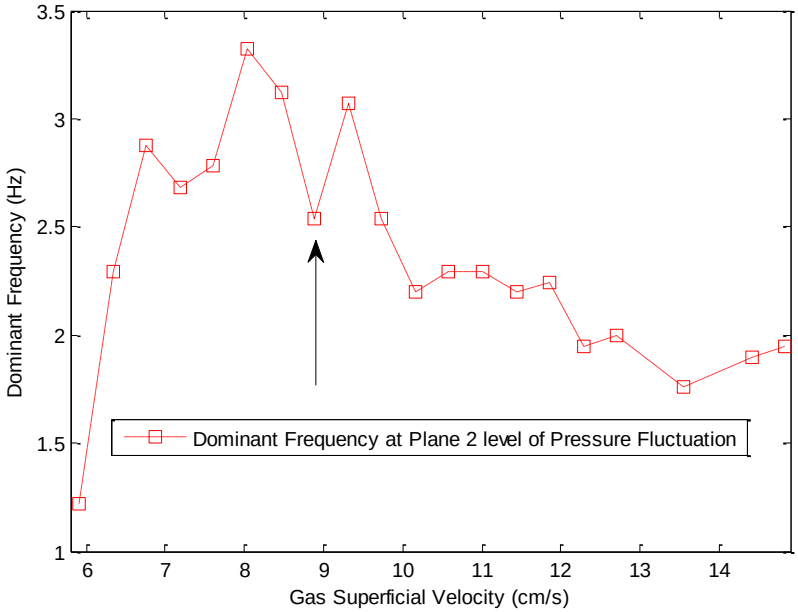

Figure 7.10: Dominant frequency at plane 2 of pressure fluctuation.

Dominant frequency estimated from the PSD at ECT equivalent plane 1 level is summarized in Figure 7.9. Clearly, the point for distinguishing the bubbling regime and slugging regime can be identified when the gas superficial velocity is between 8 cm/s and 9 cm/s. The exact gas superficial velocity of that point is 8.46 cm/s. A similar observation on the dominant frequency at ECT equivalent plane 2, shown in Figure 7.10, underpins the conclusions drawn in Figure 7.9. The corresponding gas superficial velocity at the point shown in Figure 7.10 is 8.89 cm/s. Both values of the demarcation points agree well with the derived minimum slugging regime in Chapter 5. This again suggests that the PSD obtained from pressure fluctuation measurements is able to successfully describe the bed behaviour.

7.2.3 Comparison between ECT and pressure fluctuation

In order to examine and compare the results obtained from both non-intrusive methods, averaged dominant frequency using the data estimated at both measuring planes from ECT and pressure fluctuation measurements are obtained and plotted in Figure 7.11.

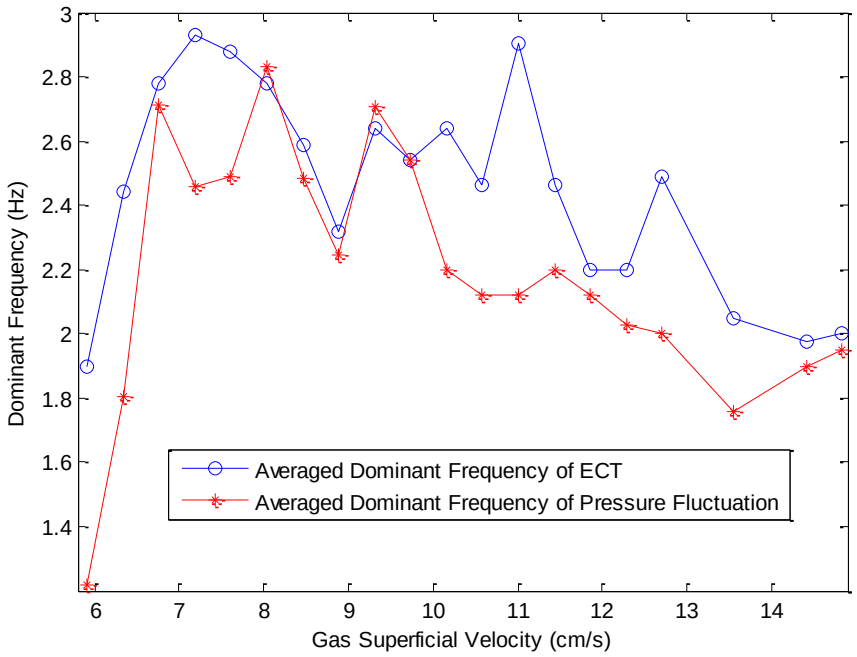

Figure 7.11: Comparison of the averaged dominant frequency between ECT and pressure fluctuation measurements

As indicated in Figure 7.11, the dominant frequency agrees well with both methods despite some minor discrepancies appearing when the gas

superficial velocities are at around 7.5 cm/s and 11 cm/s. The demarcation points derived from both methods almost coincide as showcased in Figure 7.11. A conclusion can be drawn here with confidence that both non-intrusive measurement techniques are capable of describing the bed behaviour in an effective way by means of the power spectral density function and the derived dominant frequency.

7.3 Solids Concentration Results

The local distribution of solids concentration has been regarded as one of most essential factors in gas-solids processes which includes fluidized bed and pneumatic conveying processes [193]. Because the solid concentration has determining effects on some phenomena such as heat transfer and agglomeration. The importance of it becomes even more significant in industrial scale applications where it supports safe and economic control and operation. The aim of this section is to explore the performance of both non-intrusive measurement techniques in deriving the local solids concentration information.

7.3.1 Solids concentration measured by ECT

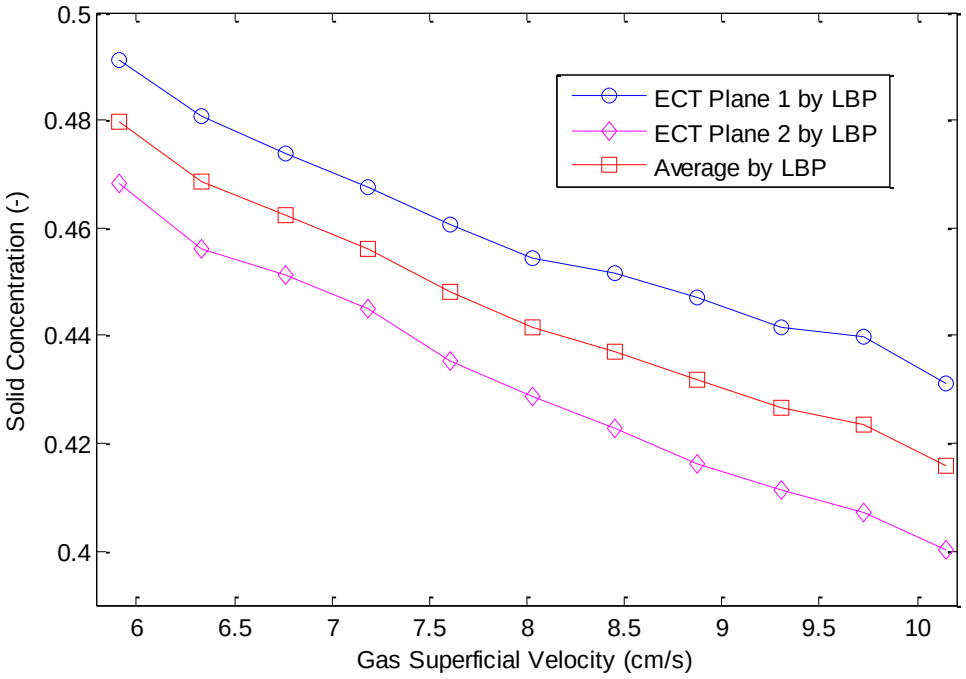

Figure 7.12: Solids concentration measured by ECT using LBP

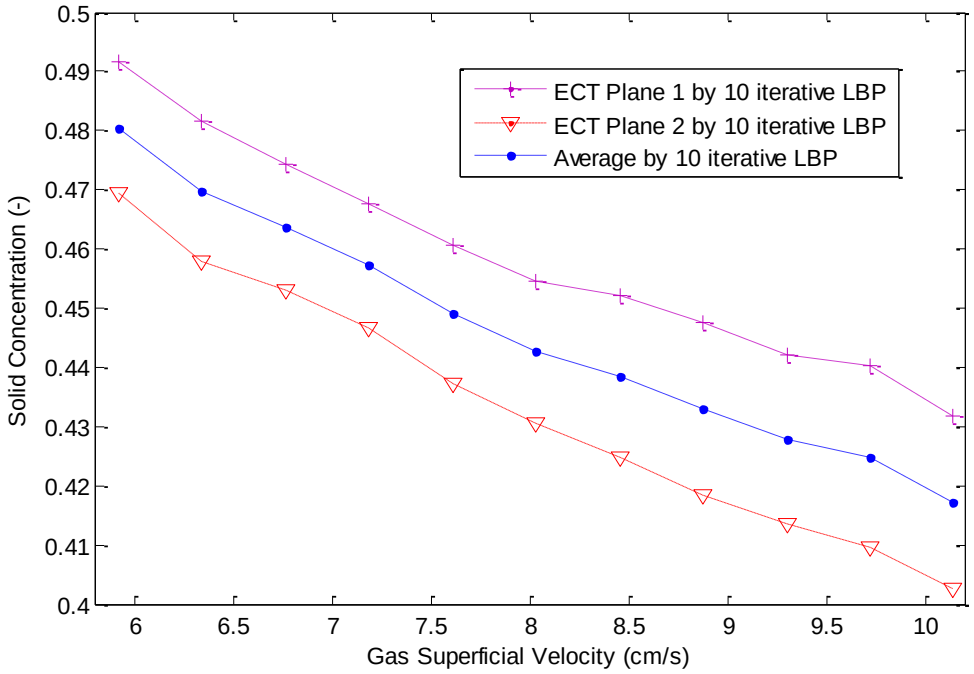

Figure 7.13: Solids concentration measured by ECT using 10 iterative LBP

Solids concentration can be derived straightforwardly from the averaged volume fraction data as they are essentially the same concept by means of the ECT measurements as indicated in Equation 5.3 in Chapter 5. However, a voidage value needs to be taken into consideration when converting the directly obtained averaged volume fraction into the solids concentration since the normalized averaged volume fraction is based on the calibration process by which the grey level of individual pixels is assumed as 1, when the bed is fully occupied by silica sand and 0, fully occupied by air. Even when the bed is fully occupied by the silica sand, there is still air surrounding the silica sand particles. Therefore, a widely used voidage value of 0.4 at the packed bed was chosen to derive the solids concentration.

For the purposes of exploring the performance of the two aforementioned image reconstruction algorithms, Figure 7.12 and Figure 7.13 present the solids concentration derived by ECT measurements using the conventional LBP and 10 iterative LBP algorithms at both ECT measuring planes respectively. In Figure 7.12, an average value is plotted as well. As it can be seen, the solids concentration declines from about 0.48 to 0.42 when the gas superficial velocity decreases from 5.91 cm/s to 10.15 cm/s. The results shown in Figure 7.13 indicate a similar trend of the curve of the solids concentration measured at plane 2 level when increasing gas superficial

velocity. It demonstrates the solids concentration derived from both image reconstruction algorithms agrees well with no exceptional changes.

7.3.2 Solids concentration measured by pressure fluctuation

Although the directly obtained data type is the pressure, the solids concentration can still be estimated with the pressure fluctuation measurements. The corresponding method was introduced by Bai et al. [194] and revised by Liu et al. [193] as described in the following mathematical expression. This was based on the assumption that only the solids present between two separated measurement locations attribute to the pressure drop. It was also demonstrated that the results obtained by this method in bubbling regime are more reliable than circulating fluidized bed by virtue of a relatively stable bubble size.

$$\delta = \frac{1000\Delta H}{\rho_s \Delta L} \qquad (7.2)$$

where δ is the solids concentration, ΔH is the pressure difference measured at locations, ρ_s is the density of silica sand, ΔL is the distance between two measurement locations.

The estimated solids concentration at various gas superficial velocities between pressure port 4 (equivalent to the ECT plane 1 level) and pressure port 5 (equivalent to the ECT plane 2 level) are summarized in Table 7.1. Standard deviation of the pressure difference between these two locations is provided to facilitate the understanding of the solids concentration. The solids concentration ranges from 0.5111 to 0.4798. Initially it decreases until one transition point at a gas superficial velocity of 8.45 cm/s is reached. The transition point has already been proved as the onset of the minimum slugging regime. After that, the solids concentration continues to decline with the increasing gas superficial velocity. Hence, solely from the solids concentration, transition between flow regimes can be described.

Table 7.1: Solids concentration obtained from pressure fluctuation measurements at various gas superficial velocities

Gas Superficial Velocity (cm/s)	Pressure Difference (Pa)	Standard Deviation (Pa)	Solids Concentration (-)
5.91	530.92	30.64	0.5111
6.34	521.92	40.01	0.5024
6.76	521.69	50.34	0.5022
7.18	521.92	67.24	0.5024
7.61	516.82	79.31	0.4975
8.03	508.84	102.64	0.4898
8.45	510.48	85.21	0.4914
8.88	512.43	62.89	0.4933
9.30	507.15	76.56	0.4882
9.72	504.19	98.14	0.4854
10.15	498.40	122.44	0.4798

7.3.3 Comparison between ECT and pressure fluctuation

For the purpose of comparing the results obtained from both ECT and pressure fluctuation measurements, the corresponding results are presented in Figure 7.14. As for the ECT measurement results, the solids concentration (averaged from both measuring planes) estimated with two different image reconstruction algorithms are plotted.

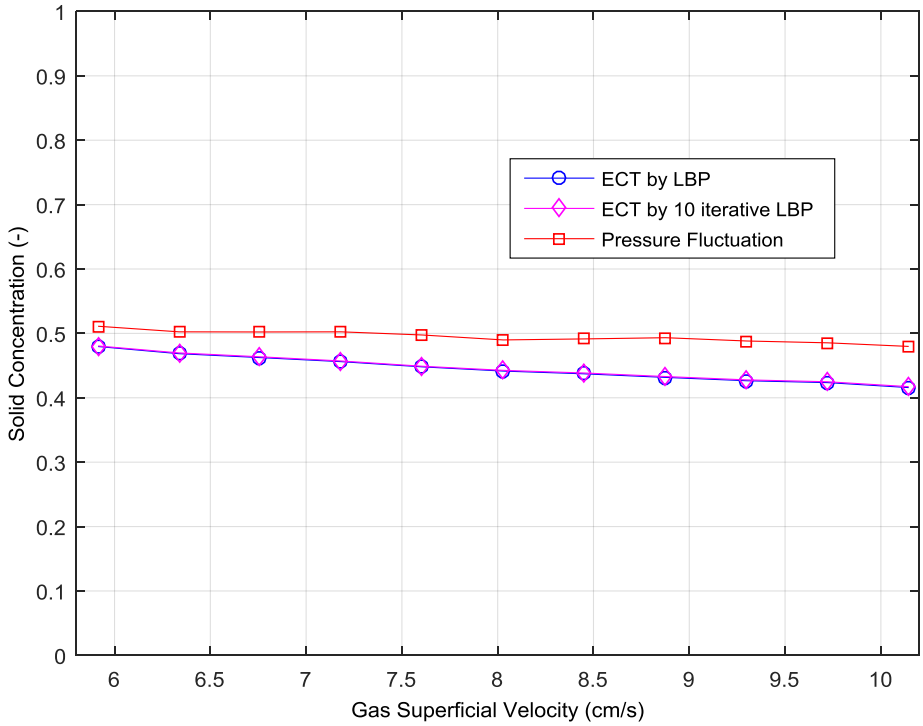

Figure 7.14: Comparison of the solids concentration measured between ECT and pressure fluctuation measurements

Figure 7.14 shows that the results obtained from both LBP and 10 iterative LBP algorithms agree well as they almost coincide at various gas superficial velocity. The decrease rate of the solids concentration with the increasing gas superficial velocity is almost linear. That means there is no obvious indication of the flow regime transition between bubbling and slugging regimes whereas the solids concentration estimated from the pressure fluctuation can provide this vital information as discussed in section 7.3.2. On the other hand, the percentage difference between the ECT and pressure fluctuation is within 14.9%, which agrees extensively with the results from Liu et al [193]. This demonstrates that both of the non-intrusive measurement techniques can provide confident information of the solids concentration.

7.4 Bubble Rising Velocity Results

Bubble rising velocity has been proved in previous chapters to be one of the most important parameters in characterizing the bubble behaviour in bubbling regime. Bubble rising velocity has been effectively estimated via the averaged volume fraction data measured by the ECT measurements, which has been introduced and discussed in Chapter 6. This section aims to derive the bubble

rising velocity by analysing the pressure fluctuation data since a small time lag can still be detected between Figure 7.3 and Figure 7.4.

Two estimation approaches (including cross-correlation technique and mathematical analysis) will be utilized to endeavour to estimate the bubble rising velocity at various gas superficial velocities. The data source is from the direct pressure fluctuation.

7.4.1 Cross-correlation method

The cross-correlation technique has been applied in Chapter 6 in deriving bubble rising velocity using the ECT measurement data. Although the original data used here was pressure fluctuation, the governing equations are similar as Equations (6.1) and (6.2) used for the data of the averaged volume fraction. Hence, the equivalent equations will not be repeated here again. In order to compare the derived results with the ones obtained from ECT measurement, pressure fluctuation measured at port 4 and port 5 (shown in Figure 4.13) are used. The corresponding normalized cross-correlation coefficients at different gas superficial velocities are presented in Figure 7.15.

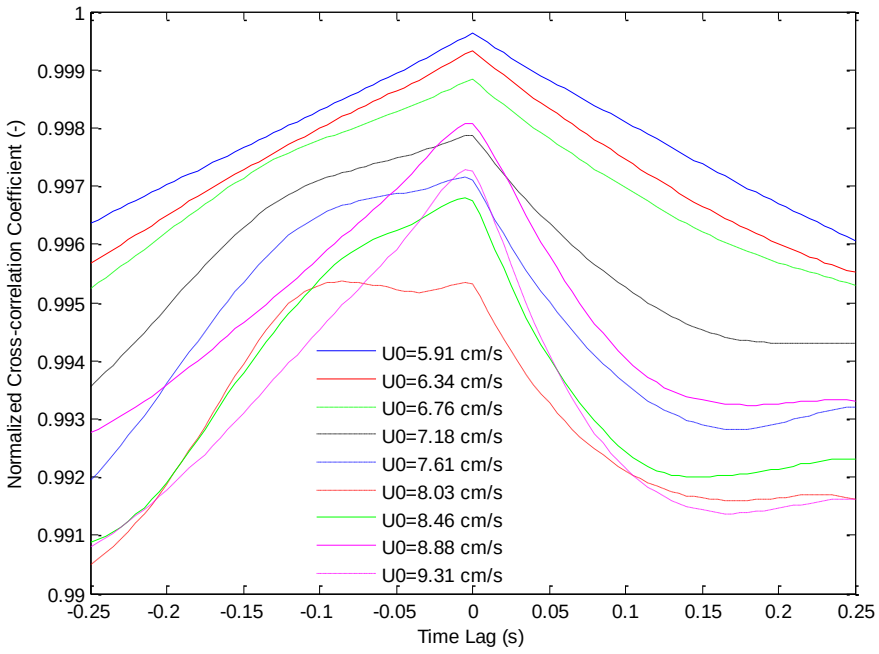

Figure 7.15: Normalized cross-correlation coefficients at various gas superficial velocity

In Figure 7.15 it is clear that at some gas superficial velocities, such as 5.91 cm/s, 6.34 cm/s and 6.76 cm/s, the maximum normalized cross-correlation coefficients have the corresponding time lags of zero. That means there is no similarity between the two time series of pressure fluctuation being detected. The results are summarized in Table 7.2. As indicated by Fan et al. [169] who suggested that two distant separated measurement locations are recommended in deriving bubble rising velocity by means of the cross-correlation technique, therefore, the cross-correlation between pressure port 4 and port 6, port 5 and port 6 and port 3 and port 6 are conducted for comparison. The time lags derived from them are shown in Table 7.2.

Table 7.2: Time lag obtained for different pressure port pairs from pressure fluctuation measurements at various gas superficial velocity

Gas Superficial Velocity (cm/s)	Time Lag Between Pressure Ports (s)			
	P4-P5	P4-P6	P5-P6	P3-P6
5.92	0	0	0	0
6.34	0	0	-0.07	0
6.76	0	-0.015	-0.1	0
7.19	0	-0.15	-0.1	-0.01
7.61	-0.005	-0.18	-0.09	-0.015
8.04	-0.085	-0.18	-0.085	-0.045
8.46	-0.005	-0.16	-0.08	-0.025
8.89	0	-0.015	-0.055	-0.01
9.31	-0.005	-0.015	-0.075	-0.015

In Table 7.2, zero denotes there is no time lag between two signals which can be derived. Negative values mean that the pressure fluctuation measured at the upper level is delayed by the corresponding absolute time lag value. It can be observed that even with increased separation between two measuring locations, the bubble rising velocity still cannot be obtained at lower gas superficial velocities. This is in contrast with the results shown by Fan et al. [169]. However, some reasons can be attributed to this. One of the reasons could stem from one possible condition suggested by Sasic et al. [8] that the time series of pressure fluctuation signal used could be the resultant signal between pressure fluctuation close to that specific location and pressure waves that propagated from other locations. This situation results in the two signals being almost identical at lower gas superficial velocities.

7.4.2 Mathematical analysis via MATLAB codes

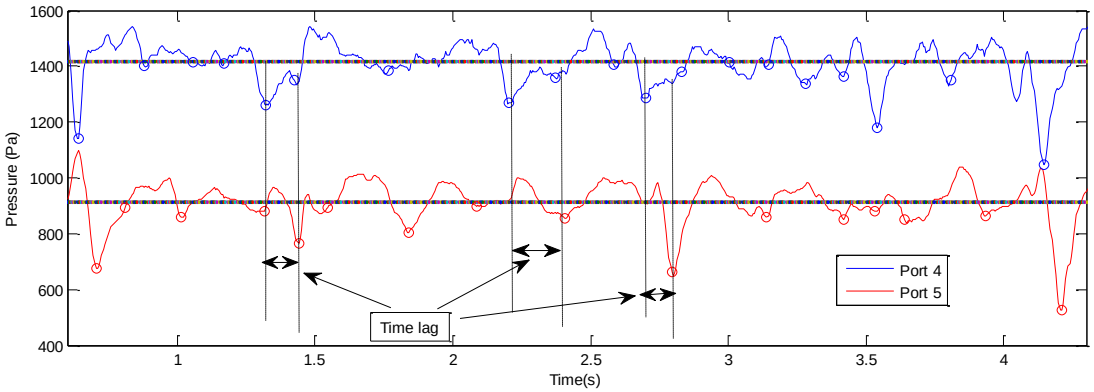

Figure 7.16: Mathematical analysis for deriving bubble rising velocity of pressure fluctuation measurements

Mathematical analysis of the original averaged volume fraction measured by the ECT system has showcased its potential in estimating bubble rising velocity in Chapter 6. Hence this section attempts to use it to derive the bubble rising velocity by using the pressure fluctuation measured at pressure port 4 and port 5. A schematic diagram is shown in Figure 7.16. This method is similar to the one explained by Equation (2.30). Therefore, this information will not be restated here. As presented in Figure 7.16, three typical bubbles are identified and the corresponding time lags are detected via MATLAB codes. The results at various gas superficial velocity are shown in Table 7.3 in order to compare the results with the cross-correlation technique and also the results obtained from ECT data.

7.4.3 Comparison between ECT and pressure fluctuation

For the purpose of comparing the capability of ECT and pressure fluctuation measurements in deriving bubble rising velocity, all the results estimated from cross-correlation and mathematical analysis at various gas superficial velocity are presented in Table 7.3. It is evident that the cross-correlation technique is not able to produce the bubble rising velocity with the pressure fluctuation measurement. At the same time, the estimated values (800 cm/s) of the bubble rising velocity are far more than the results obtained from ECT data. The reason behind this has been mentioned in section 7.4.2. However, in respect of the pressure fluctuation, the bubble rising velocity derived from it, using mathematical analysis, gave good agreement with the ECT results

either via the cross-correlation technique or the mathematical analysis. The smallest percentage difference is about 2.13% when the gas superficial velocity is at 6.76 cm/s. However, necessary visual assistance is needed most of the time to exclude some peaks which are obviously not reasonable. Meanwhile, the manual assistance of getting rid of unreasonable peaks would introduce human bias or errors which influence the results reversely. Therefore, in deriving bubble rising velocity, the ECT technique offers better potential than the pressure fluctuation measurement.

Table 7.3: Comparison of bubble rising velocity obtained from ECT and pressure fluctuation measurements at various gas superficial velocities

Gas Superficial Velocity (cm/s)	Bubble Rising Velocity (cm/s)			
	Pressure Fluctuation		ECT Measurement	
	Cross-correlation	Mathematical Analysis	Cross-correlation	Mathematical Analysis
5.92	-	19.10	26.67	25.60
6.34	-	15.08	29.63	28.01
6.76	-	31.44	30.77	27.71
7.19	-	36.20	33.33	32.36
7.61	800.00	41.27	34.78	33.61
8.04	47.06	43.29	36.36	36.95
8.46	800.00	56.13	36.36	35.96
8.89	-	28.28	34.78	39.13
9.31	800.00	20.97	34.78	35.47

7.5 Summary

A comparative study has been conducted to evaluate the non-intrusive measurement techniques, viz, ECT and pressure fluctuation measurements. Four parameters have been investigated and they are signal amplitude, dominant frequency, solids concentration and bubble rising velocity.

Signal amplitude has been qualitatively analysed. The original data from ECT measurements are the averaged volume fraction at both ECT measuring planes. The original data from pressure fluctuation measurements are the direct pressure measured at pressure port 4 and port 5. Two types of data show their own capability in describing the bed behaviour at three different flow regimes which are the fixed bed, bubbling regime and slugging regime.

The frequency domain analysis approach of the power spectral density (PSD) function was employed to describe the bed behaviour. The dominant

frequency derived from the PSD, both from ECT and pressure measurements were analysed at both measuring locations. The derived minimum slugging velocity from both methods agree well with the previous conclusion drawn in Chapter 4. Solids concentration obtained from ECT and pressure fluctuation measurements generally agree with each other. Furthermore, the results from pressure fluctuation measurements show good potential in describing the flow regime transition between the bubbling regime and the slugging regime. Finally, bubble rising velocity results obtained from the pressure measurements and ECT measurements are compared. The conclusion drawn is that the ECT measurement is more capable of deriving the bubble rising velocity than pressure fluctuation measurement.

Chapter 8
Conclusions and Future Work

8.1 Conclusions

While the ECT measurement technique has been utilized in the application of gas-solids fluidized beds for a long time, the understanding of the bubble behaviour by means of ECT is still very limited, especially in estimating the bubble diameter.

To fulfil the two general aims which has been set in the Introduction chapter of the thesis, ECT and pressure fluctuation measurements have been carried out. In order to review the objectives outlined in Chapter 1 and to seek how well they have been met, the conclusions shown below are summarized accordingly.

a) Prior to constructing a customized twin-plane ECT sensor, a numerical simulation of the electrostatic field inside of the sensor has been conducted to establish the feasibility of the proposed ECT sensor. The simulation results showcased that the proposed layout of the twin-plane sensor is expected to be compatible with the available ECT data acquisition system. Subsequently, several key issues (i.e. number and length of the measuring electrodes, arrangments of the guard electrodes and resistors) were addressed in construtcitng the sensor.

b) A detailed calibration process utilizing plastic balls to derive the reference cut-off values has been conducted. This involved with a numerical simulation to investigate the plastic ball wall effect on the simulated capacitance values between each measuring electrode pair. The results indicated that the existence of the varied plastic ball wall would have a very limited effect on the measured capacitance values. Two locations (near centre and near wall of the bed pipe cross section) of the plastic balls and two image reconstruction algorithms (conventional LBP and 10 iterative LBP) were taken into consideration. The bubble diameters were estimated through three different approaches, namely, individual cut-off values, linear fitted curves and second-order fitted curves. The derived bubble diameters were compared and evaluated against five different empirical correlations.

   The results from the estimated bubble diameter shows that the individual cut-off values derived from the No. 1 plastic ball are by no

means effective in estimating bubble diameter and the possible reason of this phenomenon has been discussed in Chapter 6. The cut-off values derived from the No. 4 and No. 5 plastic balls performed better than the other three plastic balls, considering the agreement with the five different empirical correlations especially the equation of Werther. In addition, the cut-off values derived when the two plastic balls located near the wall of the bed pipe gave better bubble diameter estimation consistency compared with the empirical correlation results either by the conventional LBP or the 10 iterative LBP algorithm. Results obtained from the linear fitted curves of cut-off values demonstrated a reasonable agreement with the results calculated from Werther's equation using both the LBP algorithm and 10 iterative LBP algorithm. In general, results estimated from the second-order fitted curves showed a better data agreement than the linear fitted curves compared with the five empirical correlation results.

c) Bubble rising velocities were estimated via different approaches using the data from the ECT measurements. The cross-correlation technique was applied to predict the bubble rising velocity by using the averaged volume fraction data. The detailed mathematical analysis and cross-correlation estimation in three dimensional form on a pixel-to-pixel basis were implemented. The results derived from them agreed well with each other. A newly proposed statistic average approach utilizing the orignal 32 x 32 images has demonstrated its potential in deriving the bubble rising velocity compared with other approaches and the empirical correlation results.

d) In predicting the minimum fluidization velocity, the results estimated from the standard deviation of the pressure fluctuation measurements and of the averaged volume fraction from ECT measurements show good agreement compared with the simple and reliable pressure drop approach. It is somewhat surprising that the overall results of the minimum fluidization velocity estimated from the standard deviation of the ECT volume fraction data gave a good consistency compared with the ones obtained from the standard deviation of the pressure fluctuation results at different measurement heights. In estimating the minimum slugging velocity, the results obtained from the standard deviation of the ECT volume fraction data from both ECT planes have

very good agreement with the result estimated from the standard deviation of pressure fluctuation with an error of 2.6%.

e) To fulfil the second aim of the thesis, pressure fluctuation measurements have been performed and the data were captured in the same sampling rate of 200 Hz in order to compare and evaluate the performance of both non-intrusive measurement techniques in characterizing bubble behaviour in the gas-solids fluidized bed. The qualitative analysis of the signal amplitude between ECT and pressure fluctuation shows that both methods can provide a good description of the behaviour of three different flow regimes. As for the dominant frequency analysis, the results agree well with each other, despite some minor discrepancies. Both methods demonstrated their capability in describing the bed behaviour by means of the power spectral density function and the derived dominant frequency.

   The solids concentration results measured at both ECT measuring planes demonstrated no obvious differences between the conventional LBP and 10 iterative LBP algorithms. By comparing the solids concentration results obtained from ECT and pressure fluctuation measurements, both methods showcased effective capability with the percentage difference of 14.9%. Additionally, the solids concentration estimated from the pressure fluctuation can provide an indication of the flow regime transition between bubbling and slugging regimes while the results from the ECT measurements cannot.

   In respect of deriving bubble rising velocity, the cross-correlation techniques can be more effectively applied by using the data from the ECT measurements than using the data from pressure fluctuation measurements. The detailed mathematical analysis of the pressure fluctuation signal can provide comparative results as the data from ECT measurements did. However, visual assistance is necessary. The ECT measurements, by all means, provide more reliable estimation than the pressure fluctuation measurements.

8.2 Future Work

Although many significant conclusions have been drawn in the previous section, there is still much more work which needs to be done in relation to the ECT measurements and pressure fluctuation measurement to further

investigate the bubble and bed behaviour in the gas-solids fluidized bed. Possible future work is outlined below.

In ECT measurements:

a) the number of plastic balls could be increased to achieve a better fitting curve, either linear or second-order, in the process of calibration. In addition, the plastic balls could be manufactured with a more precise tolerance such as using 3D printing to keep the plastic ball wall as thin as possible and as consistent as within the limited number of different plastic balls.

b) the locations of plastic balls could be extended into the radial diameter direction across the bed pipe. Moreover, further investigation of different image reconstruction algorithms is still necessary, such as the Landweber, the iterative Landweber and neutral network algorithms.

c) the permittivity model utilized in the ECT software could be extended into the series model and the Maxwell model. The estimated bubble diameter results between the parallel model, series model and Maxwell model needs to be evaluated.

In pressure fluctuation measurements:

a) Bubble diameter estimation via the cross-power spectral density function could be worth trying by using pressure fluctuation measurements. A comparative study between the bubble size estimated from this method and the results obtained from ECT measurements.

b) Multi-resolution wavelet analysis could be carried out to investigate its capability in estimating bubble diameter and bubble frequency. The estimated results could be compared with the methods of a) and ECT estimation.

c) Chaos theory has been applied both in ECT measurements and pressure fluctuation measurements within gas-solids fluidized beds. An extensive comparative study is necessary to identify the advantages or shortcomings of both non-intrusive measurement techniques.

List of References

1. Geldart, D., *Gas fluidization technology.* 1986.
2. Yates, J., *Fundamentals of fluidized bed chemical processes.* 1983.
3. Kunii, D.O.l., *Fluidization Engineering.* Tohn Wiury, NY, 1969: p. 8-9.
4. Yang, W.-c., *Handbook of fluidization and fluid-particle systems*. Vol. 91. 2003: CRC Press.
5. Mills, D., *Pneumatic conveying design guide*. 2003: Butterworth-Heinemann.
6. Jaworski, A.J. and T. Dyakowski, *Investigations of flow instabilities within the dense pneumatic conveying system.* Powder Technology, 2002. **125**(2): p. 279-291.
7. JO, M., *Perry's chemical engineers' handbook*. 2008, McGraw Hill, New York, USA.
8. Sasic, S., B. Leckner, and F. Johnsson, *Characterization of fluid dynamics of fluidized beds by analysis of pressure fluctuations.* Progress in energy and combustion science, 2007. **33**(5): p. 453-496.
9. Grace, J., J. Zhao, R. Wu, R. Senior, R. Legros, C. Brereton, and C. Lim. *Spatial variations inside a pilot scale circulating fluidized bed combustion unit*. in *Proceedings of the Workshop on Materials Issues in Circulating Fluidized Bed Combustors*. 1990. EPRI Palo Alto.
10. Yates, J. and S. Simons, *Experimental methods in fluidization research.* International Journal of Multiphase Flow, 1994. **20**: p. 297-330.
11. Sit, S. and J. Grace, *Effect of bubble interaction on interphase mass transfer in gas fluidized beds.* Chemical Engineering Science, 1981. **36**(2): p. 327-335.
12. Weber, J.M. and J.S. Mei, *Bubbling fluidized bed characterization using electrical capacitance volume tomography (ECVT).* Powder technology, 2013. **242**: p. 40-50.
13. Harrison, D., R. Clift, and J.F. Davidson, *Fluidization*. 1985: Academic Press.
14. Makkawi, Y.T. and P.C. Wright, *Electrical capacitance tomography for conventional fluidized bed measurements—remarks on the measuring technique.* Powder technology, 2004. **148**(2): p. 142-157.
15. Makkawi, Y. and P. Wright, *The voidage function and effective drag force for fluidized beds.* Chemical engineering science, 2003. **58**(10): p. 2035-2051.
16. Makkawi, Y. and P. Wright, *Fluidization regimes in a conventional fluidized bed characterized by means of electrical capacitance tomography.* Chemical Engineering Science, 2002. **57**(13): p. 2411-2437.
17. Makkawi, Y. and P. Wright, *Optimization of experiment span and data acquisition rate for reliable electrical capacitance tomography measurement in fluidization studies—a case study.* Measurement Science and Technology, 2002. **13**(12): p. 1831.
18. Werther, J., *Measurement techniques in fluidized beds.* Powder Technology, 1999. **102**(1): p. 15-36.

19. Louge, M., *Experimental techniques*, in *Circulating fluidized beds*. 1997, Springer. p. 312-368.
20. Cheremisinoff, N.P., *Review of experimental methods for studying the hydrodynamics of gas-solid fluidized beds.* Industrial & Engineering Chemistry Process Design and Development, 1986. **25**(2): p. 329-351.
21. Rüdisüli, M., T.J. Schildhauer, S.M. Biollaz, and J.R. van Ommen, *Bubble characterization in a fluidized bed by means of optical probes.* International Journal of Multiphase Flow, 2012. **41**: p. 56-67.
22. Morse, R. and C. Ballou, *The uniformity of fluidization-its measurement and use.* Chemical Engineering Progress, 1951. **47**(4): p. 199-204.
23. Werther, J. and O. Molerus, *The local structure of gas fluidized beds—II. The spatial distribution of bubbles.* International Journal of Multiphase Flow, 1973. **1**(1): p. 123-138.
24. Werther, J.t. and O. Molerus, *The local structure of gas fluidized beds—I. A statistically based measuring system.* International Journal of Multiphase Flow, 1973. **1**(1): p. 103-122.
25. Rowe, P. and H. Masson, *Interaction of bubbles with probes in gas fluidised beds.* Transactions of the Institution of Chemical Engineers, 1981. **59**(3): p. 177-185.
26. Dyakowski, T. and A.J. Jaworski, *Non‐Invasive Process Imaging‐Principles and Applications of Industrial Process Tomography.* Chemical engineering & technology, 2003. **26**(6): p. 697-706.
27. Van der Schaaf, J., J. Schouten, F. Johnsson, and C. Van den Bleek, *Non-intrusive determination of bubble and slug length scales in fluidized beds by decomposition of the power spectral density of pressure time series.* International Journal of Multiphase Flow, 2002. **28**(5): p. 865-880.
28. Chaouki, J., F. Larachi, and M.P. Dudukovic, *Noninvasive tomographic and velocimetric monitoring of multiphase flows.* Industrial & engineering chemistry research, 1997. **36**(11): p. 4476-4503.
29. Byars, M. *Developments in electrical capacitance tomography*. in *2nd World Congress on Industrial Process Tomography, Hannover*. 2001.
30. Williams, R.A. and M.S. Beck, *Process tomography: principles, techniques, and applications*. 1995: Butterworth-Heinemann.
31. Wang, S., *Measurement of fluidization dynamics in fluidized beds using capacitance tomography*. 1998.
32. Yang, W. and S. Liu, *Role of tomography in gas/solids flow measurement.* Flow measurement and Instrumentation, 2000. **11**(3): p. 237-244.
33. Dyakowski, T., R. Edwards, C. Xie, and R. Williams, *Application of capacitance tomography to gas-solid flows.* Chemical Engineering Science, 1997. **52**(13): p. 2099-2110.
34. Halow, J., G. Fasching, and P. Nicoletti. *Preliminary capacitance imaging experiments of a fluidized bed*. in *AIChE Symp. Ser*. 1990.
35. Xie, C., S. Huang, B. Hoyle, R. Thorn, C. Lenn, D. Snowden, and M. Beck. *Electrical capacitance tomography for flow imaging: system model for development of image reconstruction algorithms and design of primary sensors*. in *Circuits, Devices and Systems, IEE Proceedings G*. 1992. IET.
36. Huang, S., T. Dyakowski, C. Xie, A. Plaskowski, L. Xu, and M. Beck. *A tomographic flow imaging system based on capacitance measuring*

techniques. in *Pattern Recognition, 1988., 9th International Conference on*. 1988. IEEE.

37. Liu, S., Q. Chen, H. Wang, F. Jiang, I. Ismail, and W. Yang, *Electrical capacitance tomography for gas–solids flow measurement for circulating fluidized beds.* Flow Measurement and Instrumentation, 2005. **16**(2): p. 135-144.
38. Liu, S., W. Yang, H. Wang, F. Jiang, and Y. Su, *Investigation of square fluidized beds using capacitance tomography: preliminary results.* Measurement Science and Technology, 2001. **12**(8): p. 1120.
39. Liu, S., W. Yang, H. Wang, G. Yan, and Z. Pan, *Flow pattern identification of fluidized beds using ECT.* Journal of Thermal Science, 2001. **10**(2): p. 176-181.
40. Dyakowski, T., L.F. Jeanmeure, and A.J. Jaworski, *Applications of electrical tomography for gas–solids and liquid–solids flows—a review.* Powder technology, 2000. **112**(3): p. 174-192.
41. Chaplin, G. and T. Pugsley, *Application of electrical capacitance tomography to the fluidized bed drying of pharmaceutical granule.* Chemical Engineering Science, 2005. **60**(24): p. 7022-7033.
42. Pugsley, T., H. Tanfara, S. Malcus, H. Cui, J. Chaouki, and C. Winters, *Verification of fluidized bed electrical capacitance tomography measurements with a fibre optic probe.* Chemical Engineering Science, 2003. **58**(17): p. 3923-3934.
43. Chandrasekera, T., Y. Li, D. Moody, M. Schnellmann, J. Dennis, and D. Holland, *Measurement of bubble sizes in fluidised beds using electrical capacitance tomography.* Chemical Engineering Science, 2015. **126**: p. 679-687.
44. Wang, S., T. Dyakowski, C. Xie, R. Williams, and M. Beck, *Real time capacitance imaging of bubble formation at the distributor of a fluidized bed.* The Chemical Engineering Journal and The Biochemical Engineering Journal, 1995. **56**(3): p. 95-100.
45. Dyakowski, T. and A. Jaworski, *Application of non-invasive techniques for imaging fluidized beds—a review.* Handbook of Powder Technology, 2001. **10**: p. 807-823.
46. van Ommen, J.R., S. Sasic, J. Van der Schaaf, S. Gheorghiu, F. Johnsson, and M.-O. Coppens, *Time-series analysis of pressure fluctuations in gas–solid fluidized beds–A review.* International Journal of Multiphase Flow, 2011. **37**(5): p. 403-428.
47. Bi, H.T., *A critical review of the complex pressure fluctuation phenomenon in gas–solids fluidized beds.* Chemical Engineering Science, 2007. **62**(13): p. 3473-3493.
48. Johnsson, F., R. Zijerveld, J. Schouten, C. Van den Bleek, and B. Leckner, *Characterization of fluidization regimes by time-series analysis of pressure fluctuations.* International journal of multiphase flow, 2000. **26**(4): p. 663-715.
49. van Ommen, J.R. and R.F. Mudde, *Measuring the Gas-Solids Distribution in Fluidized Beds--A Review.* International Journal of Chemical Reactor Engineering, 2008. **6**(1).
50. van Ommen, J.R., J.C. Schouten, M.L. vander Stappen, and C.M. van den Bleek, *Response characteristics of probe–transducer systems for pressure measurements in gas–solid fluidized beds: how to prevent*

pitfalls in dynamic pressure measurements. Powder Technology, 1999. **106**(3): p. 199-218.

51. Kage, H., M. Agari, H. Ogura, and Y. Matsuno, *Frequency analysis of pressure fluctuation in fluidized bed plenum and its confidence limit for detection of various modes of fluidization.* Advanced Powder Technology, 2000. **11**(4): p. 459-475.
52. Kage, H., N. Iwasaki, H. Yamaguchi, and Y. Matsuno, *Frequency analysis of pressure fluctuation in fluidized bed plenum.* Journal of Chemical Engineering of Japan, 1991. **24**(1): p. 76-81.
53. Kwauk, M., *Fluidization: idealized and bubbleless, with applications*. 1992: Science Press.
54. Toomey, R. and H. Johnstone, *Gaseous fluidization of solid particles.* Chemical Engineering Progress, 1952. **48**(5): p. 220-226.
55. Grace, J. and R. Clift, *On the two-phase theory of fluidization.* Chemical Engineering Science, 1974. **29**(2): p. 327-334.
56. Geldart, D., *Types of gas fluidization.* Powder technology, 1973. **7**(5): p. 285-292.
57. Grace, J.R., *Contacting modes and behaviour classification of gas—solid and other two‐phase suspensions.* The Canadian Journal of Chemical Engineering, 1986. **64**(3): p. 353-363.
58. Ergun, S., *Fluid flow through packed columns.* Chem. Eng. Prog., 1952. **48**.
59. Wen, C. and Y. Yu, *A generalized method for predicting the minimum fluidization velocity.* AIChE Journal, 1966. **12**(3): p. 610-612.
60. Stewart, P.S.B. and J. Davidson, *Slug flow in fluidised beds.* Powder Technology, 1967. **1**(2): p. 61-80.
61. Grace, J.R. and H. Bi, *Introduction to circulating fluidized beds*, in *Circulating fluidized beds*. 1997, Springer. p. 1-20.
62. Rowe, P. and R. Matsuno, *Single bubbles injected into a gas fluidised bed and observed by X-rays.* Chemical Engineering Science, 1971. **26**(6): p. 923-935.
63. Rowe, P. and B. Partridge, *An x-ray study of bubbles in fluidised beds.* Transactions of the Institution of Chemical Engineers, 1965. **43**: p. 157-165.
64. Grace, J., *The viscosity of fluidized beds.* The Canadian Journal of Chemical Engineering, 1970. **48**(1): p. 30-33.
65. Darton, R., *Bubble growth due to coalescence in fluidized beds.* Chem. Eng. Res. Des., 1977. **55**: p. 274-280.
66. Karimipour, S. and T. Pugsley, *A critical evaluation of literature correlations for predicting bubble size and velocity in gas–solid fluidized beds.* Powder Technology, 2011. **205**(1): p. 1-14.
67. Miwa, K., I. Muchi, S. Mori, and T. Kato, *Behavior of bubbles in a gaseous fluidized-bed.* International Chemical Engineering, 1972. **12**(1): p. 187-&.
68. Rowe, P. and C. Yacono, *The bubbling behaviour of fine powders when fluidised.* Chemical Engineering Science, 1976. **31**(12): p. 1179-1192.
69. Rowe, P. and D. Everett, *Fluidized bed bubbles viewed by X-rays. Pt. 1. Experimental details and the interaction of bubbles with solid surfaces.* Trans Inst Chem Eng, 1972. **50**(1): p. 42-48.

70. Rowe, P. and D. Everett, *Fluidized bed bubbles viewed by X-rays. Part.2. Transition from two- to three-dimensions of undisturbed bubbles.* TRANS INST CHEM ENG, 1972. **50**(1): p. 49-54.
71. Rowe, P. and D. Everett, *Fluidized bed bubbles viewed by X-rays. Part.3. Bubble size and number when unrestrained three dimensional growth occurs.* TRANS INST CHEM ENG, 1972. **50**(1): p. 55-60.
72. Mori, S. and C. Wen, *Estimation of bubble diameter in gaseous fluidized beds.* AIChE Journal, 1975. **21**(1): p. 109-115.
73. Werther, J., *Effect of gas distributor on the hydrodynamics of gas fluidized beds.* German Chemical Engineering, 1978. **1**: p. 166-174.
74. Werther, J., *Bubbles in gas fluidised beds—part I.* Transactions of the Institution of Chemical Engineers, 1974. **52**: p. 160-169.
75. WERTHER, J., *Bubbles in gas fluidised beds -- Part II.* 1974.
76. Werther, J. *Influence of the bed diameter on the hydrodynamics of gas fluidized beds*. in *AIChE Symp. Ser*. 1974.
77. Cai, P., M. Schiavetti, G. De Michele, G. Grazzini, and M. Miccio, *Quantitative estimation of bubble size in PFBC.* Powder technology, 1994. **80**(2): p. 99-109.
78. Rowe, P.N., *Prediction of bubble size in a gas fluidised bed.* Chemical Engineering Science, 1976. **31**(4): p. 285-288.
79. Whitehead, A., D. Dent, and G. Bhat, *Fluidisation studies in large gas-solid systems Part I: Bubble rise rates.* Powder Technology, 1967. **1**(3): p. 143-148.
80. Whitehead, A., D. Dent, and A. Young, *Fluidisation studies in large gas-solid systems Part II: The effect of distributor design and solid properties on fluidisation quality.* Powder Technology, 1967. **1**(3): p. 149-156.
81. Davies, R. and G. Taylor. *The mechanics of large bubbles rising through extended liquids and through liquids in tubes*. in *Proceedings of the Royal Society of London A: Mathematical, Physical and Engineering Sciences*. 1950. The Royal Society.
82. Davidson, J.F. and D. Harrison, *Fluidised particles*. Vol. 3. 1963: Cambridge University Press London.
83. Chan, I., C. Sishtla, and T. Knowlton, *The effect of pressure on bubble parameters in gas-fluidized beds.* Powder Technology, 1987. **53**(3): p. 217-235.
84. Yasui, G. and L. Johanson, *Characteristics of gas pockets in fluidized beds.* AIChE Journal, 1958. **4**(4): p. 445-452.
85. Sobrino, C., J.A. Almendros-Ibáñez, D. Santana, C. Vázquez, and M. de Vega, *Maximum entropy estimation of the bubble size distribution in fluidized beds.* Chemical Engineering Science, 2009. **64**(10): p. 2307-2319.
86. Cui, H., N. Mostoufi, and J. Chaouki, *Characterization of dynamic gas–solid distribution in fluidized beds.* Chemical Engineering Journal, 2000. **79**(2): p. 133-143.
87. Liu, J., J.R. Grace, and X. Bi, *Novel multifunctional optical‐fiber probe: I. Development and validation.* AIChE journal, 2003. **49**(6): p. 1405-1420.
88. Oki, K. and T. Shirai, *Particle velocity in fluidized bed.* Fluidization Technology, 1976. **1**: p. 95-110.

89. Oki, K., T. Akehata, and T. Shirai, *A new method for evaluating the size of moving particles with a fiber optic probe.* Powder Technology, 1975. **11**(1): p. 51-57.
90. Vázquez, C., J.L. Nombela, M.d. Vega, J. Zubía, and D. Sánchez Montero. *Plastic fiber-optic probes for characterizing fluidized beds in bubbling regime*. 2007. 16th International Conference on Plastic Optical Fibers.
91. Schweitzer, J., J. Bayle, and T. Gauthier, *Local gas hold-up measurements in fluidized bed and slurry bubble column.* Chemical Engineering Science, 2001. **56**(3): p. 1103-1110.
92. Reyes-Vera, E., D. Dominguez-Gomez, J.D. Causado-Buelvas, P. Torres, Y. Moreno, C. Londono, and A. Molina, *Three-fiber optical probe for studying fluidized gas-solid beds in bubbling regime.* Dyna, 2011. **78**(166): p. 55-59.
93. Mainland, M.E. and J.R. Welty, *Use of optical probes to characterize bubble behavior in gas‐solid fluidized beds.* AIChE Journal, 1995. **41**(2): p. 223-228.
94. Johnsson, H. and F. Johnsson, *Measurements of local solids volume-fraction in fluidized bed boilers.* Powder Technology, 2001. **115**(1): p. 13-26.
95. Maxwell, J.C., *A treatise on electricity and magnetism*. Vol. 1. 1892: Clarendon.
96. Yutani, N., T. Ho, L. Fan, W. Walawender, and J. Song, *Statistical study of the grid zone behavior in a shallow gas—solid fluidized bed using a mini-capacitance probe.* Chemical engineering science, 1983. **38**(4): p. 575-582.
97. Geldart, D. and J. Kelsey, *The use of capacitance probes in gas fluidised beds.* Powder Technology, 1972. **6**(1): p. 45-50.
98. Hage, B., J. Werther, K. Narukawa, and S. Mori, *Capacitance probe measurement technique for local particle volume concentration in circulating fluidized bed combustors.* Journal of chemical engineering of Japan, 1996. **29**(4): p. 594-602.
99. Riley, C.A. and M. Louge, *Quantitative capacitive measurements of voidage in gas-solid flows.* Particulate science and technology, 1989. **7**(1-2): p. 51-59.
100. Hage, B. and J. Werther, *The guarded capacitance probe—a tool for the measurement of solids flow patterns in laboratory and industrial fluidized bed combustors.* Powder Technology, 1997. **93**(3): p. 235-245.
101. Rowe, P. and H. Masson, *Fluidised bed bubbles observed simultaneously by probe and by X-rays.* Chemical Engineering Science, 1980. **35**(6): p. 1443-1447.
102. Simons, S., *Imaging techniques for fluidized bed systems: a review.* The Chemical Engineering Journal and the Biochemical Engineering Journal, 1995. **56**(3): p. 83-93.
103. Geldart, D. and R. Cranfield, *The gas fluidisation of large particles.* The Chemical Engineering Journal, 1972. **3**: p. 211-231.
104. Arena, U., A. Cammarota, A. Marzocchella, and L. Massimilla, *Solids flow structures in a two-dimensional riser of a circulating fluidized bed.* Journal of chemical engineering of Japan, 1989. **22**(3): p. 236-241.

105. Hailu, L., F. Plaka, R. Clift, and J. Davidson, *Measurement of gas flow through a two-dimensional bubble in a fluidised bed: particle processing.* Chemical engineering research & design, 1993. **71**(4): p. 382-389.
106. Whiting, K. and D. Geldart, *A comparison of cylindrical and semi-cylindrical spouted beds of coarse particles.* Chemical Engineering Science, 1980. **35**(6): p. 1499-1501.
107. Geldart, D., A. Hemsworth, R. Sundavadra, and K. Whiting, *A comparison of spouting and jetting in round and half‐round fluidized beds.* The Canadian Journal of Chemical Engineering, 1981. **59**(5): p. 638-639.
108. Rowe, P., H. MacGillivray, and D. Cheesman, *Gas discharge from an orifice into a gas fluidized bed.* Trans. Inst. Chem. Eng, 1979. **57**: p. 194.
109. Kai, T., M. Misawa, T. Takahashi, I. Tiseanu, and N. Ichikawa, *Observation of 3‐D Structure of Bubbles in a Fluidized Catalyst Bed.* The Canadian Journal of Chemical Engineering, 2005. **83**(1): p. 113-118.
110. Kai, T., M. Misawa, T. Takahashi, I. Tiseanu, N. Ichikawa, and N. Takada, *Application of Fast X-ray CT Scanner to Visualization of Bubbles in Fluidized Bed.* Journal of chemical engineering of Japan, 2000. **33**(6): p. 906-909.
111. Grohse, E., *Analysis of gas‐fluidized solid systems by x‐ray absorption.* AIChE Journal, 1955. **1**(3): p. 358-365.
112. Yates, J. and D. Cheesman. *Voidage variations in the regions surrounding a rising bubble in a fluidized bed*. in *AIChE Symposium Series*. 1992. American Institute of Chemical Engineers.
113. Yates, J., R. Ruiz-Martinez, and D. Cheesman, *Prediction of bubble size in a fluidized bed containing horizontal tubes.* Chemical Engineering Science, 1990. **45**(4): p. 1105-1111.
114. Hoffmann, A. and J. Yates, *Experimental observations of fluidized beds at elevated pressures.* Chemical Engineering Communications, 1986. **41**(1-6): p. 133-149.
115. Barreto, G., J. Yates, and P. Rowe, *The effect of pressure on the flow of gas in fluidized beds of fine particles.* Chemical engineering science, 1983. **38**(12): p. 1935-1945.
116. Rowe, P., P. Foscolo, A. Hoffmann, and J. Yates, *Fine powders fluidised at low velocity at pressures up to 20 bar with gases of different viscosity.* Chemical Engineering Science, 1982. **37**(7): p. 1115-1117.
117. Rowe, P., L. Santoro, and J. Yates, *The division of gas between bubble and interstitial phases in fluidised beds of fine powders.* Chemical Engineering Science, 1978. **33**(1): p. 133-140.
118. Martin, M., P. Turlier, J. Bernard, and G. Wild, *Gas and solid behavior in cracking circulating fluidized beds.* Powder Technology, 1992. **70**(3): p. 249-258.
119. Baumgarten, P. and R. Pigford, *Density fluctuations in fluidized beds.* AIChE Journal, 1960. **6**(1): p. 115-123.
120. Seville, J., J. Morgan, and R. Clift, *Tomographic determination of the voidage structure of gas fluidised beds in the jet region*, in *Proceedings of fluidization V*. 1986.

121. Simons, S., J. Seville, R. Clift, W. Gilboy, and M. HOSSEINIASHRAFI, *Application of Gamma-ray tomography to gas-fluidized and spouted beds.* 1993.
122. Wang, M., *Industrial tomography: systems and applications*. 2015: Elsevier.
123. Marashdeh, Q., L.-S. Fan, B. Du, and W. Warsito, *Electrical capacitance tomography-a perspective.* Industrial & Engineering Chemistry Research, 2008. **47**(10): p. 3708-3719.
124. Dickin, F., B. Hoyle, A. Hunt, S. Huang, O. Ilyas, C. Lenn, . . . M. Beck. *Tomographic imaging of industrial process equipment: techniques and applications*. in *Circuits, Devices and Systems, IEE Proceedings G*. 1992. IET.
125. Jaworski, A. and T. Dyakowski. *Tomographic measurements of solids mass flow in dense pneumatic conveying. What do we need to know about the flow physics*. in *2nd World Congress on Industrial Process Tomography, Hannover, Germany*. 2001.
126. Liu, S., L. Fu, and W. Yang, *Optimization of an iterative image reconstruction algorithm for electrical capacitance tomography.* Measurement Science and Technology, 1999. **10**(7): p. L37.
127. Yang, W., J. Gamio, and M. Beck, *A fast iterative image reconstruction algorithm for capacitance tomography.* Sensors and their Applications, 1997. **8**: p. 47-52.
128. Yang, W., D. Spink, T. York, and H. McCann, *An image-reconstruction algorithm based on Landweber's iteration method for electrical-capacitance tomography.* Measurement Science and Technology, 1999. **10**(11): p. 1065.
129. Yang, W. and M. Byars, *An improved normalisation approach for electrical capacitance tomography.* Proc. 1st World Congr. on Industrial Process Tomography (Buxton, UK), 1999: p. 215-8.
130. Jaworski, A.J. and G. Meng, *On-line measurement of separation dynamics in primary gas/oil/water separators: challenges and technical solutions—a review.* Journal of Petroleum Science and Engineering, 2009. **68**(1): p. 47-59.
131. Meng, G., A.J. Jaworski, T. Dyakowski, J.M. Hale, and N.M. White, *Design and testing of a thick-film dual-modality sensor for composition measurements in heterogeneous mixtures.* Measurement Science and Technology, 2005. **16**(4): p. 942.
132. Jaworski, A. and G. Bolton, *The design of an electrical capacitance tomography sensor for use with media of high dielectric permittivity.* Measurement Science and Technology, 2000. **11**(6): p. 743.
133. Meng, G., A.J. Jaworski, and J.C. Kimber, *A multi-electrode capacitance probe for phase detection in oil–water separation processes: design, modelling and validation.* Measurement Science and Technology, 2006. **17**(4): p. 881.
134. Meng, G., A.J. Jaworski, and N.M. White, *Composition measurements of crude oil and process water emulsions using thick-film ultrasonic transducers.* Chemical Engineering and Processing: Process Intensification, 2006. **45**(5): p. 383-391.
135. Wang, H., P. Senior, R. Mann, and W. Yang, *Online measurement and control of solids moisture in fluidised bed dryers.* Chemical Engineering Science, 2009. **64**(12): p. 2893-2902.

136. Pugsley, T., G. Chaplin, and P. Khanna, *Application of advanced measurement techniques to conical lab-scale fluidized bed dryers containing pharmaceutical granule.* Food and Bioproducts Processing, 2007. **85**(3): p. 273-283.
137. Wiens, J. and T. Pugsley, *Tomographic imaging of a conical fluidized bed of dry pharmaceutical granule.* Powder technology, 2006. **169**(1): p. 49-59.
138. Ge, R., J. Ye, H. Wang, and W. Yang, *Measurement of particle concentration in a Wurster fluidized bed by electrical capacitance tomography sensors.* AIChE Journal, 2014. **60**(12): p. 4051-4064.
139. Halow, J., G. Fasching, P. Nicoletti, and J. Spenik, *Observations of a fluidized bed using capacitance imaging.* Chemical Engineering Science, 1993. **48**(4): p. 643-659.
140. Halow, J. and P. Nicoletti, *Observations of fluidized bed coalescence using capacitance imaging.* Powder Technology, 1992. **69**(3): p. 255-277.
141. Huang, S., C. Xie, R. Thorn, D. Snowden, and M. Beck, *Design of sensor electronics for electrical capacitance tomography.* IEE Proceedings G-Circuits, Devices and Systems, 1992. **139**(1): p. 83-88.
142. Huang, S., A. Plaskowski, C. Xie, and M. Beck, *Tomographic imaging of two-component flow using capacitance sensors.* Journal of Physics E: Scientific Instruments, 1989. **22**(3): p. 173.
143. Huang, S., A. Stott, R. Green, and M. Beck, *Electronic transducers for industrial measurement of low value capacitances.* Journal of Physics E: Scientific Instruments, 1988. **21**(3): p. 242.
144. Isaksen, Ø., *A review of reconstruction techniques for capacitance tomography.* Measurement Science and Technology, 1996. **7**(3): p. 325.
145. McKeen, T.R. and T.S. Pugsley, *The influence of permittivity models on phantom images obtained from electrical capacitance tomography.* Measurement Science and technology, 2002. **13**(12): p. 1822.
146. Sun, T., R. Mudde, J. Schouten, B. Scarlett, and C. Van den Bleek, *Image reconstruction of an electrical capacitance tomography system using an artificial neural network.* system, 1999. **6**: p. 6.
147. Brodowicz, K., L. Maryniak, and T. Dyakowski, *Application of capacitance tomography for pneumatic conveying processes.* Tomographic Techniques for Process Design and Operation, 1993: p. 361-8.
148. Yang, W. and S. Liu, *Electrical capacitance tomography with square sensor.* Electronics Letters, 1999. **35**(4): p. 295-296.
149. McKeen, T. and T. Pugsley, *Simulation and experimental validation of a freely bubbling bed of FCC catalyst.* Powder Technology, 2003. **129**(1): p. 139-152.
150. Svensson, A., F. Johnsson, and B. Leckner, *Fluidization regimes in non-slugging fluidized beds: the influence of pressure drop across the air distributor.* Powder Technology, 1996. **86**(3): p. 299-312.
151. Malcus, S., G. Chaplin, and T. Pugsley, *The hydrodynamics of the high-density bottom zone in a CFB riser analyzed by means of electrical capacitance tomography (ECT).* Chemical Engineering Science, 2000. **55**(19): p. 4129-4138.

152. Verloop, J. and P. Heertjes, *Periodic pressure fluctuations in fluidized beds.* Chemical Engineering Science, 1974. **29**(4): p. 1035-1042.
153. Kage, H., N. Iwasaki, and Y. Matsuno. *Frequency analysis of pressure fluctuation in plenum as a diagnostic method for fluidized beds*. in *AIChE Symposium Series*. 1993. American Institute of Chemical Engineers.
154. Musmarra, D., M. Poletto, S. Vaccaro, and R. Clift, *Dynamic waves in fluidized beds.* Powder technology, 1995. **82**(3): p. 255-268.
155. Van der Schaaf, J., J. Schouten, and C. Van den Bleek, *Origin, propagation and attenuation of pressure waves in gas—solid fluidized beds.* Powder Technology, 1998. **95**(3): p. 220-233.
156. Fan, L., T.C. Ho, S. Hiraoka, and W. Walawender, *Pressure fluctuations in a fluidized bed.* AIChE Journal, 1981. **27**(3): p. 388-396.
157. Baskakov, A., V. Tuponogov, and N. Filippovsky, *A study of pressure fluctuations in a bubbling fluidized bed.* Powder Technology, 1986. **45**(2): p. 113-117.
158. Sadasivan, N., D. Barreteau, and C. Laguerie, *Studies on frequency and magnitude of fluctuations of pressure drop in gas—solid fluidized beds.* Powder Technology, 1980. **26**(1): p. 67-74.
159. Leu, L.-P. and C.-W. Lan, *Measurement of pressure fluctuations in two-dimensional gas-solid fluidized beds at elevated temperatures.* Journal of Chemical Engineering of Japan, 1990. **23**(5): p. 555-562.
160. Ren, J., Q. Mao, J. Li, and W. Lin, *Wavelet analysis of dynamic behavior in fluidized beds.* Chemical Engineering Science, 2001. **56**(3): p. 981-988.
161. Yang, T.-Y. and L.-P. Leu, *Multi-resolution analysis of wavelet transform on pressure fluctuations in an L-valve.* International Journal of Multiphase Flow, 2008. **34**(6): p. 567-579.
162. Guo, Q., G. Yue, T. Suda, and J. Sato, *Flow characteristics in a bubbling fluidized bed at elevated temperature.* Chemical Engineering and Processing: Process Intensification, 2003. **42**(6): p. 439-447.
163. Hay, J., B. Nelson, C. Briens, and M. Bergougnou, *The calculation of the characteristics of a chaotic attractor in a gas-solid fluidized bed.* Chemical Engineering Science, 1995. **50**(3): p. 373-380.
164. Bai, D., H. Bi, and J. Grace, *Chaotic behavior of fluidized beds based on pressure and voidage fluctuations.* AIChE journal, 1997. **43**(5): p. 1357-1361.
165. Van der Schaaf, J., J. Van Ommen, F. Takens, J. Schouten, and C. Van den Bleek, *Similarity between chaos analysis and frequency analysis of pressure fluctuations in fluidized beds.* Chemical Engineering Science, 2004. **59**(8): p. 1829-1840.
166. van den Bleek, C.M., M.-O. Coppens, and J.C. Schouten, *Application of chaos analysis to multiphase reactors.* Chemical Engineering Science, 2002. **57**(22): p. 4763-4778.
167. Lee, G.S. and S.D. KIM, *Pressure fluctuations in turbulent fluidized beds.* Journal of Chemical Engineering of Japan, 1988. **21**(5): p. 515-521.
168. Bi, H., N. Ellis, I. Abba, and J. Grace, *A state-of-the-art review of gas–solid turbulent fluidization.* Chemical Engineering Science, 2000. **55**(21): p. 4789-4825.

169. Fan, L., T.C. Ho, and W. Walawender, *Measurements of the rise velocities of bubbles, slugs and pressure waves in a gas‐solid fluidized bed using pressure fluctuation signals.* AIChE Journal, 1983. **29**(1): p. 33-39.
170. Felipe, C.A.S. and S. Rocha, *Time series analysis of pressure fluctuation in gas-solid fluidized beds.* Brazilian Journal of Chemical Engineering, 2004. **21**(3): p. 497-507.
171. Yang, W., *Design of electrical capacitance tomography sensors.* Measurement Science and Technology, 2010. **21**(4): p. 042001.
172. Yan, H., F. Shao, and S. Wang. *Simulation study of capacitance tomography sensors*. in *Proceedings of the 1st World Congress on Industrial Process Tomography, Buxton, Greater Manchester, UK*. 1999.
173. Flores, N., J.C. Gamio, C. Ortiz-Alemán, and E. Damián. *Sensor modeling for an electrical capacitance tomography system applied to oil industry*. in *Excerpt from the Proceedings of the COMSOL Multiphysics User's Conference*. 2005.
174. Mohamad, E., R. Rahim, P.L. Leow, M.F. Rahiman, O. Marwah, N.N. Ayob, . . . F.M. Yunus, *An introduction of two differential excitation potentials technique in electrical capacitance tomography.* Sensors and Actuators A: Physical, 2012. **180**: p. 1-10.
175. Ltd, P.T., *Engineering Design Rules for ECT sensors.* PTL300E Application Note AN3, 2001. **4**.
176. Li, X., A. Jaworski, and X. Mao. *Application of a Twin-plane Electrical Capacitance Tomography Sensor for Characterising Bubble Behaviour in a Gas-solids Fluidized Bed*. in *Proceedings of World Congress on Engineering 2016*. 2016. London,UK: IAENG.
177. Ltd, P.T., *ECT User Guide.* PTL300E Application Note 2001.
178. Li, X., A. Jaworski, and X. Mao, *Investigation of bubble behaviour in a gas-solid fluidized bed by means of a twin-plane ECT sensor (in press).* 8th World Congress on Industrial Process Tomography, Iguassu Falls, Brazil, 2016.
179. Arko, A., R. Waterfall, M. Beck, T. Dyakowski, P. Sutcliffe, and M. Byars. *Development of electrical capacitance tomography for solids mass flow measurement and control of pneumatic conveying systems*. in *1st World Congress on Industrial Process Tomography, Buxton, Greater Manchester*. 1999.
180. Svoboda, K. and M. Hartman, *Influence of temperature on incipient fluidization of limestone, lime, coal ash, and corundum.* Industrial & Engineering Chemistry Process Design and Development, 1981. **20**(2): p. 319-326.
181. Svoboda, K. and M. Hartman, *Deviations of actual minimum fluidization velocities from theoretical predictions at different temperatures.* AIChE Journal, 1981. **27**(5): p. 866-869.
182. Botterill, J., Y. Teoman, and K. Yüregir, *The effect of operating temperature on the velocity of minimum fluidization, bed voidage and general behaviour.* Powder Technology, 1982. **31**(1): p. 101-110.
183. Wilkinson, D., *Determination of minimum fluidization velocity by pressure fluctuation measurement.* The Canadian Journal of Chemical Engineering, 1995. **73**(4): p. 562-565.

184. Punčochář, M., J. Drahoš, J. Čermák, and K. Selucký, *Evaluation of minimum fluidizing velocity in gas fluidized bed from pressure fluctuations.* Chemical Engineering Communications, 1985. **35**(1-6): p. 81-87.
185. Hong, S., B. Jo, D. Doh, and C. Choi, *Determination of minimum fluidization velocity by the statistical analysis of pressure fluctuations in a gas—solid fluidized bed.* Powder Technology, 1990. **60**(3): p. 215-221.
186. Qiu, G., J. Ye, H. Wang, and W. Yang, *Investigation of flow hydrodynamics and regime transition in a gas–solids fluidized bed with different riser diameters.* Chemical Engineering Science, 2014. **116**: p. 195-207.
187. Warsito, W. and L.-S. Fan, *Neural network multi-criteria optimization image reconstruction technique (NN-MOIRT) for linear and non-linear process tomography.* Chemical Engineering and Processing: Process Intensification, 2003. **42**(8): p. 663-674.
188. Broadhurst, T. and H. Becker, *Onset of fluidization and slugging in beds of uniform particles.* AIChE Journal, 1975. **21**(2): p. 238-247.
189. Baeyens, J. and D. Geldart, *An investigation into slugging fluidized beds.* Chemical Engineering Science, 1974. **29**(1): p. 255-265.
190. Beck, M.S. and A. Pląskowski, *Cross correlation flowmeters, their design and application*. 1987: CRC Press.
191. Wang, M., Y. Ma, N. Holliday, Y. Dai, R.A. Williams, and G. Lucas, *A high-performance EIT system.* IEEE Sensors Journal, 2005. **5**(2): p. 289-299.
192. Wu, Y., H. Li, M. Wang, and R.A. Williams, *Characterization of Air‐Water Two‐Phase Vertical Flow by Using Electrical Resistance Imaging.* The Canadian journal of chemical engineering, 2005. **83**(1): p. 37-41.
193. Liu, S., S. Wang, D. Mason, T. Dyakowski, and D. Geldart. *Measurement of solids concentration in gas-solid flows using capacitance tomography and pressure sensors*. in *Proc. 8th Conf. on Sensors and their Applications*. 1997.
194. Bai, D., E. Shibuya, N. Nakagawa, and K. Kato, *Characterization of gas fluidization regimes using pressure fluctuations.* Powder Technology, 1996. **87**(2): p. 105-111.

Appendix A
Publications

Xiaoxu LI, Artur J. JAWORSKI, and Xiaoan MAO, "Application of a Twin-plane Electrical Capacitance Tomography Sensor for Characterising Bubble Behaviour in a Gas-solids Fluidized Bed," Lecture Notes in Engineering and Computer Science: Proceedings of The World Congress on Engineering 2016, 29 June - 1 July, 2016, London, U.K., pp1100-1105

Li, X., Jaworski, A.J. and Mao, X., " Investigation of bubble behaviour in a gas-solid fluidized bed by means of a twin-plane ECT sensor." 8th World Congress on Industrial Process Tomography, Iguassu Falls, Brazil. 2016.